UNIVERSIDAD COMPLUTENSE DE MADRID

FACULTAD DE CIENCIAS FÍSICAS

TESIS DOCTORAL

Towards a more realistic description of nuclear effects in lepton-nucleus scattering

Hacia una descripción más realista de los efectos nucleares en la dispersión leptón-núcleo

MEMORIA PARA OPTAR AL GRADO DE DOCTOR

PRESENTADA POR

Tania Franco Muñoz

DIRIGIDA POR

Raúl González Jiménez
José Manuel Udías Moinelo

Universidad Complutense de Madrid
Facultad de Ciencias Físicas

Programa de Doctorado en Física

UNIVERSIDAD
COMPLUTENSE
MADRID

Towards a more realistic description of nuclear effects in lepton-nucleus scattering

Hacia una descripción más realista de los efectos nucleares en la dispersión leptón-núcleo

MEMORIA PARA OPTAR AL GRADO DE DOCTOR PRESENTADA POR

Tania Franco Muñoz

Directores:
Raúl González Jiménez
José Manuel Udías Moinelo

Madrid, 2025

A José, a Carmen, a Antonio, a Isabel,

a Mari Carmen, a Pepe,

a Borja,

por siempre creer en mi, por enseñarme tanto.

Agradecimientos

Diría que mi llegada a este doctorado fue toda una afortunada serie de catastróficas desdichas. Yo, decidida a ser física teórica desde que empecé la carrera, tras un Máster en Física Teórica y una primera fallida solicitud de beca FPU, decidí que la Física Nuclear era un bonito camino para iniciar una nueva aventura. Lo que no esperaba es que, tras enviar mi solicitud para el Máster en Física Nuclear, José Manuel me mandaría un correo a una hora un poco intempestiva ofreciéndome saltarme el paso del máster y empezar un doctorado en neutrinos, una oportunidad que no pude rechazar, y que finalmente pude desarrollar gracias a una segunda exitosa solicitud de beca FPU.

Durante estos 5 años he aprendido muchísimas cosas. Quiero empezar agradeciendo a Raúl por todo su tiempo y paciencia, por sentarse conmigo durante horas a discutir cualquier problema que tuviese, a mirar mis cálculos y mis códigos, pero sobre todo por toda la dedicación que ha tenido en este trabajo. A José Manuel, sin duda tengo que agradecerle todo su conocimiento, desde esas primeras semanas enseñándome lo más básico de la Física Nuclear, hasta estos días con discusiones mucho más avanzadas donde siempre su sabiduría ha sido una referencia clave cuando no sabía ni cómo empezar.

Por supuesto, nada hubiera sido lo mismo sin mis compañeros del GFN. Quiero empezar agradeciéndole a Javi por ser el mejor compi de neutrinos que podría tener, y por hacer siempre mejores tanto los días de trabajo como los viajes. En cuanto a despachos, no puedo dejar de mencionar a Murias, por su acogida en la antigua secretaría cuando llegué al grupo, y ahora a Andrea, Cayetano y Adrián, por su compañía en el seminario. Gracias a todos los que me disteis la bienvenida al GFN y me hicisteis sentir parte del grupo a pesar de mi poca presencia por la facultad, Pablo, Fer, Nerea, Paula, Maylin, Victor Jr, Clara, Miguel, Jaime, Victor Sr, Marcos, Nataly, Luis Mario, Joaquín, Dani, Victor M., Esther, Briz, Andrés, Tomás, Amaia, y gracias a todos los que habéis ido apareciendo por el camino para hacer esta experiencia aún mejor, Sara, Odette, Claudia, José Andrés, Susana, Bárbara D., Clara, Carlos, Pablo G., Gabriel, Bárbara

B., Pablo C., Miriam, Javi G. Muñoz, Alejandro. Me dejaré nombres en el tintero, pero esté vuestro nombre aquí o no, seguro que guardo un gran recuerdo vuestro, porque todos habéis hecho que estos años hayan sido maravillosos.

Y lo más importante, gracias a mi familia. Gracias a mis padres por estar siempre tan orgullosos de todo lo que hago, por apoyarme y creer en mí. Gracias a Borja por acompañarme durante todos estos años, por estar en los buenos y malos momentos y, sobre todo, por cuidarme tanto. Gracias a mis abuelos, por enseñarme tantas cosas.

Contents

Abstract

In recent years, neutrino physics has become one of the most active areas of scientific research. It has been firmly established that neutrinos oscillate and hence are massive particles. However, several fundamental questions related to them remain open, such as the neutrino mass hierarchy, the nature of the neutrino mass and charge-parity violation in the leptonic sector. Aiming at solving these puzzles, a next generation of accelerator-based neutrino oscillation experiments is being developed, leading to the precision era. These experiments require an unprecedented level of accuracy to succeed in determining neutrino properties. One of the main sources of systematic uncertainty arises from the modeling of neutrino interactions with the target nuclei. Therefore, achieving a precise description of these reactions has become one of the top challenges for theoretical nuclear physics. Neutrinos are produced in accelerator-based experiments as the decay products of successive reactions, resulting in broad energy fluxes. Hence, neutrino-nucleus interactions involve multiple reaction mechanisms, each dominating in different kinematic regimes, requiring robust models that properly describe these interactions over the whole experimental range. Among the possible interaction channels, our focus is placed on quasielastic scattering, which represents a significant contribution in both current and future neutrino oscillation experiments.

In this thesis, we present a fully relativistic and quantum mechanical model for the description of lepton-nucleus quasielastic scattering. The initial ground state nucleus is modeled through an unfactorized representation of the spectral function, allowing to include effects beyond the mean-field approximation, like the depletion of the occupation of the shell model states and the appearance of nucleons at higher missing energies due to nucleon-nucleon correlations. Meanwhile, the final-state nucleon is described within the relativistic distorted wave impulse approximation as a solution of the Dirac equation in the continuum using the energy-dependent relativistic mean-field potential, accounting for final-state interactions with the residual system. The main advantage of this description of the final state is that it preserves orthogonality and

consistency between the initial and final states at low energies of the final nucleon, while approaching the behavior of the phenomenological optical potentials at larger energies. We observe that this accurate and consistent treatment of the final nucleon is essential to correctly reproduce the experimental data.

The main aim of this work is to explore how pion exchange contributes to one-particle one-hole final states. We extend the usual treatment of quasielastic scattering within the impulse approximation, based on a one-body current operator, and include interactions between nucleons through one pion exchange by incorporating a two-body meson-exchange current operator. Meson-exchange currents include the Δ-resonance mechanism (electroweak excitation of the $\Delta(1232)$ resonance and its subsequent decay into $N\pi$) and the background contributions deduced from the chiral perturbation theory Lagrangian of the pion-nucleon system. The one-particle one-hole final state contribution stemming from these two-body meson-exchange currents involve an intermediate bound-nucleon state, for which different modeling strategies have been explored. We show results obtained with the most general expression of the two-body operator, in which the intermediate nucleons are described by relativistic mean-field bound states; then, we propose two approximations consisting in describing the intermediate states as nucleons in a relativistic Fermi gas, preserving the complexity and consistency in the initial and final states. These approximations simplify the calculations considerably, allowing us to provide outcomes in a reasonable computational time. The results obtained when the description of the intermediate nucleon is simplified are validated by comparing with those where the intermediate calculation is described by the relativistic mean-field.

Finally, the reliability of the model has been evaluated by comparing our theoretical predictions with electromagnetic inclusive data for a variety of nuclei, as well as with charged-current neutrino–nucleus cross section measurements from T2K and MiniBooNE collaborations. The impact of two-body meson-exchange currents with a one-particle one-hole final state is found to be significant only in the transverse channel, where the response is increased, while the longitudinal component remains largely unaffected. Overall, there is good agreement with the experimental data, which supports the predicted enhancement of the transverse channel by the two-body currents. These results pave the way for further applications of the model and contribute to a deeper understanding of lepton–nucleus interactions, thus advancing toward the precision era of neutrino physics.

Resumen

En los últimos años, la física de neutrinos se ha convertido en una de las áreas más activas de la investigación científica. Se ha establecido firmemente que los neutrinos oscilan y, por tanto, son partículas con masa. Sin embargo, siguen abiertas varias cuestiones fundamentales relacionadas con ellos, como la jerarquía de masas de los neutrinos, la naturaleza de su masa y la posible violación de la simetría carga-paridad en el sector leptónico. Con el objetivo de resolver estos enigmas, se está desarrollando una nueva generación de experimentos de oscilación de neutrinos basados en aceleradores, que marcan el inicio de una era de precisión. Estos experimentos requieren un nivel de exactitud sin precedentes para poder determinar con éxito las propiedades de los neutrinos. Una de las principales fuentes de incertidumbre sistemática proviene del modelado de las interacciones entre los neutrinos y los núcleos del blanco. Por tanto, lograr una descripción precisa de estas reacciones se ha convertido en uno de los principales desafíos de la física nuclear teórica. Los neutrinos se producen en experimentos basados en aceleradores como productos de desintegraciones sucesivas, lo que da lugar a flujos energéticos amplios. Por consiguiente, las interacciones neutrino-núcleo implican múltiples mecanismos de reacción, cada uno dominante en diferentes regímenes cinemáticos, lo que requiere modelos robustos que describan adecuadamente dichas interacciones en todo el rango experimental. Entre los distintos canales posibles de interacción, nuestro estudio se centra en la dispersión cuasielástica, que constituye una contribución significativa en los experimentos de oscilación de neutrinos tanto actuales como futuros.

En esta tesis se presenta un modelo completamente relativista y cuántico para la descripción de la dispersión cuasielástica leptón-núcleo. El estado fundamental del núcleo inicial se modela mediante una representación no factorizada de la función espectral, lo que permite incluir efectos más allá de la aproximación de campo medio, como la disminución de la ocupación de los estados del modelo de capas y la aparición de nucleones a mayores energías perdidas debido a correlaciones entre nucleones. Por su parte, el nucleón en el estado final se describe dentro de la aproximación

de impulso relativista de ondas distorsionadas, como solución de la ecuación de Dirac en el continuo utilizando un potencial de campo medio relativista dependiente de la energía, que tiene en cuenta las interacciones finales con el sistema residual. La principal ventaja de este tratamiento del estado final es que preserva la ortogonalidad y coherencia entre los estados inicial y final a bajas energías del nucleón saliente, y reproduce el comportamiento de los potenciales ópticos fenomenológicos a energías más altas. Observamos que esta descripción precisa y coherente del nucleón final es esencial para reproducir correctamente los datos experimentales.

El objetivo principal de este trabajo es explorar cómo contribuye el intercambio de piones a los estados finales partícula-hueco. Extendemos el tratamiento habitual de la dispersión cuasielástica dentro de la aproximación de impulso, basada en un operador de corriente a un cuerpo, e incorporamos interacciones entre nucleones mediante el intercambio de un pion, incluyendo un operador de corriente de intercambio de mesones a dos cuerpos. Estas corrientes incluyen el mecanismo de la resonancia Δ (excitación electrodébil de la resonancia $\Delta(1232)$ y su posterior decaimiento en $N\pi$), así como las contribuciones deducidas del lagrangiano de la teoría de perturbaciones quiral del sistema pion-nucleón. La contribución al estado final partícula-hueco que proviene de estas corrientes de intercambio de mesones a dos cuerpos implica un estado intermedio de nucleón ligado, para el cual se han explorado distintas estrategias de modelado. Mostramos resultados obtenidos con la expresión más general del operador a dos cuerpos, en la que los nucleones intermedios se describen mediante estados ligados de campo medio relativista; posteriormente, proponemos dos aproximaciones en las que estos estados intermedios se describen como nucleones en un gas de Fermi relativista, preservando la complejidad y coherencia entre los estados inicial y final. Estas aproximaciones simplifican considerablemente los cálculos, lo que nos permite obtener resultados en tiempos computacionales razonables. Los resultados obtenidos al simplificar la descripción del nucleón intermedio se validan mediante la comparación con aquellos en los que dicho estado intermedio se describe utilizando el campo medio relativista.

Finalmente, la fiabilidad del modelo se ha evaluado comparando nuestras predicciones teóricas con datos inclusivos electromagnéticos para diversos núcleos, así como con medidas de secciones eficaces neutrino-núcleo de corriente cargada obtenidas por las colaboraciones T2K y MiniBooNE. Se ha observado que el impacto de las corrientes de intercambio de mesones a dos cuerpos en el estado final partícula-hueco es relevante únicamente en el canal transversal, donde la respuesta se ve incrementada, mientras que la componente longitudinal permanece prácticamente inalterada. En conjunto, se obtiene un buen acuerdo con los datos experimentales, que respaldan la predicción del incremento de la respuesta transversal debido a las corrientes a dos cuerpos. Estos

resultados abren la puerta a futuras aplicaciones del modelo y contribuyen a una comprensión más profunda de las interacciones leptón-núcleo, avanzando así hacia una era de precisión en la física de neutrinos.

Chapter 1

Introduction

The existence of neutrinos was first proposed in 1930 by Wolfgang Pauli, who suggested their existence to explain the continuum energy spectrum observed for the emitted electron in β-decay processes. In this way, having an additional neutral and light particle in the process,

$$A_N^Z \rightarrow A_{N-1}^{Z+1} + e^- + \bar{\nu_e}, \tag{1.1}$$

would allow continuous sharing of the reaction energy between the two particles, the electron and the antineutrino. Pauli initially referred to this particle as a neutron (before the actual neutron was discovered by Chadwick in 1932). Later, in 1934, Enrico Fermi developed a theory of β-decay that formally included this particle, giving it the name neutrino (meaning little neutron in Italian) to distinguish it from the neutron. The detection of this particle was a major experimental challenge due to its extremely weak interaction with matter. It was not until 1956 that Clyde Cowan and Frederick Reines successfully confirmed the existence of the neutrino through the observation of inverse β-decay [1],

$$\bar{\nu_e} + A_N^Z \rightarrow A_{N+1}^{Z-1} + e^+. \tag{1.2}$$

Since then, the study of neutrinos has led to groundbreaking discoveries in particle physics. It has been firmly established that neutrinos oscillate and hence are massive particles (Nobel Prize in Physics, 2015). However, absolute neutrino masses, the neutrino mass hierarchy and the nature of the neutrino mass, whether neutrinos are Dirac or Majorana particles, are still open questions in physics. The Standard Model (SM) of Particle Physics is one of the essential theories in Modern Physics. However, the observation of neutrino oscillations have brought some

limitations on the validity of this model, which does not contain any mechanism to account for the neutrino masses.

In this context, understanding neutrino interactions becomes crucial. The nature of neutrinos, being electrically neutral and weakly interacting, makes them very elusive. Neutrino experiments rely on the interaction of neutrinos with complex nuclei to detect them. This requires a commensurate effort in the understanding and modeling of the hadronic and nuclear physics involved in these interactions to correctly analyze the experimental output. Therefore, reconciling theory and data is essential to walk on firmer grounds in the determination of neutrino properties [2].

Additionally, neutrinos are interesting by themselves, but also because they open the door to investigate new physics. The Universe is made of matter, instead of equal parts of matter and antimatter, but the reason why almost no antimatter survived after the Big Bang is still unknown. A necessary condition to generate such asymmetry is the violation of charge-parity (CP) symmetry in nature [3], i.e. the matter-antimatter transformation, which means that production and decay rates of particles and antiparticles are not equivalent. Therefore, there must be CP-violating processes that favor the production of matter over antimatter. CP-violation has been observed experimentally in the quark sector, for example, in the decay of K and B mesons [4]. However, the amount of CP-violation observed is not enough to explain the matter-antimatter asymmetry in the Universe. This leads to the search for other possible CP-violating processes beyond the SM, and the answer could lie in the lepton sector, particularly among neutrinos. Experimentally, a violation of CP-symmetry for neutrinos would manifest as a difference in the oscillation rates of neutrinos and antineutrinos. For example, if an electron neutrino changes into a muon neutrino at a different rate than an electron antineutrino changes into a muon antineutrino, this would be a direct sign of CP-violation. Also, neutrinos have the potential to solve other open problems, such as the dark matter search through sterile neutrinos, proton decay and supernovae analysis. Then, neutrino physics provide an extraordinary opportunity for fundamental discoveries in the near future.

1.1 Neutrino properties and oscillations

Neutrinos are produced through weak interactions in flavor eigenstates ν_e, ν_μ and ν_τ, which are labeled by the particular charged lepton produced in association, e, μ or τ. Weak interactions occur either via neutral currents (NC), where the neutrino couples to a Z^0 boson in an elastic

process that only changes its four-momentum,

$$Z^0 \to \nu_\ell + \bar{\nu}_\ell \tag{1.3}$$

or via charged-currents (CC), with the coupling to a $W^\pm$ boson, additionally exchanging an electric charge,

$$W^+ \to \ell^+ + \nu_\ell\,, \quad W^- \to \ell^- + \bar{\nu}_\ell, \tag{1.4}$$

where $\ell = e, \mu, \tau$. Therefore, charged-current interactions lead to a clear distinction between neutrinos and antineutrinos, given by the charge of the produced charged lepton.

Within the framework of the SM, neutrinos are massless leptons and exhibit purely negative helicity (spin antiparallel to their momentum), implying that antineutrinos have positive helicity (spin parallel to their momentum), i.e. only left-handed neutrinos and right-handed antineutrinos exist. Therefore, weak interactions break parity symmetry. In this massless particle limit, one can relate helicity to chirality, providing a foundation for the vector-axial structure of weak neutrino interactions. We distinguish a part of the interaction that transforms under rotations as a vector, γ_μ, and shares the same structure as electromagnetic interactions, and an axial-vector part, $\gamma_\mu\gamma_5$, that depends on helicity and is characteristic of weak interactions.

Neutrinos propagate through space as mass eigenstates ν_1, ν_2 and ν_3, i.e. neutrino states with definite mass, which do not correspond to the flavor eigenstates. The association between the neutrino flavor and mass eigenstates can be generally described in terms of an unitary 3-by-3 complex matrix as

$$\begin{pmatrix}\nu_e\\ \nu_\mu\\ \nu_\tau\end{pmatrix} = \begin{pmatrix}U_{e1} & U_{e2} & U_{e3}\\ U_{\mu1} & U_{\mu2} & U_{\mu3}\\ U_{\tau1} & U_{\tau2} & U_{\tau3}\end{pmatrix}\begin{pmatrix}\nu_1\\ \nu_2\\ \nu_3\end{pmatrix}, \tag{1.5}$$

such that a flavor state can be expressed as a linear combination of propagating states and vice-versa. A common parametrization of this mixing matrix is given by the Pontecorvo-Maki-Nakagawa-Sakata (PMNS) matrix [5; 6], and it is parametrized by three mixing angles $(\theta_{12}, \theta_{23}, \theta_{13})$ and one CP-violating complex phase $e^{i\delta_{CP}}$ as

$$U_{PMNS} = \begin{pmatrix}1 & 0 & 0\\ 0 & c_{23} & s_{23}\\ 0 & -s_{23} & c_{23}\end{pmatrix}\begin{pmatrix}c_{13} & 0 & s_{13}e^{-i\delta_{CP}}\\ 0 & 1 & 0\\ -s_{13}e^{i\delta_{CP}} & 0 & c_{13}\end{pmatrix}\begin{pmatrix}c_{12} & s_{12} & 0\\ -s_{12} & c_{12} & 0\\ 0 & 0 & 1\end{pmatrix} \tag{1.6}$$

with $c_{ij} \equiv \cos(\theta_{ij})$ and $s_{ij} \equiv \sin(\theta_{ij})$.

Neutrino oscillations, predicted by Bruno Pontecorvo [5], correspond to the phenomenon where a neutrino changes its flavor as it propagates. Given that the particle state responsible for

the weak interaction (flavor eigenstate) is not the one that propagates (mass eigenstate), neutrino oscillations occur. The first hint of neutrino oscillations appeared while studying neutrinos originating in the Sun. In the 1960s, the Homestake experiment reported an unexpectedly small flux of detected solar neutrinos [7]. Conclusive evidence of this phenomenon came in 1998 with the Super-Kamiokande experiment [8], which observed flavor transitions in atmospheric neutrinos. This discovery was later supported by results from the Sudbury Neutrino Observatory (SNO) [9], which attributed the loss of incoming solar electron neutrinos to neutrino oscillations. Over the following years, additional confirmation came from experiments employing reactor and accelerator-based neutrino sources [10].

A mass eigenstate i can be expressed as a plane wave with its time evolution given by

$$|\nu_i(t)\rangle = e^{-iE_i t}|\nu_i\rangle, \tag{1.7}$$

where E_i is the energy of a neutrino with mass m_i. Then, the evolution of an initial flavor eigenstate α can be represented as a linear combination of mass eigenstates, using Eq. 1.5, as

$$|\nu_\alpha(t)\rangle = \sum_i U_{\alpha i} e^{-iE_i t}|\nu_i\rangle, \tag{1.8}$$

and, substituting the mass eigenstate, we get

$$|\nu_\alpha(t)\rangle = \sum_\beta \sum_i U^*_{\beta i} U_{\alpha i} e^{-iE_i t}|\nu_\beta\rangle. \tag{1.9}$$

This result means that, if mass eigenstates are different from flavor states such that the U matrix is not diagonal, a neutrino produced initially with a flavor α can be detected some time later in a different flavor β. The probability that a neutrino with flavor α and energy E created in some weak interaction change its flavor to β after traveling a distance L in vacuum is then given by

$$P_{\nu_\alpha \to \nu_\beta}(t) = |\langle \nu_\beta | \nu_\alpha(t)\rangle|^2 = \sum_{ij} U_{\alpha i} U^*_{\beta i} U^*_{\alpha j} U_{\beta j} e^{-i(E_i - E_j)t} \simeq \sum_{ij} U_{\alpha i} U^*_{\beta i} U^*_{\alpha j} U_{\beta j} e^{-i\frac{\Delta m^2_{ij}}{2E}L}. \tag{1.10}$$

where the last term have been obtained by assuming that the neutrino masses are small compared to their energy, such that $E_i \simeq p + m_i^2/2p$ with p the momentum, and that $t \simeq L$. Finally, the

oscillation probability can be rewritten as

$$P_{\nu_\alpha \to \nu_\beta}(L,E) = \delta_{\alpha\beta} - 4\sum_{i>j} \mathrm{Re}(U_{\alpha i}U^*_{\beta i}U^*_{\alpha j}U_{\beta j}) \sin^2\left(\frac{\Delta m^2_{ij}L}{4E}\right) + 2\sum_{i>j} \mathrm{Im}(U_{\alpha i}U^*_{\beta i}U^*_{\alpha j}U_{\beta j}) \sin\left(\frac{\Delta m^2_{ij}L}{2E}\right), \tag{1.11}$$

with $\Delta m^2_{ij} \equiv m^2_i - m^2_j$ the mass square difference. Given this dependence of the oscillation probability on neutrino masses, a fundamental consequence of the observation of this phenomenon is that neutrinos must be massive particles, implying new physics beyond the Standard Model. A review of the up-to-date values of the neutrino oscillation parameters from [11; 12] is shown in Fig. 1.1. However, although the mass squared differences could be measured with precision in neutrino oscillation experiments, the sign of the mass splitting between m_2 and m_3 mass eigenstates is still unknown. The actual ordering of the masses remains uncertain, a question referred to as the neutrino mass hierarchy problem. If m_3 is the heaviest, this configuration is termed as normal hierarchy; if instead m_3 is the lightest, the hierarchy is called inverted. Additionally, Δm^2_{ij} is the only mass parameter that can be measured in neutrino oscillation experiments. Therefore, these experiments cannot provide information about the absolute values of the individual neutrino masses, and their determination is then addressed with other experimental approaches. One of the most direct methods to access the absolute neutrino mass scale relies on precision measurements of the electron energy spectrum in β-decay. In particular, the KATRIN experiment [13] analyzes the endpoint of tritium β-decay to constrain the effective mass of the electron neutrino.

It remains the open question whether neutrinos are Majorana particles, meaning that neutrinos and antineutrinos would be the same particle. If neutrinos are Majorana particles, two more complex phases α_1 and α_2 would be added to the PMNS matrix,

$$U = U_{PMNS} \begin{pmatrix} e^{i\alpha_1} & 0 & 0 \\ 0 & e^{i\alpha_2} & 0 \\ 0 & 0 & 1 \end{pmatrix}. \tag{1.12}$$

However, the effects of these parameters cannot be observed in neutrino oscillation experiments. A potential method to investigate this property is the search for the hypothetical neutrinoless double β-decay [16], a process that can be interpreted as two beta decays occurring simultaneously, with the resulting antineutrinos annihilating each other, but there is not yet experimental

NuFIT 6.0 (2024)

		Normal Ordering ($\Delta\chi^2 = 0.6$)		Inverted Ordering (best fit)	
		bfp $\pm 1\sigma$	3σ range	bfp $\pm 1\sigma$	3σ range
IC19 without SK atmospheric data	$\sin^2\theta_{12}$	$0.307^{+0.012}_{-0.011}$	$0.275 \to 0.345$	$0.308^{+0.012}_{-0.011}$	$0.275 \to 0.345$
	$\theta_{12}/^\circ$	$33.68^{+0.73}_{-0.70}$	$31.63 \to 35.95$	$33.68^{+0.73}_{-0.70}$	$31.63 \to 35.95$
	$\sin^2\theta_{23}$	$0.561^{+0.012}_{-0.015}$	$0.430 \to 0.596$	$0.562^{+0.012}_{-0.015}$	$0.437 \to 0.597$
	$\theta_{23}/^\circ$	$48.5^{+0.7}_{-0.9}$	$41.0 \to 50.5$	$48.6^{+0.7}_{-0.9}$	$41.4 \to 50.6$
	$\sin^2\theta_{13}$	$0.02195^{+0.00054}_{-0.00058}$	$0.02023 \to 0.02376$	$0.02224^{+0.00056}_{-0.00057}$	$0.02053 \to 0.02397$
	$\theta_{13}/^\circ$	$8.52^{+0.11}_{-0.11}$	$8.18 \to 8.87$	$8.58^{+0.11}_{-0.11}$	$8.24 \to 8.91$
	$\delta_{\rm CP}/^\circ$	177^{+19}_{-20}	$96 \to 422$	285^{+25}_{-28}	$201 \to 348$
	$\frac{\Delta m^2_{21}}{10^{-5}\ {\rm eV}^2}$	$7.49^{+0.19}_{-0.19}$	$6.92 \to 8.05$	$7.49^{+0.19}_{-0.19}$	$6.92 \to 8.05$
	$\frac{\Delta m^2_{3\ell}}{10^{-3}\ {\rm eV}^2}$	$+2.534^{+0.025}_{-0.023}$	$+2.463 \to +2.606$	$-2.510^{+0.024}_{-0.025}$	$-2.584 \to -2.438$
		Normal Ordering (best fit)		Inverted Ordering ($\Delta\chi^2 = 6.1$)	
		bfp $\pm 1\sigma$	3σ range	bfp $\pm 1\sigma$	3σ range
IC24 with SK atmospheric data	$\sin^2\theta_{12}$	$0.308^{+0.012}_{-0.011}$	$0.275 \to 0.345$	$0.308^{+0.012}_{-0.011}$	$0.275 \to 0.345$
	$\theta_{12}/^\circ$	$33.68^{+0.73}_{-0.70}$	$31.63 \to 35.95$	$33.68^{+0.73}_{-0.70}$	$31.63 \to 35.95$
	$\sin^2\theta_{23}$	$0.470^{+0.017}_{-0.013}$	$0.435 \to 0.585$	$0.550^{+0.012}_{-0.015}$	$0.440 \to 0.584$
	$\theta_{23}/^\circ$	$43.3^{+1.0}_{-0.8}$	$41.3 \to 49.9$	$47.9^{+0.7}_{-0.9}$	$41.5 \to 49.8$
	$\sin^2\theta_{13}$	$0.02215^{+0.00056}_{-0.00058}$	$0.02030 \to 0.02388$	$0.02231^{+0.00056}_{-0.00056}$	$0.02060 \to 0.02409$
	$\theta_{13}/^\circ$	$8.56^{+0.11}_{-0.11}$	$8.19 \to 8.89$	$8.59^{+0.11}_{-0.11}$	$8.25 \to 8.93$
	$\delta_{\rm CP}/^\circ$	212^{+26}_{-41}	$124 \to 364$	274^{+22}_{-25}	$201 \to 335$
	$\frac{\Delta m^2_{21}}{10^{-5}\ {\rm eV}^2}$	$7.49^{+0.19}_{-0.19}$	$6.92 \to 8.05$	$7.49^{+0.19}_{-0.19}$	$6.92 \to 8.05$
	$\frac{\Delta m^2_{3\ell}}{10^{-3}\ {\rm eV}^2}$	$+2.513^{+0.021}_{-0.019}$	$+2.451 \to +2.578$	$-2.484^{+0.020}_{-0.020}$	$-2.547 \to -2.421$

Figure 1.1: Three-flavor oscillation parameters from different global analysis of neutrino data available in September 2024 [11; 12]. The results shown in the upper (lower) section are obtained without (with) the inclusion of the tabulated χ^2 data on atmospheric neutrinos provided by the Super-Kamiokande [14] and IceCube [15] collaborations. The numbers in the 1st (2nd) column are obtained assuming normal ordering (inverted ordering), i.e. $m_3 > m_2$ ($m_1 > m_3$). Note that $\Delta m^2_{3\ell} \equiv \Delta m^2_{31} > 0$ for normal ordering and $\Delta m^2_{3\ell} \equiv \Delta m^2_{32} < 0$ for inverted ordering.

evidence of such process.

To conclude, the oscillation probability for antineutrinos, $P(\bar{\nu}_\alpha \to \bar{\nu}_\beta)$, can be obtained from the corresponding probability for neutrinos, $P(\nu_\alpha \to \nu_\beta)$, by considering the complex conjugate of U, i.e. substituting U by U^* in Eq. 1.11. If U is a real matrix, the neutrino and antineutrino probabilities satisfy $P(\nu_\alpha \to \nu_\beta) = P(\bar{\nu}_\alpha \to \bar{\nu}_\beta)$. However, this is not the case for the PMNS matrix, which contains the complex phase δ_{CP}, implying a violation of CP symmetry in the leptonic tensor unless δ_{CP} is either 0 or π or any of the mixing angles are trivial. This can be clearly seen when computing the difference between neutrino and antineutrino oscillation probabilities, referred to as the CP-violating asymmetry A^{CP},

$$\begin{aligned} A^{CP}_{\alpha\beta} &= P(\nu_\alpha \to \nu_\beta) - P(\bar{\nu}_\alpha \to \bar{\nu}_\beta) \\ &= 4 \sum_{i>j} \mathrm{Im}\left(U_{\alpha i} U^*_{\beta i} U^*_{\alpha j} U_{\beta j}\right) \sin\left(\frac{\Delta m^2_{ij} L}{2E}\right), \end{aligned} \tag{1.13}$$

and it is commonly written as

$$A^{CP}_{\alpha\beta} = 16 J_{\alpha\beta} \sin\left(\frac{\Delta m^2_{21} L}{4E}\right) \sin\left(\frac{\Delta m^2_{32} L}{4E}\right) \sin\left(\frac{\Delta m^2_{31} L}{4E}\right), \tag{1.14}$$

where $J_{\alpha\beta}$ is called the Jarlskog invariant and can be expressed in terms of the elements of the PMNS matrix as

$$J_{\alpha\beta} = c_{12} s_{12} c_{23} s_{23} c^2_{13} s_{13} \sin(\delta_{CP}) \sum_\gamma \epsilon_{\alpha\beta\gamma}, \tag{1.15}$$

where the Levi-Civita symbol, $\epsilon_{\alpha\beta\gamma}$, accounts for the sign. Then, CP-violation requires the Jarlskog invariant to be non-zero, implying that all sines and cosines of the 3 mixing angles and the sine of the δ_{CP} phase should not vanish.

1.2 Accelerator-based neutrino oscillation experiments

Neutrino sources employed in oscillation experiments are diverse, going from nuclear reactions in the center of the Sun, collisions of highly energetic cosmic rays with the atmosphere, supernovae, nuclear reactors and particle accelerators. Current experimental efforts focus on accelerator-based neutrino oscillation experiments, where L and E can be optimized to maximize the sensitivity to neutrino oscillations. These facilities aim to measure the neutrino oscillation parameters, but also produce data that can help to reduce the systematic and theoretical uncertainties related to neutrino-nucleus scattering.

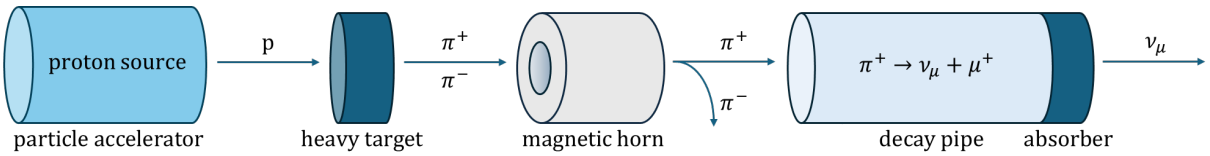

Figure 1.2: Neutrino beam production in an accelerator-based neutrino oscillation experiment.

Accelerator-based neutrino oscillation experiments create neutrino beams in accelerator facilities as the decay product of pions and kaons, covering the intermediate range of neutrino energies bewteen several hundreds of MeV up to a few GeV. As shown in Fig. 1.2, the process initiates with protons accelerated in a synchrotron, which are then extracted and directed toward a heavy, fixed target, where pions and kaons are produced. Subsequently, a set of magnetic horns isolates the produced mesons with either positive charge, to generate a neutrino-dominated flux, or negative charge, to produce an antineutrino-dominated one. The selected mesons pass through a long decay volume where they decay into leptons and neutrinos, and a final region with absorbing material stops unwanted particles from propagating with the produced neutrino beam. The dominant decay channels contributing to the neutrino-dominated flux correspond to $\pi^+ \rightarrow \mu^+ + \nu_\mu$ and $K^+ \rightarrow \mu^+ + \nu_\mu(+\pi^0)$, while for the antineutrino case these are $\pi^- \rightarrow \mu^- + \bar{\nu}_\mu$ and $K^- \rightarrow \mu^- + \bar{\nu}_\mu(+\pi^0)$. However, the resulting neutrino fluxes inevitably include contamination from both neutrinos with opposite helicity and different flavors. Undesired neutrinos mainly appear from subsequent muon decay, $\mu^+ \rightarrow e^+ + \bar{\nu}_\mu + \nu_e$ and $\mu^- \rightarrow e^- + \nu_\mu + \bar{\nu}_e$, and alternative decay modes of kaons, $K^+ \rightarrow e^+ + \nu_e + \pi^0$ and $K^- \rightarrow e^- + \bar{\nu}_e + \pi^0$. Therefore, accelerator-based experiments produce non-monochromatic beams with broad energy distributions, consisting predominantly of muon neutrinos or antineutrinos but, despite experimental setups can be optimized to reduce contamination to the percent level, these beams still include neutrinos of other helicities and flavors. As an example, the T2K flux corresponding to neutrino and antineutrino beams is shown in Fig. 1.3, consisting of a mixture of ν_μ, $\bar{\nu}_\mu$, ν_e and $\bar{\nu}_e$.

Finally, the neutrinos travel through the Earth towards a set of detectors placed strategically: a near detector and a far detector (see Fig. 1.4). The near detector is located close to the production region and measures the initial flavor composition and intensity of the neutrino beam. This measurement establishes a baseline for the number and type of neutrinos before oscillation, serving as a reference point. Additionally, near detectors serve a complementary role as a valuable resource for studying neutrino-nucleus cross sections. The far detector is located hundreds of kilometers from the source. During this journey, neutrinos oscillate, changing from one flavor to

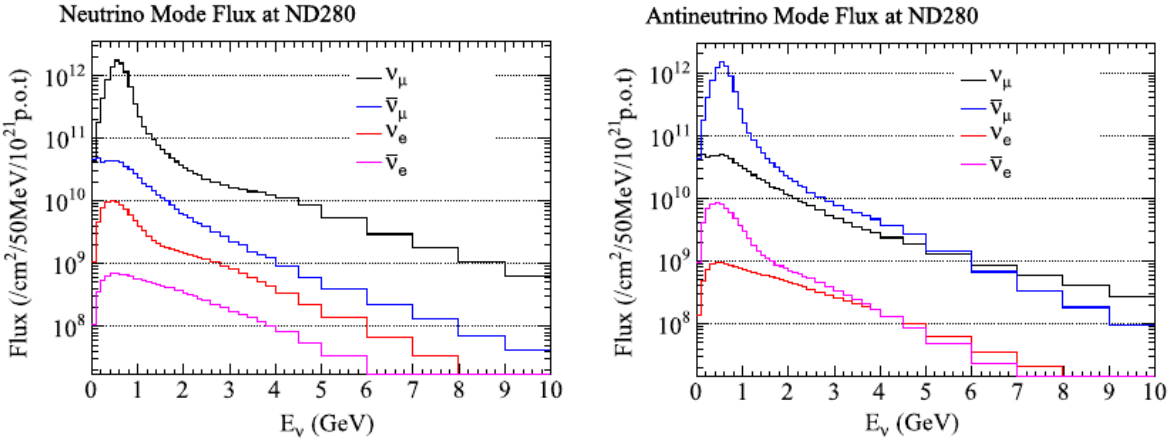

Figure 1.3: Predicted flux as a function of energy at the ND280 detector of T2K for the neutrino beam (left) and antineutrino beam (right). In each case, the ν_μ, $\bar{\nu}_\mu$, ν_e and $\bar{\nu}_e$ components of the beam are shown. Figure from [17].

another depending on their energy, travel distance and oscillation parameters. The far detector, usually located at the place where a maximum or minimum oscillation is expected, measures the flavor composition and intensity of the neutrino beam after oscillation, allowing comparison with the initial measurement from the near detector. In this way, neutrino oscillations are inferred from flavor transitions between the source and detector by measuring either the disappearance of muon (anti)neutrinos or the appearance of electron anti(neutrinos). The disappearance method measures the reduction of the expected number of muon (anti)neutrinos in the detector due to oscillations to electron or tau flavor. Meanwhile, the electron (anti)neutrino appearance measurement searches for an enhancement of electron (anti)neutrinos with respect to the initial beam.

As neutrinos only interact through the weak force, their direct observation is not possible with traditional particle detectors. Instead, one measures the particles that are produced in the interaction of the neutrino with the detector material. Given the relatively low scale of weak cross sections, huge amounts of detector material are required in order to detect neutrinos with the desired statistics. All present and future generations of neutrino oscillation experiments use complex nuclei as target material, which allows for the accumulation of tons of it, significantly increasing the number of events in the detectors. Mineral oils (CHx), water and liquid argon are examples of the targets used. This highlights the need to study neutrino-nucleus interactions, as well as the importance of the nuclear physics involved. Another challenge is that the neutrino

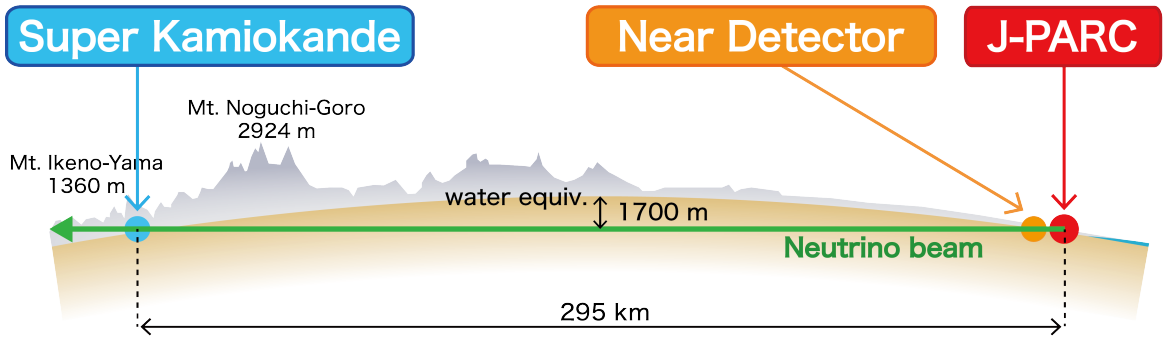

Figure 1.4: Representation of the T2K accelerator-based neutrino experiment. Figure from [18].

energy is known only as a broad distribution. As the oscillation probability depends on the neutrino energy, this has to be reconstructed in every neutrino-nucleus scattering event. Ideally, the neutrino energy would be reconstructed by measuring the energy deposited by final-state particles in the detectors. However, due to the limited detector acceptances, it is experimentally unfeasible to fully capture the complete final state. The gaps in information are addressed by using Monte Carlo (MC) event generators, which rely on theoretical models to simulate neutrino interactions and reconstruct the neutrino energy, which, however, faces further complications.

Despite these significant scientific and technical challenges, accelerator-based neutrino experiments provide an outstanding opportunity to investigate the fundamental nature of these elusive particles. Precise measurements of neutrino properties are among the highest priorities in fundamental particle physics, involving worldwide efforts through current experiments (e.g. T2K [19], NOνA [20], MINERνA [21] and MicroBooNE [22]) and next-generation facilities (e.g. Hyper-Kamiokande [23] and DUNE [24]). With the future generation of neutrino experiments, the field will enter the precision era. The statistical errors will be largely reduced and the experiments will become much more sensitive to the details of neutrino-nucleus interactions. In what follows, some neutrino experiments are briefly described.

T2K and T2HK

The Japanese neutrino program started with the Super-Kamiokande detector, which provided the first experimental evidence of atmospheric neutrino oscillations [8]. The collaboration continued with the K2K project [25], focusing on confirming the previous observations from Super-

Kamiokande, but with the main difference of using a well understood muon neutrino beam. Now, its successor, the current T2K (Tokai to Kamioka) experiment [19], is a neutrino oscillation program that operates over a long-baseline between the J-PARC accelerator-based muon neutrino source in Tokai and the Super-Kamiokande detector in Kamioka, at a distance of 295 km.

T2K studies neutrino oscillations with two separate detectors, both of which are 2.5 degrees away from the center of the neutrino beam. This method significantly narrows the flux energy distribution, with a peak around 0.6 GeV, constraining the kinematical range of neutrino-nucleus interactions. The ND280 near detector, made of hydrocarbon and hybrid water-hydrocarbon targets, is located at 280 meters of distance from the source, and measures the number of muon neutrinos in the beam before any oscillation occurs. It allows for monitoring the beam direction as well as a precise measurement of neutrino interactions. As for the far detector, T2K uses the water Cherenkov Super-Kamiokande detector. The walls of Super-Kamiokande are lined with more than 10.000 sensitive photo-multipliers which detect the Cherenkov light from charged particles. Its main advantage is that this detector has an excellent ability to distinguish muons produced by muon neutrinos from electrons produced by electron neutrinos.

In addition to neutrino oscillations, the collaboration has also worked on understanding the structure of neutrino-nucleus interactions and its impact on the systematic uncertainties in oscillation analyses. Many ND280 cross sections measurements with different event topologies, kinds of scattering neutrinos and targets have been performed, providing highly valuable experimental data for the developing of theoretical interaction models.

Next step in the Kamiokande investigations is the Tokai to Hyper-Kamiokande (T2HK) experiment [23], which will operate on the same beamline as T2K, using the upgraded Hyper-K far detector. This large size detector, equipped with improved detection techniques, will provide an enhanced sensitivity to neutrino oscillation parameters, particularly to CP-violation.

NOvA

The NOvA (NuMI Off-axis ν_e Appearance) long-baseline experiment [20; 26] studies neutrino oscillations using the NuMI beamline from Fermilab with an off-axis configuration for the near and far detectors. The far detector, made of mineral oil, is located at Minnesota, 810 km away from the muon neutrino source, which presents a narrow-band energy spectrum peaked around 2 GeV. This optimizes the sensitivity to electron neutrino appearance and muon neutrino disappearance, as the oscillation from muon neutrinos to electron neutrinos is expected to be at maximum with this configuration.

The main focus of the NOvA experiment is to measure the θ_{23}, Δm^2_{32} and δ_{CP} oscillation parameters, as well as to determine the neutrino mass ordering. The latter modifies the effects of matter when neutrinos travel through the Earth and, therefore, the oscillation rates are also affected. Due to the large baseline used by the experiment, matter effects are important for NOvA, allowing to determine the sign of Δm^2_{32} and thus the mass ordering.

MINERνA

MINERνA (Main INjector ExpeRiment $\nu - A$) is a neutrino-scattering experiment [27; 21] based at Fermilab, with its detector located on-axis of the NuMI beam. It measures neutrino interactions in an energy range from 1 GeV to 20 GeV and on a variety of nuclear targets (C, CH, Fe, H_2O, Pb), allowing to achive precise measurements of nuclear effects. MINERνA focuses on improving the modeling of neutrino-nucleus interactions in order to reduce systematic uncertainties in neutrino oscillation experiments.

MiniBooNE and MicroBooNE

MiniBooNE (Mini Booster Neutrino Experiment) [28] was a short-baseline neutrino experiment at Fermilab designed to investigate neutrino oscillations, focusing on detecting the electron neutrino appearance from the muon neutrino beam. Neutrino and antineutrino beams were produced in the Booster Neutrino Beamline (BNB) with a flux peaked around 0.7 GeV. The experiment used a single Cherenkov detector setup made of mineral oil (CH_2). Over its run, the MiniBooNE collaboration reported a low-energy excess of electron-like events in both neutrino and antineutrino modes [29].

The BooNE experiment continued with MicroBooNE [30; 31], also located along the BNB at Fermilab. MicroBooNE has been established to further investigate this low-energy excess using more advanced detection technology. Employing a Liquid Argon Time Projection Chamber (LArTPC), this detector offers high spatial resolution and accurate particle identification capabilities. Additionally, MicroBooNE plays a key role in providing precise measurements of neutrino–argon cross sections, which are essential for the interpretation of results in current and future LArTPC-based experiments, as DUNE.

DUNE

DUNE (Deep Underground Neutrino Experiment) [24] is a next-generation neutrino oscillation experiment currently under construction, and expected to start taking data in 2030's. The

collaboration is aimed at making definitive determinations of CP-violation in neutrinos, the neutrino mass hierarchy as well as searching for neutrinos beyond the currently known three. Neutrino and antineutrino beams produced at Fermilab will be detected at a LArTPC far detector located 1.5 km underground at the Sanford Underground Research Facility (SURF) in South Dakota, at 1300 km from the source, and at a near detector installed in the Long-Baseline Neutrino Facilify (LBNF) at Fermilab. DUNE is also expected to achieve important discoveries in forthcoming years related to physics beyond the Standard Model, such as the possibility of proton decay and supernova neutrino detection.

1.3 Neutrino interactions

To carry out accurate oscillation analyses, it is essential to understand the complexities of neutrino-nucleus interactions and how nuclear effects influence the measurements obtained by neutrino experiments in the detectors. Theoretical uncertainties derived from our limited understanding on neutrino-nucleus scattering propagate into systematic uncertainties in the oscillation analyses. In the next decades, the future generation of experiments will quickly accumulate an unprecedented number of neutrino interaction events and, instead of statistics, systematic uncertainties will be limiting the physics reach of the experiments. Reducing these uncertainties by improving our ability to describe neutrino-nucleus cross sections with high accuracy is therefore fundamental for the success of neutrino oscillation experiments.

As the incoming neutrino beam spans a broad energy range in present and next-generation experiments, theoretical models must be able to provide reliable descriptions of the various neutrino-nucleus reaction mechanisms that can occur. These mechanisms range from coherent interactions with the entire nucleus, to scattering off individual nucleons, and, at the highest energies, to processes that probe the internal structure of nucleons through interactions with their constituent quarks. At the lowest neutrino energies, the only available channel is elastic scattering, in which the neutrino probes the entire nucleus as a single coherent object that recoils intact. As the energy increases to a few MeV, additional channels become accessible, allowing the excitation of the nucleus into its low-lying resonant states. When the neutrino energy reaches the range from hundreds of MeV to several GeV, which corresponds to the energy range relevant for neutrino oscillation experiments, the dominant channels are:

- Quasielastic (QE) scattering. The neutrino scatters off a nucleon, bound by the nuclear potential, that is knocked-out from the nucleus.

- Multi-nucleon contributions. Nuclear effects such as short-range correlations in the nuclear medium and meson-exchange currents between nucleons can produce the ejection of more than one nucleon from the nucleus. The main contribution in this case comes from two-nucleon knock-out processes.

- Single-pion production (SPP) in the resonance region. The scattering off a bound nucleon produces its excitation into a resonance state, which subsequently decays into a pion and a nucleon (and possibly other hadrons) that are ejected from the nucleus. The main contribution comes from the $\Delta(1232)$ resonance, but also contributions from heavier resonances (N^*) are important in high energy experiments as DUNE. Other non-resonant reaction mechanisms also contribute to this pion production channel.

- Deep-inelastic scattering (DIS). A high-energy neutrino directly interacts with the constituent quarks of the nucleon, including those that make up the quark–antiquark sea, which continually emerges and vanishes due to quantum fluctuations. At relatively low momentum transfer, nucleons contain mostly up, down, and strange quarks, but at higher momentum transfer, heavier and shorter-lived quarks also come into play. This high-energy impact causes the nucleon to break apart, releasing quarks and gluons. As these particles reassemble, a cascade of hadrons is produced in the final state. The region between DIS and SPP mechanisms, referred to as shallow-inelastic scattering (SIS), is an extremely difficult-to-model part of phase space, involving a smooth transition between the different scales of physics.

A scheme of the different mechanisms discussed as a function of the energy transfer is shown in Fig. 1.5. At the kinematics of most current and future experiments, the most relevant contribution to the cross section comes from charged-current quasielastic (CCQE) scattering and pion production. In particular, the quasielastic channel is the the dominant one in the low-energy experiments T2K and MicroBooNE, and a major contribution in MINERνA, NOvA and DUNE. Motivated by this situation, in this work, we focus on quasielastic scattering in order to provide a more realistic description of this mechanism.

The interaction of a neutrino with a nucleon bound in the ground state nucleus—a strongly interacting many-body system—typically leads to a final state in which hadrons are ejected and may further interact with the residual nuclear system. Accurately modeling this process is extremely challenging, and therefore neutrino-nucleon interactions have to be described within a theoretical framework that captures the complexity of the nuclear structure and dynamics.

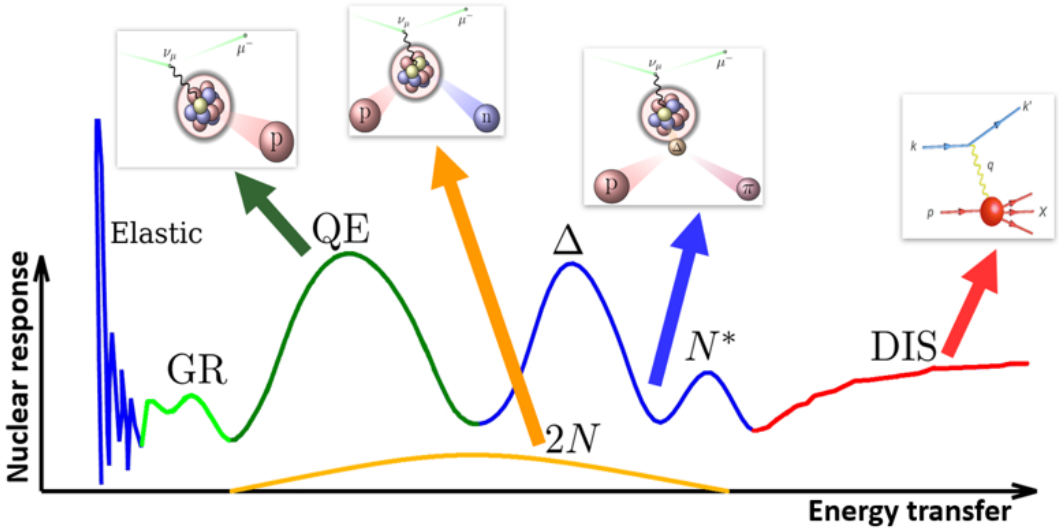

Figure 1.5: Electroweak nuclear response as a function of the energy transferred by the neutrino to the nucleus. From low to high energy transfer, the mechanisms are: elastic interaction, nuclear giant resonances (GR), quasielastic (QE) scattering, pion roduction (Δ and N^*), multi-nucleon contributions (dominated by two-nucleon knock-out reactions, 2N) and deep inelastic scattering (DIS).

For that, several models have been proposed over the years [32; 33]. The simplest choice is the global relativistic Fermi gas model, where the bound nucleons are described as free on-shell particles constrained to have a momentum below the Fermi momentum. This is the most employed model in oscillation analyses [34; 35; 36] and it allows to describe the neutrino-nucleus interaction process within a fully relativistic framework, conserving the fundamental symmetries of quantum field theory and capturing the gross features of the nuclear response. However, it is an oversimplified approach that does not reach the level of precision required by the next generation of neutrino oscillation experiments [37]. Improvements of this model have been proposed within the local Fermi gas [38; 39; 40] approach. Other models based on the factorized spectral function formalism [41; 42] have also been widely employed, offering a more realistic description of the nuclear framework. More recently, *ab initio* models have allowed quantitative and successful 'first-principles' understanding of many nuclear properties [43], but the extensive computational time they require greatly limits their practical application.

In this thesis, we employ a fully relativistic and quantum mechanical framework by means of an unfactorized representation of the spectral function. This spectral function is represented as a combination of single-particle momentum distributions computed within the relativistic mean-field (RMF) model. The mean-field approach simplifies the study of many-body systems

by replacing the complex interactions between individual particles with an average, or mean, field. Within this framework, each nucleon is treated as moving independently in an effective potential generated by the other nucleons, rather than explicitly accounting for all individual interactions, which are replaced by their effect in the average potential. Therefore, nucleons are now described as independent-particle wave functions that are solutions of the mean-field equations with an effective potential, allowing an easier treatment of the problem [44; 45]. The single-particle momentum distributions obtained within the RMF, when compared to the cross sections measured in exclusive $(e, e'p)$ experiments, where it is assured that one and only one nucleon is present in the final state, display the right shape. However, the mean-field fails to allocate or describe the observed missing energy and momentum when the energy employed in excitations of the target nucleus, to unbind one or more nucleons, is above the two-particle emission threshold. Under these conditions, correlations in the initial state, as well as final-state interactions, make it possible to knock out more than one nucleon. From the experimental point of view, in $(e, e'p)$ experiments, this appears as a contribution at large missing energies, because there is energy not detected in the final state (missing), carried by the additional knocked out nucleons that are not detected. This multi-nucleon emission generally also shows a noticeable increase in strength compared to the mean-field prediction in the high missing momentum region. This is also due to the momentum carried away by the additional knocked out nucleons that are not detected in the experiment, and thus their energy and momentum are not accounted for, thus they are 'missing'.

The probability of knocking out one nucleon from a given nucleus, i.e., the probability of one-nucleon removal with a given energy and momentum from the target nucleus, can be computed from many-body calculations in what is usually named as 'the spectral function', $S(E, p)$. Theoretical spectral functions have two contributions. The first is computed within the independent-particle shell model, that is, the contribution to the final states where only one nucleon is knocked out, thus made of single-hole states in the initial nucleus. This contribution can be compared to $(e, e'p)$ and other exclusive experimental data, in order to ascertain the shape and strength of it. The second is the 'correlated contribution', which accounts for nucleon-removal processes involving additional nucleons. This would be coming from, for instance, short-range correlations of deeply bound nucleons. These are thought to be quite universal, depending only on the nuclear density. This contribution can be easily computed in nuclear matter, and then built into the theoretical spectral function. To determine the spectral function for finite nuclei, initial nucleon occupancies are shared in between the independent-particle content of the spectral

function, which would then contain 'less nucleons' than in the calculation without correlations, and the correlated part. Occupancies of different shells and of the correlated part, as well as the momentum distributions (the shape of each contribution) are tuned to experimental data. This prescription builds a so-called 'semi-phenomenological spectral function'. This object would describe everything that contribute to knocking out a nucleon from the target nucleus, and would have a distinct missing energy and momentum content, in accordance with the observations in experiments, compared to simple mean-field calculations.

Thus, in order to achieve a more realistic description of our lepton-nucleus scattering process, we go beyond the mean-field approximation by including correlation effects, taking the semi-phenomenological spectral function formalism as reference. Contrary to other works along similar lines, we do not factorize the cross section into the spectral function times the phase space and the elementary lepton-nucleon cross section. Instead, we use a representation of the spectral function amenable to our relativistic distorted wave and unfactorized calculations.

Finally, it is worth noting that studying neutrino-nucleus interactions is of great interest in itself, beyond their relevance to the neutrino oscillation program. Such investigation offers unique insights into the weak response of nuclei and nucleons, providing crucial information that complements what is obtained through electromagnetic probes. In particular, it enables the study of the axial structure of the nucleon, which is not directly accessible via electron or photon scattering. Charged-current neutrino-nucleon interactions, in this context, are especially valuable for constraining the axial form factor of the nucleon.

1.4 Outline

This thesis focuses on the study of lepton-nucleus interactions using a realistic theoretical framework for the treatment of nuclear effects. In particular, quasielastic scattering is studied using an unfactorized representation of the spectral function, where the momentum distributions of bound nucleons are obtained from a relativistic mean-field model for finite nuclei, and the final-state nucleon is described as a scattering solution of the Dirac equation with relativistic potentials. Then, the contributions from every matrix element to the total process are consistently computed using solutions of the Dirac equation with scalar and vector potentials for the initial and final nucleons. This approach includes effects beyond the mean-field description, taking as reference the semi-phenomenological spectral functions. Our calculation is fully relativistic and includes a full quantum mechanical description of both the initial and final nucleon states. Additionally,

the usual treatment of quasi-elastic scattering, based on one-body currents, is extended by incorporating the contribution from two-body meson-exchange currents with a final one-particle one-hole state.

In Chapter 2, we present the general formalism for quasielastic lepton scattering on nuclei, as well as the approach adopted to describe the nuclear structure of the nuclei considered: ^{12}C, ^{16}O, and ^{40}Ca. In Chapter 3, we focus on the hadronic part of the interaction, describing the modeling of the initial nuclear state, the interaction dynamics and the final-state interactions undergone by the outgoing nucleon within the residual system. In Chapter 4, we introduce the contribution from two-body meson exchange currents to particle-hole excitations, accounting for those processes where the initial nucleon is interacting with another bound nucleon in the target nucleus through meson exchange. The modeling of this contribution is discussed at length, proposing three different approaches and evaluating their differences. Then, our theoretical predictions are compared with experimental data from both electron and neutrino scattering, presented in Chapters 5 and 6, respectively. Electromagnetic hadronic responses and cross sections are computed for ^{12}C, ^{16}O, and ^{40}Ca, providing a solid benchmark to validate our model before its application to neutrino interactions. Charged-current (anti)neutrino-nucleus cross sections are calculated both at fixed neutrino energy and averaged over the neutrino and antineutrino fluxes of the T2K and MiniBooNE experiments. Comparisons with the experimental results from these collaborations are presented for ν_μ and $\bar{\nu}_\mu$ reactions. Finally, conclusions are given in Chapter 7.

Chapter 2

Quasielastic lepton-nucleus scattering

Quasielastic scattering corresponds to the lepton being scattered by a single nucleon that is consequently ejected from the target nucleus. In Fig. 2.1, the Feynman diagrams corresponding to lepton-nucleon interactions are displayed. The electromagnetic (EM) interaction occurs through the exchange of a photon, while weak interactions are distinguished between charged-current processes, where a charged lepton is emitted, and neutral-current ones, where the neutrino does not change in the final state.

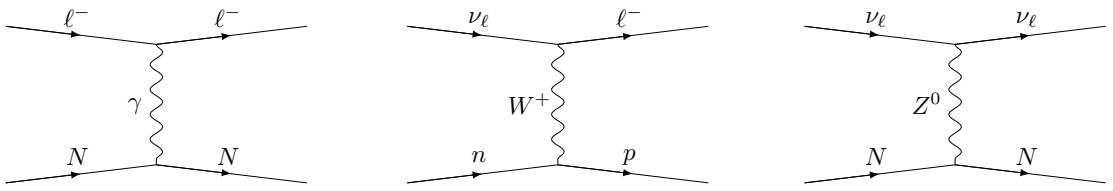

(a) Electromagnetic scattering (b) Charged-current scattering (c) Neutral-current scattering

Figure 2.1: Lepton-nucleon scattering processes. N denotes either a proton or a neutron.

In this chapter, we present the kinematics and general formalism for the calculation of the quasielastic lepton-nucleus scattering cross section. Given the connection between electron and neutrino scattering, and the wealth of electron scattering data with well-defined beam energies, an effective way to enhance our understanding of neutrino-nucleus interactions is through electron-nucleus scattering experiments. Accordingly, in this work, electron-nucleus scattering will be used as benchmark to assess the validity of our theoretical neutrino interaction approach. On the other hand, CC processes are the primary contributors to the signals observed in neutrino

oscillation experiments, as they produce charged leptons that are readily detectable and provide clear flavor identification. The experimental study of NC neutrino processes is significantly more challenging than that of CC reactions, due to the smaller cross sections involved and the absence of charged leptons in the final state. As a result, event identification relies solely on hadron detection. Therefore, this work focuses on the study of the electron-scattering processes

$$\begin{aligned} e^- + A &\to e^- + p + (A-1), \\ e^- + A &\to e^- + n + (A-1), \end{aligned} \tag{2.1}$$

and the corresponding charged-current (anti)neutrino-scattering ones,

$$\begin{aligned} \nu_\ell + A &\to \ell^- + p + (A-1), \\ \bar{\nu}_\ell + A &\to \ell^+ + n + (A-1), \end{aligned} \tag{2.2}$$

with $\ell \equiv e, \mu, \tau$, A the nuclear target and $(A-1)$ the residual nucleus after the interaction. The resulting expressions are general and can be directly applied to both interactions.

The leptonic part of the interaction is readily described within the plane-wave Born approximation, treating the leptons as plane waves. In contrast, the hadronic part is more complex, as it contains all the information related to the boson-nucleon interaction and the nuclear model. The chapter concludes with a discussion of the approach used to describe the nuclear structure of the target nucleus, while further details on this part of the interaction are provided in the following chapter.

Finally, it is also important to stress that due to the fact that the energy (ω) and momentum (q) transfer between the lepton and the nucleus are in some cases comparable or larger than the mass scale set by the nucleon mass, relativistic effects, both in the kinematics and dynamics, are relevant.

2.1 Kinematics

The kinematics for the quasielastic lepton-nucleus scattering are shown in Fig. 2.2. The incoming lepton has four-momentum $K_i = (E_i, \mathbf{k}_i)$, and its interaction with the target nucleus leads to a scattered lepton in the final state with four-momentum $K_f = (E_f, \mathbf{k}_f)$. In this work, we appeal to the first-order Born approximation, where only one boson is exchanged between the lepton and the hadronic system. The four-momentum transferred to the hadronic system is

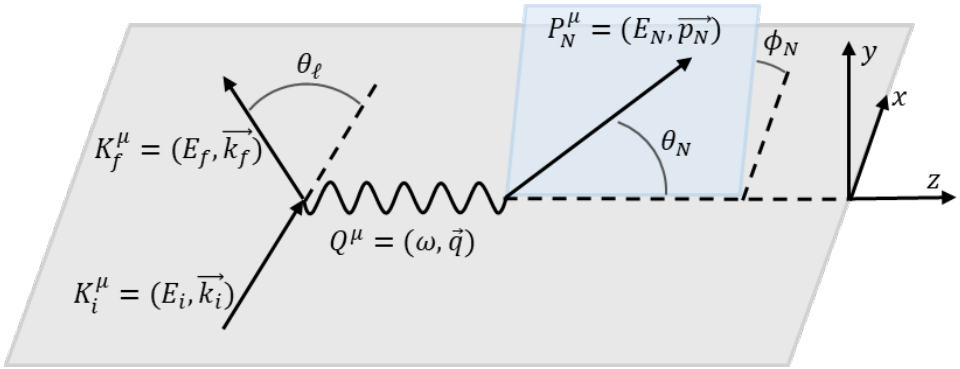

Figure 2.2: Kinematics for the one-nucleon knock-out lepton-nucleus interaction.

$Q = K_i - K_f = (\omega = E_i - E_f, \mathbf{q} = \mathbf{k}_i - \mathbf{k}_f)$ and leads to the invariant quantity $Q^2 = \omega^2 - q^2 < 0$. We work in the coordinate system with the z axis along the transfer momentum $\mathbf{q}$, such that $Q^\mu = (\omega, 0, 0, q)$, and the lepton scattering plane coincides with the xz plane. The target nucleus has four-momentum $P_A = (E_A, \mathbf{p}_A)$ and the residual nucleus and outgoing nucleon have $P_B = (E_B, \mathbf{p}_B)$ and $P_N = (E_N, \mathbf{p}_N)$, respectively. We chose the laboratory reference frame for the calculation, in which the target nucleus is at rest, such that $P_A = (M_A, 0)$.

The residual nucleus may be left in an excited state rather than in its ground state. To account for this possible scenario, we define a missing energy

$$E_m = M_B + M_N - M_A \approx E_B^* + M_B^0 + M_N - M_A, \tag{2.3}$$

where M_B is mass of the excited state, and we have approached it as $M_B \approx E_B^* + M_B^0$ [1] with M_B^0 the mass of the residual nucleus in its ground state and E_B^* the internal excitation energy. In this way, the missing energy refer to the part of the transferred energy, ω, that transforms into internal energy of the residual nucleus.

It results convenient to study and understand the number of independent variables needed to describe lepton-nucleus quasielastic scattering. The initial state consists in an incoming lepton and the target nucleus, while in the final state we find the scattered lepton, the knocked-out nucleon and the undetected residual nucleus. This means that there are 20 unknown variables, 4 for every particle involved. However, there are constraints in the process that reduce the number of independent variables. Energy-momentum conservation gives 4 constraints. The energy-mass

[1] The relation $M_B \approx E_B^* + M_B^0$ is obtained when the kinetic energy of the recoiling nuclear system is neglected. The residual nucleus is heavy, so its recoil energy is small in comparison to its mass at rest, i.e. it can gain momentum with a relatively small gain in kinetic energy. It allows us to simplify the kinematics of the problem such that $E_B^* = E_B - E_B^0 \approx M_B - M_B^0$.

relation of the on-shell particles ($E^2 = p^2 + M^2$) provides 4 additional ones. Note that the masses of all particles are known, except for that of the undetected residual system. After the interaction, the nucleus may be left in an excited state, therefore, this constraint does not apply to it. Finally, the three-momenta of the initial state particles are assumed to be fixed: we work in the laboratory reference frame, where the target nucleus is at rest; we fix the the coordinate system relative to the lepton beam, such that its direction is known; and we select the incoming lepton energy, being a fix value for electrons and an average according to the flux distribution for neutrinos. This eliminates 6 variables and, then, the number of independent variables reduces to 6. All the four-vectors involved in the scattering can be written in terms of these 6 independent variables and the fixed three-momentum of the incoming particles.

2.2 Cross section

The general formula for the cross section is given by

$$d\sigma = \frac{|\overline{S_{fi}}|^2}{\Phi_{inc}\, T}\, dN_f. \tag{2.4}$$

where $|\overline{S_{fi}}|^2$ is the squared matrix element, T is a normalization time, Φ_{inc} is the incident flux and $\mathrm{d}N_f$ represents the number of final of states in phase space. A general Lorentz-invariant expression of the cross section is possible if one uses the definition of the flux [46]

$$\Phi_{inc} = \frac{1}{V} \frac{\sqrt{(K_i \cdot P_A)^2 - m_i^2\, M_A^2}}{E_i\, E_A}, \tag{2.5}$$

where V is the normalization volume. In this work, we consider the target nucleus at rest and neglect the mass of the leptons, in which case the incident flux simplifies to

$$\Phi_{inc} = \frac{1}{V}. \tag{2.6}$$

The number of states within a momentum range $d\mathbf{p}_f$ for each on-shell fermion in the final state is

$$dN_f = V \frac{d\mathbf{p}_f}{(2\pi)^3}. \tag{2.7}$$

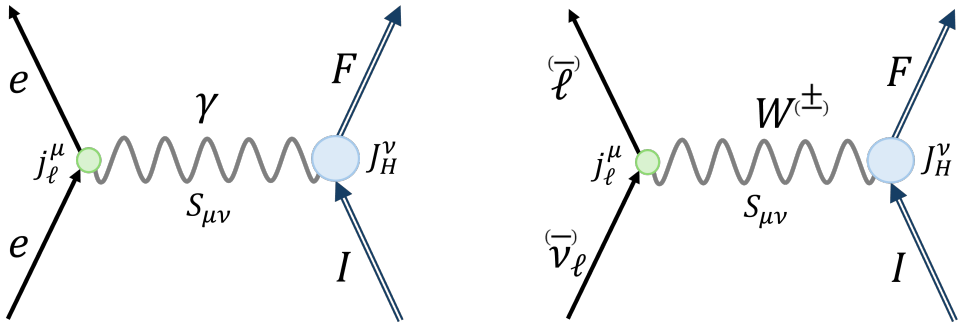

(a) Electron-nucleus interaction. **(b)** CC (anti)neutrino-nucleus interaction.

Figure 2.3: Feynman diagrams for lepton-nucleus quasielatic scattering. The initial nucleus is denoted by I, meanwhile the final hadronic system, containing both the knocked-out nucleon and the residual nucleus, is denoted by F.

In our case, the particles in the final state are the scattered lepton, the knocked-out nucleon and the residual nucleus, then

$$dN_f = \frac{V}{(2\pi)^3} d\mathbf{k}_f \frac{V}{(2\pi)^3} d\mathbf{p}_N \frac{V}{(2\pi)^3} d\mathbf{p}_B \, \rho(E_m) dE_m, \tag{2.8}$$

where $\rho(E_m)$ is the missing energy profile of the target nucleus. The term $\rho(E_m)dE_m$ accounts for the fact that the residual nucleus may not necessarily appear in its ground state, as a result, there is no direct correlation between its energy and momentum. This term represents the number of accessible final states for the residual system within a given missing energy range dE_m, hence, $\rho(E_m)$ is a probability density distribution.

The matrix element, S_{fi}, contains the dynamics of the process. The interaction is schematically represented by the Feynman diagrams in Fig. 2.3, where we distinguish between electromagnetic and charged-current interactions. Using the Feynman rules given in Appendix B, it is given by

$$S_{fi} = i \int d^4X \, i \int d^4Y \, j_\ell^\mu(X) \, S_{\mu\nu}(X,Y) \, J_H^\nu(Y), \tag{2.9}$$

where j_ℓ and J_H are the leptonic and hadronic currents, respectively, and S is the boson propagator.

The modeling of the scattering process is performed within the first-order Born approximation, in which one considers that only one boson is exchanged between the lepton and the nuclear

system. The boson propagator is given by

$$S_{\mu\nu}(X,Y) = \int \frac{\mathrm{d}^4Q}{(2\pi)^4} \frac{-ig_{\mu\nu}}{Q^2 - M_Q^2} e^{iQ(X-Y)}, \tag{2.10}$$

where M_Q denotes the mass of the exchanged boson. Then,

$$S_{\mu\nu}^{EM}(X,Y) = \int \frac{\mathrm{d}^4Q}{(2\pi)^4} \frac{-ig_{\mu\nu}}{Q^2} e^{iQ(X-Y)} \tag{2.11}$$

in the EM case and

$$S_{\mu\nu}^{CC}(X,Y) = \int \frac{\mathrm{d}^4Q}{(2\pi)^4} \frac{-ig_{\mu\nu}}{Q^2 - M_W^2} e^{iQ(X-Y)} \approx \int \frac{\mathrm{d}^4Q}{(2\pi)^4} \frac{ig_{\mu\nu}}{M_W^2} e^{iQ(X-Y)} \tag{2.12}$$

in the CC case, where we have neglected Q^2 with respect to M_W^2 ($M_W \simeq 80.4$ GeV/c^2), as the energies involved in the process are significantly smaller than the mass of the W boson.

The leptonic current, j_ℓ, is defined as

$$j_\ell^\mu(X) = \Psi_{\ell,f}(X) \mathcal{O}_{Q\ell\ell}^\mu \Psi_{\ell,i}(X). \tag{2.13}$$

In the electromagnetic process, the leptonic current involves only vector components. Meanwhile, in charged-current interactions, it is constructed as a sum of vector and axial terms, where the axial part leads to parity violation in weak interactions. Then, the leptonic current operator, $\mathcal{O}_{Q\ell\ell}^\mu$, is given by

$$\mathcal{O}_{\gamma ee}^\mu = e\Gamma_{\gamma ee}^\mu = e\gamma^\mu \tag{2.14}$$

for the EM interaction and

$$\mathcal{O}_{W\nu_\ell\ell}^\mu = \frac{-g}{2\sqrt{2}} \Gamma_{W\nu_\ell\ell}^\mu = \frac{-g}{2\sqrt{2}} \gamma^\mu (1 + h\gamma^5), \tag{2.15}$$

for the CC interaction, with $h = -1(+1)$ for (anti)neutrinos and the projection operator, $\frac{1}{2}(1 + h\gamma^5)$, selects right-handed neutrino or left-handed antineutrino. Considering the leptons as plane waves (Plane Wave Born Approximation, PWBA), such that their wave function is given by A.23, we get

$$j_\ell^\mu(X) = \frac{\sqrt{m_i m_f}}{V\sqrt{E_i E_f}} \overline{u}(\mathbf{k}_f, s_f) \mathcal{O}_{Q\ell\ell}^\mu u(\mathbf{k}_i, s_i) e^{i(K_f - K_i)X}. \tag{2.16}$$

Finally, the hadronic current, J_H, is computed as

$$J_H^\nu = \langle f|\hat{\mathcal{O}}^\mu|i\rangle, \tag{2.17}$$

where i refer to the initial A-body nuclear ground state and f to the final scattering state, i.e. an $A-1$-body residual nucleus and a scattered nucleon. $\hat{\mathcal{O}}^\mu$ is the hadronic current operator, which ideally includes all processes that lead to a final one-particle one-hole (1p-1h) state. Factoring out the coupling constants, we write it as

$$\hat{\mathcal{O}}^\mu_{EM} = -e\hat{\Gamma}^\mu_{EM} \tag{2.18}$$

for the EM interaction and

$$\hat{\mathcal{O}}^\mu_{CC} = \frac{-g\cos\theta_c}{2\sqrt{2}}\hat{\Gamma}^\mu_{CC} \tag{2.19}$$

for the CC interaction, with $\cos\theta_c = 0.974$ the Cabibbo quark mixing angle.

We can now introduce the expressions of the propagator, Eq. 2.10, and the leptonic current within PWBA, Eq. 2.16, in the S-matrix element, Eq. 2.9. Then, the integral over X can be performed immediately using Eq. A.40, leading to an energy-momentum conservation Dirac delta for the leptonic vertex that, integrating over Q, gives the relation $Q = K_i - K_f$. The resulting expression for the S-matrix is

$$S_{fi} = -i\mathcal{F}_X \frac{1}{V\sqrt{E_i E_f}} j_\mu \times \int d^4Y e^{-iQY} \langle \Psi_F|\hat{\Gamma}^\mu_X|\Psi_I\rangle, \tag{2.20}$$

with $X \equiv EM, CC$,

$$\mathcal{F}_{EM} = \frac{e^2}{Q^2} = \frac{4\pi\alpha}{Q^2}, \quad \mathcal{F}_{CC} = \frac{g^2\cos\theta_c}{8M_W^2} = \frac{G_F\cos\theta_c}{\sqrt{2}}, \tag{2.21}$$

with α the fine structure constant and we have redefined the leptonic current as

$$j_\mu = \sqrt{m_i m_f}\ \overline{u}(\mathbf{k}_f, s_f)\Gamma_{Q\ell\ell,\mu}u(\mathbf{k}_i, s_i). \tag{2.22}$$

Now, we focus on the hadronic current. In our framework, the contributions to the process will be obtained as matrix elements of an independent-particle shell model calculation, where each nucleon is subjected to a central potential created by the others. Then, the initial and final nuclear states can be described in terms of single-particle wave functions orthogonal to each other. In addition, factorizing the center of mass, the initial nuclear state is given by the product

of a single-nucleon independent-particle wave function coupled to the rest of the initial nucleus, and the wave function for these remaining $A-1$ nucleons. The final state is given by the product of a wave function for the $A-1$ residual nucleus, which we assume to be a hole state of the initial A-body nucleus, and a distorted wave describing the ejected nucleon. Taking into account all these considerations, the hadronic current can be expressed in terms of the initial and final single-particle states [47; 48], we finally get

$$\int d^4Y e^{-iQY}\langle f|\hat{\Gamma}^\mu_X|i\rangle = \sqrt{\frac{M_A}{VE_A}}\sqrt{\frac{M_B}{VE_B}}(2\pi)^4\delta^4(P_A+Q-P_B-P_N)\times \\ \times\int d\mathbf{y}e^{i\mathbf{q}\cdot\mathbf{y}}\ \langle\alpha_N;\alpha|\hat{\Gamma}^\mu_X|F\rangle. \quad (2.23)$$

where $|F\rangle$ denotes the ground state of the target nucleus and $|\alpha\rangle$ and $|\alpha_N\rangle$ represent the initial bound nucleon and the knocked-out final nucleon, respectively. Further, most often the impulse approximation (IA) is employed in the QE region, meaning that the lepton interacts only with one nucleon, that is subsequently knocked-out from the nucleus. Then, the hadronic current operator reduces to a one-body current operator and the hadronic matrix element is given by

$$\int d\mathbf{y}e^{i\mathbf{q}\cdot\mathbf{y}}\ \langle\alpha_N;\alpha|\hat{\Gamma}^\mu_X|F\rangle = \int d\mathbf{y}\ e^{i\mathbf{q}\cdot\mathbf{y}}\overline{\Psi}^{s_N}(\mathbf{p}_N,\mathbf{y})\Gamma^\mu_{1b,X}\Psi^{m_j}_\kappa(\mathbf{y}). \quad (2.24)$$

For convenience, we change the hadronic wave functions in position space to momentum space using the Fourier transform, A.38, and redefine the hadronic current as

$$J^\mu_\kappa = \sqrt{V}\int d\mathbf{y}\ \overline{\Psi}^{s_N}(\mathbf{p}_N,\mathbf{y})\Gamma^\mu_{1b,X}e^{i\mathbf{q}\cdot\mathbf{y}}\Psi^{m_j}_\kappa(\mathbf{y}) = \sqrt{V}\int d\mathbf{p}\ \overline{\Psi}^{s_N}(\mathbf{p}_N,\mathbf{p}'_N=\mathbf{p}+\mathbf{q})\Gamma^\mu_{1b,X}\Psi^{m_j}_\kappa(\mathbf{p}). \quad (2.25)$$

The initial nucleon is described by a bound wave function, $\Psi^{m_j}_\kappa$, where $\mathbf{p}$ is its momentum, κ represents the nuclear shell and m_j is the third-component of its total angular momentum j. The wave function of the knocked-out final nucleon, Ψ^{s_N}, is a distorted wave function with $\mathbf{p}_N$ the asymptotic momentum, $\mathbf{p}'_N$ its momentum inside the nucleus, which is related by momentum conservation to the other particle states involved in the hadronic vertex, and s_N its spin. It is described as an energy-eigenstate with energy $E^2_N = E'^2_N = p^2_N + M^2_N$. The form of the one-body current operator, as well as more details about the bound and distorted wave functions are given in Chapter 3. An extension of this model by including two-body meson-exchange currents is presented in Chapter 4.

The matrix element for a given initial shell κ reads

$$S_{fi,\kappa} = -i\mathcal{F}_X \frac{1}{V^{5/2}} \frac{1}{\sqrt{E_i E_f}} \frac{\sqrt{M_A M_B}}{\sqrt{E_A E_B}} (2\pi)^4 \delta^4(P_A + Q - P_B - P_N) j_\mu J^\mu_\kappa, \tag{2.26}$$

and the squared matrix element is given by

$$|\overline{S_{fi,\kappa}}|^2 = \overline{\sum}_{i,f} |S_{fi,\kappa}|^2 = \mathcal{F}_X^2 \frac{T}{V^4} \frac{1}{E_i E_f} \frac{M_A M_B}{E_A E_B} (2\pi)^4 \delta^4(P_A + Q - P_B - P_N) L_{\mu\nu} H^{\mu\nu}_\kappa, \tag{2.27}$$

where $\overline{\sum}_{i,f}$ denote the appropriate sum over the final and average over the initial particles' unobserved degrees of freedom. The squared matrix element have been decomposed in terms of leptonic and hadronic tensors, $L_{\mu\nu}$ and $H^{\mu\nu}_\kappa$, respectively. Therefore, introducing the first-order Born approximation——assuming the exchange of a single boson——and applying the plane-wave Born approximation for the leptons allows us to treat the lepton and hadron parts separately.

The leptonic tensor for the electromagnetic interaction is computed as

$$L^{EM}_{\mu\nu} = \frac{1}{2} \sum_{s_i} \sum_{s_f} j_\mu j^\dagger_\nu = \frac{m_e^2}{2} \sum_{s_i} \sum_{s_f} \overline{u}(\mathbf{k}_f, s_f) \gamma_\mu u(\mathbf{k}_i, s_i) [\overline{u}(\mathbf{k}_f, s_f) \gamma_\nu u(\mathbf{k}_i, s_i)]^\dagger, \tag{2.28}$$

where m_e denotes the electron mass. The sum over initial and final helicities allow us to use the closure relation of Dirac spinors, A.35, then

$$L^{EM}_{\mu\nu} = \frac{1}{8} Tr[(\not{K}_i + m_e)\gamma_\mu(\not{K}_f + m_e)\gamma_\nu], \tag{2.29}$$

and, using the properties of the γ matrices, we finally obtain

$$L^{EM}_{\mu\nu} = \frac{1}{2}[K_{i,\mu} K_{f,\nu} + K_{i,\nu} K_{f,\mu} - g_{\mu\nu}(K_i \cdot K_f + m_e^2)]. \tag{2.30}$$

The result for the CC interaction can be readily derived by following the same steps, leading to

$$L^{CC}_{\mu\nu} = \sum_{s_i} \sum_{s_f} j_\mu j^*_\nu = 2[K_{i,\mu} K_{f,\nu} + K_{i,\nu} K_{f,\mu} - g_{\mu\nu}(K_i \cdot K_f) - ih\epsilon_{\mu\nu\alpha\beta} K_i^\alpha K_f^\beta], \tag{2.31}$$

with $\epsilon^{\mu\nu\alpha\beta}$ the Levi-Civita symbol. Note that in the (anti)neutrino case only left(right)-handed (anti)neutrinos interact. There is no average over the two spin states, but we can sum over it because the $V + A$ term will only give contribution to the adequate case. Then, there is a factor 2 with respect to the ordinary sum and average.

The hadronic tensor for the interaction with a nucleon in the κ shell is defined as

$$H_\kappa^{\mu\nu} = \frac{1}{2j+1}\sum_{m_j}\sum_{s_N} J_\kappa^\mu (J_\kappa^\nu)^\dagger. \tag{2.32}$$

In contrast to the other particles, for the initial bound nucleon we average over the $2j+1$ possible m_j states, rather than over the spin.

Finally, the differential cross section reads

$$\frac{d^{10}\sigma_\kappa}{d\mathbf{k}_f d\mathbf{p}_N d\mathbf{p}_B dE_m} = \rho_\kappa(E_m)\mathcal{F}_X^2 \frac{1}{E_i E_f}\frac{M_B}{E_B}\frac{1}{(2\pi)^5}\delta^4(P_A+Q-P_B-P_N)L_{\mu\nu}H_\kappa^{\mu\nu}, \tag{2.33}$$

where, since the target nucleus is at rest, we have taken into account that $E_A = M_A$. We use the delta of 3-momentum to integrate over the undetected residual system, then

$$\frac{d^7\sigma_\kappa}{d\mathbf{k}_f d\mathbf{p}_N dE_m} = \rho_\kappa(E_m)\mathcal{F}_X^2 \frac{1}{E_i E_f}\frac{M_B}{E_B}\frac{1}{(2\pi)^5}\delta(E_A+\omega-E_B-E_N)L_{\mu\nu}H_\kappa^{\mu\nu}. \tag{2.34}$$

The remaining energy-conservation delta is used to integrate over p_N. This integration is carried out by taking into account that E_B is a function of the independent variables and using the property of the delta function given in equation A.42,

$$\delta[f(p_N)] = \frac{\delta(p_N - p_N^0)}{|\partial f(p_N)/\partial p_N|_{p_N=p_N^0}} \tag{2.35}$$

with

$$f(p_N) = M_A + \omega - \sqrt{(E_m - M_N + M_A)^2 + q^2 + p_N^2 - 2qp_N\cos\theta_{qN}} - \sqrt{M_N^2 + p_N^2}, \tag{2.36}$$

and p_N^0 satisfies $f(p_N^0) = 0$. Then, it is given by

$$p_N^0 = \frac{Cq\cos\theta_{qN} - A\sqrt{q^2\cos\theta_{qN}{}^2 M_N^2 + C^2 - A^2 M_N^2}}{q^2\cos\theta_{qN}{}^2 - A^2} \tag{2.37}$$

where

$$A \equiv M_A + \omega, \qquad C \equiv \frac{1}{2}(q^2 + M_B^2 - A^2 - M_N^2). \tag{2.38}$$

The derivative of $f(p_N)$ with respect to p_N yields,

$$\left|\frac{\partial f(p_N)}{\partial p_N}\right| = \left|\frac{p_N - q\cos\theta_{qN}}{E_B} + \frac{p_N}{E_N}\right| = \frac{E_A p_N}{E_N E_B}\left|1 + \frac{\omega p_N - qE_N\cos\Theta_N}{E_A p_N}\right| \tag{2.39}$$

with $E_A = E_B + E_N - \omega$ and, from this result, we define the recoil factor

$$f_{rec} = \left| 1 + \frac{\omega p_N - q E_N \cos\Theta_N}{E_A p_N} \right|_{p_N = p_N^0}, \tag{2.40}$$

which is a correction to the phase space due to the kinetic energy carried away by the residual nucleus. The most differential cross section reads,

$$\frac{d^6\sigma_\kappa}{dk_f d\Omega_f d\Omega_N dE_m} = \rho_\kappa(E_m)\mathcal{F}_X^2 \frac{k_f^2}{E_i E_f} \frac{p_N E_N M_B}{E_A f_{rec}} \frac{1}{(2\pi)^5} L_{\mu\nu} H_\kappa^{\mu\nu}. \tag{2.41}$$

The inclusive cross section corresponds to the case where the outgoing nucleon is not detected. This implies the summation over all active occupied nuclear shells of the target nucleus and the integration over the outgoing nucleon variables. The inclusive cross section is then given by

$$\frac{d^3\sigma}{dk_f d\Omega_f} = \sum_\kappa \int d\phi_N \int d\cos\theta_N \int dE_m \; \rho_\kappa(E_m)\mathcal{F}_X^2 \frac{k_f^2}{E_i E_f} \frac{p_N E_N M_B}{E_A f_{rec}} \frac{1}{(2\pi)^5} L_{\mu\nu} H_\kappa^{\mu\nu}. \tag{2.42}$$

Note that, in the electromagnetic interaction, the electron can scatter on a neutron or a proton, so both possibilities must be summed, while in the (anti)neutrino case the charged-current interaction occurs only with neutrons (protons). Therefore, the sum over κ runs over neutron and proton occupied shells for the EM case and over neutron (proton) shells for the (anti)neutrino CC interaction.

To conclude, it is convenient to define a hadronic reference system $\{\hat{1}, \hat{2}, \hat{3}\}$ with its axes oriented such that the transferred momentum is aligned with the 3 (z) axis and we perform a rotation over ϕ_N along the 3 axis. Then, the system is defined by the following vectors

$$\hat{3} = \hat{z} = \frac{\mathbf{q}}{q}, \;\; \hat{2} = \frac{\mathbf{q} \times \mathbf{p}_N}{|\mathbf{q} \times \mathbf{p}_N|}, \;\; \hat{1} = \hat{2} \times \hat{3}. \tag{2.43}$$

The hadronic tensor is independent of ϕ_N in this hadronic reference system. Therefore, the dependence on ϕ_N in the $\{\hat{x}, \hat{y}, \hat{z}\}$ system is factorized in the Lorentz transformation that relates both coordinate systems. The rotation does not affect the time-like and longitudinal (parallel with q) elements, then

$$H^{00} = H^{00}_{123}, \qquad H^{03} = H^{03}_{123}, \qquad H^{30} = H^{30}_{123}, \qquad H^{33} = H^{33}_{123}, \tag{2.44}$$

meanwhile, the purely transverse components of the hadronic tensor and the mix up with the

time-like and longitudinal ones change according to

$$
\begin{aligned}
H^{11} &= \cos^2\phi_N H^{11}_{123} + \sin^2\phi_N H^{22}_{123} - \cos\phi_N \sin\phi_N (H^{12}_{123} + H^{21}_{123}),\\
H^{22} &= \sin^2\phi_N H^{11}_{123} + \cos^2\phi_N H^{22}_{123} + \cos\phi_N \sin\phi_N (H^{12}_{123} + H^{21}_{123}),\\
H^{12} &= \cos^2\phi_N H^{12}_{123} - \sin^2\phi_N H^{21}_{123} + \cos\phi_N \sin\phi_N (H^{11}_{123} - H^{22}_{123}),\\
H^{21} &= \cos^2\phi_N H^{21}_{123} - \sin^2\phi_N H^{12}_{123} + \cos\phi_N \sin\phi_N (H^{11}_{123} - H^{22}_{123}),\\
H^{01} &= \cos\phi_N H^{01}_{123} - \sin\phi_N H^{02}_{123} \quad , \quad H^{10} = \cos\phi_N H^{10}_{123} - \sin\phi_N H^{20}_{123},\\
H^{02} &= \sin\phi_N H^{01}_{123} + \cos\phi_N H^{02}_{123} \quad , \quad H^{20} = \sin\phi_N H^{10}_{123} + \cos\phi_N H^{20}_{123},\\
H^{31} &= \cos\phi_N H^{31}_{123} - \sin\phi_N H^{32}_{123} \quad , \quad H^{13} = \cos\phi_N H^{13}_{123} - \sin\phi_N H^{23}_{123},\\
H^{32} &= \sin\phi_N H^{31}_{123} + \cos\phi_N H^{32}_{123} \quad , \quad H^{23} = \sin\phi_N H^{13}_{123} + \cos\phi_N H^{23}_{123},
\end{aligned}
\tag{2.45}
$$

with H and H_{123} the hadronic tensor in the $\{\hat{x},\hat{y},\hat{z}\}$ and $\{\hat{1},\hat{2},\hat{3}\}$ reference systems, respectively. In the inclusive cross section (Eq. 2.42), only the hadronic tensor depends on ϕ_N, so the integration over this variable can be analytically performed. It implies a straightforward integration of sines and cosines, obtaining

$$
\begin{aligned}
&H^{00} = 2\pi H^{00}_{123}, && H^{03} = 2\pi H^{03}_{123}, && H^{30} = 2\pi H^{30}_{123}, && H^{33} = 2\pi H^{33}_{123},\\
&H^{11} = \pi H^{11}_{123} + \pi H^{22}_{123}, && H^{22} = \pi H^{11}_{123} + \pi H^{22}_{123}, && H^{12} = \pi H^{12}_{123} - \pi H^{21}_{123}, && H^{21} = \pi H^{21}_{123} - \pi H^{12}_{123},\\
&H^{01} = 0, && H^{10} = 0, && H^{02} = 0, && H^{20} = 0,\\
&H^{31} = 0, && H^{13} = 0, && H^{32} = 0, && H^{23} = 0.
\end{aligned}
\tag{2.46}
$$

Therefore, the computation of the hadronic tensor in the hadronic reference system allows us to avoid the numerical integration over ϕ_N by simply substituting it according to Eq. 2.46.

2.2.1 Hadronic Inclusive Responses

The coordinate system used in this work, with the z axis along the transferred momentum, allows us to decompose the contraction of leptonic and hadronic tensors in physically meaningful variables [49]. In this way, the differential cross section can be expressed as a linear combination of hadronic responses, which includes all the information about the nuclear dynamics.

Electromagnetic inclusive responses

The electromagnetic inclusive cross section can be expressed as [48]

$$\frac{d\sigma}{dE_f d\Omega_f} = \sigma_{Mott}[v_L R_L + v_T R_T], \tag{2.47}$$

where the subindices L and T refer to the longitudinal and transverse components of the currents with respect to the direction of the exchanged boson. The factor is the Mott cross section

$$\sigma_{Mott} = \frac{4\alpha^2}{Q^4} E_f^2 \cos^2\theta_e/2. \tag{2.48}$$

The functions v_k contain all the lepton kinematic information,

$$v_L = \left(\frac{Q^2}{q^2}\right)^2 \quad , \quad v_T = \tan^2\theta_e/2 - \frac{1}{2}\frac{Q^2}{q^2}. \tag{2.49}$$

R_K are the inclusive hadronic response functions,

$$R_K = \sum_\kappa 2\pi \int d\cos\theta_N \int dE_m \mathcal{R}_K^\kappa, \tag{2.50}$$

where $K \equiv L, T$ and the sum over κ includes both neutron and proton occupied shells. $\mathcal{R}_K^\kappa$ are the exclusive hadronic response functions for each particular shell, which are obtained by taking the appropriate components of the hadronic tensor as

$$\begin{aligned} \mathcal{R}_L^\kappa &= \frac{q^2}{Q^2}\left[\mathcal{W}_\kappa^{00} - \frac{\omega}{q}(\mathcal{W}_\kappa^{03} + \mathcal{W}_\kappa^{30}) + \frac{\omega^2}{q^2}\mathcal{W}_\kappa^{33}\right], \\ \mathcal{R}_T^\kappa &= \mathcal{W}_\kappa^{11} + \mathcal{W}_\kappa^{22}, \end{aligned} \tag{2.51}$$

where

$$\mathcal{W}_\kappa^{\mu\nu} = \rho_\kappa(E_m)\frac{M_B E_N p_N}{M_A f_{rec}} H_{123,\kappa}^{\mu\nu}. \tag{2.52}$$

Note that the integration over the angle ϕ_N have been already performed in Eq. 2.50 taking into account the results of Eq. 2.46, this leads to the global 2π factor.

Charged-current inclusive responses

In the (anti)neutrino case, the charge-changing inclusive cross section can be written as [50]

$$\frac{d^2\sigma}{dE_f d\Omega_f} = \sigma_0[v_{CC}R_{CC} + 2v_{CL}R_{CL} + v_{LL}R_{LL} + v_T R_T + h(2v_{T'}R_{T'})], \tag{2.53}$$

where we have an expression of the cross section with charge-charge (CC), charge-longitudinal (CL), longitudinal-longitudinal (LL) and two types of transverse (T, T') responses. The cross section factor is given by

$$\sigma_0 = \frac{G_F^2 \cos\theta_c{}^2}{2\pi^2} k_f E_f \cos^2\tilde{\Theta}/2, \tag{2.54}$$

with $\tilde{\Theta}$ the generalized scattering angle. It reads

$$\tan\tilde{\Theta}/2 = \frac{|Q^2|}{v_0} \ , \ v_0 = (E_i + E_f) - q^2 = 4E_i E_f - |Q^2|. \tag{2.55}$$

The lepton kinematic functions are given by

$$\begin{aligned}
v_{CC} &= 1 - \delta^2 \tan^2\frac{\tilde{\Theta}}{2}, \\
v_{CL} &= \nu + \frac{\delta^2}{\rho'}\tan^2\frac{\tilde{\Theta}}{2}, \\
v_{LL} &= \nu^2 + \delta^2\tan^2\frac{\tilde{\Theta}}{2}\left(1 + \frac{2\nu}{\rho'} + \rho\delta^2\right), \\
v_T &= \left[\frac{1}{2}\rho + \tan^2\frac{\tilde{\Theta}}{2},\right] - \frac{\delta^2}{\rho'}\tan^2\frac{\tilde{\Theta}}{2}\left(\nu + \frac{1}{2}\rho\rho'\delta^2\right), \\
v_{T'} &= \left[\frac{1}{\rho'}\tan^2\frac{\tilde{\Theta}}{2}\right](1 - \nu\rho'\delta^2),
\end{aligned} \tag{2.56}$$

where the neutrino mass has been assumed to be zero and we have defined

$$\delta = \frac{m_f}{\sqrt{|Q^2|}}, \tag{2.57}$$

$$\nu = \frac{\omega}{q}, \tag{2.58}$$

$$\rho = \frac{|Q^2|}{q^2} = 1 - \nu^2, \tag{2.59}$$

$$\rho' = \frac{q}{(E_f + E_i)} = \frac{\tan(\tilde{\Theta}/2)}{\sqrt{\rho + \tan^2\tilde{\Theta}/2}} \ \in \ [0, 1]. \tag{2.60}$$

The inclusive hadronic response functions are given by

$$R_K = \sum_\kappa 2\pi \int d\cos\theta_N \int dE_m \mathcal{R}_K^\kappa \tag{2.61}$$

with $K \equiv CC, CL, LL, T, T'$ and the sum over κ includes the neutron (proton) occupied shells for the (anti)neutrino interaction. As in the electromagnetic case, the integral over ϕ_N have been analytically performed using the results obtained in Eq. 2.46. The exclusive hadronic responses are computed in terms of the components of the hadronic tensor as

$$\begin{aligned}
\mathcal{R}^{\kappa}_{CC} &= \mathcal{W}^{00}_{\kappa}, \\
\mathcal{R}^{\kappa}_{CL} &= -\frac{1}{2}(\mathcal{W}^{03}_{\kappa} + \mathcal{W}^{30}_{\kappa}), \\
\mathcal{R}^{\kappa}_{LL} &= \mathcal{W}^{33}_{\kappa}, \\
\mathcal{R}^{\kappa}_{T} &= \mathcal{W}^{11}_{\kappa} + \mathcal{W}^{22}_{\kappa}, \\
\mathcal{R}^{\kappa}_{T'} &= -\frac{i}{2}(\mathcal{W}^{12}_{\kappa} - \mathcal{W}^{21}_{\kappa}),
\end{aligned} \tag{2.62}$$

where $\mathcal{W}_{\kappa}$ is obtained according to Eq. 2.52.

2.3 Nuclear structure

We now introduce the framework employed to describe the structure of the target nucleus. In this work, we adopt a shell model description basis space, so to say. This allows the hadronic current to be easily computed from the added-up contribution of single-particle-like matrix element calculations. We can use an extreme independent-particle shell model (IPSM), where occupancies and momentum distributions for each nucleon in the bound state are taken from the mean-field calculation, or we can go beyond this IPSM picture which does not fully capture the complexity of nuclei. Indeed, we introduce a more realistic treatment of the nuclear structure by employing a missing energy profile, $\rho(E_m)$ (see Eq. 2.8), based on the semi-phenomenological spectral function (SF) formalism. This study focuses on three nuclear targets, ^{12}C, ^{16}O and ^{40}Ca, all of which have a closed-shell structure and are isospin symmetric nuclei, making them a suitable choice for the initial development of the model. ^{12}C is particularly relevant, as it is used as the target material in the near detectors of several neutrino experiments, including MiniBooNE, MINERvA, T2K and NOMAD [28; 27; 19; 51]. Moreover, the availability of extensive ^{12}C-electron scattering data makes it possible to benchmark our model against well-established electromagnetic measurements. While the experimental data for electron scattering on ^{16}O is significantly more limited, studying this nucleus remains essential for T2K and Hyper-Kamiokande neutrino oscillation experiments, which use water Cherenkov detectors [19; 23]. Finally, ^{40}Ca is

interesting by itself, but also because its close similarity to ^{40}Ar, the target material in several neutrino experiments: ICARUS, MicroBooNE, SBND and DUNE [52; 22; 24; 53].

2.3.1 Missing energy profile

In an independent-particle shell model, also referred to as pure shell model, ^{12}C is made of 2 and 4 nucleons in the $1s_{1/2}$ and $1p_{3/2}$ states, and accordingly for ^{16}O and ^{40}Ca, as shown in Tables 2.2 and 2.4. Each shell has a unique binding energy, E_m^κ, which means that the missing energy distribution predicted by the model would be the sum of one Dirac delta per shell, normalized to its occupancy (see Fig. 2.4),

$$\rho_{IPSM}(E_m) = \sum_\kappa N_\kappa \delta(E_m - E_m^\kappa), \tag{2.63}$$

with $N_\kappa = 2j + 1$ the occupation of the shell in the pure shell model. However, the IPSM is a very crude approximation to describe the missing energy distribution of nuclei, which has been measured for carbon, oxygen, calcium and other nuclei in $(e, e'p)$ and $(p, 2p)$ experiments [54; 55; 56; 57; 58; 59]. The experimental data reveals that the energy response of each shell exhibits a finite width. Additionally, it is observed that the occupancy of the shells is depleted with respect to the independent-particle shell model predictions [60; 61; 62], and that these 'missing nucleons' re-appear in deeper missing energy (E_m) and missing momentum (p_m) regions [63; 64]. This behavior is due to effects beyond the independent-particle approach, ascribed to short- and long-range correlations [65; 66; 67; 68]. To say it in a few words, whenever there is enough energy transferred to the nucleus, so that more than one nucleon may be knocked-out (that is, beyond the two nucleon emission threshold), correlations in the initial state would make possible the emission of additional nucleons (spectators in the impulse approximation), which will carry energy and momentum.

The analysis of $(e, e'p)$, both below and above the two nucleon threshold, made it possible to obtain a semi-phenomenological spectral function [69; 70], composed from discrete and continuum contributions. The discrete spectral function arises from the mean-field contribution at low and intermediate missing energy regions, it is sharply peaked in E_m around the bound energy values of the single-particle states in the nuclear shell model. The continuum contribution, coming from strongly correlated nucleons, produces the depletion of the discrete part of the SF, with a shift of strength (that is, probability of knocking out nucleons from the initial state) to higher excitation

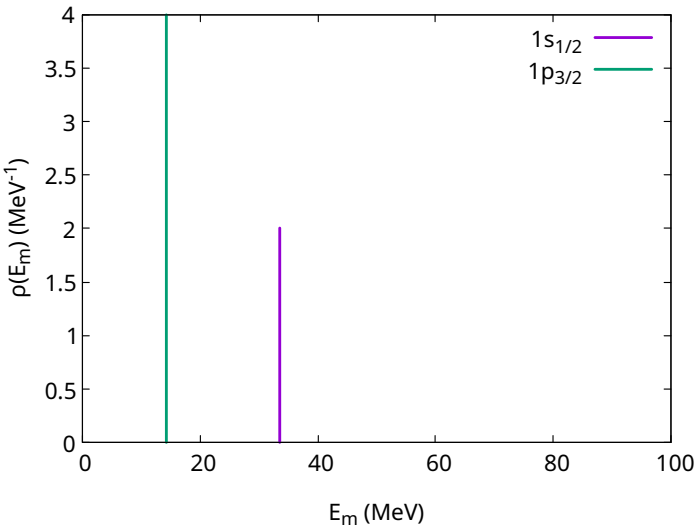

Figure 2.4: Missing energy profile of protons in ^{12}C within the independent-particle shell model.

energies, among other reasons because correlations allow to knock-out additional nucleons, even if the exchanged boson interacts only with one nucleon.

The spectral function, $S(E_m, p_m)$, incorporates the probability of finding the nucleon in the initial state with certain energy and momentum. Within a fully factorized scheme, it is easy to incorporate this formalism in a plane wave calculation [37], with the exclusive 6-differential cross section given by

$$\frac{d^6\sigma}{dk_f d\Omega_f dp_N d\Omega_N} = KS(E_m, p_m)\sigma_{\ell N}, \tag{2.64}$$

where K is a function containing kinematical factors and $\sigma_{\ell N}$ is the elastic lepton-nucleon cross section for an off-shell nucleon with initial momentum p_m.

In this work, following Ref. [71; 72], we take as reference the semi-phenomenological spectral function formalism, but using a representation of the spectral function amenable to our relativistic distorted wave and unfactorized calculations. We substitute the discrete component of the momentum distribution by the one given by RMF single-particle states and construct a continuous missing energy profile, including the depletion of the shell model occupations, inspired by the one of the spectral function

$$\rho_{SF}(E_m) = 4\pi \int dp_m p_m^2 S(E_m, p_m). \tag{2.65}$$

Thus, we reproduce the SF missing energy profile by identifying each discrete contribution with

the corresponding shell, taking into account the missing energy region where it appears, and artificially construct the missing energy distribution of each shell using a Gaussian distribution normalized to the SF occupation, together with a representation of the contribution from correlations. The resulting missing energy profile is of the form,

$$\rho(E_m) = \rho_{SM}(E_m) + \rho_{corr}(E_m) = \sum_{\kappa} \rho_{\kappa}(E_m) + \rho_{corr}(E_m), \tag{2.66}$$

with

$$\rho_{\kappa}(E_m) = \frac{S_{\kappa}}{\sqrt{2\pi}\sigma_{\kappa}} exp\left[-\left(\frac{E_m - \mu_{\kappa}}{2\sigma_{\kappa}}\right)^2\right], \tag{2.67}$$

where μ_{κ} is the mean value, σ_{κ} is the standard deviation and S_{κ} is the occupation number from the SF approach. We use the same occupations for protons and neutrons in all cases.

For ^{12}C and ^{16}O, the missing energy profiles of protons are constructed to reproduce those of the Rome spectral function for each nucleus [69; 73]. The contributions from the shells are parametrized using the Gaussian function of Eq. 2.67 with the parameters given in Tables 2.1 and 2.2. We use the same missing energy profile for neutrons, but with a shift in the energy peaks to account for the Coulomb interaction in the proton case. This shift is computed as the difference between proton and neutron separation energies from nuclear mass tables [74]. For ^{12}C, we get

$$E_s^p = M_{12C} - M_{11B} - M_p = -15.96 \text{ MeV}, \tag{2.68}$$

$$E_s^n = M_{12C} - M_{11C} - M_n = -18.72 \text{ MeV}, \tag{2.69}$$

and for ^{16}O,

$$E_s^p = M_{16O} - M_{15N} - M_p = -12.13 \text{ MeV}, \tag{2.70}$$

$$E_s^n = M_{16O} - M_{15O} - M_n = -15.67 \text{ MeV}, \tag{2.71}$$

with M_{AX} the nuclear mass.

For ^{40}Ca, the missing energy profile has been constructed taking as reference the results from several analysis [56; 58; 57; 62; 60; 61; 59]. For the most external shell, $1d_{3/2}$, we use the separation energy from nuclear mass tables [74] to set the peak in the proton and neutron

κ	N_κ	n_κ	$\mu_{\kappa,p}$ (MeV)	$\mu_{\kappa,n}$ (MeV)	σ_κ (MeV)
$1p_{3/2}$	4	0.82	16.0	18.7	2.0
$1s_{1/2}$	2	0.90	36.0	38.7	10.0

Table 2.1: Parameters of the missing energy profile for the ^{12}C shells. κ is the shell model state; N_κ is the occupation of the shells according to the independent-particle shell model; n_κ is the occupation probability of the shells from the SF approach, the corresponding occupation is computed as $S_\kappa = n_\kappa \times N_\kappa$; $\mu_{\kappa,N}$ and σ_κ are the parameters of the Gaussian function in Eq. 2.67, where the subscript N indicates the isospin of the nucleon.

κ	N_κ	n_κ	$\mu_{\kappa,p}$ (MeV)	$\mu_{\kappa,n}$ (MeV)	σ_κ (MeV)
$1p_{1/2}$	2	0.76	13.0	16.5	1.0
$1p_{3/2}$	4	0.87	19.0	22.5	1.0
$1s_{1/2}$	2	0.81	45.0	48.5	15.0

Table 2.2: Parameters of the missing energy profile for the ^{16}O shells. κ is the shell model state; N_κ is the occupation of the shells according to the independent-particle shell model; n_κ is the occupation probability of the shells from the SF approach, the corresponding occupation is computed as $S_\kappa = n_\kappa \times N_\kappa$; $\mu_{\kappa,N}$ and σ_κ are the parameters of the Gaussian function in Eq. 2.67, where the subscript N indicates the isospin of the nucleon.

distributions. These are

$$E_s^p = M_{40Ca} - M_{39K} - M_p = -8.46 \text{ MeV}, \tag{2.72}$$

$$E_s^n = M_{40Ca} - M_{39Ca} - M_n = -15.62 \text{ MeV}. \tag{2.73}$$

For the internal shells, the peaks of the proton distribution have been taken from [58], and for neutrons, as done in the case of ^{12}C and ^{16}O, we shift the proton values to account for the Coulomb interaction using the difference between the neutron and proton separation energies. Again, the missing energy distribution for each shell is parametrized as the Gaussian distribution in Eq. 2.67, narrower for the external shells, and wider for the deeper ones, with the parameters given in Table 2.3. Nevertheless, we stress that the inclusive observables that are studied in this work, responses and cross sections, are mostly sensitive to the overall occupation probability of the shells and not to fine details of the missing energy profile. Finally, in this case, occupation ranges for the shells have been introduced to account for the uncertainties and discrepancies of the different studies, the used values are shown in Table 2.4.

Until now, only the discrete part of the spectral function, coming from the shell model states,

κ	$\mu_{\kappa,p}$ (MeV)	$\mu_{\kappa,n}$ (MeV)	σ_κ (MeV)
$2s_{1/2}$	11.0	18.3	2.0
$1d_{3/2}$	8.5	15.6	2.0
$1d_{5/2}$	15.7	23.0	4.0
$1p_{1/2}$	29.8	37.1	8.0
$1p_{3/2}$	34.7	42.0	8.0
$1s_{1/2}$	53.6	60.9	15.0

Table 2.3: Parameters of the missing energy profile for the ^{40}Ca shells. κ is the shell model state, $\mu_{\kappa,N}$ and σ_κ are the parameters of the Gaussian function in Eq. 2.67, where the subscript N indicates the isospin of the nucleon.

		n_κ					
κ	N_κ	(e,e'p) [56]	(e,e'p) [62]	(e,e'p) [60]	(e,e'p) [61]	(p,2p) [57]	This work
$2s_{1/2}$	2	0.58 - 0.70	0.57 - 0.63	0.48 - 0.54	0.51	0.49 - 0.57	0.50 - 0.70
$1d_{3/2}$	4	0.58 - 0.72	0.67 - 0.75	0.72 - 0.8	0.49 - 0.69	0.60 - 0.70	0.50 - 0.70
$1d_{5/2}$	6	0.78 - 0.88				0.76 - 0.94	0.60 - 0.80
$1p_{1/2}$	2					0.42 - 0.56	0.60 - 0.80
$1p_{3/2}$	4					0.42 - 0.56	0.60 - 0.80
$1s_{1/2}$	2					0.80 - 0.98	0.70 - 0.85

Table 2.4: ^{40}Ca shell model states (κ), their occupations according to the independent-particle shell model (N_κ), and occupation probabilities (n_κ) from the references [56; 62; 60; 61; 57] and the ranges used in this work, the corresponding occupation is computed as $S_\kappa = n_\kappa \times N_\kappa$.

has been considered. This implies that a fraction of nucleons remains unaccounted for in the model, corresponding to the continuum contribution. To incorporate this missing component, an additional contribution is included to represent knock-out of correlated nucleons, i.e., more than one nucleon is knocked-out in the process due to correlations, and that shows up in the high missing energy and momentum regions. In what follows, we refer to this contribution as the background. The momentum distribution of this contribution is modeled as an s-wave, broad in momentum space, fitted to reproduce the correlated part of the Rome spectral function. A comparison between the resulting momentum distribution and that of the Rome spectral function for ^{12}C is shown in Fig. 2.5. Notably, for the kinematical settings included in this work, inclusive cross sections and responses are anyway very insensitive to the actual shape of the momentum distribution of this background component. With respect to the missing energy profile, the background contribution starts at the two-nucleon emission threshold, it has a soft maximum at around 100 MeV and follows an exponential decay extending to high momentum [71; 72]. In the region $25 \lesssim E_m \lesssim 100$ MeV, both the discrete contribution from the deeper shells and the continuum one from the background coexist. The missing energy profile in this region is parametrized as

$$\rho_{corr}(E_m) = S_{corr} \frac{a \exp(-100b)}{\exp[-(E_m - c)/w] + 1}. \tag{2.74}$$

Meanwhile, in the region $E_m \gtrsim 100$ MeV, we assume that there is only background, which is well described by an exponential fall-off

$$\rho_{corr}(E_m) = S_{corr}\, a \exp(-bE_m), \tag{2.75}$$

where $a = 0.022078$ MeV^{-1}, $b = 0.0112371$ MeV^{-1}, $c = 40$ MeV, $w = 5$ MeV and S_{corr} represents the number of nucleons in the background such that, after summing over all shells, the 12, 16 and 40 nucleons of ^{12}C, ^{16}O and ^{40}Ca, respectively, are recovered.

Finally, the missing energy profiles of carbon, oxygen and calcium used in this work are shown in Figs. 2.6, 2.7 and 2.8. In the case of calcium, the missing energy distribution, as well as the results of this work, are presented as bands that account for the uncertainty in the occupation probability of the single-particle states. To obtain these bands, we have generated 10^4 random configurations for the ^{40}Ca shell occupations within the limits shown in Table 2.4, and the number of nucleons in the background is set such that the total number of protons and neutrons is 20. However, using this method, we can get configurations with up to 42% of nucleons in the background, which is clearly unrealistic. Therefore, a certain configuration is only

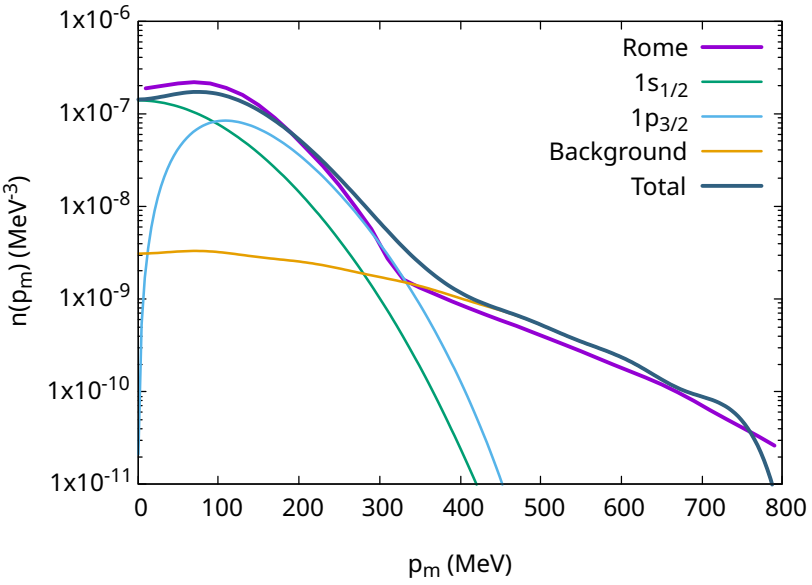

Figure 2.5: Momentum distribution of protons in ^{12}C from the Rome spectral function [69; 73] and from our representation.

accepted if satisfies the constraint that the amount of nucleons in the background is between 20% and 35% of the total number of nucleons. The two extremes of these 10^4 configurations, which correspond to the limits of the bands, are taken as those with the most and least nucleons in the background within the allowed values (see Table 2.5). Nonetheless, we stress that a background containing the 35% of the total amount of nucleons may still be an overestimated scenario. Recent works have estimated about 20% [63; 64] of short-range correlated pairs in nuclei, therefore, when considering a larger contribution, we should take into account that our large background is effectively accounting for other mechanisms, as long-range correlations. A more accurate modeling of these effects would be required to fully capture the complexity of nuclear dynamics. For instance, short- and long-range correlations have been investigated using microscopic approaches that incorporate correlation functions [75; 76; 77; 78; 79]. However, a detailed treatment of such effects lies beyond the scope of the present work and is left for future investigations.

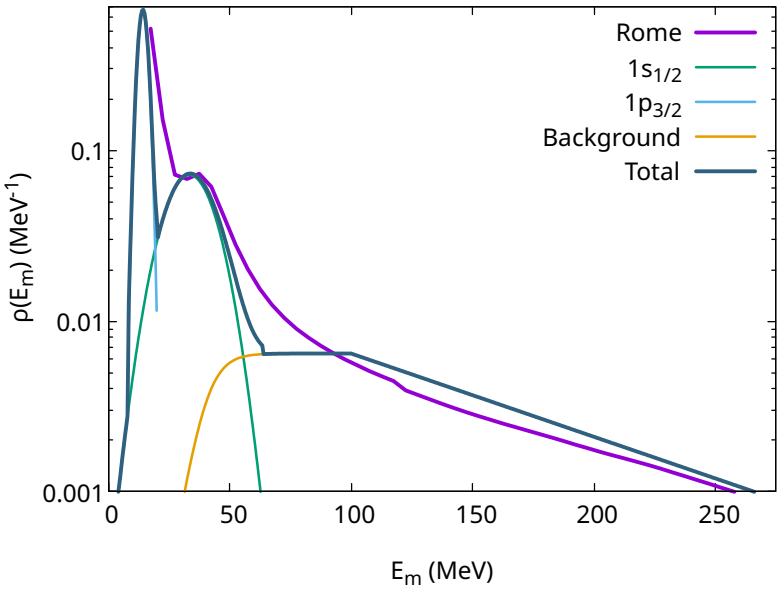

Figure 2.6: Missing energy profile of protons in ^{12}C from the Rome spectral function [69; 73] and from our representation.

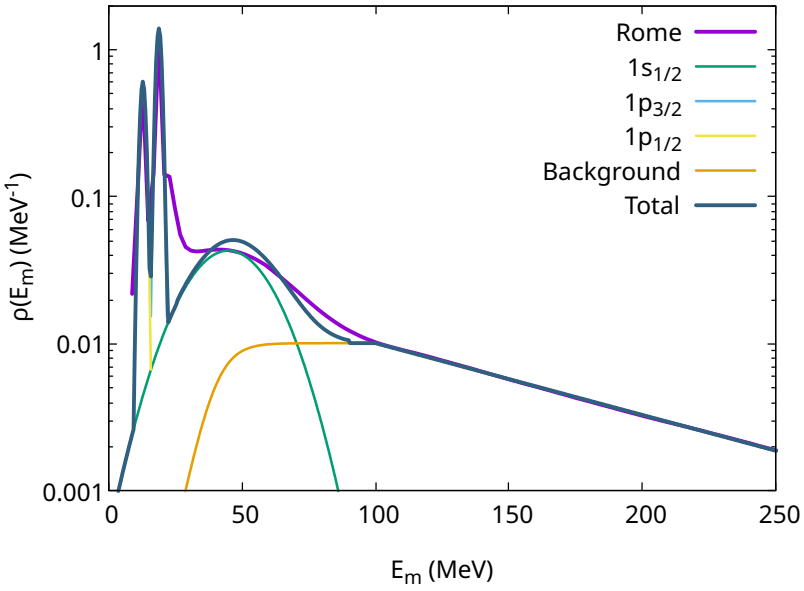

Figure 2.7: Missing energy profile of protons in ^{16}O from the Rome spectral function [69; 73] and from our representation.

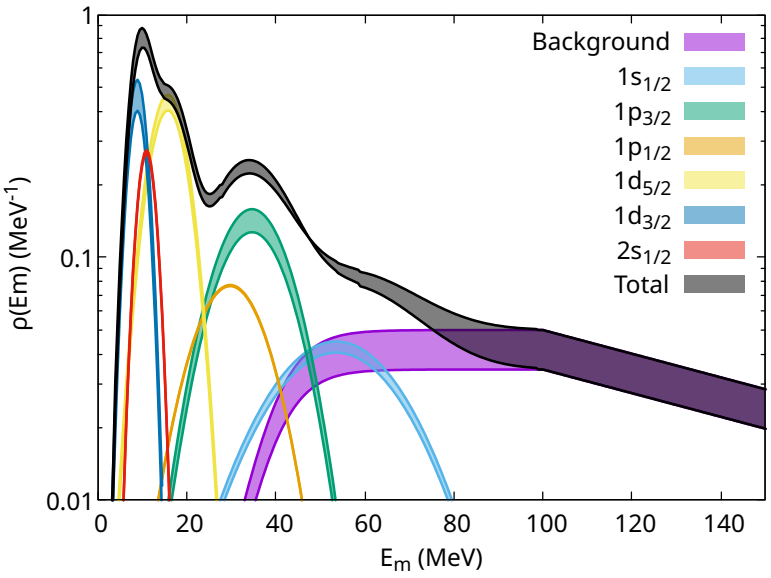

Figure 2.8: Missing energy profile of protons in ^{40}Ca from our representation.

κ	n_κ	
	Lower limit	Upper limit
$2s_{1/2}$	0.69	0.67
$1d_{3/2}$	0.68	0.50
$1d_{5/2}$	0.78	0.67
$1p_{1/2}$	0.77	0.76
$1p_{3/2}$	0.79	0.64
$1s_{1/2}$	0.85	0.76
Background	0.24	0.35

Table 2.5: ^{40}Ca shell model states (κ) and their occupation probabilities (n_κ) in the limits of the bands of the missing energy profile.

Chapter 3

Hadronic current

In our approach, considering the first-order Born approximation and describing the leptons within the plane wave Born approximation, the cross section can be expressed as the contraction of leptonic and hadronic tensors. The leptonic part can be readily obtain in this scenario. Meanwhile, the hadronic tensor requires further study, as it contains all the information about the boson-nucleus interaction as well as the hadronic final-state interactions. As shown in Sec. 2.2, the hadronic tensor is computed in terms of the hadronic current which, within the independent-particle shell model, is given by

$$J^{\mu}_{\kappa} = \sqrt{V} \int d\mathbf{p}\ \overline{\Psi}^{s_N}(\mathbf{p}_N, \mathbf{p}'_N)\Gamma^{\mu}\Psi^{m_j}_{\kappa}(\mathbf{p}). \tag{3.1}$$

We distinguish three components: the initial bound nucleon, $\Psi^{m_j}_{\kappa}(\mathbf{p})$; the hadronic current operator, Γ^{μ}; and the final knocked-out nucleon, $\overline{\Psi}^{s_N}(\mathbf{p}_N, \mathbf{p}'_N)$. In this chapter we discuss in detail how we describe these three parts of the computation.

3.1 Initial bound nucleon

Within the independent-particle shell model, bound nucleons occupy discrete shells that are eigenstates of a spherically symmetric potential. These states are labeled by the angular momentum quantum numbers κ and m_j, with a fixed energy eigenvalue for every κ, while there is a degeneracy in m_j. Depending on the level of detail required, the chosen potential can vary from a simple harmonic oscillator to a sophisticated microscopic model with realistic nucleon-nucleon interactions. In this work, we consider a potential derived from a relativistic mean-field model. This model extends the original σ–ω framework by including non-linear couplings of

the σ meson [80]. Its starting point is the construction of a phenomenological Lorentz-covariant Lagrangian density that includes the nucleon-nucleon interaction through meson exchange. The parameters are adjusted by fitting general properties of nuclear matter and some finite nuclei (see Appendix E for more details). Finally, the bound wave function is given by the general solution of the Dirac equation in the presence of scalar and vector central potentials,

$$\Psi_\kappa^{m_j}(\mathbf{r}) = \begin{pmatrix} g_\kappa(r)\Phi_\kappa^{m_j}(\Omega_r) \\ i f_\kappa(r)\Phi_{-\kappa}^{m_j}(\Omega_r) \end{pmatrix}, \tag{3.2}$$

where the spin-spherical harmonics, $\Phi_\kappa^{m_j}(\Omega_r)$, contain the angular dependence of the wave function and are given by

$$\Phi_\kappa^{m_j}(\Omega_r) = \sum_{m_l,m_s} \langle l, m_l; \frac{1}{2}, m_s | j, m_j \rangle Y_l^{m_l}(\Omega_r)\chi_{m_s}. \tag{3.3}$$

The relativistic quantum number κ is related to the total angular momentum by $j = |\kappa| - 1/2$ and to the orbital angular momentum by

$$l = \begin{cases} \kappa & \text{if} \quad \kappa > 0, \\ -\kappa - 1 & \text{if} \quad \kappa < 0. \end{cases} \tag{3.4}$$

m_l and m_s are the projections of the orbital angular momentum and the spin, $s = 1/2$, respectively. $\langle l, m_l; \frac{1}{2}, m_s | j, m_j \rangle$ are Clebsch-Gordan coefficients, $Y_l^{m_l}$ are the spherical harmonics and χ_{m_s} is a Pauli spinor of two components, with $\chi_{+1/2} = \begin{pmatrix} 1 \\ 0 \end{pmatrix}$ and $\chi_{-1/2} = \begin{pmatrix} 1 \\ 0 \end{pmatrix}$. The radial functions $g_\kappa(r)$ and $f_\kappa(r)$ are solutions of the following coupled differential equations

$$\begin{aligned} \frac{df_\kappa(r)}{dr} &= \frac{\kappa - 1}{r} f_\kappa(r) - [E - M_N - S(r) - V(r)] g_\kappa(r), \\ \frac{dg_\kappa(r)}{dr} &= -\frac{\kappa + 1}{r} g_\kappa(r) + [E + M_N + S(r) - V(r)] f_\kappa(r), \end{aligned} \tag{3.5}$$

with $S(r)$ and $V(r)$ the relativistic mean-field scalar and vector potentials, respectively. Although an explicit dependence on the isospin has not been introduced, the difference between neutron and proton wave functions is given by the vector potential (Eq. E.8).

The Fourier transform yields the bound state wave function in momentum space,

$$\Psi_\kappa^{m_j}(\mathbf{p}) = (-i)^l \begin{pmatrix} g_\kappa(p) \\ S_\kappa f_\kappa(p) \frac{\boldsymbol{\sigma}\cdot\mathbf{p}}{p} \end{pmatrix} \Phi_\kappa^{m_j}(\Omega_p). \tag{3.6}$$

where $S\kappa = \kappa/|\kappa|$, $\boldsymbol{\sigma}$ is a row vector containing the Pauli matrices and

$$\Phi^{m_j}_{-\kappa}(\Omega_p) = -\frac{\boldsymbol{\sigma}\cdot\mathbf{p}}{p}\Phi^{\mu}_{\kappa}(\Omega_p). \tag{3.7}$$

The radial functions in momentum space are obtained from the respective functions in coordinate space as

$$\begin{aligned} g_\kappa(p) &= \sqrt{\frac{2}{\pi}}\int_0^\infty dr\, r^2 g_\kappa(r) j_l(pr), \\ f_\kappa(p) &= \sqrt{\frac{2}{\pi}}\int_0^\infty dr\, r^2 f_\kappa(r) j_{\bar{l}}(pr), \end{aligned} \tag{3.8}$$

with j_l the Riccati-Bessel functions and $\bar{l}$ is defined as

$$\bar{l} = \begin{cases} \kappa - 1 & \text{if} \quad \kappa > 0, \\ |\kappa| & \text{if} \quad \kappa < 0. \end{cases} \tag{3.9}$$

Finally, the relativistic wave functions in either space are normalized as

$$\int dr\, r^2 (g^2_\kappa(r) + f^2_\kappa(r)) = \int dp\, p^2 (g^2_\kappa(p) + f^2_\kappa(p)) = 1, \tag{3.10}$$

and the integral over the solid angles is trivial as the spin-spherical harmonics are normalized to one.

3.2 Hadronic current operator

The hadronic current operator ideally includes all the processes that lead to a final 1p-1h state. However, this computation poses a significant challenge, so it results necessary to appeal to some approximations. The usual treatment of the quasielastic scattering relies on the impulse approximation, in which one considers that the boson couples only to the knocked-out nucleon (see Fig. 3.1). It gives the main contribution to the QE response, through the one-body current. An extension of the model, going beyond IA and including one-pion exchange effects by incorporating two-body meson-exchange currents with a final paticle-hole state is presented in the next chapter.

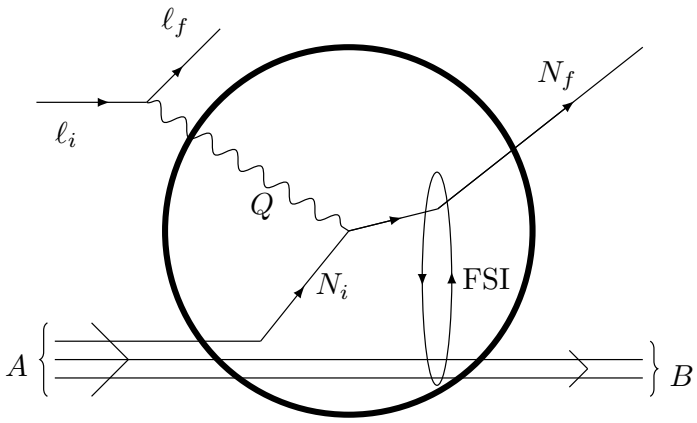

Figure 3.1: Scheme for the process $A(\ell, \ell' N)B$ within the impulse approximation.

3.2.1 One-body current operator

The one-body current is computed as

$$J^{\mu}_{1b} = \sqrt{V} \int d\mathbf{p}\ \overline{\Psi}^{s_N}(\mathbf{p}_N, \mathbf{p}+\mathbf{q})\Gamma^{\mu}_{1b}\Psi^{m_j}_{\kappa}(\mathbf{p}), \tag{3.11}$$

with Γ^{μ}_{1b} the one-body current operator. In this work, it is computed using the CC2 prescription [60; 81; 82].

The one-body current operator for the electromagnetic interaction, as in the leptonic case, only contains vector current contributions. It is given by

$$\Gamma^{\mu}_{1b,EM} = \Gamma^{\mu}_{\gamma NN} = F_1^{p,n}(Q^2)\gamma^{\mu} + i\frac{F_2^{p,n}(Q^2)}{2M_N}\sigma^{\mu\alpha}Q_{\alpha}, \tag{3.12}$$

where $\sigma^{\mu\sigma} = (i/2)[\gamma^{\mu}, \gamma^{\alpha}]$. Unlike the leptonic current, where the involved particles are point-like, nucleon form factors are now introduced in the hadronic current operator to account for the inner structure of nucleons. $F_1^{p/n}$ and $F_2^{p/n}$ are, respectively, the Pauli and Dirac electromagnetic form factors of proton or neutron and they are computed using Kelly's parametrization [83].

In the charged-current case, the one-body current operator now contains vector and axial terms,

$$\Gamma^{\mu}_{1b,CC} = \Gamma^{\mu}_{WNN} = \Gamma^{\mu}_{V} - \Gamma^{\mu}_{A}. \tag{3.13}$$

The vector current operator is

$$\Gamma_V^\mu = F_1^V(Q^2)\gamma^\mu + i\frac{F_2^V(Q^2)}{2M_N}\sigma^{\mu\alpha}Q_\alpha, \tag{3.14}$$

being $F_{1,2}^V$ the weak vector form factors, which are related to the electromagnetic ones for protons and neutrons by the conserved vector current (CVC) hypothesis as $F_{1,2}^V = F_{1,2}^p - F_{1,2}^n$. The axial current operator is

$$\Gamma_A^\mu = G_A(Q^2)\gamma^\mu\gamma^5 + \frac{G_P(Q^2)}{M_N^2}\not{Q}Q^\mu\gamma^5, \tag{3.15}$$

with G_A the axial form factor and G_P the pseudo-scalar axial form factor. A standard dipole parametrization is used for the axial form factor, which is computed as

$$G_A(Q^2) = \frac{g_A}{(1 - Q^2/M_A^2)^2}, \tag{3.16}$$

where $g_A = 1.26$ is known from β-decay and we use a value of the axial mass, M_A, of 1.05 GeV extracted from neutrino-deuteron scattering and pion electro-production experiments [84; 85; 86; 87; 88]. However, it is worth noting that recent Lattice-QCD calculations and measurements of antineutrino-proton scattering from MINERνA collaboration suggest a significantly larger axial form factor, as well as a shallower fall-off for $Q^2 > 0.3$ GeV^2 [89; 90; 91; 92; 93]. Axial form factors consistent with these results have been introduced in theoretical GFMC and spectral function calculations, and in the Monte Carlo neutrino event generator GENIE, obtaining an increase of the inclusive cross section [43; 94; 92]. Finally, partial conservation of the axial current (PCAC) and pion-pole dominance allow us to write the pseudo-scalar form factor in terms of G_A as

$$G_P(Q^2) = \frac{G_A(Q^2)M_N^2}{m_\pi^2 - Q^2}, \tag{3.17}$$

where m_π denotes the pion mass.

3.3 Final knocked-out nucleon

In a particle-hole excitation, the outgoing nucleon may interact with the remaining $A-1$ nucleons in its way out of the residual system, leading to a different final state compared to one created in the interaction vertex. For instance, transitions to unobserved channels, that produce a reduction of the cross section, or elastic interactions with the nuclear medium can occur. We

refer to these processes as final-state interactions (FSI) and, in our framework, the scattered nucleon is described within the relativistic distorted wave impulse approximation (RDWIA).

The distorted wave function of the knocked-out nucleon, Ψ^{s_N}, is obtained as a solution of the Dirac equation in the continuous with central scalar and vector potentials. It is expressed as a partial wave expansion [47]

$$\Psi^{s_N}(\mathbf{p}'_N, \mathbf{p}_N) = 4\pi\sqrt{\frac{E_N + M_N}{2E_N V}} \sum_{\kappa, m_j, m_l} i^l e^{-i\delta^*_\kappa} \langle l, m_l; \frac{1}{2}, s_N | j, m_j \rangle Y_l^{m_l *}(\Omega_{p_N}) \Psi_\kappa^{m_j}(\mathbf{p}'_N), \quad (3.18)$$

where $\mathbf{p}_N$ is the asymptotic momentum of the outgoing nucleon, $\mathbf{p}'_N$ is its momentum inside the nucleus and s_N corresponds to its spin. The scattered nucleon is described as an energy eigenstate, therefore, $E_N^2 = E_N'^2 = p_N^2 + M_N^2$. $\Psi_\kappa^{m_j}(\mathbf{p}'_N)$ are spinors as in Eq. 3.6 [60; 82; 95]. The distorted wave function is normalized such that in the absence of a potential it would be a plane wave.

There are several choices for the potential used to describe the final state, depending on whether or not the outgoing nucleon is detected. For exclusive experimental signatures, where the scattered nucleon is detected and the kinematics ensure that it is the only possible nucleon in the final state (i.e. below the two-nucleon knockout threshold; see, e.g., Refs. [56; 54; 55]), only elastic propagation of the nucleon in the residual nucleus needs to be considered. Contributions from inelastic channels are either forbidden (if the residual system is left in its ground state) or strongly suppressed. In this case, FSI are introduced through relativistic optical potentials (ROP) that include both real and imaginary terms. The imaginary part removes inelastic channels, which means that the knocked-out nucleon in its way out of the nucleus only interacts elastically and no other hadrons are created in the process. Meanwhile, in the context of this work, where only inclusive processes are considered, the distorted nucleon is computed using real potentials that conserve the total flux, i.e., the real potential makes sure that all strength is retained. The outgoing nucleon may rescatter, be absorbed, knock out additional nucleons, and undergo any type of FSI in general, but any of these cases should still contribute to the cross section. In what follows, we discuss the various possible approaches.

Relativistic optical potentials obtained from phenomenological fits to elastic proton-nucleus scattering data has been shown to be quite effective in describing inclusive observables when only its real part (rROP) is considered. The total flux is conserved, and the energy dependent real part becomes weaker in a way which is empirically found to describe the inclusive quasielastic cross section [96]. Nevertheless, at small nucleon energies, one has to deal with the fact that

the rROP will produce wave functions which are inconsistent and non-orthogonal with respect to the initial state described by the RMF.

Then, another possibility is to describe the outgoing nucleon using the same RMF potential that is considered for the bound nucleon. This results in good model consistency, with the initial and final nucleon wave functions being orthogonal as they are both solutions of the same Dirac equation. It seems to be a reasonable framework at least at low energies and momenta, like those of bound nucleons, where we can expect a similar effect from the residual nuclear system. However, when the nucleon energy becomes larger, the RMF potential is too strong. The phenomenology tells us that the interaction of the nucleon with the residual system should weaken at large energies. This lead us to the next proposal, the energy dependent relativistic mean-field (ED-RMF) potential. The ED-RMF potential is constructed as the RMF potential used in the bound state but multiplied by a phenomenological function that weakens the scalar and vector potentials for increasing nucleon momenta [97; 98; 96]. The ED-RMF parametrization is inspired by the SuSAv2 analysis of inclusive (e, e') scattering data [99; 100; 101]. Within SuSAv2, the description of the quasielastic peak relies on scaling functions for inclusive nuclear responses derived from calculations within RDWIA, using the RMF potential, and the relativistic plane wave impulse approximation (RPWIA), where the final nucleon is described as a plane wave. These scaling functions are combined using weights which depend on the momentum transfer such that, at low q, the RMF contribution dominates, while at higher q, the cross section approaches the RPWIA prediction. These weights are then used to determine the energy-dependent function, which multiplies both vector and scalar RMF potentials, leading to the ED-RMF approach. This empirical blending function, shown in Fig. 3.2, was obtained as a fit to the SuSAv2 RMF-to-RPWIA transition functions for ^{12}C. For $T_N < 100$ MeV, the RMF model agrees with data well, so the function is close to 1, while as T_N increases the magnitude of the RMF potentials is reduced. Although this ED-RMF function has been fitted to electron scattering data on ^{12}C, this method can be safely applied to other nuclei independently of their mass and isospin [97]. The main advantage of this choice is that it preserves the orthogonality between the initial and final states at low energies of the final nucleon, while approaching the behavior of the phenomenological optical potentials at larger energies.

Finally, in some cases, it results convenient to simplify the problem introducing the relativistic plane wave impulse approximation. We neglect the effect of final-state interactions on the outgoing nucleon, describing it as a relativistic plane wave. Although RPWIA is an oversimplified description of the process that is not suitable for realistic predictions, it is a very common

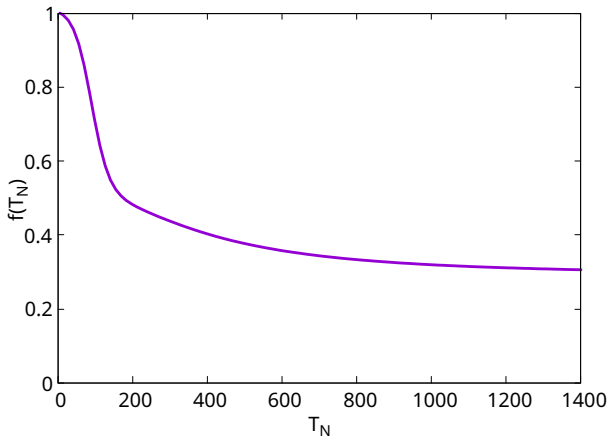

Figure 3.2: Function that scales the RMF potentials in the ED-RMF approach [97]. It is parametrized as $f(T_N) = \frac{0.85}{(T_N/200)^2+3.5} + \frac{0.48}{exp[(T_N-90)/23]+1} + 0.29$ with T_N the kinetic energy of the outgoing nucleon in the laboratory frame and in MeV.

first-order theoretical estimate that can help in improving our understanding. Additionally, this approximation results particularly convenient, as it simplifies the hadronic current to

$$J^{\mu}_{\kappa} = (2\pi)^{3/2}\sqrt{\frac{M_N}{E_N}}\overline{u}(\mathbf{p}_N, s_N)\Gamma^{\mu}\Psi^{m_j}_{\kappa}(\mathbf{p}_N - \mathbf{q}), \tag{3.19}$$

where $\mathbf{p}_N = \mathbf{p}'_N = \mathbf{p} + \mathbf{q}$ and $u(\mathbf{p}_N, s_N)$ is the free Dirac spinor representing the outgoing nucleon.

A comparison of the electromagnetic inclusive responses of ^{12}C computed using the real part of the relativistic optical potential EDAI-C, RMF and ED-RMF potentials, as well as within RPWIA, is shown in Fig. 3.3. Our theoretical results are compared to experimental data extracted by means of a Rosenbluth analysis by Jourdan [102] and Barreau et al. [103].

As expected, RPWIA calculations overestimate the data, especially at low values of momentum transfer. Furthermore, the low-energy behavior of the responses significantly deviates from the experimental results. This may be attributed to the distortion of the final nucleon that is not being included in RPWIA, which, among other effects, gives rise to spurious contributions to the responses due to the lack of orthogonality between initial and final states. The effect of distortion, as shown in the EDAI-C, RMF and ED-RMF approaches, is to shift the peak of the responses to the correct position, according to the data, to reduce the total strength and to redistribute it from the peak to the tails, particularly to the low energy end of the responses.

On the other hand, the RMF computation is able to reproduce the data at relatively small

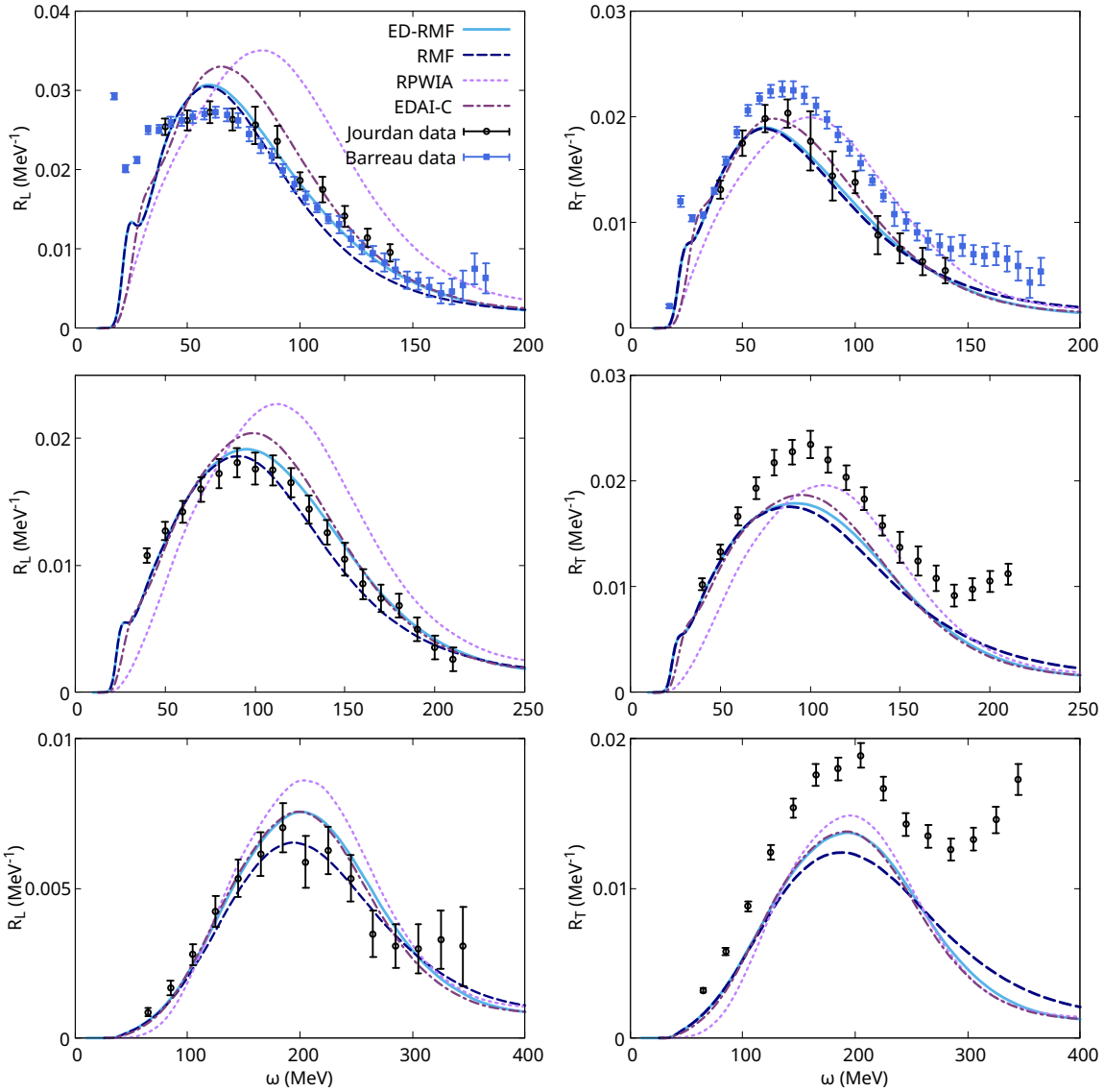

Figure 3.3: Longitudinal (left) and transverse (right) electromagnetic inclusive responses of ^{12}C within the ED-RMF, RMF, EDAI-C and RPWIA models. The transferred momentum q is (from up to bottom) 300, 380 and 570 MeV/c. The theoretical predictions are compared with experimental data from [102; 103].

momentum transfers. However, consistent with expectations, this energy independent potential predicts too much reduction of the quasielastic peak when the transferred momentum reaches 400–500 MeV/c, with the strength moved to the high-ω tail and a departure from the experimental data. When the ED-RMF potential is employed, these effects are mitigated, leading to a remarkably good agreement with the data in the longitudinal sector.

For the calculation with rROP, we employ the phenomenological energy-dependent A-independent carbon relativistic optical potential EDAI-C [104]. This type of potentials depends on the energy of the scattered nucleon but lacks an explicit dependence on the mass number, A, as they are fitted to data from a single nucleus. Despite this, they generally provide an excellent description of the observables included in the fit. The EDAI-C potential was extracted by fitting elastic proton-carbon scattering data in the range $30 < T_p < 1040$ MeV, T_p being the proton kinetic energy. This approach provides very similar results to the ED-RMF ones for large enough values of the momentum transfer, $q > 300$ MeV/c [96]. However, the EDAI-C, unlike the ED-RMF, does not preserve exact orthogonality between the initial and final states; hence, when the momentum of the final nucleon is comparable to the momentum of the bound nucleon (i.e., approximately up to $p_N < 300$ MeV/c), the spurious non-orthogonality contributions become an issue for EDAI-C as well as for RPWIA. This is confirmed by our results, in which one observes that even though EDAI-C and ED-RMF calculations are similar both in shape and magnitude, the agreement with the data is slightly better for ED-RMF, specially, at the low energy tails. Meanwhile, for q larger than around 500 MeV/c, the overlap between the initial and final states is negligible and orthogonality is not an issue, obtaining essentially the same predictions.

To conclude, we stress that these results have been computed considering only the one-body current operator. However, our theoretical predictions significantly underestimate the transverse responses. In order to improve the description of the transverse channel, the next chapter goes beyond the impulse approximation and includes the contribution from two-body meson-exchange currents with a final particle-hole state.

3.4 Current conservation

The conserved vector current hypothesis postulates that the isovector part of the vector current in electromagnetic and weak interactions corresponds to the same current [105]. An implication of this hypothesis is that, since the electromagnetic current is conserved, also the vector part of the weak current must be conserved. Current conservation is expressed by the relation

$$\partial_\mu J^\mu_V = Q_\mu J^\mu_V = \omega J^0_V - q J^3_V = 0, \tag{3.20}$$

with $\mathbf{q}$ along the z-axis, and J_V denotes the vector component of the hadronic current. Since the electromagnetic interaction only occurs through vector currents, in this case we identify $J^\mu_V = J^\mu$. Meanwhile, the weak interaction has both vector and axial components, and the

CVC hypothesis applies only to the former. The axial component of the weak current exhibits a divergence proportional to the pion mass [106; 107],

$$\partial_\mu J^\mu_A(x) = Q_\mu J^\mu_A(q) = f_\pi m^2_\pi \phi_\pi(Q), \tag{3.21}$$

where ϕ_π is the pion field. This relation implies that the axial current is conserved in the chiral limit $m_\pi \to 0$, which is known as the partially conserved axial current hypothesis.

Vector current can be conserved if the initial and final states are described within the same potential—in our case, the RMF potential. However, this does not hold when using the energy-dependent potentials introduced above, or even when using the RMF potential in charged-current interactions, where an initial-state proton is converted into a final-state neutron (or vice-versa). In such cases, the Coulomb potential, which only affects protons, leads to a violation of current conservation. Additionally, the use of single-nucleon current operators derived for free nucleons in nuclear matrix elements introduces a degree of ambiguity, as they are applied to bound nucleons that are generally off-shell. As a result, the current operators for scattering on free nucleons are not entirely consistent in this case. In fact, there is no rigorous prescription that fully incorporates the off-shell dependence of the nucleon into the hadronic current. This often leads to violation of vector current conservation.

Hence, CVC violation may arise from the fact that the initial and final states are not treated consistently, but also from the off-shellness of the initial state. Then, vector current conservation can be explicitly imposed by removing the longitudinal component in favor of the temporal one as

$$J^3_V = \frac{\omega}{q} J^0_V. \tag{3.22}$$

This approach is adopted throughout this work unless explicitly stated otherwise. The procedure to restore current conservation is not unique, and other option is the opposite approach, where J^0_V is defined in terms of J^3_V. However, the former is the usually employed one as the 0 component is related to the conserved charge and is assumed to be more accurately described.

In Fig. 3.4, we compare the longitudinal electromagnetic responses of ^{12}C within RPWIA, RMF and ED-RMF models, with and without explicitly imposing CVC by setting $J^3_V = (\omega/q)J^0_V$. If both descriptions differ, current conservation is violated. Results for the transverse response are not included, as this component is not affected by CVC, i.e., the results are exactly the same as previously obtained. In the RMF approach, both calculations yield essentially identical

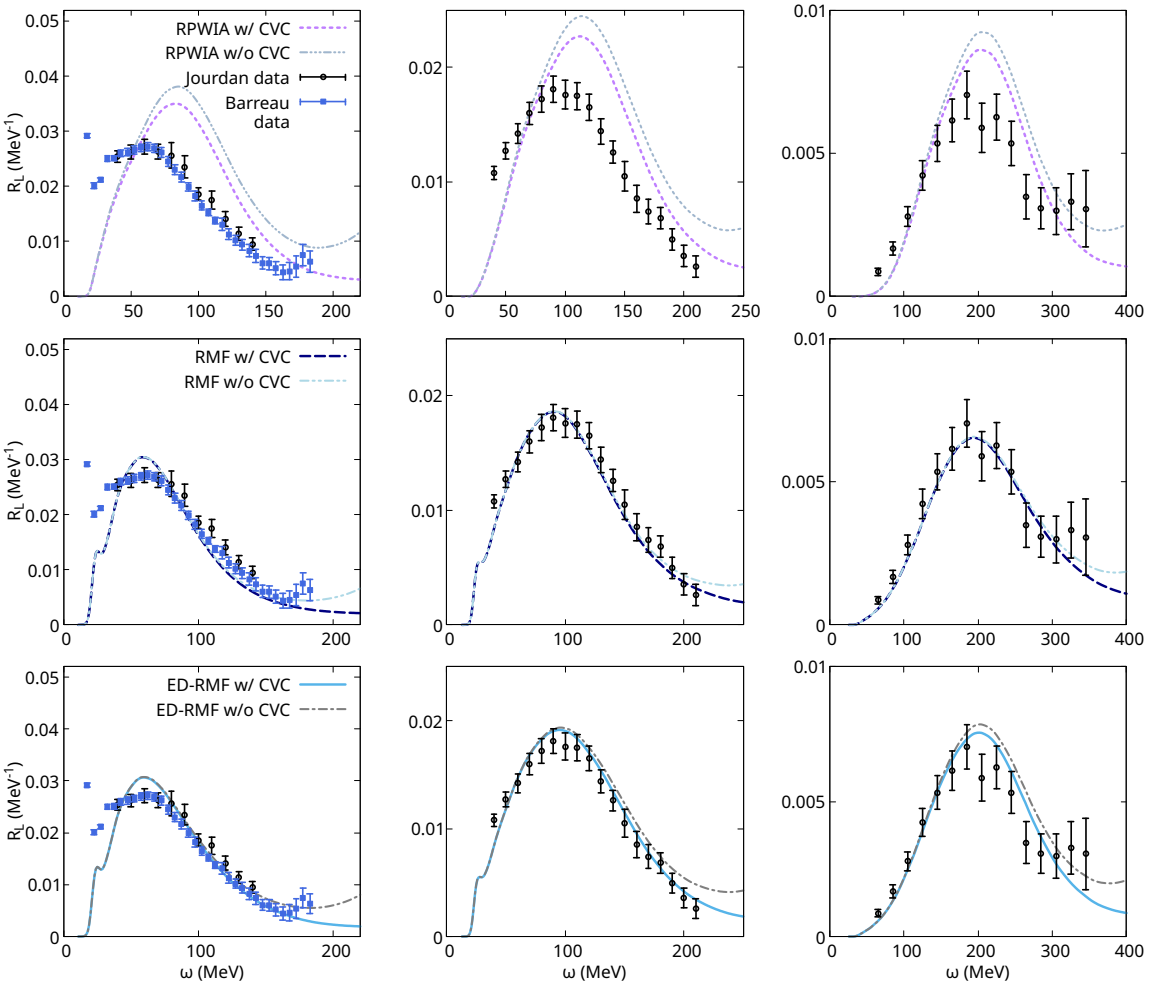

Figure 3.4: Longitudinal electromagnetic inclusive responses of ^{12}C within RPWIA, RMF and ED-RMF models, with and without explicitly imposing CVC by setting $J_V^3 = (\omega/q)J_V^0$. The transferred momentum q is (from left to right) 300, 380 and 570 MeV/c. The theoretical predictions are compared with experimental data from [102; 103].

results, except for the background contribution, for which the discrepancy is ascribed to the over-simplified treatment of this correlated component of the spectral function. In contrast, RPWIA results present significant differences between the two prescriptions, given by the inconsistent description of the initial and final states using different potentials, leading to the violation of current conservation. Finally, in the ED-RMF case, the violation is much less pronounced, with only a minor deviation observed at large momentum transfers.

Chapter 4

Two-body meson-exchange currents

The strong interaction between nucleons, through the nuclear force, is commonly described in terms of the exchange of virtual mesons, such as π, ρ and ω [106]. Therefore, when an electroweak boson interacts with a nucleon, the latter can also be interacting through meson-exchange with another nucleon, bound in the target nucleus. We refer to this interaction as a two-body meson-exchange current (MEC), and it can result in the knock-out of one or both nucleons from the nucleus. The pion plays a special role since it is the lightest of the mesons ($m_\pi \simeq 135$ MeV), meaning that the range for the interaction is much larger than that for the heavier mesons ρ and ω ($m_\rho \simeq 775$ MeV, $m_\omega \simeq 782$ MeV). Therefore, in this work, we focus on those interactions with one pion exchange.

We distinguish two different contributions to MEC: i) the Δ-resonance mechanism and ii) the contributions deduced from the chiral perturbation theory (ChPT) Lagrangian of the pion-nucleon system (ChPT background terms in what follows). The Feynman diagrams for two-nucleon knock-out reactions through these two-body meson-exchange currents are shown in Figs. 4.1 and 4.2.

Nucleon resonances are excited states of the nucleon that exist for a short time before decaying. They are characterized by their invariant mass, width, isospin, spin and parity. Resonance excitation provides significant strength in scattering experiments, as is the case in lepton-induced single-pion production on nuclear targets, where the resonant reactions dominate over the non-resonant background [108]. Here, the resonance contribution corresponds to the electroweak excitation of the nucleon to a resonance and its subsequent decay into a nucleon and a pion, the latter being captured on another nucleon in the nuclear medium. We limit this work to the contribution from the $\Delta(1232)$ resonance. Although electroweak reactions can excite higher

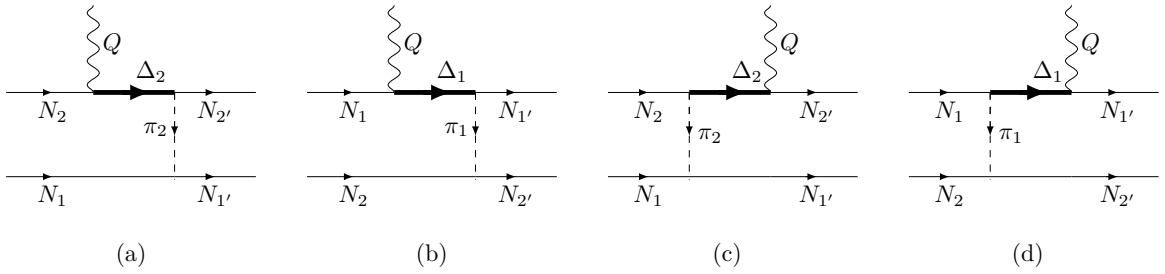

Figure 4.1: Direct [(a) and (b)] and cross [(c) and (d)] Δ-resonance diagrams contributing to the two-body meson exchange currents.

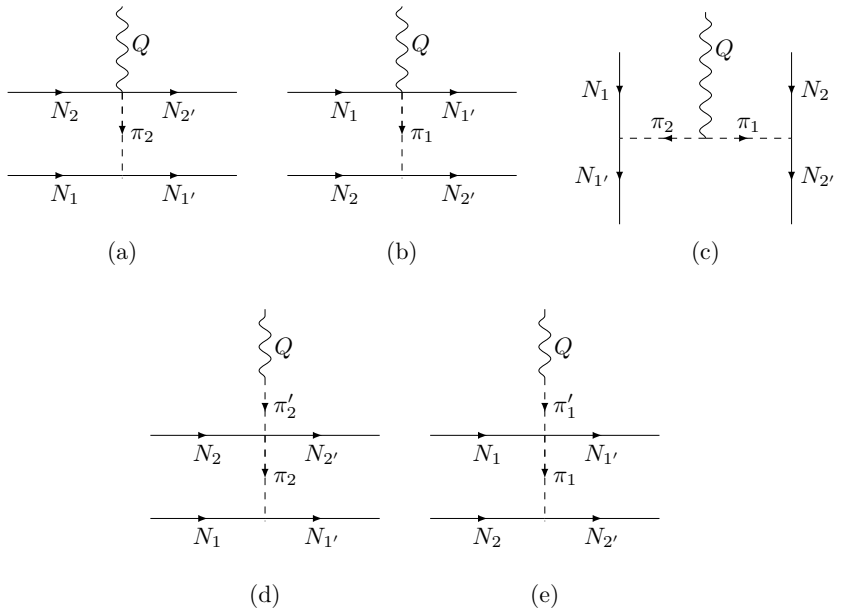

Figure 4.2: ChPT background diagrams contributing to the two-body meson exchange currents: seagull or contact [CT, (a) and (b)], pion-in-flight [PF,(c)] and pion pole [PP, (d) and (e)].

resonances, they are of little significance within the energy range studied [109; 110].

The ChPT background contribution corresponds to those interactions in which no nucleon resonance excitation occurs. These terms are required by chiral symmetry. Starting from an SU(2) non-linear σ model involving pions and nucleons, which implements the pattern of spontaneous chiral symmetry breaking of QCD, the corresponding vector and axial currents are derived, determining the structure of the chiral non-resonant terms [109]. They are commonly referred to as the seagull or contact, the pion-in-flight and the pion-pole terms.

Previous works have computed the contribution from pion-exchange currents to 1p-1h and 2p-2h responses and cross sections within different frameworks. There is a consensus that the effect of MEC in the 2p-2h sector leads to a significant contribution in the dip region between the QE and the Δ-resonance peaks within a shell model approach [111], a global relativistic Fermi gas [112; 113; 114], a local Fermi gas [38; 109] and a factorized spectral function scheme [115; 42]. The role of MEC in the 1p-1h responses has been, however, much less explored. In [116], within a non-relativistic shell model that incorporates final-state interactions, it was obtained that the two-body current produced a small decrease of the transverse electromagnetic response (R_T). Similar results were found in [117] but the exclusive $(e, e'p)$ responses were studied in this case. In [118], using a similar nuclear model as in [116], it was found that the two-body currents enhance R_T by around 20-30%. In both approaches, by construction, the two-body operator does not affect the longitudinal response (R_L). More recently, the non-relativistic *ab initio* Green's function Monte Carlo (GFMC) model of [119; 120; 121; 122] has confirmed the essential role of two-body mechanisms to describe the electromagnetic responses of light nuclei. They observed a slight reduction of the longitudinal response in the threshold region, meanwhile an enhancement of the strength is generated in the transverse sector when two-body contributions are incorporated. Similar results have been also obtained in recent computations within the variational Monte Carlo method with the short-time approximation [123]. *Ab initio* GFMC calculations have been also carried out in the case of charged-current interactions [43], obtaining a significant increase in the magnitude of the response functions that consequently lead to an increase of flux-folded inclusive cross section results. These previous works employed non-relativistic approaches subjected to hold only at relatively low momentum transfer. Hence, MEC contributions to 1p-1h final states have also been studied within fully relativistic frameworks, for example [124; 125; 126; 127; 128]. However, these approaches, based on the relativistic Fermi gas model, oversimplify the nuclear structure and dynamics. Another relativistic approach is that of [94], based on the factorized spectral function formalism, where it was found that two-body

contributions enhance the transverse electromagnetic response functions and the charged-current cross sections. Spectral function approaches incorporate nuclear complexity beyond mean-field predictions, thus representing a more realistic response of the nucleus to the external lepton probe. They require, however, to compute the cross section in a factorized fashion, which is not always a good approximation [129; 98] and that precludes including final-state interactions in a consistent way [97]. This motivated us to develop this work, where the contribution of the two-body meson-exchange currents with one-nucleon knock-out is studied within a representation of the spectral function without resorting to factorization.

4.1 Particle-hole excitation

In this work, we go beyond the impulse approximation and explore the contribution from two-body meson-exchange currents to 1p-1h excitations, i.e., with a final particle-hole state. Then, the hadronic current now reads

$$J^{\mu}_{\kappa} = J^{\mu}_{1b} + J^{\mu}_{2b}. \tag{4.1}$$

1p-1h excitations occur through two-body meson-exchange currents when, in the two-particle two-hole interactions of Figs. 4.1 and 4.2, one of the outgoing nucleons remains bound to the nucleus. In what follows, we refer to this nucleon as an intermediate bound-nucleon state. Hence, the hadronic final state consists in just one scattered nucleon. The resulting contributions are shown in Figs. 4.3 and 4.4. N' denotes the intermediate bound-nucleon state, N_i the initial bound nucleon and N_f the final scattered nucleon. Therefore, for electromagnetic interactions, N_i and N_f could be either both protons or both neutrons, meanwhile, in charged-current interactions, N_i corresponds to a neutron (proton) and N_f to a proton (neutron) for (anti)neutrinos.

Within the second quantization formalism, the general expression for any two-body operator is

$$\hat{J} = \frac{1}{2} \sum_{\alpha_1,\alpha_{1'},\alpha_2,\alpha_{2'}} c^{\dagger}_{\alpha_{1'}} c^{\dagger}_{\alpha_{2'}} c_{\alpha_2} c_{\alpha_1} J(\alpha_1, \alpha_{1'}, \alpha_2, \alpha_{2'}), \tag{4.2}$$

where, denoting F as the ground state of the target nucleus,

$$c_{\alpha} = \begin{cases} a_{\alpha} & \text{if} \quad \alpha > F, \\ b^{\dagger}_{\alpha} & \text{if} \quad \alpha < F, \end{cases} \tag{4.3}$$

therefore,

$$c_{\alpha} = \Theta(\alpha - F) a_{\alpha} + \Theta(F - \alpha) b^{\dagger}_{\alpha}, \tag{4.4}$$

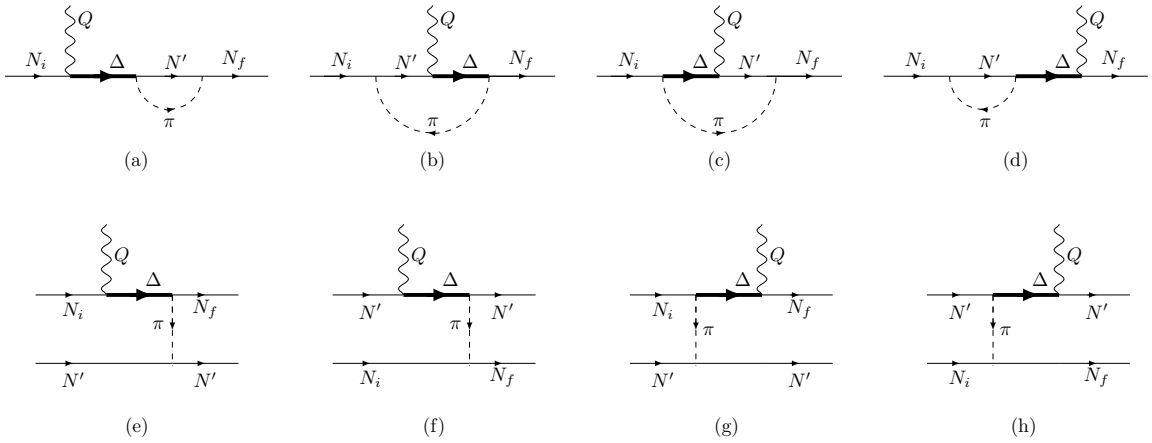

Figure 4.3: Exchange [(a),(b),(c),(d)] and direct [(e),(f),(g),(h)] Δ-resonance diagrams contributing to the two-body meson exchange currents with a final one-particle one-hole state. N' denotes the intermediate bound-nucleon state.

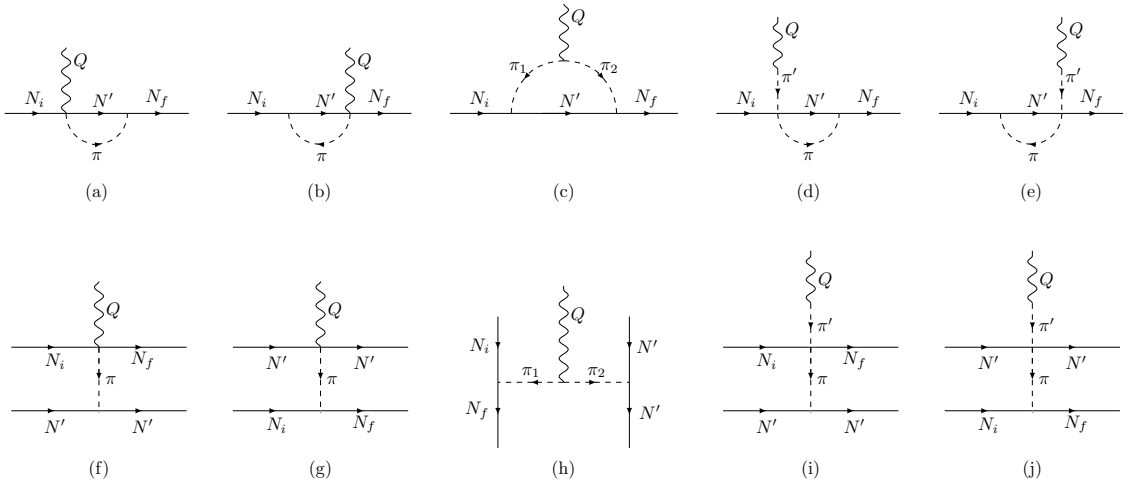

Figure 4.4: Exchange [CT, (a) and (b); PF, (c); and PP, (d) and (e)] and direct [CT, (f) and (g); PF, (h); and PP, (i) and (j)] ChPT background diagrams contributing to two-body meson exchange currents with a final one-particle one-hole state. N' denotes the intermediate bound-nucleon state.

with $a^\dagger_\alpha$ (a_α) and $b^\dagger_\alpha$ (b_α) the particle and hole creation (annihilation) operators, respectively. Holes, $\alpha < F$, are described by bound wave functions in the target nucleus and particles, $\alpha > F$, by distorted wave functions in the continuous. The subindex α represents the quantum numbers that label the single-particle states of the system, thus, they are different in each case. For holes, the quantum numbers are κ, m_j and the isospin and, for particles, the momenta, the spin and the isospin.

We are interested in a particle-hole final state, in which a nucleon of the target nucleus in state $|\alpha \equiv \kappa, m_j, \tau\rangle$ is knocked-out and detected in state $|\alpha_N \equiv P_N, s_N, \tau_N\rangle$,

$$|\alpha_N; \alpha\rangle = a^\dagger_{\alpha_N} b^\dagger_\alpha |F\rangle. \tag{4.5}$$

Then, the matrix element of a two-body operator between the ground state and a particle-hole excited state, taking into account Eqs. 4.2 and 4.5, reads

$$\langle \alpha_N; \alpha | \hat{J} | F \rangle = \frac{1}{2} \sum_{\alpha_1, \alpha_{1'}, \alpha_2, \alpha_{2'}} J(\alpha_1, \alpha_{1'}, \alpha_2, \alpha_{2'}) \times \langle F | b_\alpha a_{\alpha_N} c^\dagger_{\alpha_{1'}} c^\dagger_{\alpha_{2'}} c_{\alpha_2} c_{\alpha_1} | F \rangle. \tag{4.6}$$

Rewriting c_α in terms of particle and hole operators according to Eq. 4.4, taking into account the property

$$a_\alpha |F\rangle = 0, \qquad b_\alpha |F\rangle = 0, \tag{4.7}$$

and the anticommutation relations,

$$\begin{aligned} &\{a_\beta, a^\dagger_\gamma\} = \delta_{\beta\gamma}, \qquad \{b_\beta, b^\dagger_\gamma\} = \delta_{\beta\gamma}, \\ &\{a_\beta, a_\gamma\} = \{a^\dagger_\beta, a^\dagger_\gamma\} = \{b_\beta, b_\gamma\} = \{b^\dagger_\beta, b^\dagger_\gamma\} = 0, \\ &\{b_\beta, a_\gamma\} = \{b^\dagger_\beta, a_\gamma\} = \{b_\beta, a^\dagger_\gamma\} = \{b^\dagger_\beta, a^\dagger_\gamma\} = 0, \end{aligned} \tag{4.8}$$

we finally get

$$\langle \alpha_N; \alpha | \hat{J} | F \rangle = \frac{1}{2} \sum_{\alpha' < F} [J(\alpha, \alpha_N, \alpha', \alpha') + J(\alpha', \alpha', \alpha, \alpha_N) - J(\alpha', \alpha_N, \alpha, \alpha') - J(\alpha, \alpha', \alpha', \alpha_N)], \tag{4.9}$$

where antisymmetrization is implicitly included in the second quantization formalism. Additionally, taking into account the symmetry of the hadronic current $J(\alpha_1, \alpha_{1'}, \alpha_2, \alpha_{2'}) = J(\alpha_2, \alpha_{2'}, \alpha_1, \alpha_{1'})$,

the two-body hadronic current with a final particle-hole state reads

$$\langle \alpha_N; \alpha | \hat{J} | F \rangle = \sum_{\alpha' < F} [J(\alpha, \alpha_N, \alpha', \alpha') - J(\alpha', \alpha_N, \alpha, \alpha')]. \tag{4.10}$$

α' denotes the quantum numbers of the intermediate bound-nucleon state and its summation runs over all occupied levels in the ground state. The terms $J(\alpha, \alpha_N, \alpha', \alpha')$ and $J(\alpha', \alpha_N, \alpha, \alpha')$ represent the direct and exchange contributions, respectively. In the exchange terms, the 1p-1h excitation results when one of the outgoing nucleons of the 2p-2h process fills in the hole left by the other, so that it remains bound. In the direct terms, one of the final nucleons remains in its initial bound state after the interaction.

In the general case, the intermediate bound particles are described using the RMF model, so $\alpha' \equiv \kappa', m'_j, \tau'$, and we refer to it as the intermediate RMF-nucleon approach. Other possibility is the simplification of the computation by describing the intermediate bound nucleons as free Dirac spinors in a relativistic Fermi gas, with quantum numbers $\alpha' \equiv \mathbf{p}\,', s', \tau'$. This is referred to as the intermediate RFG-nucleon approximation. Then, an important difference between the RMF and the RFG approaches is that the momentum is not a quantum number of the RMF-bound states, i.e., there is no restriction to the momentum of the intermediate nucleons to be the same in the RMF calculation.

Finally, the one-particle one-hole hadronic currents involving two-body meson-exchange are obtained by substituting into Eq. 4.10 the two-particle two-hole hadronic currents derived from the Feynman diagrams shown in Figs. 4.1 and 4.2. For the Δ-resonance diagrams in Fig. 4.1, the two-particle two-hole hadronic currents are given by

$$\begin{aligned} J^{\mu}_{\Delta} = & \int d\mathbf{z}\, \overline{\Psi}_{2'}(\mathbf{z}) \mathcal{O}^{\mu}_{\Delta\pi N} \int \frac{d\mathbf{p}_{\Delta_2}}{(2\pi)^3} e^{i\mathbf{p}_{\Delta_2}(\mathbf{z}-\mathbf{y})} S_{\Delta,\alpha\beta} \int d\mathbf{y}\, e^{i\mathbf{q}\mathbf{y}}\, \mathcal{O}^{\beta\mu}_{Q\Delta N} \Psi_2(\mathbf{y}) \\ & \times \int \frac{d\mathbf{k}_{\pi_2}}{(2\pi)^3} \frac{e^{i\mathbf{k}_{\pi_2}(\mathbf{w}-\mathbf{z})}}{K^2_{\pi_2} - m^2_{\pi}} \int d\mathbf{w}\, \overline{\Psi}_{1'}(\mathbf{w}) \mathcal{O}_{\pi NN} \Psi_1(\mathbf{w}) + (1 \leftrightarrow 2), \end{aligned} \tag{4.11}$$

$$\begin{aligned} J^{\mu}_{C\Delta} = & \int d\mathbf{y}\, e^{i\mathbf{q}\mathbf{y}}\, \overline{\Psi}_{2'}(\mathbf{y}) \overline{\mathcal{O}}^{\alpha\mu}_{Q\Delta N} \int \frac{d\mathbf{p}_{\Delta_2}}{(2\pi)^3} e^{i\mathbf{p}_{\Delta_2}(\mathbf{y}-\mathbf{z})} S_{\Delta,\alpha\beta} \int d\mathbf{z}\, \mathcal{O}^{\beta}_{\Delta\pi N} \Psi_2(\mathbf{z}) \\ & \times \int \frac{d\mathbf{k}_{\pi_2}}{(2\pi)^3} \frac{e^{i\mathbf{k}_{\pi_2}(\mathbf{w}-\mathbf{z})}}{K^2_{\pi_2} - m^2_{\pi}} \int d\mathbf{w}\, \overline{\Psi}_{1'}(\mathbf{w}) \mathcal{O}_{\pi NN} \Psi_1(\mathbf{w}) + (1 \leftrightarrow 2), \end{aligned} \tag{4.12}$$

where the J_{Δ} and $J_{C\Delta}$ refer to the contributions from the direct and cross diagrams, respectively, $\mathcal{O}$ denotes the interaction vertices and S_{Δ} is the propagator of the Δ-resonance. For the ChPT

diagrams in Fig. 4.2, we have

$$J^{\mu}_{CT} = -\int d\mathbf{y}\, e^{i\mathbf{qy}}\, \overline{\Psi}_{2'}(\mathbf{y})\mathcal{O}^{\mu}_{Q\pi NN}\Psi_2(\mathbf{y}) \int \frac{d\mathbf{k}_{\pi_2}}{(2\pi)^3}\frac{e^{i\mathbf{k}_{\pi_2}(\mathbf{z}-\mathbf{y})}}{K^2_{\pi_2}-m^2_{\pi}} \int d\mathbf{z}\, \overline{\Psi}_{1'}(\mathbf{z})\mathcal{O}_{\pi NN}\Psi_1(\mathbf{z}) + (1 \leftrightarrow 2), \tag{4.13}$$

$$\begin{aligned} J^{\mu}_{PF} &= \int d\mathbf{y}\, e^{i\mathbf{qy}}\mathcal{O}^{\mu}_{Q\pi\pi} \int \frac{d\mathbf{k}_{\pi_1}}{(2\pi)^3}\frac{e^{i\mathbf{k}_{\pi_1}(\mathbf{z}-\mathbf{y})}}{K^2_{\pi_1}-m^2_{\pi}} \int \frac{d\mathbf{k}_{\pi_2}}{(2\pi)^3}\frac{e^{i\mathbf{k}_{\pi_2}(\mathbf{w}-\mathbf{y})}}{K^2_{\pi_2}-m^2_{\pi}} \\ &\times \int d\mathbf{z}\, \overline{\Psi}_{2'}(\mathbf{z})\mathcal{O}_{\pi NN}\Psi_2(\mathbf{z}) \int d\mathbf{w}\, \overline{\Psi}_{1'}(\mathbf{w})\mathcal{O}_{\pi NN}\Psi_1(\mathbf{w}) \\ &= \int d\mathbf{z} \int d\mathbf{w} \int \frac{d\mathbf{k}_{\pi_1}}{(2\pi)^3}\, \mathcal{O}^{\mu}_{Q\pi\pi}\frac{e^{i\mathbf{k}_{\pi_1}\mathbf{z}}}{K^2_{\pi_1}-m^2_{\pi}}\overline{\Psi}_{2'}(\mathbf{z})\mathcal{O}_{\pi NN}\Psi_2(\mathbf{z})\frac{e^{i\mathbf{k}_{\pi_2}\mathbf{w}}}{K^2_{\pi_2}-m^2_{\pi}}\overline{\Psi}_{1'}(\mathbf{w})\mathcal{O}_{\pi NN}\Psi_1(\mathbf{w}), \end{aligned} \tag{4.14}$$

$$\begin{aligned} J^{\mu}_{PP} &= \int d\mathbf{y}\, e^{i\mathbf{qy}}\mathcal{O}^{\mu}_{Q\pi} \int \frac{d\mathbf{k}_{\pi'_2}}{(2\pi)^3}\frac{e^{i\mathbf{k}_{\pi'_2}(\mathbf{z}-\mathbf{y})}}{K^2_{\pi'_2}-m^2_{\pi}} \int d\mathbf{z}\, \overline{\Psi}_{2'}(\mathbf{z})\mathcal{O}_{\pi\pi NN}\Psi_2(\mathbf{z}) \\ &\times \int \frac{d\mathbf{k}_{\pi_2}}{(2\pi)^3}\frac{e^{i\mathbf{k}_{\pi_2}(\mathbf{w}-\mathbf{z})}}{K^2_{\pi_2}-m^2_{\pi}} \int d\mathbf{w}\, \overline{\Psi}_{1'}(\mathbf{w})\mathcal{O}_{\pi NN}\Psi_1(\mathbf{w}) + (1 \leftrightarrow 2) \\ &= \int d\mathbf{z} \int d\mathbf{w} \int \frac{d\mathbf{k}_{\pi_2}}{(2\pi)^3}\frac{e^{i\mathbf{qz}}\mathcal{O}^{\mu}_{Q\pi}}{Q^2-m^2_{\pi}}\overline{\Psi}_{2'}(\mathbf{z})\mathcal{O}_{\pi\pi NN}\Psi_2(\mathbf{z})\frac{e^{i\mathbf{k}_{\pi_2}(\mathbf{w}-\mathbf{z})}}{K^2_{\pi_2}-m^2_{\pi}}\overline{\Psi}_{1'}(\mathbf{w})\mathcal{O}_{\pi NN}\Psi_1(\mathbf{w}) + (1 \leftrightarrow 2). \end{aligned} \tag{4.15}$$

The final expressions for the pion-in-flight and pion pole diagrams have been obtained by integrating over $\mathbf{y}$ using Eq. A.40. This leads to a momentum conservation Dirac delta that is used to integrate over $\mathbf{k}_{\pi_2}$ and $\mathbf{k}_{\pi'_2}$, respectively. Then, taking into account energy conservation in the vertices, we have the relations $K_{\pi_2} = Q - K_{\pi_1}$ and $K_{\pi'_2} = Q$.

To conclude, we use the Fourier transform of the hadronic wave functions, given by Eq. A.38, to get expressions in momentum space,

$$\begin{aligned} J^{\mu}_{\Delta} &= \frac{1}{(2\pi)^3}\int d\mathbf{p}_{2'}\int d\mathbf{p}_2\int d\mathbf{p}_1 \left[\overline{\Psi}(\mathbf{p}_{2'})\mathcal{O}^{\alpha}_{\Delta N\pi}S_{\Delta,\alpha\beta}\mathcal{O}^{\beta\mu}_{Q\Delta N}\Psi(\mathbf{p}_2)\frac{1}{K^2_{\pi_2}-m^2_{\pi}}\overline{\Psi}(\mathbf{p}_{1'})\mathcal{O}_{\pi NN}\Psi(\mathbf{p}_1)\right. \\ &\left. + \overline{\Psi}(\mathbf{p}_{1'})\mathcal{O}^{\alpha}_{\Delta N\pi}S_{\Delta,\alpha\beta}\mathcal{O}^{\beta\mu}_{Q\Delta N}\Psi(\mathbf{p}_1)\frac{1}{K^2_{\pi_1}-m^2_{\pi}}\overline{\Psi}(\mathbf{p}_{2'})\mathcal{O}_{\pi NN}\Psi(\mathbf{p}_2)\right], \end{aligned} \tag{4.16}$$

$$\begin{aligned} J^{\mu}_{C\Delta} &= \frac{1}{(2\pi)^3}\int d\mathbf{p}_{2'}\int d\mathbf{p}_2\int d\mathbf{p}_1 \left[\overline{\Psi}(\mathbf{p}_{2'})\overline{\mathcal{O}}^{\alpha\mu}_{Q\Delta N}S_{\Delta,\alpha\beta}\mathcal{O}^{\beta}_{\Delta\pi N}\Psi(\mathbf{p}_2)\frac{1}{K^2_{\pi_2}-m^2_{\pi}}\overline{\Psi}(\mathbf{p}_{1'})\mathcal{O}_{\pi NN}\Psi(\mathbf{p}_1)\right. \\ &\left. + \overline{\Psi}(\mathbf{p}_{1'})\overline{\mathcal{O}}^{\alpha\mu}_{Q\Delta N}S_{\Delta,\alpha\beta}\mathcal{O}^{\beta}_{\Delta\pi N}\Psi(\mathbf{p}_1)\frac{1}{K^2_{\pi_1}-m^2_{\pi}}\overline{\Psi}(\mathbf{p}_{2'})\mathcal{O}_{\pi NN}\Psi(\mathbf{p}_2)\right], \end{aligned} \tag{4.17}$$

with $P_{1'} = P_2+P_1+Q-P_{2'}$, $K_{\pi_2} = Q+P_2-P_{2'}$, $P_{\Delta_2} = P_2+Q$, $P_{C\Delta_2} = P'_2-Q$, $K_{\pi_1} = Q+P_1-P_{1'}$,

$P_{\Delta_1} = P_1 + Q$ and $P_{C\Delta_1} = P_1' - Q$, and

$$J^{\mu}_{CT} = -\frac{1}{(2\pi)^3}\int d\mathbf{p}_{2'}\int d\mathbf{p}_2\int d\mathbf{p}_1\left[\overline{\Psi}(\mathbf{p}_{2'})\mathcal{O}^{\mu}_{Q\pi NN}\Psi(\mathbf{p}_2)\frac{1}{K^2_{\pi_2}-m^2_{\pi}}\overline{\Psi}(\mathbf{p}_{1'})\mathcal{O}_{\pi NN}\Psi(\mathbf{p}_1)\right.$$
$$\left. + \overline{\Psi}(\mathbf{p}_{1'})\mathcal{O}^{\mu}_{Q\pi NN}\Psi(\mathbf{p}_1)\frac{1}{K^2_{\pi_1}-m^2_{\pi}}\overline{\Psi}(\mathbf{p}_{2'})\mathcal{O}_{\pi NN}\Psi(\mathbf{p}_2)\right], \tag{4.18}$$

$$J^{\mu}_{PF} = \frac{1}{(2\pi)^3}\int d\mathbf{p}_{2'}\int d\mathbf{p}_2\int d\mathbf{p}_1\frac{\mathcal{O}^{\mu}_{Q\pi\pi}}{(K^2_{\pi_2}-m^2_{\pi})(K^2_{\pi_1}-m^2_{\pi})}\overline{\Psi}(\mathbf{p}_{2'})\mathcal{O}_{\pi NN}\Psi(\mathbf{p}_2)\overline{\Psi}(\mathbf{p}_{1'})\mathcal{O}_{\pi NN}\Psi(\mathbf{p}_1), \tag{4.19}$$

$$J^{\mu}_{PP} = \frac{1}{(2\pi)^3}\int d\mathbf{p}_{2'}\int d\mathbf{p}_2\int d\mathbf{p}_1\left[\frac{\mathcal{O}^{\mu}_{Q\pi}}{Q^2-m^2_{\pi}}\overline{\Psi}(\mathbf{p}_{2'})\mathcal{O}^{\mu}_{\pi\pi NN}\Psi(\mathbf{p}_2)\frac{1}{K^2_{\pi_2}-m^2_{\pi}}\overline{\Psi}(\mathbf{p}_{1'})\mathcal{O}_{\pi NN}\Psi(\mathbf{p}_1)\right.$$
$$\left. + \frac{\mathcal{O}^{\mu}_{Q\pi}}{Q^2-m^2_{\pi}}\overline{\Psi}(\mathbf{p}_{1'})\mathcal{O}^{\mu}_{\pi\pi NN}\Psi(\mathbf{p}_1)\frac{1}{K^2_{\pi_1}-m^2_{\pi}}\overline{\Psi}(\mathbf{p}_{2'})\mathcal{O}_{\pi NN}\Psi(\mathbf{p}_2)\right], \tag{4.20}$$

with $P_{1'} = P_2 + P_1 + Q - P_{2'}$, $K_{\pi_2} = Q + P_2 - P_{2'}$ and $K_{\pi_1} = P_2' - P_2$.

4.1.1 Intermediate RMF-nucleon approach

We begin this study by using an RMF-bound state to describe the intermediate bound-nucleon state of the two-body meson-exchange hadronic current with a final particle-hole state, following the same approach as for the initial bound nucleon. Then, the sum over the quantum numbers of the intermediate bound-nucleon state in Eq. 4.10 corresponds to

$$\sum_{\alpha'} \rightarrow \sum_{\kappa',m'_j,\tau'} \tag{4.21}$$

and it runs over all occupied shells in the ground state. Substituting the two-particle two-hole hadronic currents of Eqs. 4.16, 4.17, 4.18, 4.19 and 4.20 into Eq. 4.10, with the corresponding wave function for each nucleon, we get

$$J^{\mu}_{2b} = \sqrt{V}\int d\mathbf{p}\int\frac{d\mathbf{p}_p}{(2\pi)^{3/2}}\int\frac{d\mathbf{p}_h}{(2\pi)^{3/2}}\overline{\Psi}^{s_N}(\mathbf{p}+\mathbf{p}_h+\mathbf{q}-\mathbf{p}_p,\mathbf{p}_N)\Gamma^{\mu}_{2b}\Psi^{m_j}_{\kappa}(\mathbf{p}), \tag{4.22}$$

with $\mathbf{p}_p$ and $\mathbf{p}_h$ the momenta of the intermediate outgoing and ingoing nucleons, respectively. The two-body meson-exchange current operator is the sum of the Δ-resonance and ChPT background

contributions

$$\Gamma^{\mu}_{2b} = \Gamma^{\mu}_{ChPT} + \Gamma^{\mu}_{\Delta}. \tag{4.23}$$

Introducing the explicit expressions of the interaction vertices, which are obtained from the Lagrangians in Appendices C and D, the hadronic current operators for the Δ-resonance terms of Fig. 4.3 read

$$\Gamma^{\mu}_{\Delta,(a)} = -F_{\pi NN}F_{\pi\Delta N}\frac{g_A}{2f_\pi}\not{K}_\pi\gamma^5\frac{\Lambda(\mathbf{p}_h,\mathbf{p}_p)}{K_\pi^2-m_\pi^2}\Gamma^{\alpha}_{\Delta\pi N}S_{\Delta,\alpha\beta}\Gamma^{\beta\mu}_{Q\Delta N}, \tag{4.24}$$

with $P^{(a)}_{\Delta} = P+Q$ and $K^{(a)}_{\pi} = P+Q-P_p$,

$$\Gamma^{\mu}_{\Delta,(b)} = -F_{\pi NN}F_{\pi\Delta N}\frac{g_A}{2f_\pi}\Gamma^{\alpha}_{\Delta\pi N}S_{\Delta,\alpha\beta}\Gamma^{\beta\mu}_{Q\Delta N}\frac{\Lambda(\mathbf{p}_h,\mathbf{p}_p)}{K_\pi^2-m_\pi^2}\not{K}_\pi\gamma^5, \tag{4.25}$$

with $P^{(b)}_{\Delta} = Q+P_h$ and $K^{(b)}_{\pi} = P_p-P$,

$$\Gamma^{\mu}_{\Delta,(c)} = -F_{\pi NN}F_{\pi\Delta N}\frac{g_A}{2f_\pi}\not{K}_\pi\gamma^5\frac{\Lambda(\mathbf{p}_h,\mathbf{p}_p)}{K_\pi^2-m_\pi^2}\bar{\Gamma}^{\alpha\mu}_{Q\Delta N}S_{\Delta,\alpha\beta}\Gamma^{\beta}_{\Delta\pi N}, \tag{4.26}$$

with $P^{(c)}_{\Delta} = P_p-Q$ and $K^{(c)}_{\pi} = P+Q-P_p$

$$\Gamma^{\mu}_{\Delta,(d)} = -F_{\pi NN}F_{\pi\Delta N}\frac{g_A}{2f_\pi}\bar{\Gamma}^{\alpha\mu}_{Q\Delta N}S_{\Delta,\alpha\beta}\Gamma^{\beta}_{\Delta\pi N}\frac{\Lambda(\mathbf{p}_h,\mathbf{p}_p)}{K_\pi^2-m_\pi^2}\not{K}_\pi\gamma^5, \tag{4.27}$$

with $P^{(d)}_{\Delta} = P+P_h-P_p$ and $K^{(d)}_{\pi} = P_p-P$,

$$\Gamma^{\mu}_{\Delta,(e)} = F_{\pi NN}F_{\pi\Delta N}\frac{g_A}{2f_\pi}\frac{\Lambda_\pi(\mathbf{p}_h,\mathbf{p}_p,K_\pi)}{K_\pi^2-m_\pi^2}\Gamma^{\alpha}_{\Delta\pi N}S_{\Delta,\alpha\beta}\Gamma^{\beta\mu}_{Q\Delta N} \tag{4.28}$$

with $P^{(e)}_{\Delta} = P+Q$ and $K^{(e)}_{\pi} = P_p-P_h$,

$$\Gamma^{\mu}_{\Delta,(f)} = F_{\pi NN}F_{\pi\Delta N}\frac{g_A}{2f_\pi}\frac{\Lambda_\Delta(\mathbf{p}_h,\mathbf{p}_p,P_\Delta)}{K_\pi^2-m_\pi^2}\not{K}_\pi\gamma^5, \tag{4.29}$$

with $P^{(f)}_{\Delta} = Q+P_h$ and $K^{(f)}_{\pi} = Q+P_h-P_p$,

$$\Gamma^{\mu}_{\Delta,(g)} = F_{\pi NN}F_{\pi\Delta N}\frac{g_A}{2f_\pi}\frac{\Lambda_\pi(\mathbf{p}_h,\mathbf{p}_p,K_\pi)}{K_\pi^2-m_\pi^2}\bar{\Gamma}^{\alpha\mu}_{Q\Delta N}S_{\Delta,\alpha\beta}\Gamma^{\beta}_{\Delta\pi N} \tag{4.30}$$

with $P_\Delta^{(g)} = P + P_h - P_p$ and $K_\pi^{(g)} = P_p - P_h$,

$$\Gamma^\mu_{\Delta,(h)} = F_{\pi NN} F_{\pi \Delta N} \frac{g_A}{2f_\pi} \frac{\bar{\Lambda}_\Delta(\mathbf{p}_h, \mathbf{p}_p, P_\Delta)}{K_\pi^2 - m_\pi^2} \not{K}_\pi \gamma^5, \tag{4.31}$$

with $P_\Delta^{(h)} = P_p - Q$ and $K_\pi^{(h)} = Q + P_h - P_p$. The vertex function

$$\bar{\Gamma}^{\alpha\mu}_{Q\Delta N}(K^\mu, Q^\mu) = \gamma^0 \left[\Gamma^{\alpha\mu}_{Q\Delta N}(K^\mu, -Q^\mu)\right]^\dagger \gamma^0 \tag{4.32}$$

has been introduced in the cross Δ-resonance diagrams, with K the momentum of the outgoing nucleon in the vertex. The explicit expressions for the strong $\Delta\pi N$ and electroweak $Q\Delta N$ vertices and the Δ-resonance propagator are given in Appendix D.

Continuing with the ChPT background contribution, the hadronic current operator for the exchange contact term diagrams contains vector and axial contributions, $\Gamma^\mu_{eCT} = \Gamma^\mu_{eCT,V} + \Gamma^\mu_{eCT,A}$, with

$$\Gamma^\mu_{eCT,V} = F_{CT} \frac{g_A^2}{2f_\pi^2} \left[F^2_{\pi NN,1} \not{K}_{\pi_1} \gamma^5 \frac{\Lambda(\mathbf{p}_h, \mathbf{p}_p)}{K_{\pi_1}^2 - m_\pi^2} \gamma^\mu \gamma^5 - F^2_{\pi NN,2} \gamma^\mu \gamma^5 \frac{\Lambda(\mathbf{p}_h, \mathbf{p}_p)}{K_{\pi_2}^2 - m_\pi^2} \not{K}_{\pi_2} \gamma^5 \right], \tag{4.33}$$

$$\Gamma^\mu_{eCT,A} = -\frac{g_A}{2f_\pi^2} \left[F_{\rho,1} F^2_{\pi NN,1} \not{K}_{\pi_1} \gamma^5 \frac{\Lambda(\mathbf{p}_h, \mathbf{p}_p)}{K_{\pi_1}^2 - m_\pi^2} \gamma^\mu - F_{\rho,2} F^2_{\pi NN,2} \gamma^\mu \frac{\Lambda(\mathbf{p}_h, \mathbf{p}_p)}{K_{\pi_2}^2 - m_\pi^2} \not{K}_{\pi_2} \gamma^5 \right], \tag{4.34}$$

for the exchange pion-in-flight diagram, the contribution is purely vector, with

$$\Gamma^\mu_{ePF} = F_{PF} F_{\pi NN,1} F_{\pi NN,2} \frac{g_A^2}{2f_\pi^2} \frac{(Q + 2P - 2P_p)^\mu}{(K_{\pi_1}^2 - m_\pi^2)(K_{\pi_2}^2 - m_\pi^2)} \not{K}_{\pi_1} \gamma^5 \Lambda(\mathbf{p}_h, \mathbf{p}_p) \not{K}_{\pi_2} \gamma^5, \tag{4.35}$$

and for the exchange pion pole diagrams, the contribution is purely axial, with

$$\Gamma^\mu_{ePP} = \frac{g_A}{4f_\pi^2} \frac{Q^\mu}{Q^2 - m_\pi^2} \left[F_{\rho,1} F^2_{\pi NN,1} \not{K}_{\pi_1} \gamma^5 \frac{\Lambda(\mathbf{p}_h, \mathbf{p}_p)}{K_{\pi_1}^2 - m_\pi^2} (\not{K}_{\pi_1} + \not{Q}) \right.$$
$$\left. - F_{\rho,2} F^2_{\pi NN,2} (\not{K}_{\pi_2} + \not{Q}) \frac{\Lambda(\mathbf{p}_h, \mathbf{p}_p)}{K_{\pi_2}^2 - m_\pi^2} \not{K}_{\pi_2} \gamma^5 \right], \tag{4.36}$$

where $K_{\pi_1} = Q + P - P_p$ and $K_{\pi_2} = P_p - P$. For the direct contact term diagrams, the hadronic

current operator is computed as $\Gamma^{\mu}_{dCT} = \Gamma^{\mu}_{dCT,V} + \Gamma^{\mu}_{dCT,A}$, with

$$\Gamma^{\mu}_{dCT,V} = -F_{CT}\frac{g_A^2}{2f_\pi^2}\left[F^2_{\pi NN,1d}\frac{\Lambda_\pi(\mathbf{p}_h,\mathbf{p}_p,K_{\pi_{1d}})}{K^2_{\pi_{1d}}-m^2_\pi}\gamma^\mu\gamma^5 - F^2_{\pi NN,2d}\frac{\Lambda^\mu_{\gamma^{\mu 5}}(\mathbf{p}_h,\mathbf{p}_p)}{K^2_{\pi_{2d}}-m^2_\pi}\not{K}_{\pi_{2d}}\gamma^5\right], \quad (4.37)$$

$$\Gamma^{\mu}_{dCT,A} = \frac{g_A}{2f_\pi^2}\left[F_{\rho,1d}F^2_{\pi NN,1d}\frac{\Lambda_\pi(\mathbf{p}_h,\mathbf{p}_p,K_{\pi_{1d}})}{K^2_{\pi_{1d}}-m^2_\pi}\gamma^\mu - F_{\rho,2d}F^2_{\pi NN,2d}\frac{\Lambda^\mu_{\gamma^{\mu}}(\mathbf{p}_h,\mathbf{p}_p)}{K^2_{\pi_{2d}}-m^2_\pi}\not{K}_{\pi_{2d}}\gamma^5\right], \quad (4.38)$$

for the direct pion-in-flight diagram, the current operator is given by

$$\Gamma^{\mu}_{dPF} = -F_{PF}F_{\pi NN,1d}F_{\pi NN,2d}\frac{g_A^2}{2f_\pi^2}\frac{(2P_p-2P_h-Q)^\mu}{(K^2_{\pi_{1d}}-m^2_\pi)(K^2_{\pi_{2d}}-m^2_\pi)}\Lambda_\pi(\mathbf{p}_h,\mathbf{p}_p,K_{\pi_{1d}})\not{K}_{\pi_{2d}}\gamma^5, \quad (4.39)$$

and for the direct pion pole diagrams,

$$\Gamma^{\mu}_{dPP} = -\frac{g_A}{4f_\pi^2}\frac{Q^\mu}{Q^2-m^2_\pi}\left[F_{\rho,1d}F^2_{\pi NN,1d}\frac{\Lambda_\pi(\mathbf{p}_h,\mathbf{p}_p,K_{\pi_{1d}})}{K^2_{\pi_{1d}}-m^2_\pi}(\not{K}_{\pi_{1d}}+\not{Q})-\right.$$
$$\left. F_{\rho,2d}F^2_{\pi NN,2d}\frac{\Lambda_{\not{K}}(\mathbf{p}_h,\mathbf{p}_p,K_{\pi_{2d}}+Q)}{K^2_{\pi_{2d}}-m^2_\pi}\not{K}_{\pi_{2d}}\gamma^5\right], \quad (4.40)$$

where $K_{\pi_{1d}} = P_p - P_h$ and $K_{\pi_{2d}} = Q + P_h - P_p$.

To shorten the expressions we have introduced the intermediate RMF projectors,

$$\Lambda_X = \sum_{\tau'} I_{N'}\Lambda_{XN'} = I_p\Lambda_{Xp} + I_n\Lambda_{Xn}, \quad (4.41)$$

with

$$\Lambda_{N'}(\mathbf{p},\mathbf{p}') = \sum_{\kappa',m'_j}\Psi^{m'_j}_{\kappa'}(\mathbf{p})\overline{\Psi}^{m'_j}_{\kappa'}(\mathbf{p}'), \quad (4.42)$$

$$\Lambda_{\pi N'}(\mathbf{p},\mathbf{p}',K_\pi) = \sum_{\kappa',m'_j}\overline{\Psi}^{m'_j}_{\kappa'}(\mathbf{p}')\not{K}_\pi\gamma^5\Psi^{m'_j}_{\kappa'}(\mathbf{p}), \quad (4.43)$$

$$\Lambda_{\Delta N'}(\mathbf{p},\mathbf{p}',P_\Delta) = \sum_{\kappa',m'_j}\overline{\Psi}^{m'_j}_{\kappa'}(\mathbf{p}')\Gamma^{\alpha}_{\Delta\pi N}S_{\Delta,\alpha\beta}\Gamma^{\beta\mu}_{Q\Delta N}\Psi^{m'_j}_{\kappa'}(\mathbf{p}), \quad (4.44)$$

$$\bar{\Lambda}_{\Delta N'}(\mathbf{p},\mathbf{p}',P_\Delta) = \sum_{\kappa',m'_j}\overline{\Psi}^{m'_j}_{\kappa'}(\mathbf{p}')\bar{\Gamma}^{\alpha\mu}_{Q\Delta N}S_{\Delta,\alpha\beta}\Gamma^{\beta}_{\Delta\pi N}\Psi^{m'_j}_{\kappa'}(\mathbf{p}), \quad (4.45)$$

$$\Lambda^\mu_{\gamma^{\mu 5}N'}(\mathbf{p},\mathbf{p}') = \sum_{\kappa',m'_j}\overline{\Psi}^{m'_j}_{\kappa'}(\mathbf{p}')\gamma^\mu\gamma^5\Psi^{m'_j}_{\kappa'}(\mathbf{p}), \quad (4.46)$$

$$\Lambda^{\mu}_{\gamma^{\mu}N'}(\mathbf{p},\mathbf{p}') = \sum_{\kappa',m'_j} \overline{\Psi}^{m'_j}_{\kappa'}(\mathbf{p}')\gamma^{\mu}\Psi^{m'_j}_{\kappa'}(\mathbf{p}), \tag{4.47}$$

$$\Lambda_{\not{K}N'}(\mathbf{p},\mathbf{p}',K) = \sum_{\kappa',m'_j} \overline{\Psi}^{m'_j}_{\kappa'}(\mathbf{p}')\not{K}\Psi^{m'_j}_{\kappa'}(\mathbf{p}). \tag{4.48}$$

The sum over the isospin of the intermediate nucleon state is explicitly done in Eq. 4.41, where the contribution from an intermediate proton or neutron is weighted by an isospin coefficient ($I_{N'}$), and the sum over κ', m'_j in Eqs. 4.43-4.48 runs over all occupied shells of the corresponding intermediate nucleon. The isospin coefficient of each diagram, given in Tables 4.1 and 4.2, depends on the process and the isospin of the involved nucleons.

For the EM interaction, the direct terms of the ChPT background diagrams vanish due to the isospin dependence of the ChPT Lagrangian. Hence, only the exchange terms contribute. On the other hand, the Δ-resonance part has contributions from both exchange and direct terms. Additionally, note that only vector contributions should be considered due to the nature of the EM interaction. In the CC case, both direct and exchange terms of the ChPT and Δ-resonance diagrams, as well as their vector and axial components, contribute.

To conclude, a variety of form factors have been introduced in the hadronic current operators to account for different effects. In the vector component of the ChPT background, we include form factors to account for the nucleon structure, with

$$F_{CT}(Q^2) = F_{PF}(Q^2) = F_1^V(Q^2). \tag{4.49}$$

The isovector nucleon form factor, F_1^V, has been introduced following the single-pion production model of Ref. [108], where it was originally included to ensure consistency with the conserved vector current hypothesis. This leads to the condition

$$Q_{\mu}(J^{\mu}_{CT} + J^{\mu}_{PF} + J^{\mu}_{NP}) = 0. \tag{4.50}$$

Here, J_{NP} refers to the contribution from nucleon pole diagrams, which are typically excluded in mean-field calculations because they represent correlations already accounted for in the corresponding wave functions. Consequently, in the present work, vector current is not directly conserved. Nevertheless, we retain the same vertex structure for the contact term and pion-in-flight diagrams as in Ref. [108], and thus include the form factors in the same way. In the pion pole terms, to account for the ρ-dominance of the $\pi\pi NN$ coupling [130; 131], we have introduce

Channel	eCT	ePF	ePP	dCT	dPF	dPP	Δ (a, d, e, g)	Δ (b, c, f, h)
p → p (N'=p)	0	0	0	0	0	0	$1/\sqrt{3}$	$1/\sqrt{3}$
p → p (N'=n)	1	1	0	0	0	0	$-1/\sqrt{3}$	$1/\sqrt{3}$
n → n (N'=p)	-1	-1	0	0	0	0	$1/\sqrt{3}$	$-1/\sqrt{3}$
n → n (N'=n)	0	0	0	0	0	0	$-1/\sqrt{3}$	$-1/\sqrt{3}$

Table 4.1: Isospin coefficients ($I_{N'}$) for the meson-exchange contributions to the different reaction channels in the case of EM interactions. N' denotes the intermediate bound-nucleon state. CT, PF and PP refer to the exchange (e) and direct (d) ChPT background diagrams in Fig. 4.4, while Δ(a-h) refers to the Δ-resonance diagrams in Fig. 4.3.

Channel	eCT	ePF	ePP	dCT	dPF	dPP	Δ(a, e)	Δ(b, f)	Δ(c, h)	Δ(d, g)
n → p (N'=p)	1	1	1	1	1	1	$-1/\sqrt{3}$	$\sqrt{3}$	$1/\sqrt{3}$	$1/\sqrt{3}$
n → p (N'=n)	1	1	1	-1	-1	-1	$1/\sqrt{3}$	$1/\sqrt{3}$	$\sqrt{3}$	$-1/\sqrt{3}$
p → n (N'=p)	1	1	1	-1	-1	-1	$1/\sqrt{3}$	$1/\sqrt{3}$	$\sqrt{3}$	$-1/\sqrt{3}$
p → n (N'=n)	1	1	1	1	1	1	$-1/\sqrt{3}$	$\sqrt{3}$	$1/\sqrt{3}$	$1/\sqrt{3}$

Table 4.2: Isospin coefficients ($I_{N'}$) for the meson-exchange contributions to the different reaction channels in the case of CC interactions. The first two rows correspond to neutrino-induced reactions. The second two rows correspond to their antineutrino counterparts. N' denotes the intermediate bound-nucleon state. CT, PF and PP refer to the exchange (e) and direct (d) ChPT background diagrams in Fig. 4.4, while Δ(a-h) refers to the Δ-resonance diagrams in Fig. 4.3.

the form factor

$$F_\rho(K^2) = \frac{m_\rho^2}{m_\rho^2 - K^2}, \tag{4.51}$$

with $K = Q - K_\pi$ and $m_\rho = 775.8$ MeV. This form factor has also been introduced in the axial component of the contact term to preserve partial conservation of axial current (PCAC). Lastly, we add a strong form factor in the $Q\pi NN$ and πNN vertices, $F_{\pi NN}$, and in the $\pi\Delta N$ vertex, $F_{\pi\Delta N}$, which accounts for the off-shell nature of the pion,

$$F_{\pi NN}(K_\pi^2) = \frac{\Lambda^2 - m_\pi^2}{\Lambda^2 - K_\pi^2}, \quad F_{\pi\Delta N}(K_\pi^2) = \frac{\Lambda_{\pi\Delta N}^2}{\Lambda_{\pi\Delta N}^2 - K_\pi^2}, \tag{4.52}$$

with $\Lambda = 1.3$ GeV [127; 124] and $\Lambda_{\pi\Delta N}^2 = 1.5 M_N^2$ [113; 124].

However, the computation of the two-body meson-exchange hadronic current with a final

particle-hole state within the intermediate RMF-nucleon approach, Eq. 4.22, implies the calculation of a 9-dimensional integral and several operators with a complex structure. This requires high computational effort and time, making it unfeasible to obtain predictions for several kinematics and nuclei, and motivating us to introduce two approximations: the description of the intermediate state as free Dirac spinors in a relativistic Fermi gas (RFG) and its extension including modified mass and energy that account for the relativistic interaction of nucleons. These two approaches are described in what follows.

4.1.2 Intermediate RFG-nucleon approximation

In this subsection, we approximate the intermediate bound-nucleon state by describing it as free Dirac spinors in an RFG, in the same way as done in infinite nuclear matter [127]. We refer to this approach as the intermediate RFG-nucleon approximation. Then, the summation over the occupied levels of the ground state in Eq. 4.10 now implies a sum over the intermediate momentum, $\mathbf{p}_{ph}$, spin, s', and isospin, τ',

$$\sum_{\alpha'} \to \sum_{\mathbf{p}_{ph},s',\tau'} \Theta(p_F - p_{ph}) \tag{4.53}$$

with p_F the Fermi momentum of the target nucleus. In contrast with the RMF-nucleon case discussed above, here one has the constraint that the momentum of the intermediate nucleons must be the same.

Substituting the two-particle two-hole hadronic currents of Eqs. 4.16, 4.17, 4.18, 4.19 and 4.20 into Eq. 4.10, and introducing the corresponding wave function for each nucleon, we get expressions with the general form

$$J_d \propto \int d\mathbf{p} \int d\mathbf{p}_p \int d\mathbf{p}_h \sum_{\mathbf{p}_{ph},s',\tau'} \Theta(p_F - p_{ph}) \\ \times \overline{\Psi}^{PW}(\mathbf{p}_p, \mathbf{p}_{ph}) \mathcal{O} \Psi^{PW}(\mathbf{p}_h, \mathbf{p}_{ph}) \, \overline{\Psi}^{s_N}(\mathbf{p} + \mathbf{p}_h + \mathbf{q} - \mathbf{p}_p, \mathbf{p}_N) \mathcal{O} \Psi_\kappa^{m_j}(\mathbf{p}), \tag{4.54}$$

for the direct terms and

$$J_e \propto \int d\mathbf{p} \int d\mathbf{p}_p \int d\mathbf{p}_h \sum_{\mathbf{p}_{ph},s',\tau'} \Theta(p_F - p_{ph}) \\ \times \overline{\Psi}^{s_N}(\mathbf{p} + \mathbf{p}_h + \mathbf{q} - \mathbf{p}_p, \mathbf{p}_N) \mathcal{O} \Psi^{PW}(\mathbf{p}_h, \mathbf{p}_{ph}) \overline{\Psi}^{PW}(\mathbf{p}_p, \mathbf{p}_{ph}) \mathcal{O} \Psi_\kappa^{m_j}(\mathbf{p}), \tag{4.55}$$

for the exchange terms. The Dirac plane wave function in momentum space for a nucleon with momentum $\mathbf{p}$ is given by

$$\Psi^{PW}(\mathbf{p}',\mathbf{p}) = (2\pi)^{3/2}\delta(\mathbf{p}'-\mathbf{p})\sqrt{\frac{M_N}{EV}}u(\mathbf{p},s), \tag{4.56}$$

leading to two Dirac deltas that can be used to integrate over $\mathbf{p}_h$ and $\mathbf{p}_p$. Then,

$$J_d \propto \frac{1}{V}\int d\mathbf{p} \sum_{\mathbf{p}_{ph},s',\tau'} \Theta(p_F - p_{ph})\ \bar{u}(\mathbf{p}_{ph},s')\mathcal{O}u(\mathbf{p}_{ph},s')\ \overline{\Psi}^{s_N}(\mathbf{p}+\mathbf{q},\mathbf{p}_N)\mathcal{O}\Psi_\kappa^{m_j}(\mathbf{p}), \tag{4.57}$$

$$J_e \propto \frac{1}{V}\int d\mathbf{p} \sum_{\mathbf{p}_{ph},s',\tau'} \Theta(p_F - p_{ph})\overline{\Psi}^{s_N}(\mathbf{p}+\mathbf{q},\mathbf{p}_N)\mathcal{O}u(\mathbf{p}_{ph},s')\bar{u}(\mathbf{p}_{ph},s')\mathcal{O}\Psi_\kappa^{m_j}(\mathbf{p}), \tag{4.58}$$

where the discrete summation over the intermediate momentum can be converted into a continuous integration with the usual phase-space factor

$$\sum_{\mathbf{p}_{ph}} \to V\int \frac{d^3\mathbf{p}_{ph}}{(2\pi)^3}, \tag{4.59}$$

and we can introduce in the exchange diagrams the relation $\sum_{s'} u(\mathbf{p}_{ph},s')\bar{u}(\mathbf{p}_{ph},s') = \frac{\not{p}_{ph}+M_N}{2M_N}$.

Taking all this into account, the two-body meson-exchange current with a final particle-hole state within the intermediate RFG-nucleon approximation can be finally written as

$$J^\mu_{2b,RFG} = \sqrt{V}\int d\mathbf{p}\int \frac{d\mathbf{p}_{ph}}{(2\pi)^3}\Theta(p_F - p_{ph})\overline{\Psi}^{s_N}(\mathbf{p}+\mathbf{q},\mathbf{p}_N)\Gamma^\mu_{2b,RFG}\Psi_\kappa^{m_j}(\mathbf{p}), \tag{4.60}$$

reducing the computation to a 6-dimensional integral. Note that, now, we can reorganize the expression of the two-body current and write the hadronic current including one- and two-body contributions, Eq. 4.1, as

$$J^\mu_\kappa = \sqrt{V}\int d\mathbf{p}\ \overline{\Psi}^{s_N}(\mathbf{p}+\mathbf{q},\mathbf{p}_N)\Gamma^\mu\Psi_\kappa^{m_j}(\mathbf{p}), \tag{4.61}$$

with

$$\Gamma^\mu = \Gamma^\mu_{1b} + \int \frac{d\mathbf{p}_{ph}}{(2\pi)^3}\Theta(p_F - p_{ph})\Gamma^\mu_{2b,RFG}. \tag{4.62}$$

As in the previous case, the two-body meson-exchange current operator is the sum of the Δ-resonance and ChPT background contributions from Figs. 4.3 and 4.4,

$$\Gamma^\mu_{2b,RFG} = \Gamma^\mu_{ChPT} + \Gamma^\mu_\Delta. \tag{4.63}$$

However, since the wave function for intermediate neutrons and protons is the same within this approximation and, in this work, we are considering isospin symmetric nuclei, with the same Fermi momentum for protons and neutrons, the ChPT direct terms contributing to the CC interaction and the Δ-resonance diagrams (a), (d), (e) and (g) vanish due to the sum over the isospin of the intermediate bound-nucleon state.

For the contributing Δ-resonance terms, the hadronic current operators read

$$\Gamma^{\mu}_{\Delta,(b)} = -IF_{\pi NN}F_{\pi\Delta N}\frac{g_A}{2f_\pi}\frac{M_N}{E_{ph}}\Gamma^{\alpha}_{\Delta\pi N}S_{\Delta,\alpha\beta}\Gamma^{\beta\mu}_{Q\Delta N}\frac{\Lambda(P_{ph})}{K_\pi^2-m_\pi^2}\not{K}_\pi\gamma^5, \tag{4.64}$$

with $P^{(b)}_\Delta = Q + P_{ph}$ and $K^{(b)}_\pi = P_{ph} - P$,

$$\Gamma^{\mu}_{\Delta,(c)} = -IF_{\pi NN}F_{\pi\Delta N}\frac{g_A}{2f_\pi}\frac{M_N}{E_{ph}}\not{K}_\pi\gamma^5\frac{\Lambda(P_{ph})}{K_\pi^2-m_\pi^2}\bar{\Gamma}^{\alpha\mu}_{Q\Delta N}S_{\Delta,\alpha\beta}\Gamma^{\beta}_{\Delta\pi N}, \tag{4.65}$$

with $P^{(c)}_\Delta = P_{ph} - Q$ and $K^{(c)}_\pi = P + Q - P_{ph}$,

$$\Gamma^{\mu}_{\Delta,(f)} = IF_{\pi NN}F_{\pi\Delta N}\frac{g_A}{2f_\pi}\frac{M_N}{E_{ph}}\frac{\Lambda_\Delta(\mathbf{p}_{ph},P_\Delta)}{K_\pi^2-m_\pi^2}\not{K}_\pi\gamma^5, \tag{4.66}$$

with $P^{(f)}_\Delta = Q + P_{ph}$ and $K^{(f)}_\pi = Q$,

$$\Gamma^{\mu}_{\Delta,(h)} = IF_{\pi NN}F_{\pi\Delta N}\frac{g_A}{2f_\pi}\frac{M_N}{E_{ph}}\frac{\bar{\Lambda}_\Delta(\mathbf{p}_{ph},P_\Delta)}{K_\pi^2-m_\pi^2}\not{K}_\pi\gamma^5, \tag{4.67}$$

with $P^{(h)}_\Delta = P_{ph} - Q$ and $K^{(h)}_\pi = Q$.

For the ChPT background terms, the vector and axial contributions of the exchange contact term diagrams, with $\Gamma^{\mu}_{CT} = \Gamma^{\mu}_{CT,V} + \Gamma^{\mu}_{CT,A}$, are given by

$$\Gamma^{\mu}_{CT,V} = IF_{CT}\frac{g_A^2}{2f_\pi^2}\frac{M_N}{E_{ph}}\left[F^2_{\pi NN,1}\not{K}_{\pi_1}\gamma^5\frac{\Lambda(P_{ph})}{K^2_{\pi_1}-m^2_\pi}\gamma^\mu\gamma^5 - F^2_{\pi NN,2}\gamma^\mu\gamma^5\frac{\Lambda(P_{ph})}{K^2_{\pi_2}-m^2_\pi}\not{K}_{\pi_2}\gamma^5\right], \tag{4.68}$$

$$\Gamma^{\mu}_{CT,A} = -I\frac{g_A}{2f_\pi^2}\frac{M_N}{E_{ph}}\left[F_{\rho,1}F^2_{\pi NN,1}\not{K}_{\pi_1}\gamma^5\frac{\Lambda(P_{ph})}{K^2_{\pi_1}-m^2_\pi}\gamma^\mu - F_{\rho,2}F^2_{\pi NN,2}\gamma^\mu\frac{\Lambda(P_{ph})}{K^2_{\pi_2}-m^2_\pi}\not{K}_{\pi_2}\gamma^5\right], \tag{4.69}$$

for the exchange pion-in-flight diagram, the purely vector contribution is given by

$$\Gamma^{\mu}_{PF} = IF_{PF}F_{\pi NN,1}F_{\pi NN,2}\frac{g_A^2}{2f_\pi^2}\frac{M_N}{E_{ph}}\frac{(Q+2P-2P_p)^\mu}{(K^2_{\pi_1}-m^2_\pi)(K^2_{\pi_2}-m^2_\pi)}\not{K}_{\pi_1}\gamma^5\Lambda(P_{ph})\not{K}_{\pi_2}\gamma^5, \tag{4.70}$$

and for the exchange pion pole diagrams, the purely axial contribution is given by

$$\Gamma^{\mu}_{PP} = I\frac{g_A}{4f_\pi^2}\frac{M_N}{E_{ph}}\frac{Q^\mu}{Q^2-m_\pi^2}\left[F_{\rho,1}F^2_{\pi NN,1}\not{K}_{\pi_1}\gamma^5\frac{\Lambda(P_{ph})}{K^2_{\pi_1}-m^2_\pi}(\not{K}_{\pi_1}+\not{Q})\right.$$
$$\left.-F_{\rho,2}F^2_{\pi NN,2}(\not{K}_{\pi_2}+\not{Q})\frac{\Lambda(P_{ph})}{K^2_{\pi_2}-m^2_\pi}\not{K}_{\pi_2}\gamma^5\right], \quad (4.71)$$

where $K_{\pi_1} = Q + P - P_{ph}$ and $K_{\pi_2} = P_{ph} - P$.

To shorten the expressions we have introduced the intermediate RFG projectors,

$$\Lambda(P_{ph}) = \frac{\not{P}_{ph}+M_N}{2M_N}, \quad (4.72)$$
$$\Lambda_\Delta(\mathbf{p},P_\Delta) = \sum_{s'}\bar{u}(\mathbf{p}_{ph},s')\Gamma^{\alpha}_{\Delta\pi N}S_{\Delta,\alpha\beta}\Gamma^{\beta\mu}_{Q\Delta N,A}u(\mathbf{p}_{ph},s'), \quad (4.73)$$
$$\bar{\Lambda}_\Delta(\mathbf{p},P_\Delta) = \sum_{s'}\bar{u}(\mathbf{p}_{ph},s')\bar{\Gamma}^{\alpha\mu}_{Q\Delta N,A}S_{\Delta,\alpha\beta}\Gamma^{\beta}_{\Delta\pi N}u(\mathbf{p}_{ph},s'), \quad (4.74)$$

where the contribution from the Λ_Δ and $\bar{\Lambda}_\Delta$ projectors is purely axial, as the vector part of the terms $\sum_{s'}\bar{u}(\mathbf{p}_{ph},s')\Gamma^{\alpha}_{\Delta\pi N}S_{\Delta,\alpha\beta}\Gamma^{\beta\mu}_{Q\Delta N}u(\mathbf{p}_{ph},s')$ and $\sum_{s'}\bar{u}(\mathbf{p}_{ph},s')\bar{\Gamma}^{\alpha\mu}_{Q\Delta N}S_{\Delta,\alpha\beta}\Gamma^{\beta}_{\Delta\pi N}u(\mathbf{p}_{ph},s')$ vanishes. This means that the two direct Δ-resonance diagrams (f) and (h) only contribute to the CC interaction.

The isospin coefficient (I) of each diagram is given in Tables 4.3 and 4.4. It already includes the sum over the isospin of the intermediate bound-nucleon state, as the operator for a particular diagram is the same for an intermediate neutron or proton except for this quantity. We remark that, for the EM interactions, only vector contributions should be taken into account, meanwhile both vector and axial terms contribute to the CC interactions.

Channel	CT	PF	PP	Δ (b, c)	Δ (f, h)
p $\to$ p	1	1	0	$2/\sqrt{3}$	0
n $\to$ n	-1	-1	0	$-2/\sqrt{3}$	0

Table 4.3: Isospin coefficients (I) for the meson-exchange contributions to the different reaction channels in the case of EM interactions. CT, PF and PP refer to the exchange ChPT background diagrams in Fig. 4.4, while Δ(b, c, f, h) refers to the Δ-resonance diagrams in Fig. 4.3.

Channel	CT	PF	PP	Δ (b, c)	Δ (f, h)
n → p	2	2	2	$4/\sqrt{3}$	$4/\sqrt{3}$
p → n	2	2	2	$4/\sqrt{3}$	$4/\sqrt{3}$

Table 4.4: Isospin coefficients (I) for the meson-exchange contributions to the different reaction channels in the case of CC interactions. The first row corresponds to neutrino-induced reactions. The second row corresponds to their antineutrino counterparts. CT, PF and PP refer to the exchange ChPT background diagrams in Fig. 4.4, while Δ(b, c, f, h) refers to the Δ-resonance diagrams in Fig. 4.3.

4.1.3 Intermediate modified RFG-nucleon approximation

The intermediate RFG-nucleon approximation reduces the two-body meson-exchange hadronic current with a final particle-hole state to a 6-dimensional integral, Eq. 4.60, with a reduced number of contributing diagrams and a simpler structure of their operators. Therefore, this approach results useful to reduce the computational effort and time required by these calculations. However, considering the intermediate bound nucleons as free Dirac spinors could be an oversimplification. In this subsection, we propose a more realistic description, without affecting the computational improvement obtained, by extending the RFG-nucleon approximation to account for the relativistic interaction of nucleons with the mean-field potential through modified mass and energy terms arising from the scalar and vector potentials.

The attractive scalar potential is accounted for in the relativistic effective mass,

$$M_N^* = m^* M_N < M_N. \tag{4.75}$$

Meanwhile, the vector potential produces a repulsive energy, which is added to the on-shell energy to obtain the modified nucleon energy,

$$E^* = E + E_v, \tag{4.76}$$

where $E = \sqrt{p^2 + (M_N^*)^2}$ is the on-shell energy with effective mass M_N^*. Then, the two-body meson-exchange current is computed as in the intermediate RFG-nucleon case, with the substitutions $M_N \to M_N^*$ and $E_{ph} \to E_{ph}^*$ in the intermediate nucleon variables and wave functions. The only exception is the ΔQN vertex, which retains the unmodified mass [132].

The values of the effective mass and vector energy are set following Ref. [133; 134; 135]. The effective mass is obtained from the superscaling approach with relativistic effective mass

(SuSAM*), where 1p-1h quasielastic cross sections are constructed by multiplying single nucleon averaged cross sections by a phenomenological scaling function. Within this approach, in the particular case of 1p-1h excitations computed with only one-body currents, the hadronic responses depend on the difference between initial and final energies. Therefore, the vector energy cancels and does not appear, only the effective mass can be obtained. The scaling function, as well as the effective mass and Fermi momentum for a nucleus, is get from fits to electron scattering cross section data, leading to $m^* = 0.8$, 0.79 and 0.73 for ^{12}C, ^{16}O and ^{40}Ca, respectively, [133]. With respect to the vector energy, its value is obtained in [134] from the 2p-2h meson-exchange current contributions to the cross section. The 2p-2h MEC component is computed using the model developed in [136] for the RFG, with the same contributions presented in this work (Figs. 4.1 and 4.2), but modifying it by including the nucleon effective mass and vector energy. In this case, the dependence on the vector energy is canceled in the ChPT contributions, but not in the Δ-resonance part, appearing in the Δ propagator. The inclusion of the vector energy affects the position of the Δ peak in the cross section, which allows to determine its value from experimental data. Alternatively, the vector energy can also be constrained by the following argument. In the direct Δ-resonance diagram, which corresponds to the dominant contribution to the 2p-2h cross section, the maximum of the propagator occurs approximately for $(P+Q)^2 - M_\Delta^2 = 0$. Considering the initial nucleon at rest, in the RFG, this implies that

$$\omega - E_S = \sqrt{M_\Delta^2 + q^2} - M_N, \tag{4.77}$$

with $E_S \simeq 40$ MeV the separation energy of two nucleons. On the other hand, introducing the modified mass and energy of the nucleons, the condition is

$$\omega = \sqrt{M_\Delta^2 + q^2} - M_N^* - E_v, \tag{4.78}$$

where the separation energy is not included as it is implicitly done in the scalar potential that leads to the relativistic effective mass. Finally, combining Eqs. 4.77 and 4.78, we get

$$M_N - E_S = M_N^* + E_v \tag{4.79}$$

obtaining $E_v = M_N - M_N^* - E_S \simeq 148$ MeV for ^{12}C. In [134], the value of E_v fitted from ^{12}C-electron scattering data, and the one used in this work, is 141 MeV, so the result from this estimation is in agreement. In the cases of ^{16}O and ^{40}Ca, there are not available values for E_v

obtained from experimental data, so we use the estimation above, yielding $E_v \simeq 162$ and 210 MeV, respectively.

To validate this approach, in Figs. 4.5, 4.6 and 4.7, we compare electromagnetic inclusive responses computed within RPWIA and a relativistic Fermi gas with a modified initial nucleon (RFG*), both cases evaluated with only one-body currents. In RPWIA, the initial nucleon is described by a bound wave function within the RMF model, so one would expect the results of RFG* and RPWIA to be similar. Indeed, modifying the mass and energy of the initial nucleon in the RFG produces a slight decrease of the strength and a shift of the response to higher transferred energy, looking more like the RPWIA result. Motivated by these findings, we have adopted this procedure for the study of two-body meson-exchange current contributions. In what follows, we will refer to it as the intermediate RFG*-nucleon approximation.

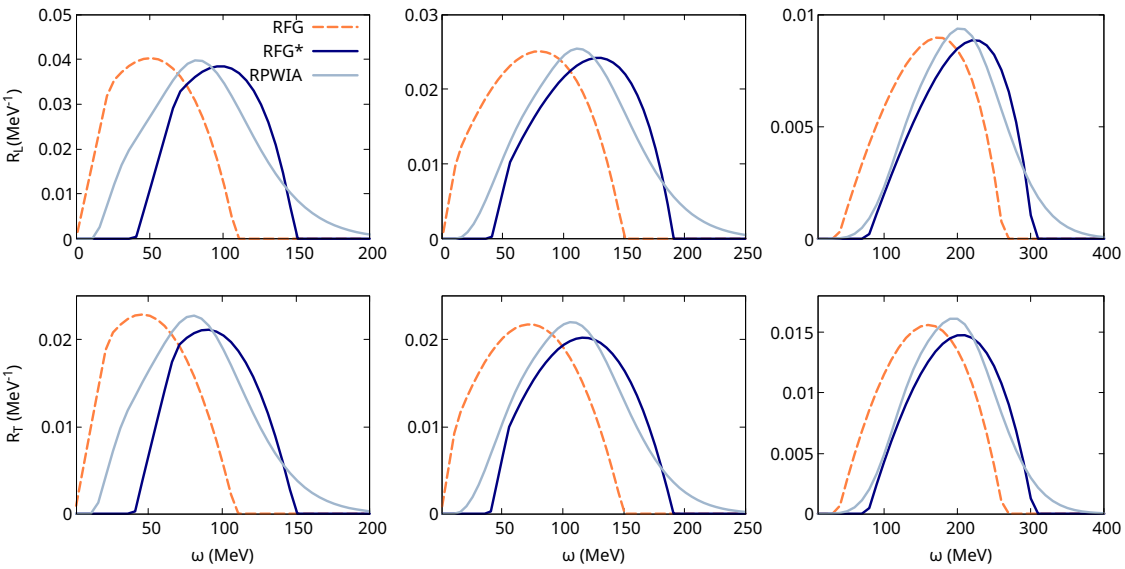

Figure 4.5: ^{12}C longitudinal (up) and transverse (bottom) electromagnetic inclusive response functions considering only one-body currents. The transferred momentum q is (from left to right) 300, 380 and 570 MeV/c. We show results for the relativistic Fermi gas (RFG), the relativistic Fermi gas with a modified initial nucleon (RFG*) and the relativistic plane wave impulse approximation (RPWIA).

4.1.4 Comparison of approaches

Fig. 4.8 shows the comparison of the ^{12}C electromagnetic inclusive responses at $q = 380$ MeV/c using the different approaches that can be taken to describe the intermediate bound-nucleon state: the simplest case, RFG nucleons, its extension including scalar and vector potentials and,

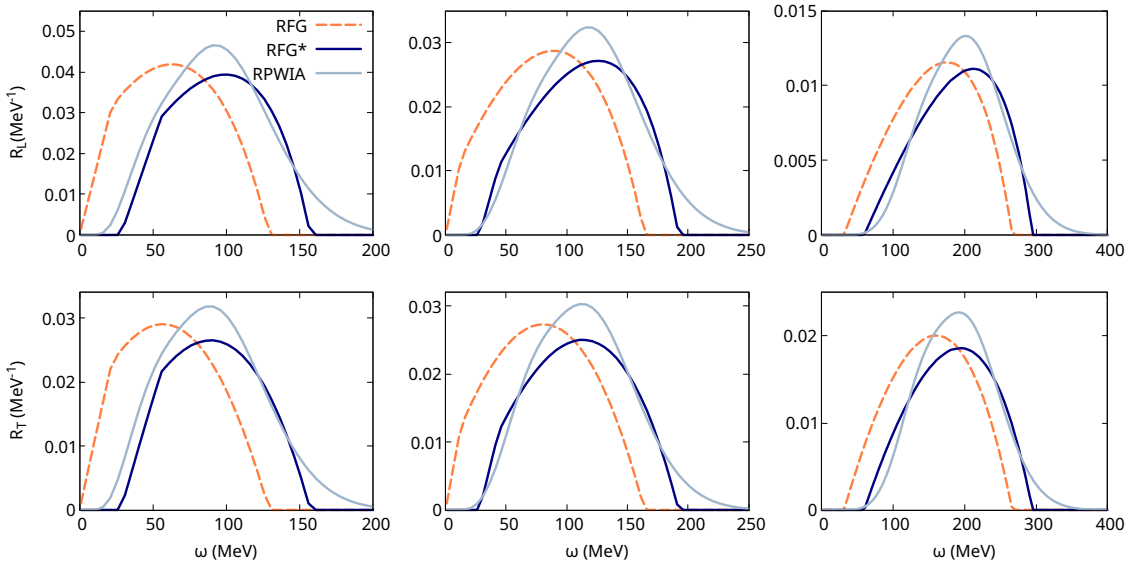

Figure 4.6: ^{16}O longitudinal (up) and transverse (bottom) electromagnetic inclusive response functions considering only one-body currents. The transferred momentum q is (from left to right) 335, 400 and 570 MeV/c. We show results for the relativistic Fermi gas (RFG), the relativistic Fermi gas with a modified initial nucleon (RFG*) and the relativistic plane wave impulse approximation (RPWIA).

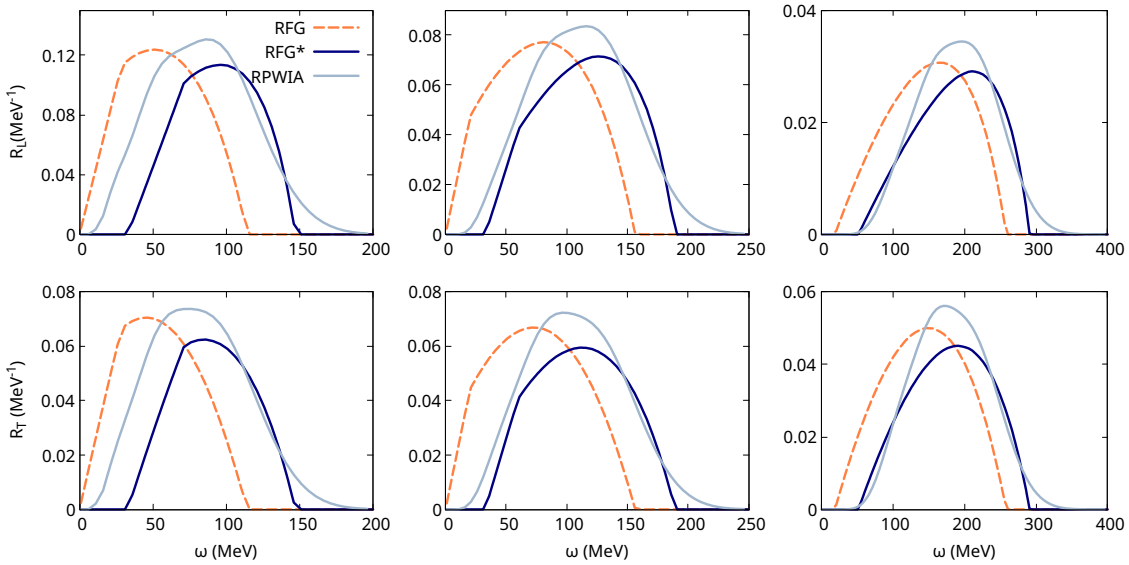

Figure 4.7: ^{40}Ca longitudinal (up) and transverse (bottom) electromagnetic inclusive response functions considering only one-body currents. The transferred momentum q is (from left to right) 300, 380 and 550 MeV/c. We show results for the relativistic Fermi gas (RFG), the relativistic Fermi gas with a modified initial nucleon (RFG*) and the relativistic plane wave impulse approximation (RPWIA).

finally, the most complete approach with intermediate RMF nucleons. Our predictions, computed using the ED-RMF potential to describe the final nucleon, are compared to data extracted by Jourdan [102] by means of a Rosenbluth separation. In general terms, the two-body meson-exchange current operator leads to an increase in the transverse response, while its effect on the longitudinal sector is negligible. The more realistic the treatment of the intermediate bound-nucleon state, the lower the increase. Specifically, the transverse response rises by up to 31%, 25% and 19% for the intermediate RFG-nucleon case, its extension including scalar and vector potentials, and the RMF one, respectively. Since the longitudinal channel is not affected by the two-body meson-exchange contribution, the agreement of our results with data keeps being outstanding, whereas it is improved in the transverse sector with the introduction of the two-body currents.

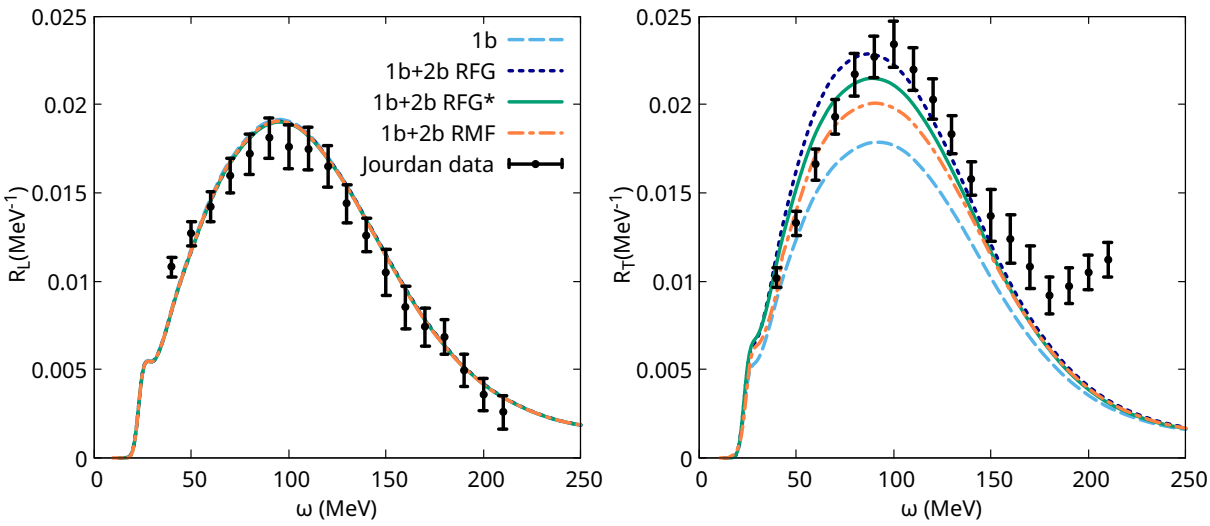

Figure 4.8: ^{12}C longitudinal (left) and transverse (right) electromagnetic inclusive response functions. The transferred momentum q is 380 MeV/c. We show our results, computed using the ED-RMF potential to describe the final nucleon, when the intermediate bound-nucleon state is described in terms of free particles in an RFG, including a modified mass and energy (RFG*), and RMF nucleons. Data are from Jourdan [102].

An additional comparison of these three approaches for four different kinematics is made in Fig. 4.9. We show the responses computed within the intermediate RFG-, RFG*- and RMF-nucleon approaches, but given the extremely high computational cost only a few points are shown for the latter. At low q, the RMF description of the intermediate nucleons reduces the transverse increase, especially, at low energy transfer. However, the difference between the RFG*- and RMF-nucleon approaches decreases as the value of q increases, obtaining essentially

identical results for momentum transfer around and above 500 MeV/c. Meanwhile, the increase obtained in the intermediate RFG-nucleon computation remains consistently larger in all cases. These differences between approaches can be attributed to two main effects. Firstly, at low q, only certain regions of the intermediate projectors appearing in the two-body current operators contribute, i.e., the kinematics do not encompass the entire objects. Therefore, when summing, the involved parts may differ between approaches. For instance, RMF wave functions exhibit tails that are absent in the RFG ones. At large q, the complete objects are accounted for, making any differences disappear, as observed in the RMF- and RFG*-nucleon cases. Secondly, the remaining mismatch with the RFG approximation, even at large q, can be explained by the lack of distortion of the intermediate nucleons. This is consistent with our study of the effect of using different potentials to describe the final-state nucleon in Sec. 3.3. The use of the ED-RMF potential reduces the total strength in comparison with RPWIA, in which the final nucleon is described by a relativistic plane wave. We understand that, analogously, when the intermediate RFG-nucleon approach is used instead of the RMF one, spurious contributions appear due to the lack of the bound condition of the nucleons.

As mentioned, the intermediate RFG*-nucleon approximation has the advantage of reducing the two-body meson-exchange current from a 9- to a 6-dimensional integral with fewer contributing diagrams, compared to the RMF case. While the ^{12}C inclusive responses can be computed in a manageable amount of time using the RFG* approach, the computational effort required by the RMF one makes it impractical for predicting neutrino-nucleus cross sections, which additionally involve an integral over the neutrino flux. We have verified that this simplified treatment of the intermediate state yields, at large enough q, the same results as the calculation with intermediate RMF-bound states, but at a fraction of the computational cost. At lower q,the discrepancy remains small, up to about 7%. Luckily, in most of accelerator-based neutrino experiments, the neutrino energy centers at around 1 GeV or above, and for those energies most of the strength of the cross section comes from $q > 500$ MeV/c [101]. Therefore, the RFG* approach would be an excellent approximation to the complete model, which consequently led to the choice of this framework for the following calculations.

Finally, we point out that it is expected to underestimate the inclusive data, especially in the high energy transfer region, where other processes, as 2p-2h MEC and pion production, contribute.

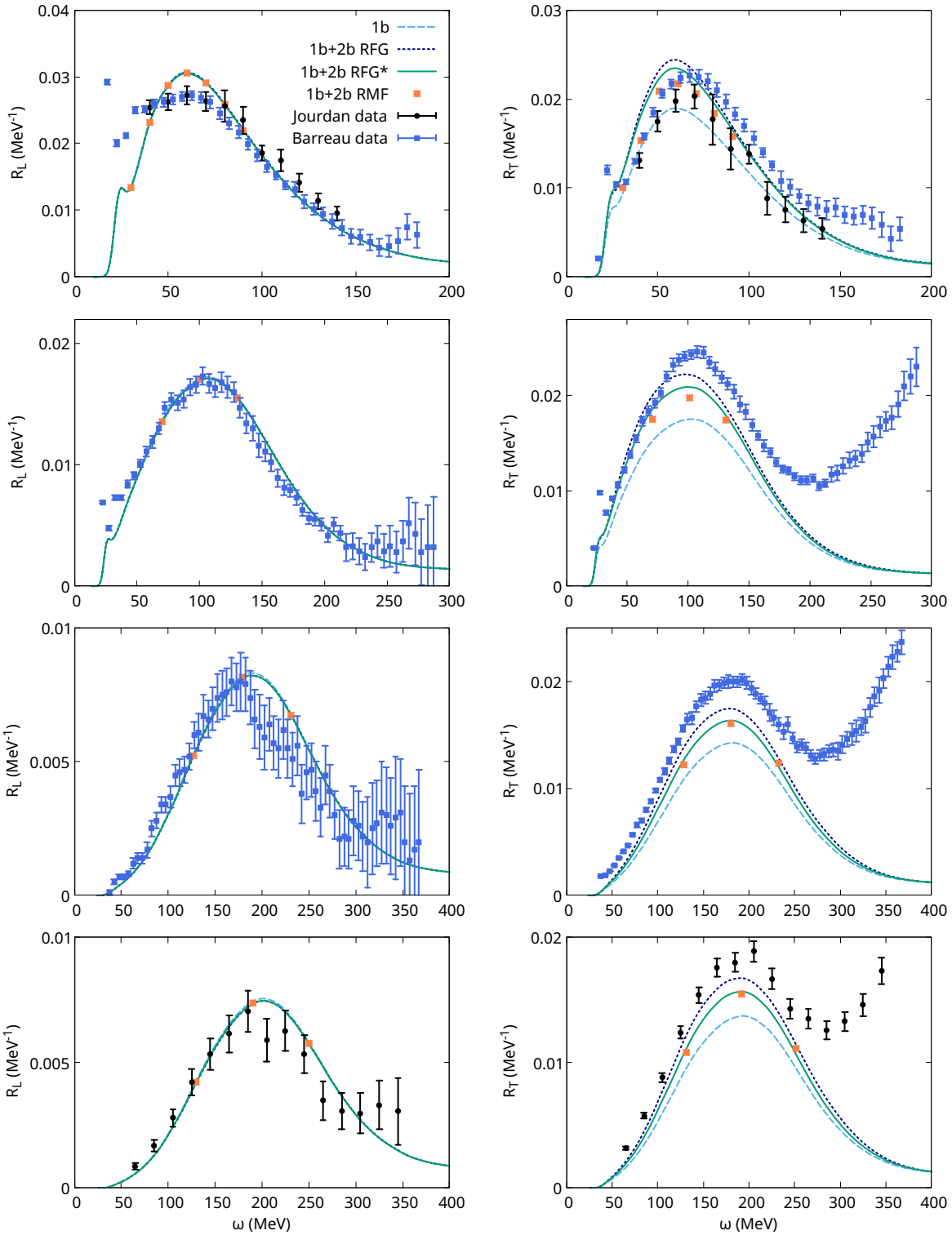

Figure 4.9: ^{12}C longitudinal (left) and transverse (right) electromagnetic inclusive responses. The transferred momentum q is (from up to bottom) 300, 400, 550 and 570 MeV/c. We show our results when the intermediate bound-nucleon state is described in terms of free particles in an RFG, including a modified mass and energy (RFG*), and RMF nucleons. Data are from Jourdan [102] and Barreau et al. [103].

Chapter 5

Electron-nucleus scattering

Electron scattering is one of the most precise methods to determine the internal structure of atomic nuclei and, due to its connection with neutrino-nucleus interaction, the interest on it has been renewed [114; 33; 137; 138]. The exponentially growing experimental effort in neutrino-nucleus scattering, related to neutrino oscillation experiments, makes it necessary to understand the nuclear interactions in the target nuclei, which otherwise would prevent the extraction of neutrino properties from these experiments [2; 33].

At the very least, the theory employed to describe nuclear effects when analyzing neutrino-nucleus experiments should compare fairly well when put at test against the available electron scattering data under similar kinematics. In contrast to neutrino beams, where the incident neutrino energy is not known a priori and only flux distributions are available, electron scattering has the advantage of nearly monochromatic beams. Therefore, before applying any model in neutrino oscillation analyses, the comparison with electron experimental data provides a first and necessary benchmark for the validation of the common vector component of electromagnetic and weak interactions. However, while essential, such a test is not sufficient to ensure the validity of the model, as the additional axial-vector component of the weak interaction cannot be tested in parity conserving electron scattering from nuclei.

Of particular interest are the few experimental data available on which not only the cross sections, but also the different contributions from separated nuclear responses have been measured. Nuclear responses, while should be similar in electron and neutrino scattering, would be combined differently in both processes. This means that a good agreement with just electron scattering cross sections would not be enough to ascertain the reliability of the model, while agreement to every separate nuclear response would be a much more compelling evidence of

adequacy of the model. These data allow for a robust validation of theoretical nuclear models by the simultaneous comparison with the different components of the electromagnetic responses rather than with just the cross section.

In this chapter, longitudinal (R_L) and transverse (R_T) responses, as well as cross sections, for inclusive electron scattering off ^{12}C, ^{16}O, and ^{40}Ca nuclei are computed within our fully relativistic model with one- and two-body current operators leading to a final particle-hole state.

5.1 Carbon responses

Our results for the inclusive longitudinal and transverse responses of ^{12}C, computed with one- and two-body operators, are shown in Fig. 5.1. The theoretical responses are compared to experimental data extracted by means of a Rosenbluth analysis by Jourdan [102]. We also show the *ab initio* non-relativistic Green's function Monte Carlo responses of [121], based on realistic two- and three-nucleon interactions and associated one- and two-body currents. We highlight the following features. The main effect of two-body meson-exchange currents with respect to the one-body approach appears in the transverse channel, while in the longitudinal one the 1p-1h MEC contribution is hardly visible. The transverse response increases by up to 30% in our calculation using the ED-RMF potential. The agreement of our results with data is good, outstanding for the longitudinal response. It is also remarkable the good agreement between ED-RMF and GFMC calculations, despite the fact that they represent quite different theoretical approaches.

Additionally, this same Fig. 5.1 also shows the two-body contribution only. For the transverse and longitudinal responses, it is nearly two and four orders of magnitude smaller than the one-body contribution, respectively. Therefore, it is clear that the increase of the transverse response is due to the interference between one- and two-body contributions.

A comparison of our ED-RMF predictions with ^{12}C longitudinal and transverse electromagnetic response functions extracted from a global analysis of all available electron scattering data on carbon has been performed in [139] (see Fig. 5.2 and figures therein). In contrast to previous extractions by Barreau et al. [103] and Jourdan [102], which were based on a limited set of cross-sectional data and thus only available for a narrow range of q and ω values, the analysis in [139] provides ^{12}C longitudinal and transverse responses at 18 distinct values of both q and Q^2 by including the full set of electron scattering measurements available on carbon. The extracted response functions span the nuclear excitation, quasielastic, resonance, and inelastic continuum

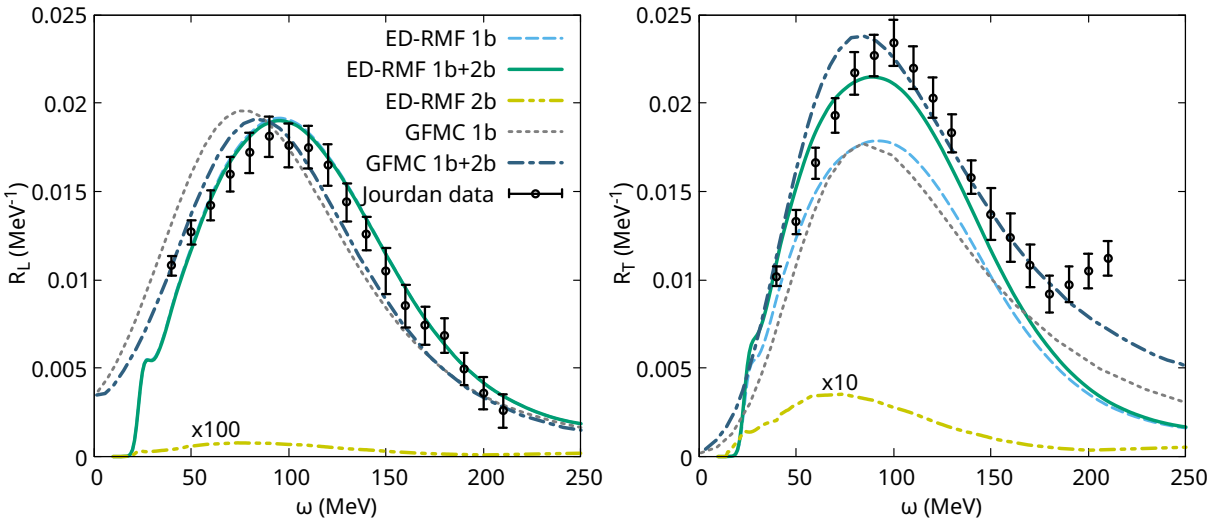

Figure 5.1: ^{12}C longitudinal (left) and transverse (right) electromagnetic inclusive response functions computed with one- and two-body operators. The transferred momentum q is 380 MeV/c. We show our ED-RMF results and the GFMC responses taken from [121], showing a fair agreement of both calculations. The theoretical predictions are compared with experimental data from [102].

regions. Therefore, we expect our model to agree with the experimental data in the kinematic regimes where QE scattering dominates. Among the theoretical predictions considered in [139], the ED-RMF approach provides the best description of R_L and R_T for QE scattering, covering the largest kinematic range in Q^2 and ω. At larger energy and momentum transfers, however, our theoretical predictions underestimate the data, indicating the need to incorporate processes with two nucleons or pions in the final state to correctly reproduce the full response.

In Fig. 5.3, we proceed as in Sec. 3.3 and study the sensitivity of our calculations including two-body currents with the description of the knocked-out nucleon, i.e., we address the effect of the treatment of final-state interactions and issues related with the (lack of) orthogonality between initial and final states. Our theoretical predictions are given within the RPWIA, EDAI-C and ED-RMF approaches. For the sake of simplicity, the RMF result is omitted from the figure. Results are consistent with previously established conclusions. Within RPWIA, the absence of final-state interactions and the lack of orthogonality between the initial and final nucleon states lead to an overestimation of the data. In contrast, in the ED-RMF approach, the nucleon wave functions are eigenstates of the same Hamiltonian, ensuring orthogonality, and obtaining a good agreement with data. This orthogonality condition is not fully satisfied in the EDAI-C model, whose results, although similar to those of ED-RMF, exhibit spurious contributions at low q. Therefore, accurately accounting for nucleon distortion while maintaining orthogonality between

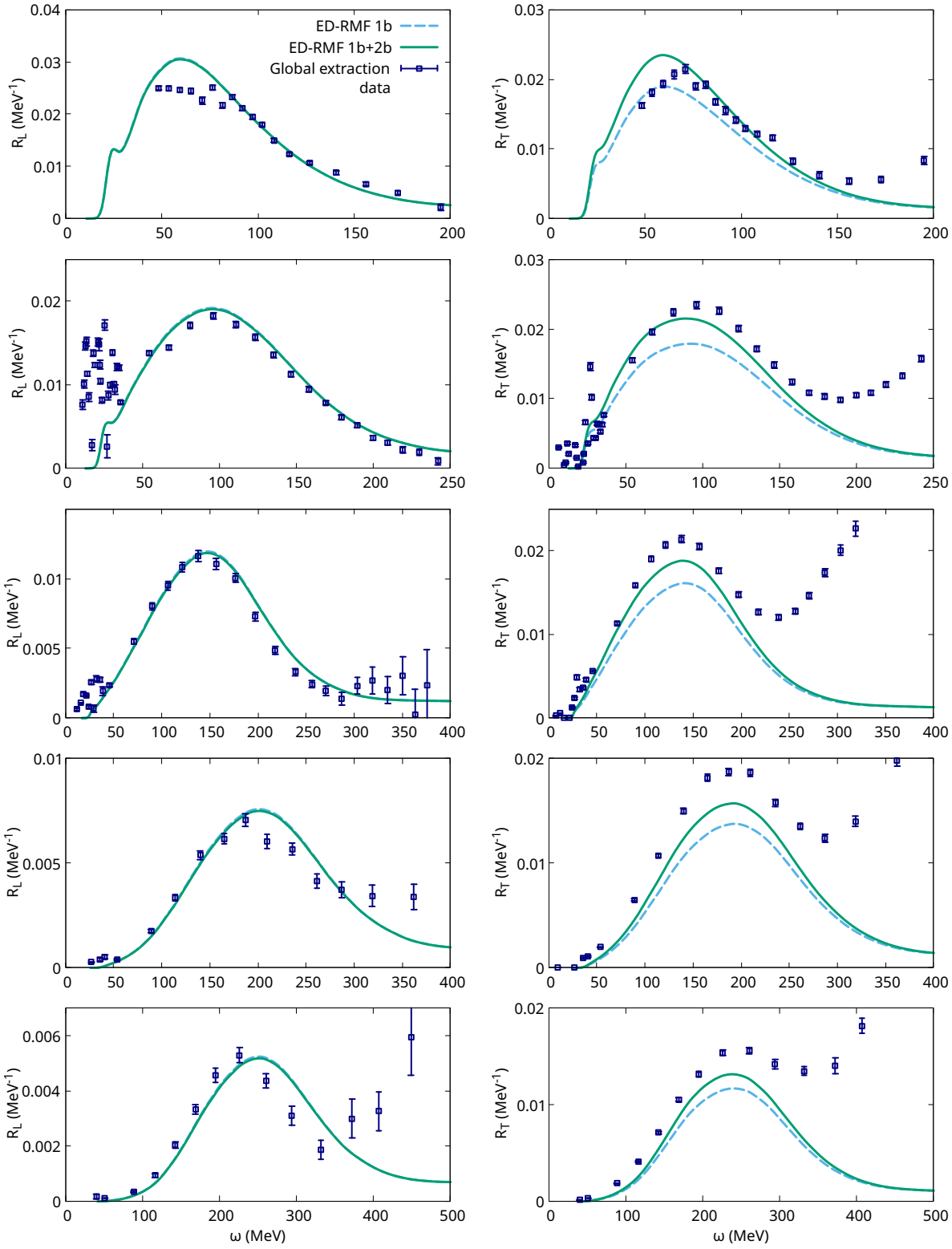

Figure 5.2: ^{12}C longitudinal (left) and transverse (right) electromagnetic inclusive response functions computed with one- and two-body operators within the ED-RMF model. The transferred momentum is (from up to bottom) 300, 380, 475, 570 and 649 MeV/c. The theoretical predictions are compared with experimental data from [139].

initial and final states is essential to reproduce both the magnitude and shape of the nuclear responses in carbon. Taking this into account, all subsequent results in this work have been computed using the ED-RMF potential.

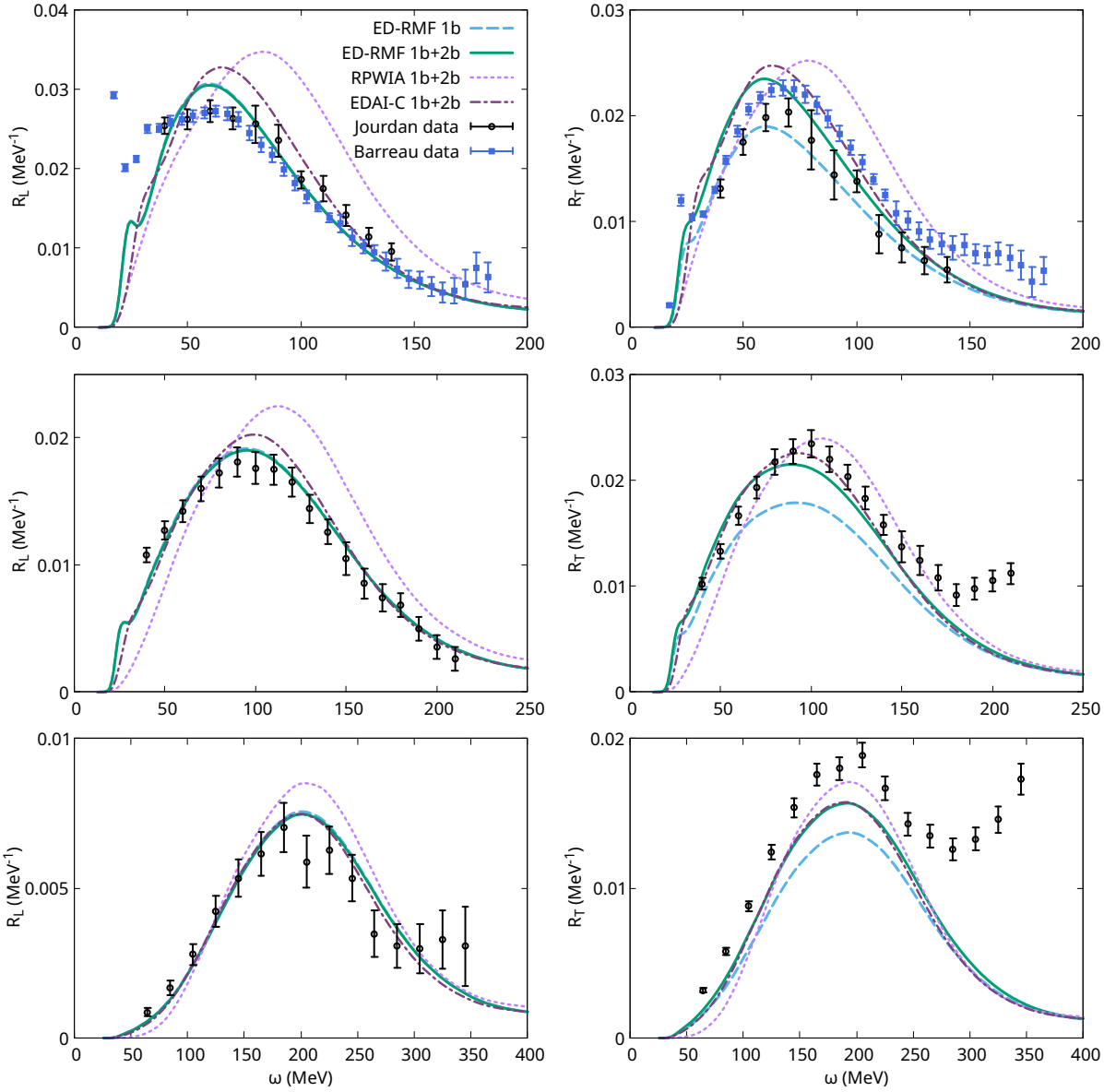

Figure 5.3: Longitudinal (left) and transverse (right) electromagnetic inclusive responses of ^{12}C within the ED-RMF, RPWIA and EDAI-C models. The transferred momentum q is (from up to bottom) 300, 380 and 570 MeV/c. The theoretical predictions are compared with experimental data from [102; 103].

Finally, in Fig. 5.4, we address the impact of current conservation on the longitudinal re-

sponse when two-body meson-exchange currents are included. Given the small contribution of the two-body operators, the effect of current conservation remains essentially unchanged from the one-body case. Only a minor impact is observed at large momentum transfers, with the exception of the correlated background contribution, for which the discrepancy is attributed to its oversimplified description.

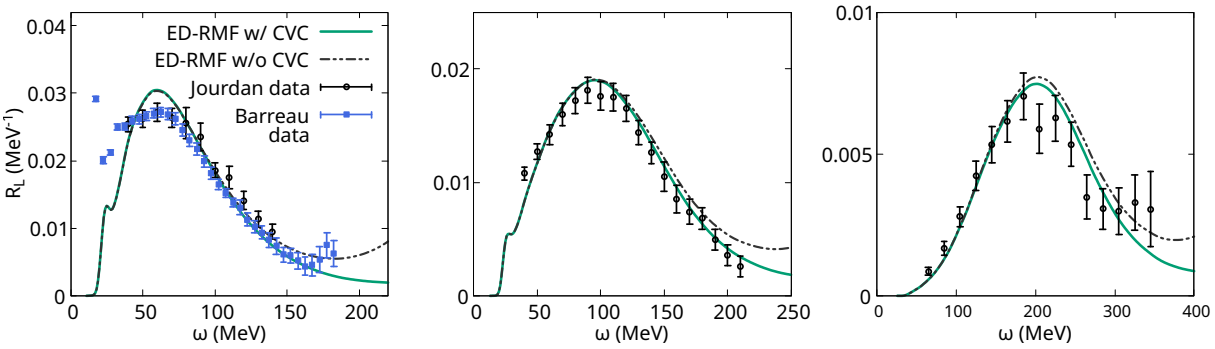

Figure 5.4: Longitudinal electromagnetic inclusive responses of ^{12}C including two-body currents within the ED-RMF model, with and without explicitly imposing CVC by setting $J^3_V = (\omega/q)J^0_V$. The transferred momentum q is (from left to right) 300, 380 and 570 MeV/c. The theoretical predictions are compared with experimental data from [102; 103].

5.2 Oxygen responses

Our predictions for the inclusive responses of ^{16}O are shown in Fig. 5.5. To our knowledge, no Rosenbluth separation has been carried out to obtain experimental longitudinal and transverse responses for this nucleus, owing to the limited amount of available experimental cross section data. Therefore, it is not possible to separately compare the resulting longitudinal and transverse response functions with experimental measurements. However, we can compare our theoretical predictions with the recent ones obtained from the Bayesian artificial neural network (BNN) framework presented in Ref. [140] and the coupled-cluster theory in conjunction with the Lorentz integral transform method (LIT-CC) of [141]. The BBN is trained on (e, e') scattering data of several symmetric nuclei to perform the extraction of longitudinal and transverse response functions, which are obtained directly as the output of this architecture. Its predictions are presented with the corresponding uncertainty, which is quite large in this case due to the scarcity of data. This method captures all reaction mechanisms contributing to the training datasets and, therefore, its results cover processes ranging from elastic and quasielastic scattering to the deep inelastic scattering region. Meanwhile, the *ab initio* quantum many-body LIT-CC

method employs nuclear forces derived from chiral effective field theory, considering two- and three-nucleon interactions optimized to simultaneously reproduce low-energy nucleon-nucleon scattering and selected nuclear structure data. The electromagnetic transition operator comprises only one-body current contributions in this case.

At momentum transfer $q = 335$ MeV/c, the main difference between our predictions and those from BNN and LIT-CC appears at low energy transfers and, in particular, in the longitudinal channel. In this region, excitations of low-lying nuclear states occur. While these contributions are present in the BNN and LIT-CC curves, such interaction mechanisms cannot be described within the relativistic mean-field model used in our approach, explaining the observed discrepancy. In the transverse sector, we obtain a good agreement between our one-body results and those of LIT-CC, as two-body contributions are not included in the latter. Meanwhile, when comparing with the BNN prediction, which includes the contributions from all reaction mechanisms, there is better agreement with our complete calculation including two-body currents. Nevertheless, the BNN result appears to be above our ED-RMF prediction at energies larger than the quasielastic peak. This behavior is reassuring, as it leaves room for pion production in the Δ peak, which is not included in this work and will produce strength in that region.

For the second kinematic considered, at $q = 400$ MeV/c, the results follow a similar trend. Again, and more noticeably for this higher momentum transfer kinematic, the BNN prediction for the transverse response remains consistently larger than ours beyond the quasielastic peak, due to the absence of pion production mechanisms in our framework. Furthermore, the agreement in the longitudinal sector remains affected by contributions from low-lying nuclear states. In that sense, comparisons to kinematics with larger momentum transfer would be especially meaningful, minimizing these low-energy contributions and allowing us to disentangle other possible differences. Finally, we remark that the extraction of the longitudinal and transverse responses from BNN for ^{16}O is particularly subject to larger uncertainties, due to the scarcity of cross section data for this nucleus.

One last result is shown at $q = 570$ MeV/c. Although it is not possible to compare our predictions with the theoretical ones from the BNN and LIT-CC methods, we observe a similar behavior to the ^{12}C case, with a significant effect of two-body currents in the transverse sector.

Although a comparison with experimental data would be necessary to ensure the validity of the model, the overall agreement with BNN and LIT-CC responses provides an initial validation of our approach. This is especially relevant considering how different these frameworks are.

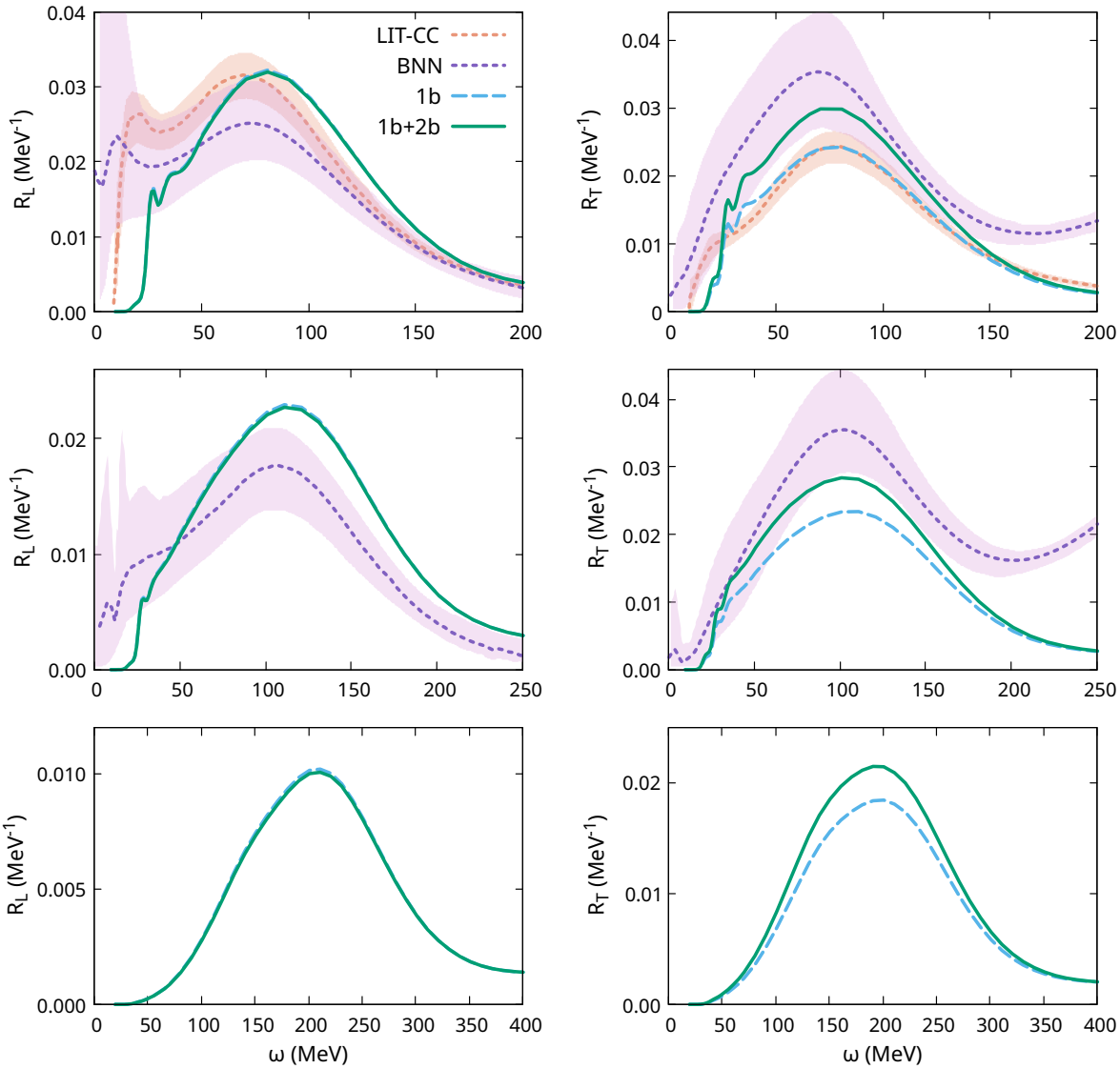

Figure 5.5: Longitudinal (left) and transverse (right) electromagnetic inclusive responses of ^{16}O within the ED-RMF model. The transferred momentum q is (from up to bottom) 335, 400 and 570 MeV/c. The theoretical predictions are compared to those from the Bayesian artificial neural network (BNN) of [140] and the coupled-cluster theory in conjunction with the Lorentz integral transform method (LIT-CC) of [141].

5.3 Calcium responses

The electromagnetic inclusive responses of ^{40}Ca are shown in Fig. 5.6. Our results are now presented as bands that incorporate the uncertainty associated with the occupation probability of the single-particle states. Following the procedure described in Sec. 2.3, the limits of the bands

corresponds to the occupations given in Table 2.5, which have been obtained as those configurations with the most and least nucleons in the background among 10^4 random configurations generated within the limits of Table 2.4 and with the constraint that the amount of nucleons in the background is between 20% and 35% of the total number of nucleons. An additional dark-solid line is shown, it corresponds to the case with the mean value of the occupations of Table 2.4, this means 32% of the nucleons in the background. The results are compared to the available experimental data from [102; 142; 143; 144].

For the longitudinal responses, at momentum transfer $q = 300$ MeV/c, the data from Jourdan [102] and Williamson [144] agree fairly well with each other, and with our results. At $q = 350$ MeV/c, we underestimate the quasielastic peak with respect to the predictions from Williamson [144]. Meanwhile, at $q = 380$ MeV/c, there is a good agreement with Jourdan data [102]. Regarding the transverse response, for these three kinematics, we observe a good agreement of our one-body results with the experimental data, leading to an overestimation when two-body meson-exchange currents are introduced. Nevertheless, our one-body current results in the transverse sector are similar to those obtained with the mean-field approach of [145] and the different *ab initio* approach of [146; 147]. Hence, it is expected that these other calculations also show an overestimation of the responses similar to what we get here when two-body currents are included. We stress that the transverse enhancement due to two-body currents is supported by the analyses of inclusive EM responses for ^{3}He, ^{4}He and ^{12}C [119; 120; 122; 121; 148].

The fourth kinematic corresponds to $q = 400$ MeV/c, which is compared with data at $q = 400$ MeV/c from [144] and $q = 410$ MeV/c from [142; 143]. Our longitudinal result lies in between both datasets, which are in large disagreement. Meanwhile, the transverse response including two-body currents seems to agree better with [143], although it would be necessary to have a better control of the occupations, and then obtain a narrower band, to draw a clear conclusion. The large difference between the two datasets is remarkable and cannot be explained by the 10 MeV difference in momentum transfers, which is illustrated by showing in the same figure our 1b+2b current calculation for $q = 410$ MeV/c (short-dashed red line, the mean value of the occupations was employed).

For the last momentum transfer considered, $q = 550$ MeV/c, there is a fair agreement between our results and the data from [144] and [142] up to an energy transfer around 150 MeV. In the transverse sector, the situation is similar to the results obtained for carbon, with an increase of the transverse response up to 25% which improves the agreement with data.

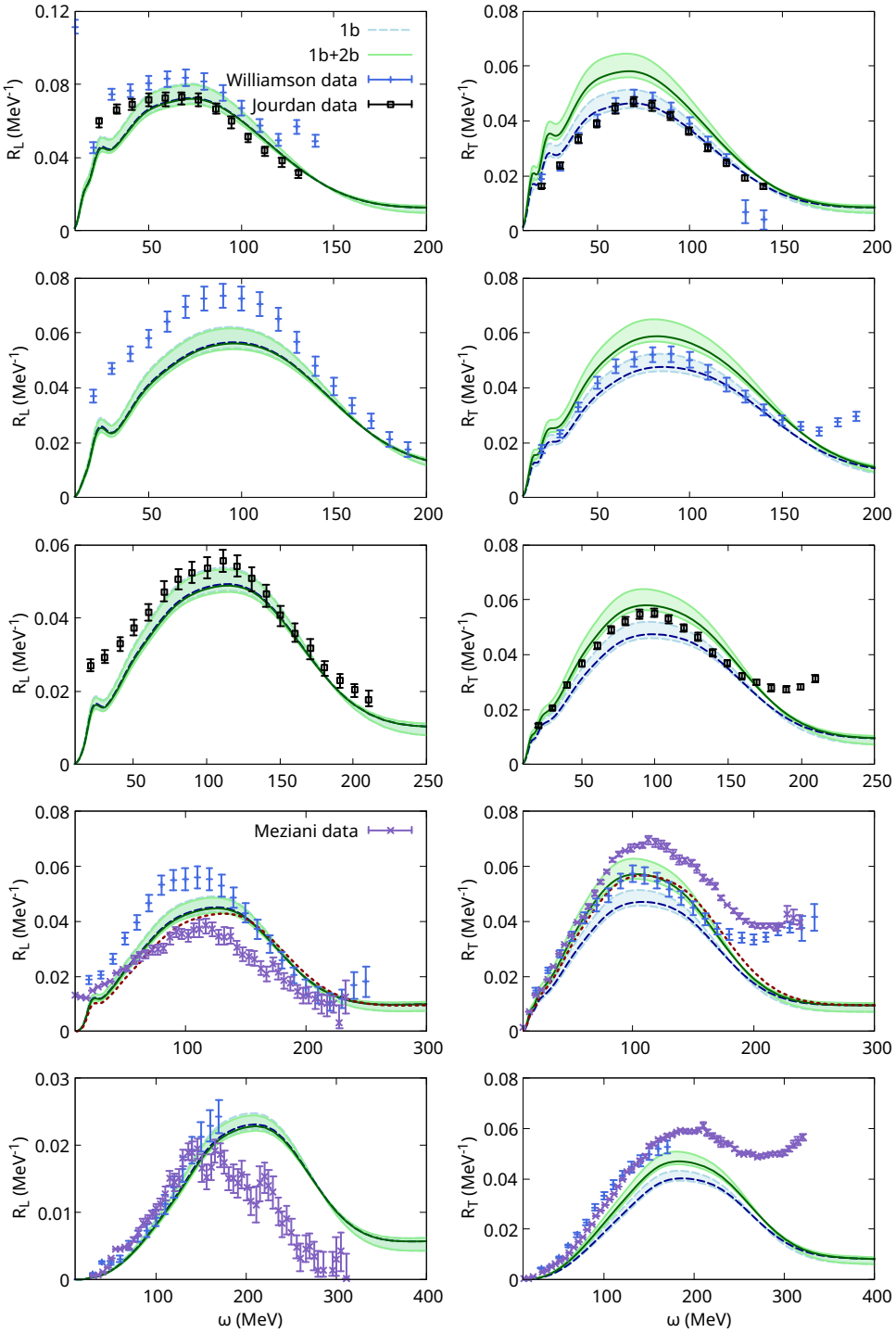

Figure 5.6: ^{40}Ca longitudinal (left) and transverse (right) electromagnetic inclusive responses using the ED-RMF model. The transferred momentum q is (from up to bottom) 300, 350, 380, 400 and 550 MeV/c. The theoretical predictions are compared with experimental data from [102; 142; 143; 144]. In the case of $q = 400$ MeV/c, Meziani data and red line correspond to $q = 410$ MeV/c, the theory line was computed with 1b+2b currents. Results are presented as bands accounting for the uncertainty in the occupation probability of the single-particle states and with a dark-solid line that corresponds to average occupations of Table 2.4.

We recall that the extraction of the responses from inclusive cross section data was performed using a Rosenbluth procedure, which is very sensitive to the treatment of Coulomb distortion effects in electrons. In carbon, this is expected to be a very small correction. But in calcium, it is a non-negligible effect which introduces uncertainties that are difficult to quantify. The disagreement among different datasets for the separated responses in calcium may point to unadequate treatment of Coulumb distortion. For this reason, in the next section we compare directly with inclusive cross section data.

5.4 Cross sections

In Figs. 5.7, 5.8, 5.9 and 5.10 we show inclusive electron-^{12}C, -^{16}O and -^{40}Ca cross sections at various beam energies and scattering angles. Our 1p-1h 1b and 1b+2b ED-RMF predictions are compared to experimental data from [103; 149; 150; 151; 152; 153; 154] for carbon, [155; 150] for oxygen and [142; 144; 149] for calcium.

For the studied kinematics, the two-body meson-exchange contributions to particle-hole excitations produce an increase of the cross section coming from the increase in the transverse part. The relative increase is larger for larger values of beam energy, E_i, and lepton scattering angle, θ_e, as the contribution of the transverse response is more significant in those cases. We stress that our calculation is only for the QE 1p-1h channel. Thus, there is strength in the experimental data unaccounted for in our prediction, coming from other reaction channels, such as 2p-2h meson-exchange currents and pion production (see e.g. the review article [114]). Aiming at making comparisons more meaningful, we include the 2p-2h MEC contribution (dashed-dotted purple line) from [113; 156], which should be added incoherently to the QE result. We point out that this 2p-2h MEC corresponds to a relativistic Fermi gas model, it is expected that a shell model calculation of this channel [157; 75] and the incorporation of in-medium effects in the Δ-resonance decay width [158] yield a somewhat smaller contribution.

Since the longitudinal part of the cross section is basically not affected by the two-body currents, we identify kinematics with a small transverse contribution to benchmark our occupation probabilities. For carbon, Fig. 5.7, the panels corresponding to $E_i = 200$ MeV at $\theta_e = 60$ deg, and 320 and 400 MeV at 36 deg are mostly longitudinal. In these cases, we find good agreement with data. For oxygen, Fig. 5.9, the most longitudinal kinematic, although with a significant transverse contribution yet, corresponds to $Ei = 537$ MeV at $\theta_e = 37.1$ deg. The quasielastic

peak appears to be shifted to higher energy transfers compared to the experimental data, resulting in poor agreement and a considerable amount of missing strength at low energy transfers. For the $Ei = 700$ MeV at $\theta_e = 32$ deg kinematic, a significant discrepancy is also observed, with the data in the quasielastic peak being inconclusive. However, the remaining kinematics exhibit good agreement in the position of the quasielastic peak. The scarcity of data at lower energies and different scattering angles makes it difficult to draw clear conclusions. For calcium, Fig. 5.10, the most longitudinal kinematics correspond to $E_i = 160$, 200 and 240 MeV at 60 deg. The agreement with data is good for energies larger than 30 MeV, where the quasielastic contribution dominates. For energies below 30 MeV, there is qualitative agreement, but in this region one would have to include discrete resonances in the calculation to agree with data. To conclude, current conservation is analyzed in Fig. 5.11 for these kinematics, as the dominance of the longitudinal response makes them the most suitable for its study. The results obtained with and without explicitly enforcing CVC are essentially identical, indicating that our calculation largely preserves current conservation.

Analogously, we identify kinematics that are essentially transverse. For carbon, these are 560 MeV at 145 deg and the recent measurement from the Mainz Microtron (MAMI) experiment at 855 MeV and 70 deg [154] shown in Fig. 5.8. For oxygen, these are 1080, 1200 ad 1500 MeV at 32 deg. For calcium, these are 320, 327 and 400 MeV at 140 deg. In all these cases, the data support the enhancement of the cross section due to the two-body contributions.

In the case of calcium, for most of the kinematics studied, the upper part of our 1b+2b bands is often above the data, or it would be if one introduces the contribution from other reaction channels, such as 2p-2h MEC. In other words, our results fit better the data when around $30-35\%$ of the nucleons are placed in the background, which contributes mostly in the high-ω tail and little in the QE peak. Recent works have estimated about 20% [63; 64] of SRC pairs in nuclei. Therefore, the relatively small occupation probabilities that our comparison with data suggests and, consequently, our large background are effectively accounting for other mechanisms that lead to a reduction of the cross section in the QE peak. Our approach, based on simply reducing the occupancies of the mean-field shells and placing those nucleons in the background, reveals its limitations. At this point, it becomes both preferable and necessary to employ microscopic models that dynamically describe these nuclear effects, such as long-range correlations, which are particularly relevant in relatively heavy nuclei, like ^{40}Ca, and at low Q^2 [159; 145].

Additionally, different ^{40}Ca datasets, corresponding to the same lepton scattering angle and similar or identical beam energy, allow us to asses possible inconsistencies between them. At 140

deg and 320 and 327 MeV, 90 deg and 200 MeV, and 90 deg and 360 and 372 MeV, we found datasets from Meziani [142] (black points) and Williamson [144] (blue points). In these cases, we obtain a better agreement with Meziani's sets, which are systematically larger than those from Williamson. At 60 deg and 480 and 500 MeV, we found datasets from Meziani and Whitney [149] (gray points), which seem to be consistent with each other and with our predictions using the intermediate value for the occupations.

Finally, in Fig. 5.12, we compare our results obtained using full shell occupations from the IPSM, where correlations are neglected, with those from the spectral function approach employed in this work. Cross sections computed within the IPSM overestimate the data, making clear that a more realistic treatment of the nuclear structure results fundamental to correctly describe the experimental cross sections.

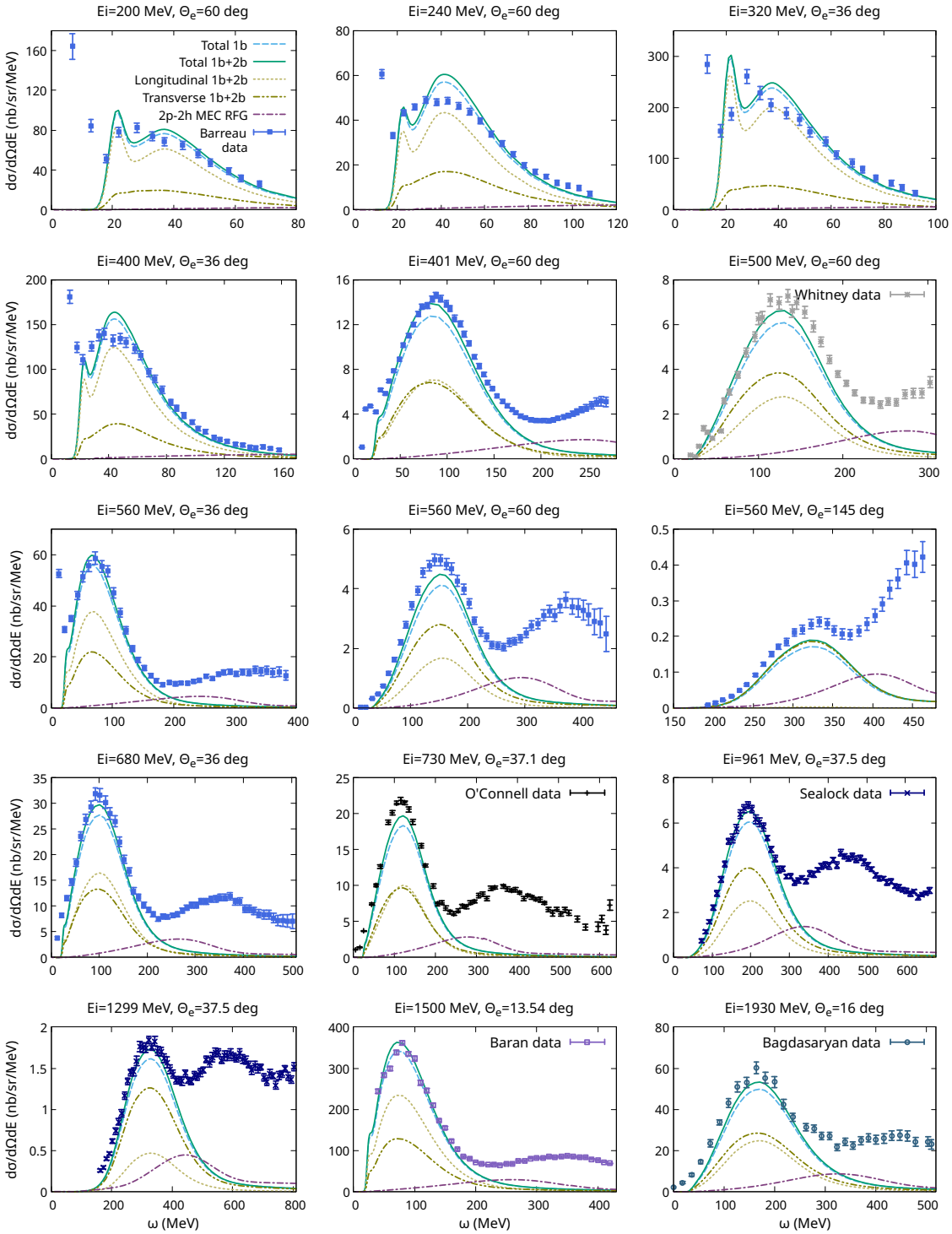

Figure 5.7: ^{12}C electromagnetic inclusive cross sections at various beam energies and scattering angles. We show the 1b and 1b+2b ED-RMF cross section (total), its longitudinal and transverse contributions, and the 2p-2h MEC from [156]. Theoretical predictions are compared with experimental data from [103; 149; 150; 151; 152; 153].

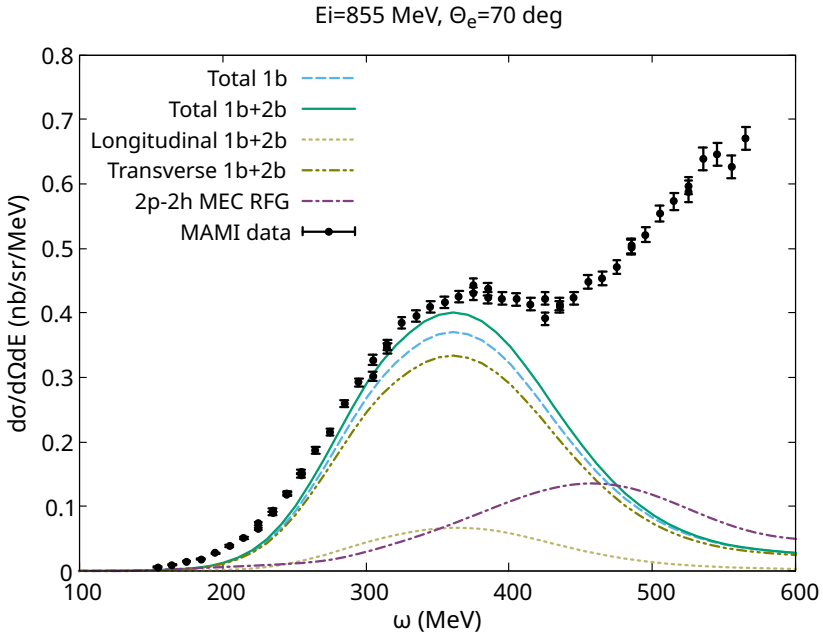

Figure 5.8: ^{12}C electromagnetic inclusive cross sections at beam energy 855 MeV and scattering angle 70 deg. We show the 1b and 1b+2b ED-RMF cross section (total), its longitudinal and transverse contributions, and the 2p-2h MEC from [156]. Theoretical predictions are compared with the recent experimental data from [154].

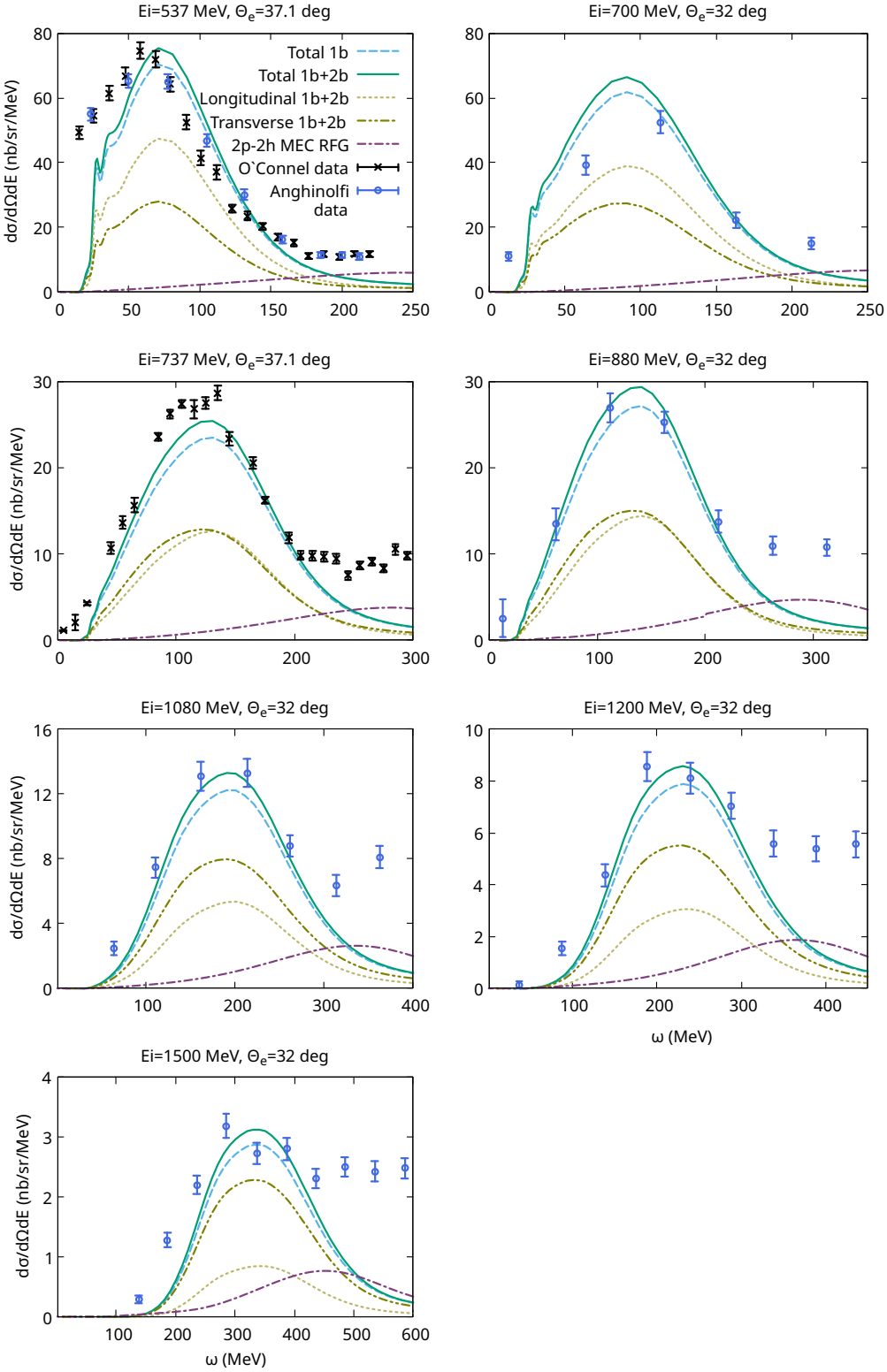

Figure 5.9: ^{16}O electromagnetic inclusive cross sections at various beam energies and scattering angles. We show the 1b and 1b+2b ED-RMF cross section (total), its longitudinal and transverse contributions, and the 2p-2h MEC from [156]. Theoretical predictions are compared with experimental data from [155; 150].

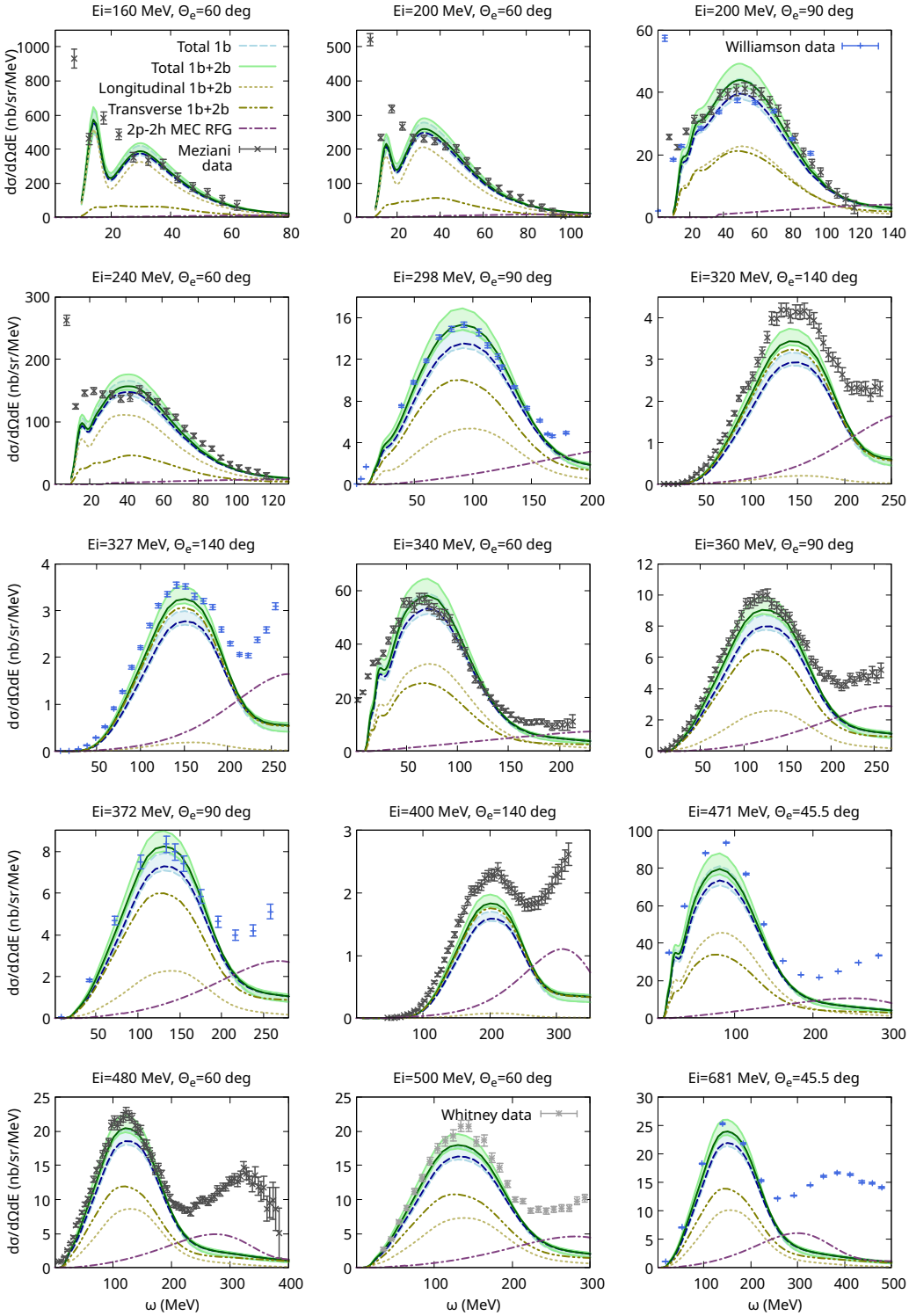

Figure 5.10: ^{40}Ca electromagnetic inclusive cross sections at various beam energies and scattering angles. We show the 1b and 1b+2b ED-RMF cross section (total), its longitudinal and transverse contributions, and the 2p-2h MEC from [156]. Theoretical predictions are compared with experimental data from [142; 144; 149]. The bands represent the uncertainty in the occupation of the single-particle states according to Table 2.4, and the dark-solid line corresponds to the case with the average value of these occupations.

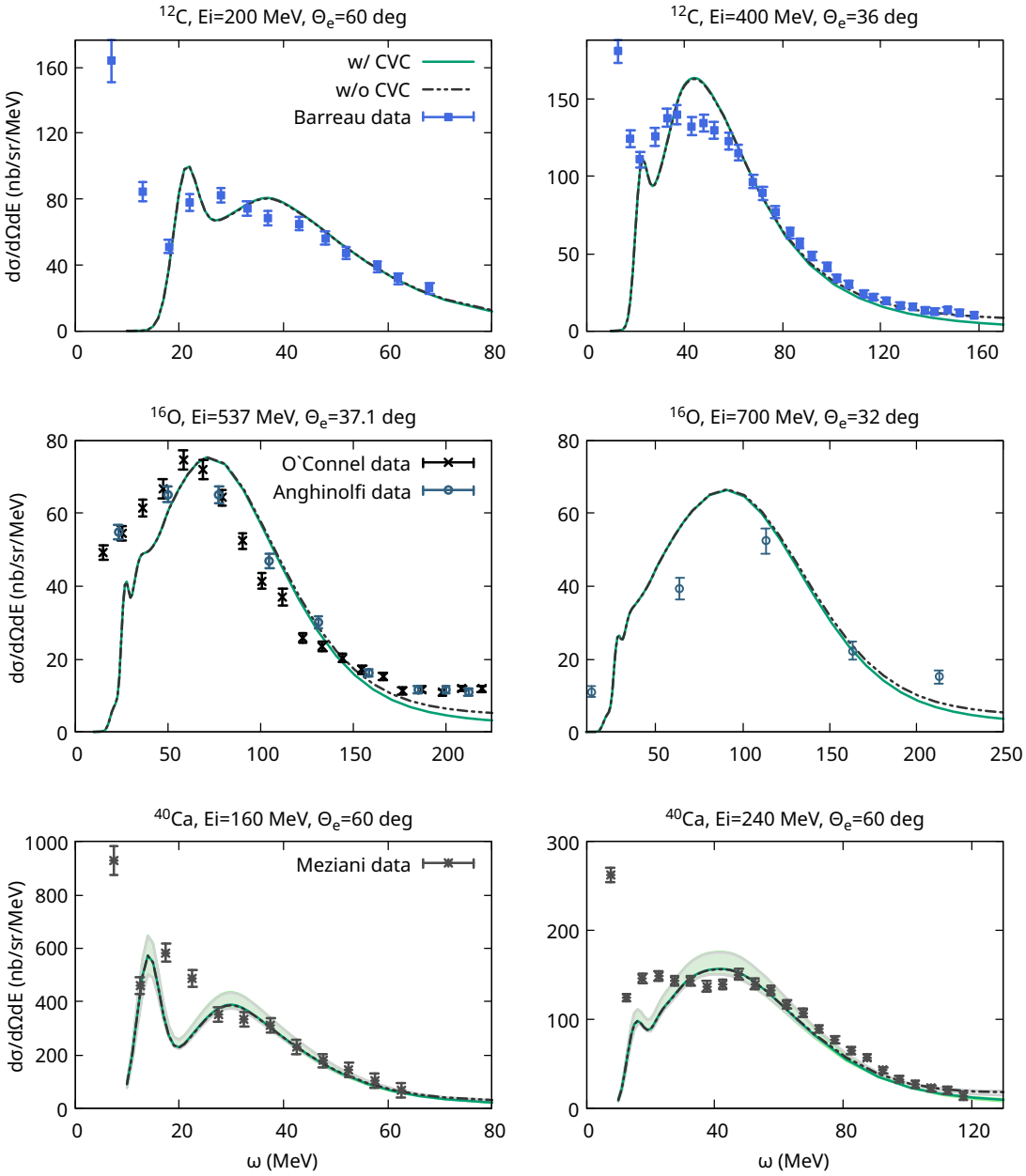

Figure 5.11: ^{12}C (top), ^{16}O (middle) and ^{40}Ca (bottom) electromagnetic inclusive cross sections at various beam energies and scattering angles. We show the 1b+2b ED-RMF cross section, with and without explicitly imposing CVC by setting $J^3_V = (\omega/q)J^0_V$. The theoretical predictions are compared with data from [103; 150; 155; 142].

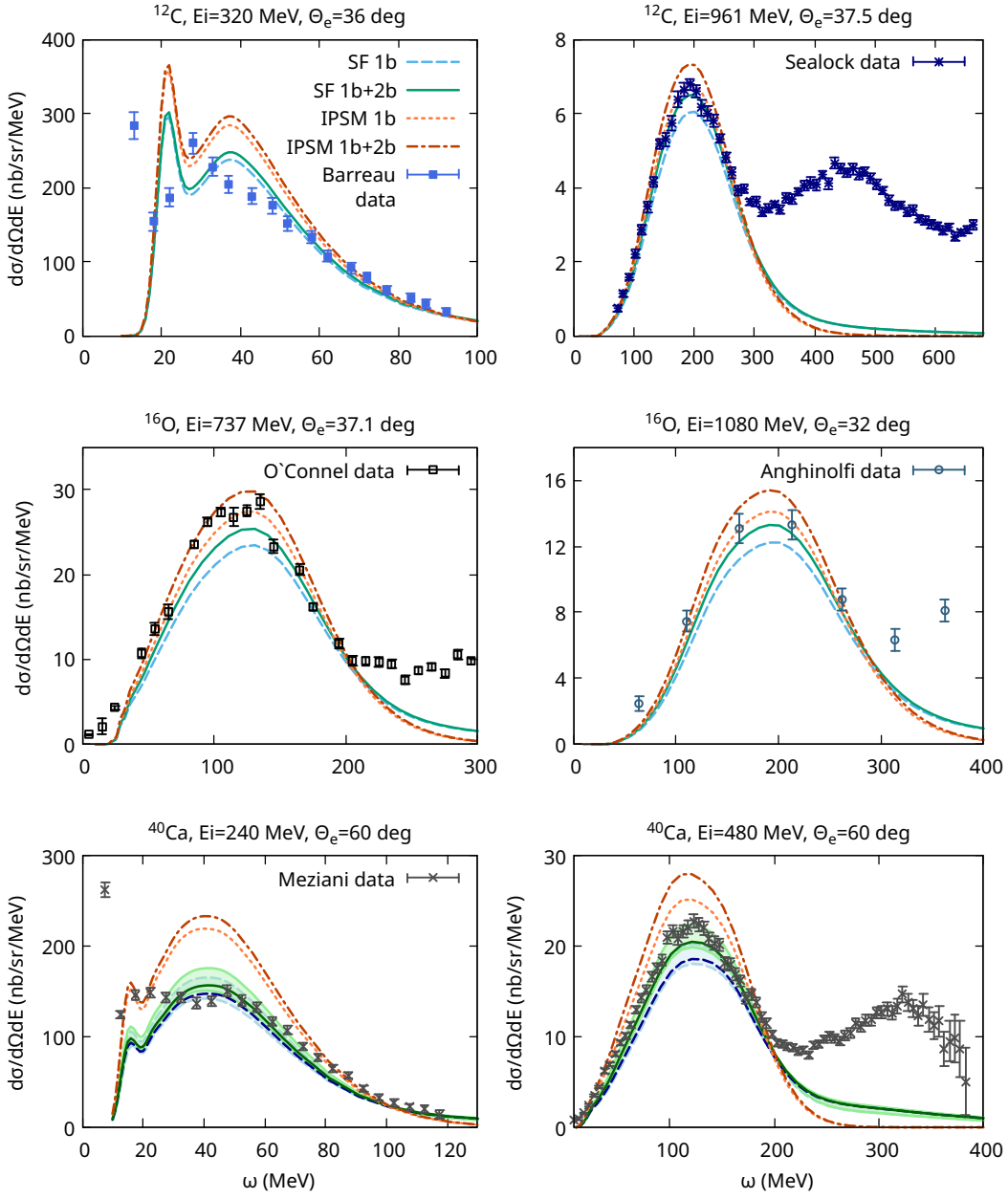

Figure 5.12: ^{12}C (top), ^{16}O (middle) and ^{40}Ca (bottom) electromagnetic inclusive cross sections at various beam energies and scattering angles. We show the 1b and 1b+2b ED-RMF cross section computed with shell occupations from the independent-particle shell model (IPSM) and the spectral function approach (SF). The theoretical predictions are compared with data from [103; 151; 150; 155; 142].

Chapter 6

Charged-current neutrino-nucleus scattering

Next-generation of accelerator-based neutrino oscillation experiments, DUNE [24] and T2HK [23; 19], require an unprecedented level of accuracy to succeed in extracting neutrino oscillation parameters. However, one of the main sources of systematic uncertainties comes from the limited precision in the modeling of neutrino-nucleus interactions. Neutrino beams are produced in accelerator-based experiments with a broad flux distribution, making the exact energy of the interacting neutrino unknown. In order to extract the oscillation parameters, it is necessary to reconstruct the incident neutrino energy from the reaction products. The reconstruction method depends strongly on neutrino interaction physics, as the interactions observed in the detector result from the folding of the energy-dependent neutrino flux, cross section and nuclear (strong- and electroweak-interaction) effects. The wealth of electron scattering data available, along with the growing collection of measurements from accelerator-based neutrino experiments, have revealed limitations in the models of lepton-nucleus cross sections that are commonly employed in neutrino event generators [160; 161; 162; 138]. Therefore, an accurate description of these reactions has become one of the top challenges for theoretical nuclear physics [2].

The broad energy range of neutrino fluxes in both current and future experiments, spanning from a few hundred of MeV to several tens of GeV, implies that measured neutrino-nucleus cross sections may encompass contributions from distinct energy- and momentum-transfer regions of the nuclear weak response, where different dynamical regimes govern the interactions. These range from the structure and collective behavior of low-lying nuclear excitations to the quark substructure of individual nucleons in the deep inelastic scattering region. Therefore, reliable

analyses of neutrino-nucleus interactions present significant challenges, requiring all possible reaction channels that contribute to the experimental signal to be accurately taken into account. Among all mechanisms, quasielastic scattering provides a significant contribution to the signal in current and future oscillation experiments, being the dominant one in T2K and MicroBooNE.

In this chapter, we carry out our fully relativistic and within a quantum mechanical framework calculations for charged-current quasielastic interactions off ^{12}C and ^{16}O. Accurately modeling (anti)neutrino-nucleus scattering, essential for extracting neutrino oscillation parameters from long- and short-baseline experiments, requires retaining as many quantum-mechanical effects as possible. The good agreement with electron scattering experimental data supports the use of our approach to describe the analogous neutrino-induced scattering reaction, allowing us to include the contribution from two-body meosn-exchange currents. We compute inclusive cross sections for fixed values of the initial (anti)neutrino energy, as well as integrated over the (anti)neutrino flux of accelerator-based experiments. While for electromagnetic interactions a vast amount of data exists, allowing to benchmark lepton-nucleus reaction models, the amount of available data for charged-current weak processes is much more limited and with poorer quality. Apart from the limited statistics, the complicating factor in these datasets is the fact that the incoming neutrino energy is not well-defined, but is instead given by a broad distribution. Then, in order to compare theoretical predictions with experimental measurements, it is necessary to integrate the cross section over all possible initial neutrino energies weighted by the normalized experimental neutrino flux. The flux-folded cross section is computed as

$$\left\langle \frac{d\sigma}{dp_f d\Omega_f} \right\rangle = \int dE_\nu \phi(E_\nu) \frac{d\sigma(E_\nu)}{dp_f d\Omega_f}, \tag{6.1}$$

where the inclusive cross section for a fixed neutrino energy is given by Eq. 2.42, $\phi(E_\nu)$ is the normalized (anti)neutrino flux and the integral over ϕ_f can be trivially done yielding a factor 2π. The experimental data are usually binned in $\cos\theta_f$ bins, thus, when comparing to these data, the calculated cross sections are averaged over the corresponding bin.

The extraction of cross section data based on the interaction mode involves significant model-dependent corrections. In particular, charged-current quasielastic scattering measurements are affected by two main backgrounds: multi-nucleon knock-out and pion absorption. On the one hand, multi-nucleon knock-out processes, in which 2p-2h excitations constitute the dominant contribution, can mimic CCQE interactions in detectors, as they produce similar final-state signatures—namely a charged lepton and two or more nucleons—making them difficult to dis-

tinguish from genuine 1p-1h quasielastic events. On the other hand, interpreting events with no pions in the final state as purely quasielastic is not correct. A major complication arises from the fact that pions can be not seen in the detector or initially produced at the interaction vertex but subsequently undergo reabsorption within the nuclear medium [163], leading to their misidentification as quasielastic events. The correct identification of these contributions is problematic and model-dependent, requiring a detailed and accurate description of both the cross section for pion production and the mechanisms governing their reabsorption. At present, these effects are primarily estimated through Monte Carlo event generators, introducing additional sources of uncertainty. Consequently, the CCQE cross sections extracted from experimental data are subject to significant systematic uncertainties, further complicating their interpretation. Therefore, experimental collaborations have shifted toward publishing data of a more objective nature by focusing on the topology of the final state observed in the detector. CCQE cross section measurements have been replaced by inclusive CC or CC0π experimental signatures, where only a final-state charged lepton (i.e., an electron or a muon) is detected in presence or not of pions in the final state, respectively.

Our predictions for ^{12}C and ^{16}O flux-averaged inclusive cross sections, differential in the outgoing lepton energy and scattering angle, are compared with experimental datasets corresponding to charged-current interactions from MiniBooNE and T2K collaborations [164; 165; 166; 167; 17; 168; 169], whose main features have been discussed in Chapter 1. As previously stated, when considering the CC0π experimental signature, datasets tend to have a mix of contributions characterized by the absence of pions in the observed final state. This includes CCQE, 2p-2h and those pion production processes where the pion is absorbed. Therefore, it is expected that our 1p-1h predictions underestimate the data when 2p-2h excitations and pion absorption are relevant.

6.1 Cross sections at fixed neutrino energy

Before comparing our predictions to neutrino scattering data, which are averaged over experimental fluxes, we examine inclusive cross sections at a fixed energy of the initial (anti)neutrino, close to the mean flux energy of the experiments considered. This allows us to isolate and analyze the effect of two-body meson-exchange currents, providing a deeper understanding, without blurring the results due to the flux-folding in the neutrino energy.

Fig. 6.1 present our results for charged-current inclusive cross sections with an incoming muon (anti)neutrino of energy 750 MeV and fixed values of the outgoing (anti)muon angle $\theta_\mu = 15$, 30 and 60 deg. The separation in longitudinal and transverse components is also shown according to Eq. 2.53, where the longitudinal component (L) includes the contributions from the CC, CL and LL channels. In all cases, the dominant contribution to the cross section comes from the T channel. The two-body currents lead to an increase in the magnitude of both T and T' responses, while the longitudinal contribution remains unchanged, with practically no effect on the CC, CL and LL responses separately. Differences between neutrino and antineutrino cross sections arise from the nuclear charge of the involved nucleons in each case, but the most significant effect appears in the leptonic tensor and affects the sign of the T' contribution, which adds up for neutrino scattering but reduces strength in the antineutrino case, almost canceling out the T component at high enough scattering angles. Therefore, the relative increase in the cross sections due to two-body currents is larger for neutrinos compared to antineutrinos as, for the latter, the enhancement of the T and T' responses has opposite signs, diminishing the overall effect. Additionally, the negative T' contribution for antineutrino reactions increases the relative importance of the longitudinal channel, making it essential to correctly interpret antineutrino scattering at backward angles, even though its overall contribution is the smallest among the response functions.

Electromagnetic inclusive cross sections at the same kinematics are shown in Fig. 6.2. Here, the relative strength of the longitudinal and transverse components depends on the kinematics, in contrast to the charged-current case, where transverse dominance is consistently observed. In charged-current cross sections, the contribution from the longitudinal channel is significantly smaller compared to the electromagnetic case, and the transverse component dominates across all kinematics. Consequently, the effect of two-body currents becomes more significant, especially in neutrino scattering.

Current conservation is addressed in Fig. 6.3. In this case, charged-current inclusive cross sections contain vector and axial contributions, but the conserved current hypothesis only applies to the former. We present results for both neutrino and antineutrino scattering, along with their longitudinal components, which are the only ones sensitive to CVC. As in the electromagnetic case, the impact of explicitly imposing current conservation is minimal, with the longitudinal response remaining practically unchanged. Additionally, this effect on the cross section is further mitigated by the fact that, in charged-current reactions, the longitudinal contribution is subdominant across all kinematics, making it even less significant. In antineutrino scattering, the

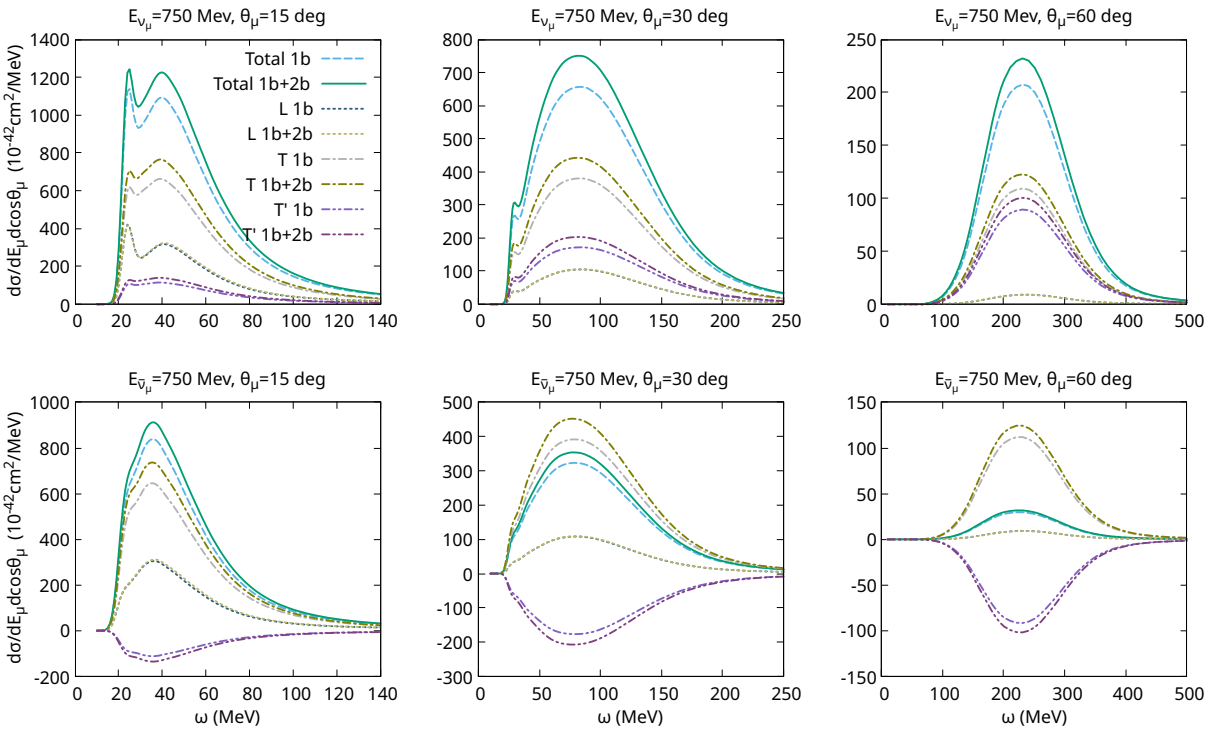

Figure 6.1: Charged-current inclusive cross sections for neutrino (top) and antineutrino (bottom) scattering off ^{12}C at beam energy 750 MeV and various scattering angles. We show the 1b and 1b+2b ED-RMF cross section (total), and its longitudinal (L) and transverse (T and T') contributions.

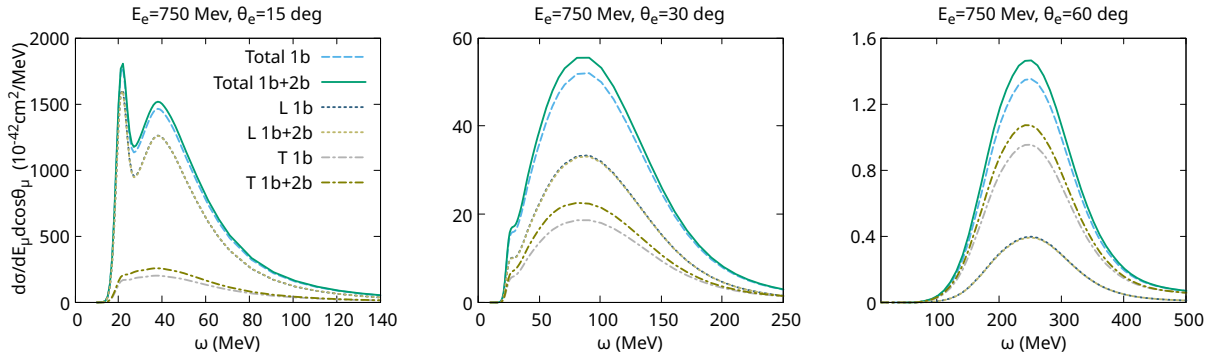

Figure 6.2: Electromagnetic inclusive cross sections for electron scattering off ^{12}C at beam energy 750 MeV and various scattering angles. We show the 1b and 1b+2b ED-RMF cross section (total), and its longitudinal (L) and transverse (T) contributions.

negative contribution from the T' response slightly enhances the relative importance of the longitudinal component, leading to a marginally more visible impact from CVC. Nevertheless, even under these conditions, the differences remain negligible. In conclusion, no significant violations of the conserved vector current hypothesis are observed in our calculations.

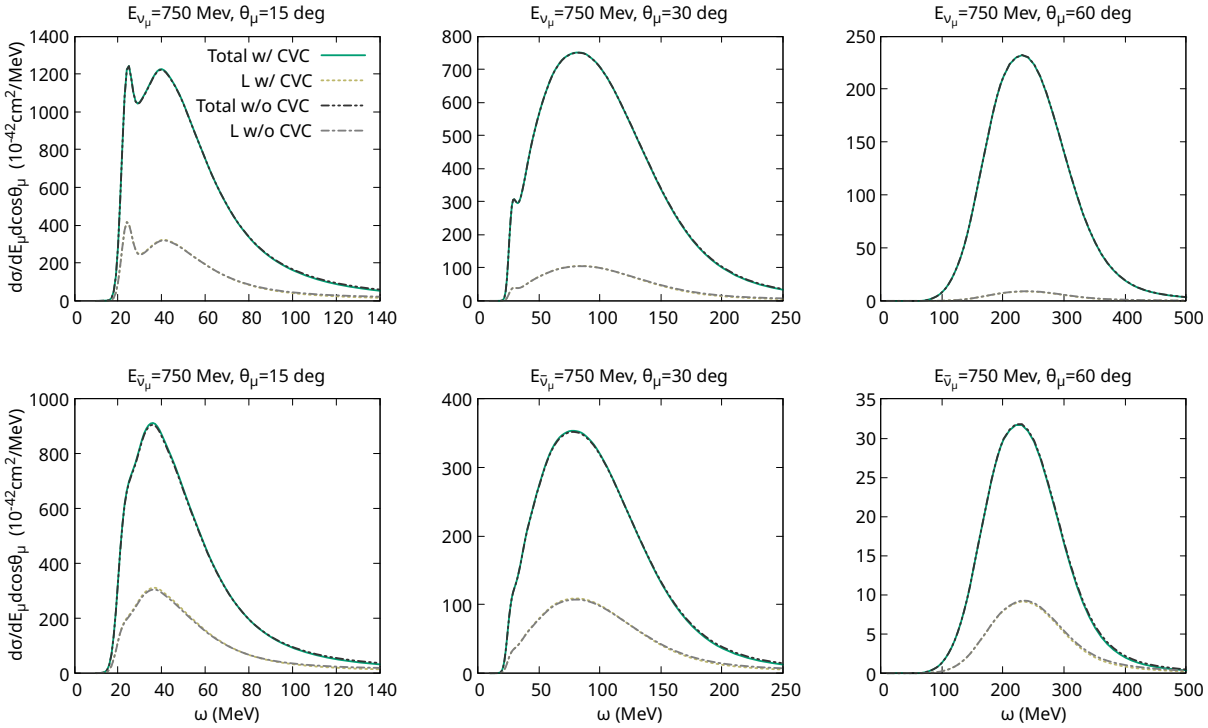

Figure 6.3: Charged-current inclusive cross sections for neutrino (top) and antineutrino (bottom) scattering off ^{12}C at beam energy 750 MeV and various scattering angles. We show the 1b+2b ED-RMF cross section (total) and its longitudinal (L) contribution, with and without explicitly imposing CVC by setting $J^3_V = (\omega/q)J^0_V$.

Finally, in Figs. 6.4 and 6.5, we show the separation of the cross section, along with its longitudinal and transverse components, in terms of the vector and axial contributions of the hadronic responses. At forward scattering angles, the cross section is dominated by the axial contribution, while as the scattering angle increases, the vector-axial interference becomes more significant, and the vector and axial terms remain comparable. The L channel is always dominated by the vector component, with a small contribution from the axial one. This explains the transverse dominance of charged-current cross sections, as the T channel is now enhanced by the axial component of the responses, whereas such enhancement does not occur in the longitudinal sector. The main contribution to the T response comes from the axial part at small scattering

angles, but it eventually becomes comparable to the vector component as one moves to more backward angles. None of these L and T components have any contribution from the vector-axial interference term, whose strength is entirely contained in the T' channel.

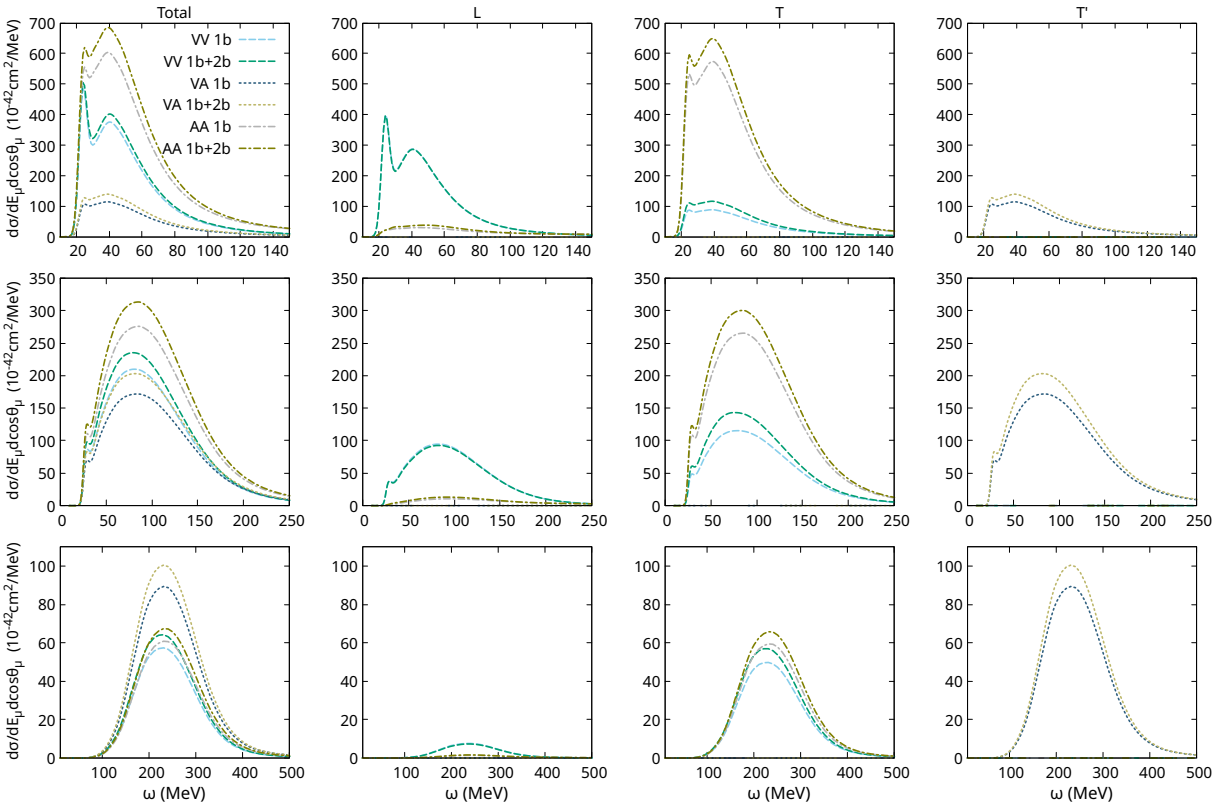

Figure 6.4: Charged-current inclusive cross sections for neutrino scattering off ^{12}C at beam energy 750 MeV and scattering angle 15 deg (top), 30 deg (middle) and 60 deg (bottom) separated in terms of vector (VV), vector-axial (VA) and axial (AA) components of the responses. We show our 1b and 1b+2b ED-RMF results for, from left to right, cross section (total), and its longitudinal (L) and transverse (T and T') contributions.

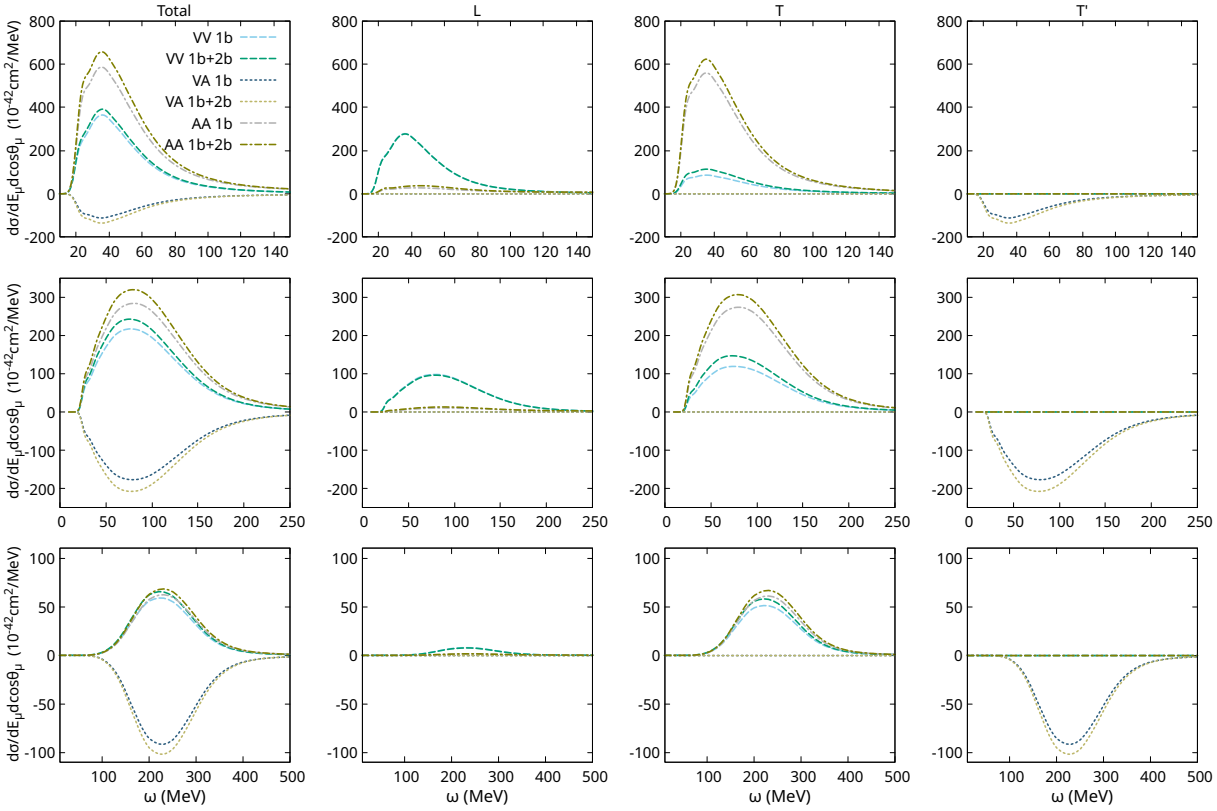

Figure 6.5: Charged-current inclusive cross sections for antineutrino scattering off ^{12}C at beam energy 750 MeV and scattering angle 15 deg (top), 30 deg (middle) and 60 deg (bottom) separated in terms of vector (VV), vector-axial (VA) and axial (AA) components of the responses. We show our 1b and 1b+2b ED-RMF results for, from left to right, cross section (total), and its longitudinal (L) and transverse (T and T') contributions.

6.2 T2K

Quasielastic scattering represents the dominant contribution to the cross section in the energy regime of T2K, shown in Fig. 6.6, making experimental measurements from this collaboration particularly relevant for validation purposes. Additionally, the near detector ND280 includes hydrocarbon and water targets, allowing us to test our model across different nuclei. Thus, in this section, we compare our theoretical predictions to T2K experimental data for CC0π and CC inclusive (anti)neutrino scattering on ^{12}C and ^{16}O. As mentioned above, CC0π scattering refers to interactions where no pions are detected in the final state, while the number of outgoing nucleons remains unrestricted. Therefore, pion absorption, as well as multi-nucleon excitations—primarily driven by 2p-2h contributions—also play a role in the measured cross sections, leading to a strength that is not accounted for in our approach.

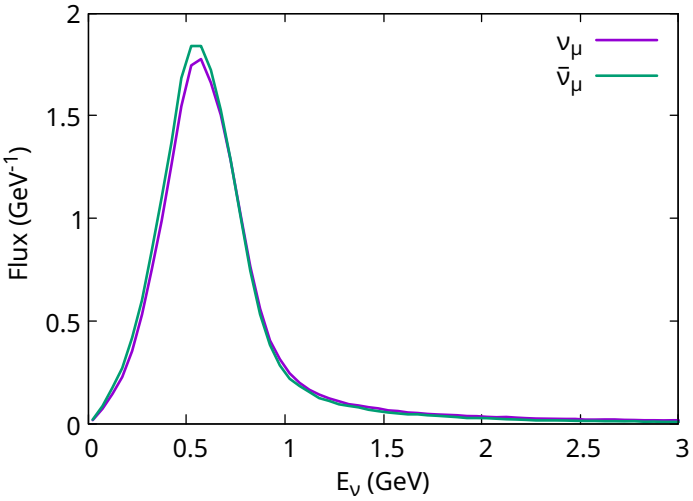

Figure 6.6: Normalized ν_μ and $\bar{\nu}_\mu$ fluxes of T2K.

6.2.1 ν_μ reactions

In Figs. 6.7, 6.8 and 6.9, we present our results for the flux-averaged double differential muon neutrino scattering cross section on hydrocarbon, while Figs. 6.10 and 6.11 show the corresponding results on water. Cross sections are plotted against the muon momentum, and each panel corresponds to a certain bin in the scattering angle. The theoretical predictions are compared to experimental measurements without pions in the final state from T2K [164; 166; 167]. Ref. [164] includes two datasets for the cross section on hydrocarbon obtained through different analyses,

labelled I and II, both of which are considered equally valid and mutually consistent. Meanwhile, Ref. [166] reports the first measurement on water. Finally, in Ref. [167], cross sections on hydrocarbon and water have been simultaneously extracted. Measuring interactions on these two nuclear targets at the same time provides a better understanding of their differences and serves to complement, validate and improve the previous data obtained separately for each nucleus. This approach also allows for a consistent treatment of correlations, as scattering on carbon constitutes the main background for oxygen measurements. Therefore, given that interactions with both nuclei are governed by the same underlying physics, assuming that carbon reactions are known in order to extract those on oxygen would lead to inconsistencies. A joint extraction is thus the most reliable method to disentangle the oxygen contribution from that of carbon. It is worth noting that, although this measurement additionally permits the calculation of the cross section ratio, which provides a way to validate the models' ability to extrapolate between carbon and oxygen nuclear targets, the differences between these nuclei are so small, and the uncertainties so large, that the data have very limited constraining power. Therefore, this comparison is not included in the present work.

In general, experimental measurements are well reproduced by our theoretical predictions. Due to the large uncertainties shown by the data, both one-body results and those including two-body contributions are in accordance with the experiment in several kinematic regions. However, the data seem to prefer the incorporation of two-body meson-exchange currents, leading to an increase in strength that improves the agreement with data when the one-body calculation underestimates it, while never causing an overestimation. As the cross section is averaged over the neutrino flux, the contribution from two-body currents remains approximately constant across all $\cos\theta_\mu$ bins, leading to an increase by up to 12%. Of particular interest is the behavior observed at the most forward angles. While in other cases the cross section significantly decreases as the muon momentum increases, at small scattering angles it remains stabilized at non-zero values. This effect arises due to the high-energy tail of the T2K neutrino flux (see Fig. 1.3). As a final point, the results present little room for the contribution from higher-energy reaction mechanisms. In Ref. [170; 171], the 2p-2h contribution has been computed within the SuSAv2 model, obtaining a relative small effect, which supports the agreement of our 1p-1h results with data. This is attributed to the shape of the T2K neutrino flux, with a narrow distribution around a peak energy of 0.6 GeV, significantly reducing the contribution from the energy regime where this reaction channel appears.

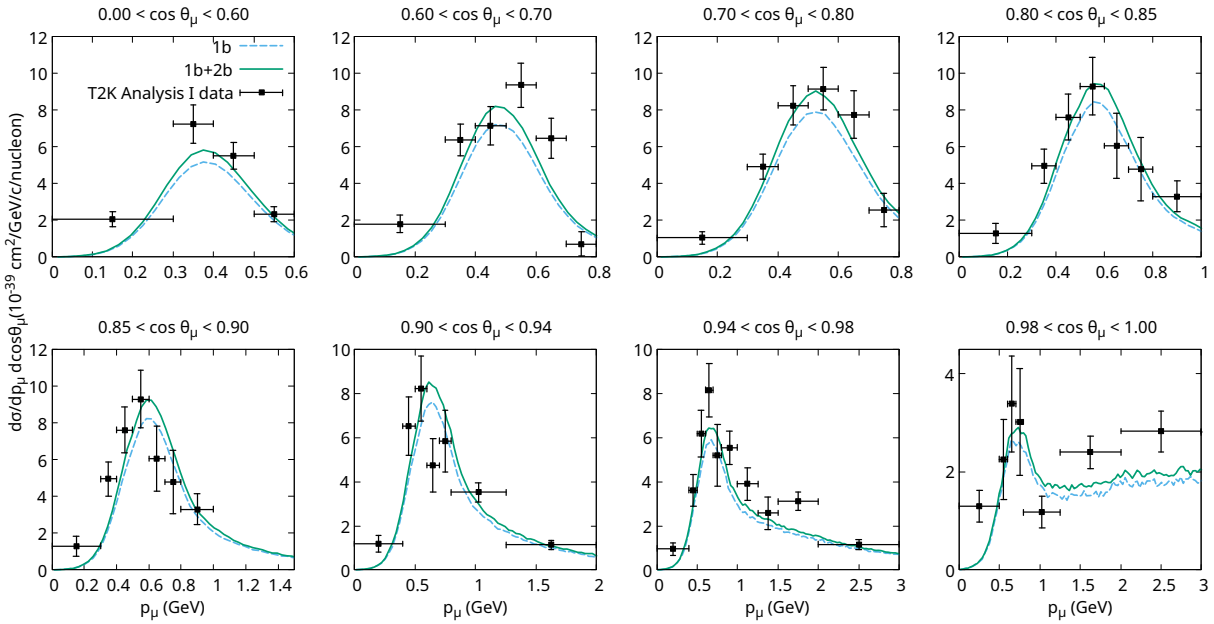

Figure 6.7: T2K flux-folded double-differential cross sections per nucleon for ν_μ-CC0π scattering on hydrocarbon displayed as a function of the muon momentum p_μ for different bins of $\cos\theta_\mu$. Theoretical predictions are compared with experimental data from the Analysis I of Ref. [164].

To conclude, Fig. 6.12 shows a comparison of our theoretical predictions with measurements of muon neutrino charged-current inclusive cross sections on hydrocarbon from T2K [165]. In contrast to the previous datasets, the experimental signature now consists in one charged lepton and any number of nucleons and pions in the final state. Therefore, as expected, our predictions underestimate the data, requiring the addition of pion production processes to correctly describe it [170; 172; 173].

6.2.2 ν_μ and $\overline{\nu}_\mu$ combined reactions

In Figs. 6.13-6.17, we compare our theoretical predictions with the T2K results from Ref. [17] for the combined measurement of muon neutrino and antineutrino charged-current cross sections on hydrocarbon without pions in the final state. These data were obtained using neutrino and antineutrino beams, both centered at the same energy peak, and their combination allows for a robust antineutrino cross section measurement, effectively accounting for the relatively large background of neutrino interactions in the antineutrino sample. Furthermore, the correlation between the datasets can be exploited to further improve the accuracy of the results. In addition to the individual cross sections, their sum, difference and asymmetry are computed to

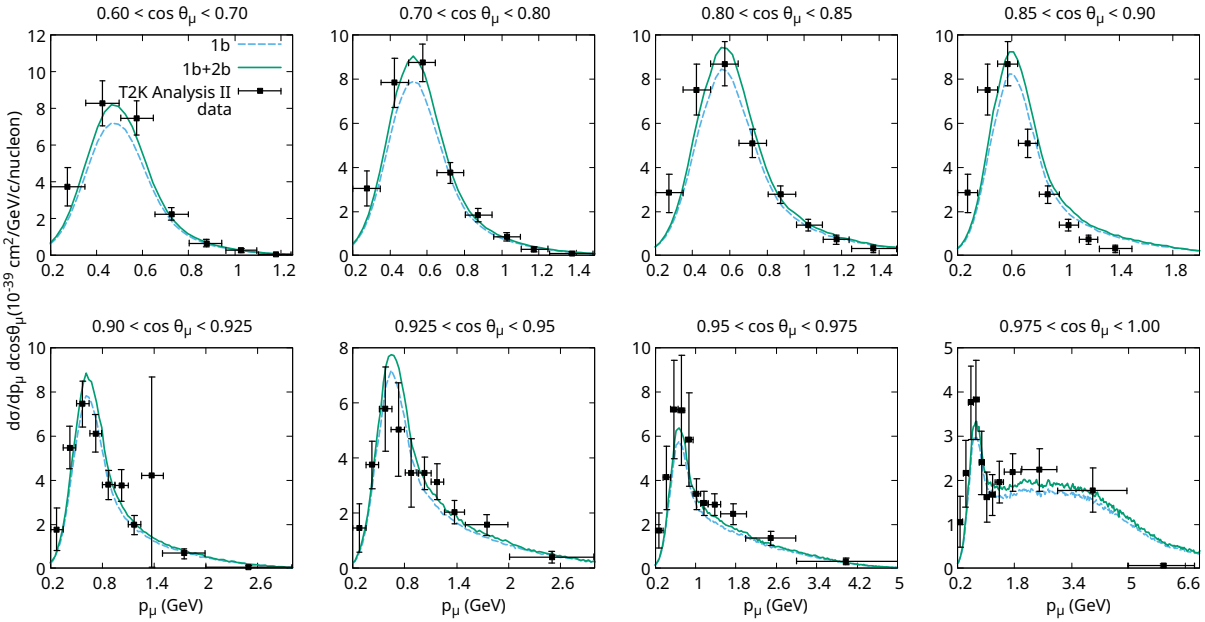

Figure 6.8: T2K flux-folded double-differential cross sections per nucleon for ν_μ-CC0π scattering on hydrocarbon displayed as a function of the muon momentum p_μ for different bins of $\cos\theta_\mu$. Theoretical predictions are compared with experimental data from the Analysis II of Ref. [164].

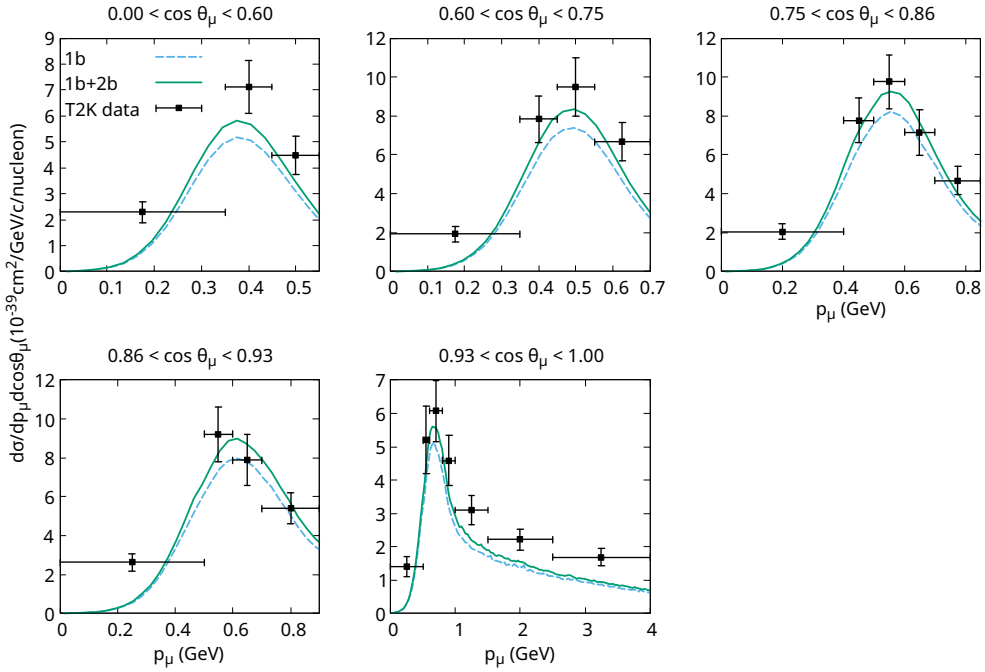

Figure 6.9: T2K flux-folded double-differential cross sections per nucleon for ν_μ-CC0π scattering on hydrocarbon displayed as a function of the muon momentum p_μ for different bins of $\cos\theta_\mu$. Theoretical predictions are compared with experimental data from Ref. [167].

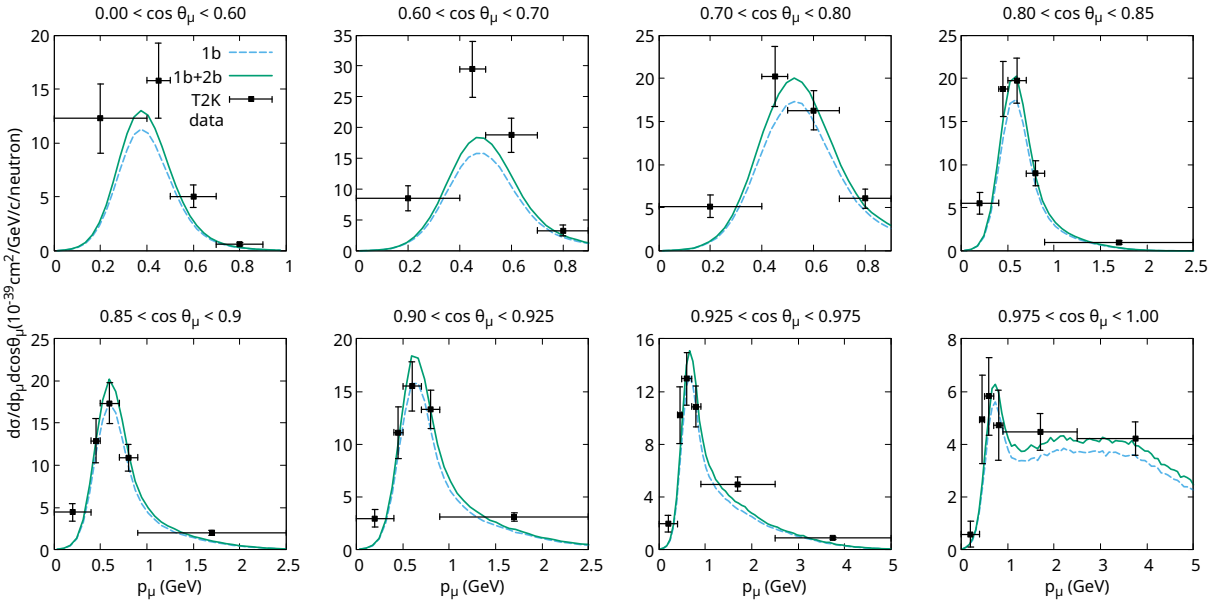

Figure 6.10: T2K flux-folded double-differential cross sections per neutron for ν_μ-CC0π scattering on water displayed as a function of the muon momentum p_μ for different bins of $\cos\theta_\mu$. Theoretical predictions are compared with experimental data from Ref. [166].

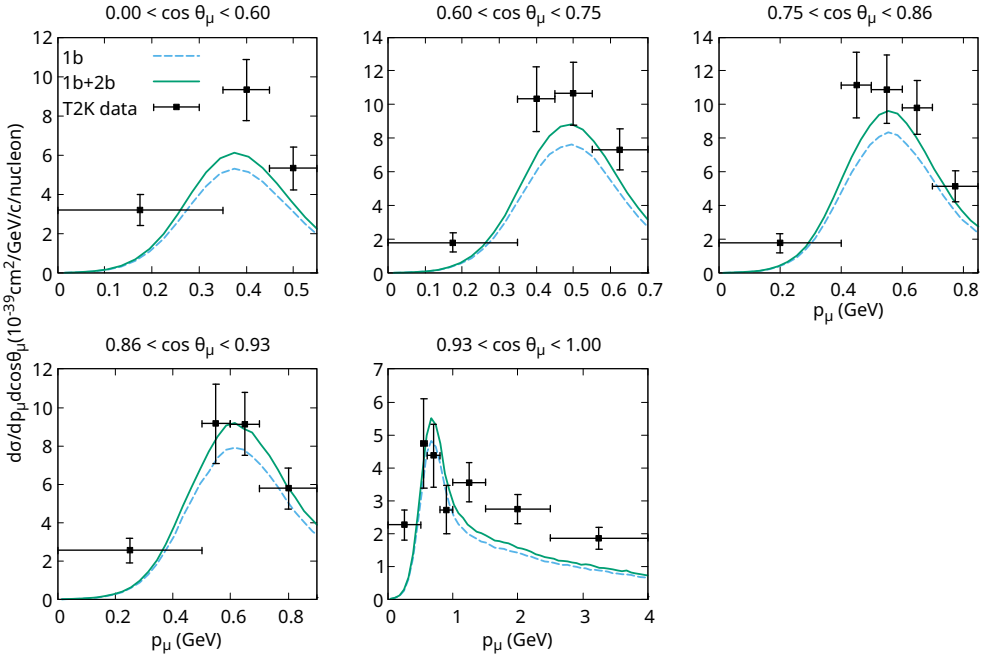

Figure 6.11: T2K flux-folded double-differential cross sections per nucleon for ν_μ-CC0π scattering on water displayed as a function of the muon momentum p_μ for different bins of $\cos\theta_\mu$. Theoretical predictions are compared with experimental data from Ref. [167].

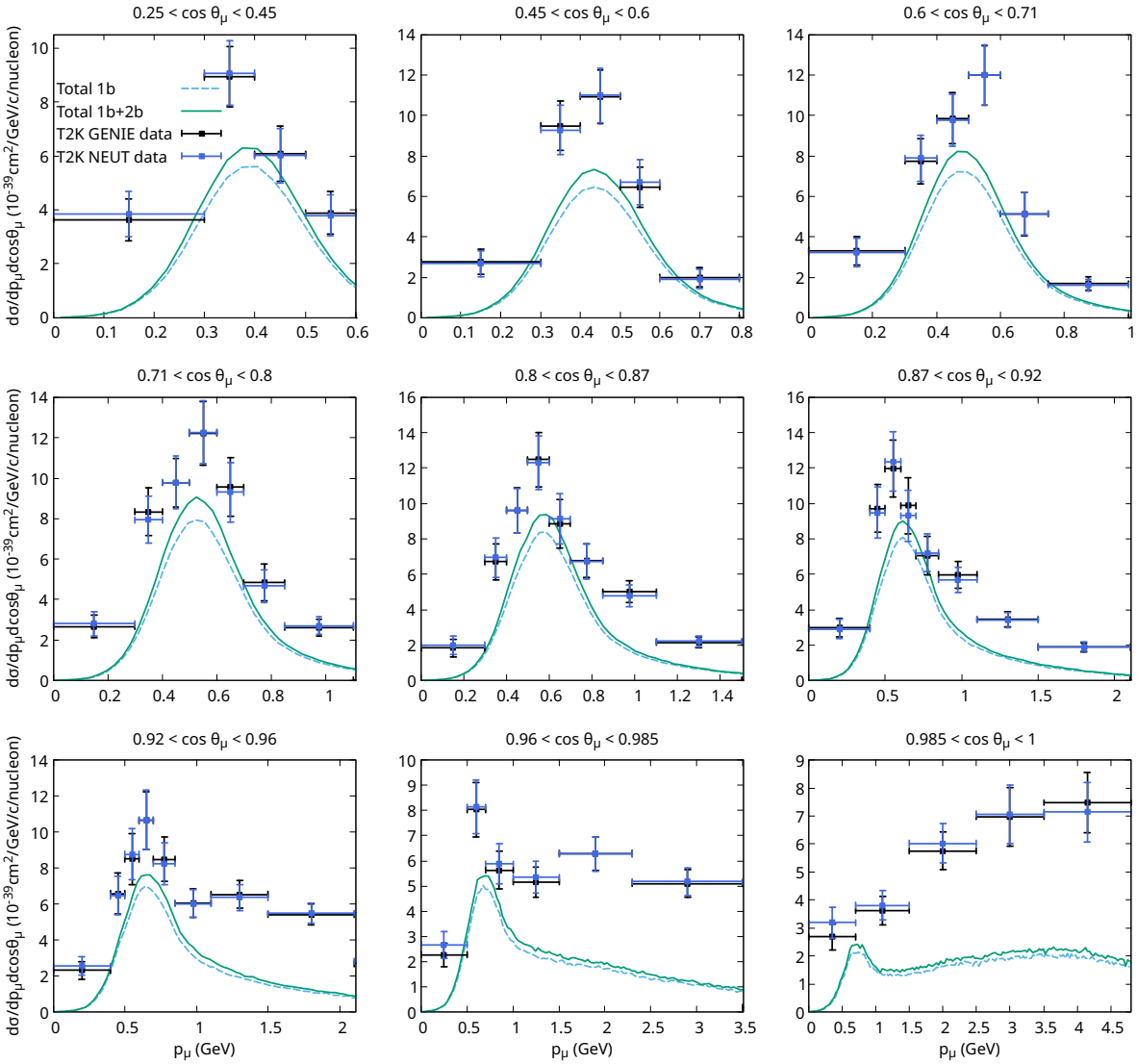

Figure 6.12: T2K flux-folded double-differential cross sections per nucleon for ν_μ-CC inclusive scattering on ^{12}C displayed as a function of the muon momentum p_μ for different bins of $\cos\theta_\mu$. Theoretical predictions are compared with experimental data from Ref. [165].

obtain a better understanding of the nuclear effects involved in charged-current interactions. The neutrino-antineutrino cross section asymmetry is computed as the ratio of the difference to the sum. This quantity results particularly relevant in the search for CP violation in neutrino oscillations, as most uncertainties and nuclear medium effects cancel out.

The comparison with the neutrino data leads to the same conclusions as in the previous subsection, showing good agreement between our predictions and the experimental measurements, which is improved when the contribution from two-body currents is included. The antineutrino results, in addition to the scattering cross section on ^{12}C, now also include the interaction on the hydrogen of the hydrocarbon molecule. This reaction is modeled as the interaction of the antineutrino with a free proton and, therefore, only occur through one-body currents. The results show a much smaller increase from two-body currents compared to the neutrino case, as the opposite sign in the T' term removes strength rather than adding it. In the same way, the 2p–2h contribution is expected to be less significant for antineutrinos than for neutrinos. This further supports the agreement with the data, which is already well reproduced without requiring a sizable 2p–2h component.

In a purely theoretical framework, and neglecting the small isospin differences between nucleons, the flux-folded double differential cross section of Eq. 6.1, hereafter denoted by $\langle\sigma\rangle$, can be expressed as $\langle\sigma_\nu\rangle = \langle\sigma_{VV+AA}\rangle + \langle\sigma_{VA}\rangle$ and $\langle\sigma_{\bar{\nu}}\rangle = \langle\sigma_{VV+AA}\rangle - \langle\sigma_{VA}\rangle$. Then, the sum and difference of neutrino and antineutrino flux-folded cross sections reads

$$\begin{aligned}\langle\sigma_\nu\rangle + \langle\sigma_{\bar{\nu}}\rangle &= \int dE_\nu \phi_\nu(E_\nu)\sigma_\nu(E_\nu) + \int dE_{\bar{\nu}} \phi_{\bar{\nu}}(E_{\bar{\nu}})\sigma_{\bar{\nu}}(E_{\bar{\nu}}) \\ &= \int dE[(\phi_\nu + \phi_{\bar{\nu}})\sigma_{VV+AA} + (\phi_\nu - \phi_{\bar{\nu}})\sigma_{VA}] \end{aligned} \tag{6.2}$$

and

$$\begin{aligned}\langle\sigma_\nu\rangle - \langle\sigma_{\bar{\nu}}\rangle &= \int dE_\nu \phi_\nu(E_\nu)\sigma_\nu(E_\nu) - \int dE_{\bar{\nu}} \phi_{\bar{\nu}}(E_{\bar{\nu}})\sigma_{\bar{\nu}}(E_{\bar{\nu}}) \\ &= \int dE[(\phi_\nu - \phi_{\bar{\nu}})\sigma_{VV+AA} + (\phi_\nu + \phi_{\bar{\nu}})\sigma_{VA}]. \end{aligned} \tag{6.3}$$

As a result, given the T2K neutrino and antineutrino fluxes, which have very similar shapes, the sum of neutrino and antineutrino cross sections mostly eliminates the vector-axial interference term, whereas the difference isolates it. This allows us to have a deeper insight into the two-body contributions, as the increase they produce is no longer canceled out in any case. We note that some bins exhibit a negative cross section difference. This is due to the additional

antineutrino interaction with hydrogen, which lead to a higher antineutrino cross section than that of neutrinos.

For the sum, our results show a good agreement with the experimental measurements when two-body contributions are included, leaving small but enough room for the 2p-2h contribution. Meanwhile, the results for the difference are less conclusive, specially at forward angles where the experimental data present significant uncertainties and dispersion. Additionally, the various 2p-2h models considered in [17] have quite different predictions for the vector-axial component, making it difficult to determine the impact of this contribution on the final result.

Lastly, in [17], it has been observed that the neutrino-antineutrino cross-section asymmetry shows little dependence on the 2p-2h contribution, except in the low-momentum region and at forward angles. This makes it an interesting observable to compare with our purely 1p-1h predictions. Although our theoretical results seem to reproduce the experimental data, the latter are quite scattered and subject to large uncertainties, making it difficult to draw definite conclusions or determine whether the two-body contribution plays a significant role.

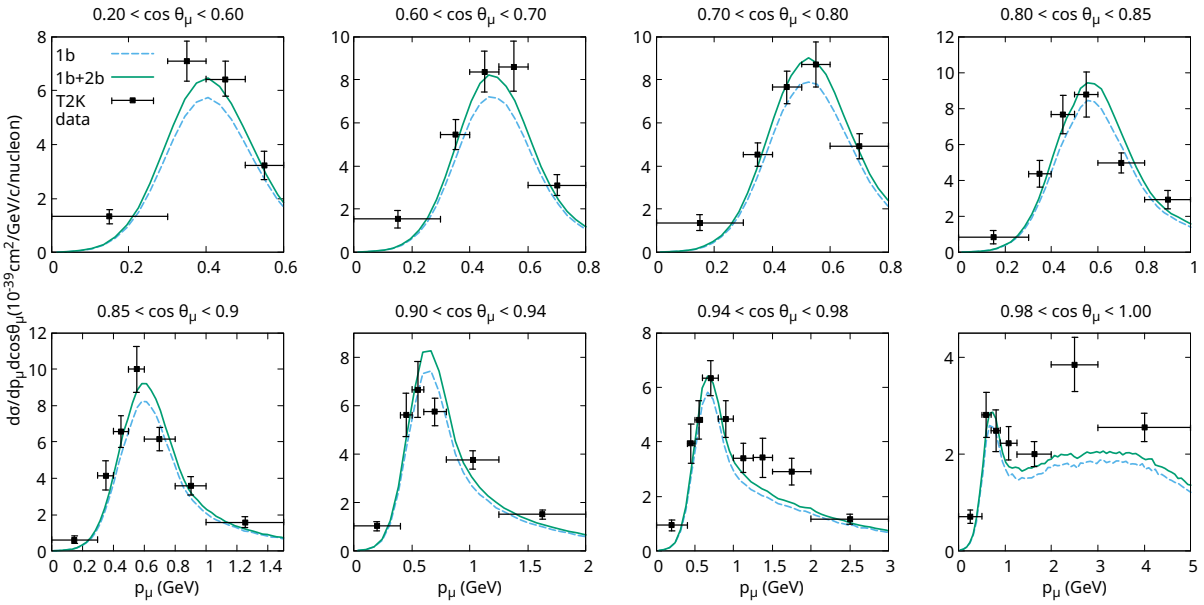

Figure 6.13: T2K flux-folded double-differential cross sections per nucleon for ν_μ-CC0π inclusive scattering on hydrocarbon displayed as a function of the muon momentum p_μ for different bins of $\cos\theta_\mu$. Theoretical predictions are compared with experimental data from Ref. [17].

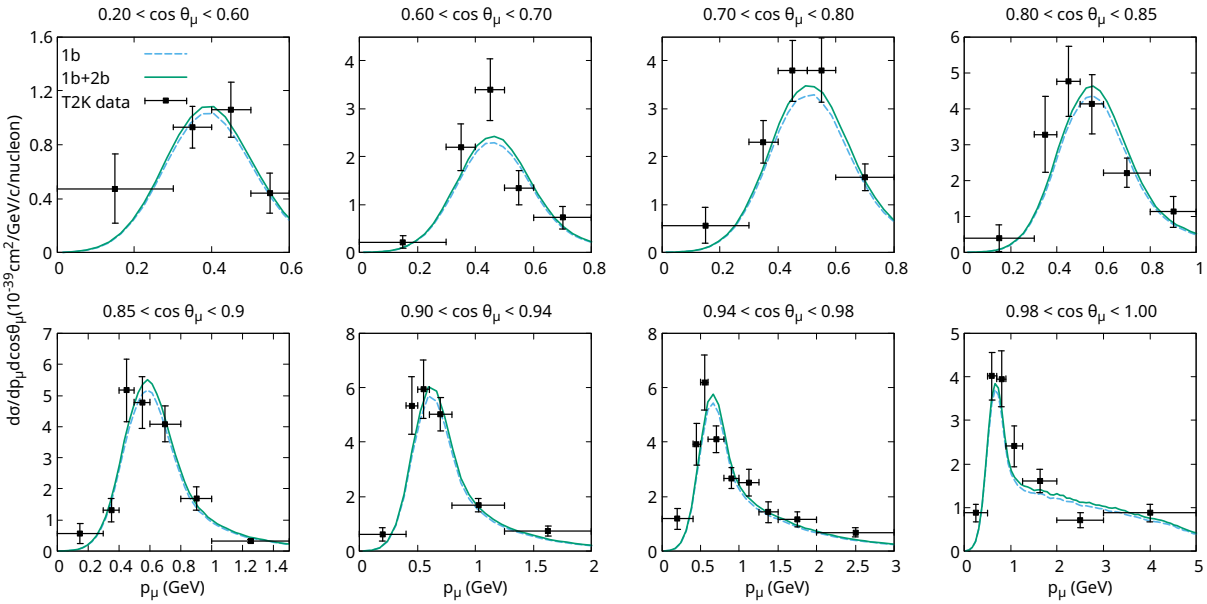

Figure 6.14: T2K flux-folded double-differential cross sections per nucleon for $\bar{\nu}_\mu$-CC0π inclusive scattering on hydrocarbon displayed as a function of the muon momentum p_μ for different bins of $\cos\theta_\mu$. Theoretical predictions are compared with experimental data from Ref. [17].

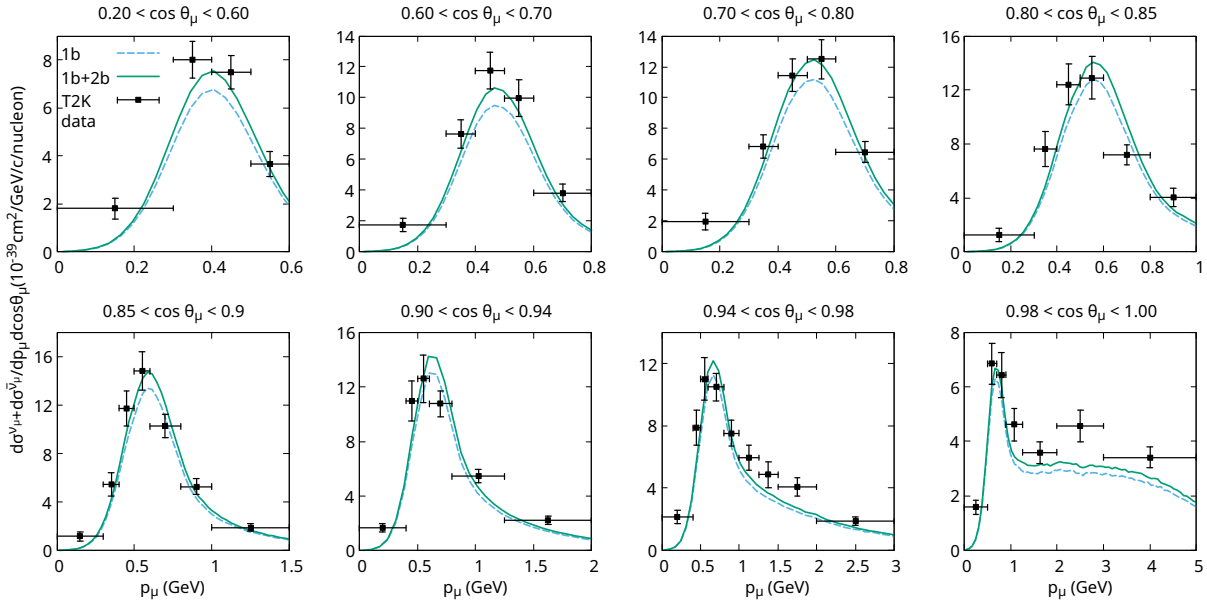

Figure 6.15: Sum of T2K flux-folded double-differential cross sections per nucleon for $\nu_\mu+\bar{\nu}_\mu$-CC0π inclusive scattering on hydrocarbon displayed as a function of the muon momentum p_μ for different bins of $\cos\theta_\mu$. Theoretical predictions are compared with experimental data from Ref. [17].

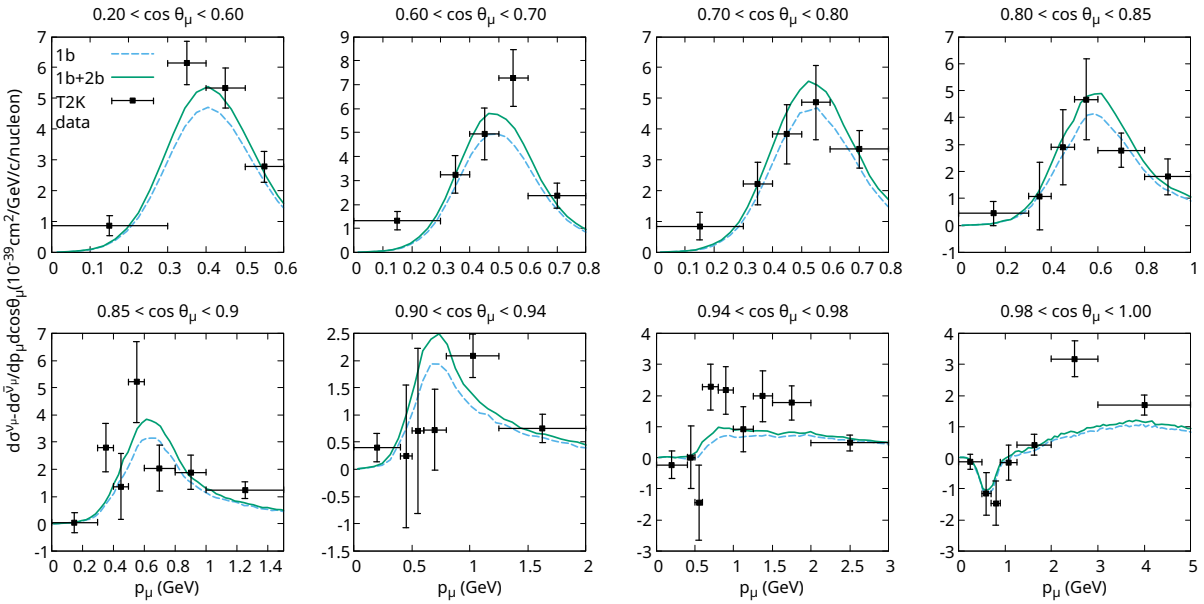

Figure 6.16: Difference of T2K flux-folded double-differential cross sections per nucleon for $\nu_\mu - \bar{\nu}_\mu$-CC0π inclusive scattering on hydrocarbon displayed as a function of the muon momentum p_μ for different bins of $\cos\theta_\mu$. Theoretical predictions are compared with experimental data from Ref. [17].

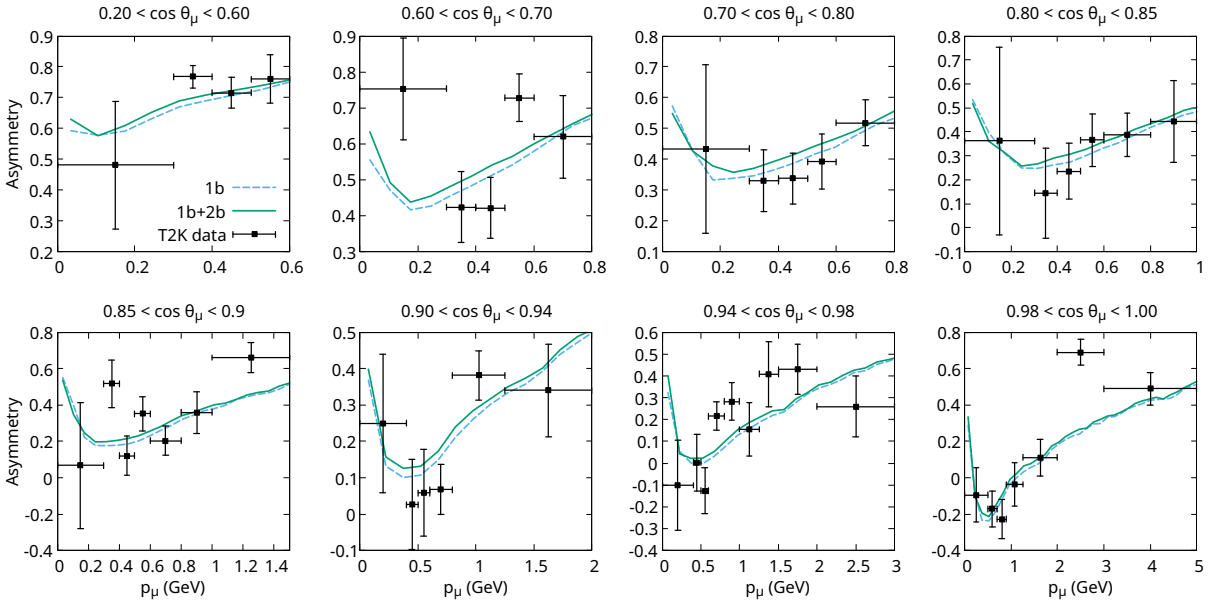

Figure 6.17: Asymmetry of T2K flux-folded double-differential cross sections for CC0π inclusive scattering on hydrocarbon displayed as a function of the muon momentum p_μ for different bins of $\cos\theta_\mu$. Theoretical predictions are compared with experimental data from Ref. [17].

6.3 MiniBooNE

Neutrino and antineutrino fluxes in MiniBooNE experiment peak at 0.788 GeV and 0.665 GeV, respectively, extending from 0 up to approximately 7 GeV, with the most significant contributions concentrated below 3 GeV (see Fig. 6.18). Within this energy range, quasielastic scattering represents the dominant contribution to the cross section. Therefore, we now compare our theoretical predictions with the muon neutrino and antineutrino CCQE-like and CCQE cross section measurements on hydrocarbon from the MiniBooNE collaboration [168; 169]. CCQE-like events correspond to the CC0π experimental signature, being defined as those processes containing no pions in the final state. Meanwhile, CCQE observables are obtained by subtracting the background contribution from pions created at the interaction vertex and subsequently reabsorbed in the nuclear medium. Although this background is partially constrained by their own measurements [34], its extraction from the experimental signal introduces a degree of model dependence in the resulting data. Moreover, discrepancies have been identified between the MiniBooNE π^+ production data and the corresponding results reported by T2K [36] and MINERνA [174], [175]. Thus, to better assess the uncertainties related to this procedure, both CCQE and CCQE-like datasets are included in our comparisons. Additionally, in both cases, due to the lack of experimental sensitivity to the outgoing hadrons in the final state, multi-nucleon excitations are inseparable from the experimental measurements. Even though these contributions are not CCQE, they should also be taken into account for a proper interpretation of the data.

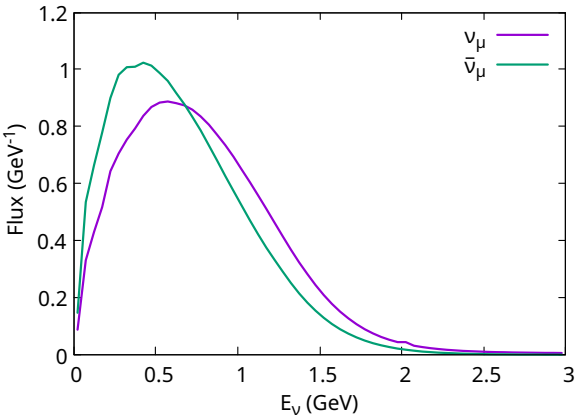

Figure 6.18: Normalized ν_μ and $\bar{\nu}_\mu$ fluxes of MiniBooNE.

6.3.1 ν_μ and $\overline{\nu}_\mu$ reactions

Figs. 6.19 and 6.20 show our theoretical predictions for the flux-averaged double differential muon neutrino and antineutrino scattering cross section on hydrocarbon. The results are plotted against the kinetic energy of the final muon, and each panel corresponds to a certain bin in the scattering angle. The experimental data correspond to the CCQE and CCQE-like measurements from MiniBooNE [168; 169], where the CCQE-like data are constructed by adding the reported background to the CCQE cross section. Antineutrino scattering data on ^{12}C have been also obtained in [169] by subtracting the hydrogen component, which stems from scattering on a quasifree proton. However, we do not include a comparison with these data, as the subtraction procedure used to isolate the ^{12}C component introduces additional model dependence into the results. Finally, one should keep in mind that the MiniBooNE collaboration reports a normalization error which is not taken into account in the error bars.

Our theoretical predictions provide a good description of the neutrino experimental data at forward scattering angles. This agreement is improved by including the two-body current contribution, which produces a sizable increase. Moving toward more backward angles, the calculations tend to saturate the data at low T_μ, while underestimating it at higher values. Similar observations have been pointed out in [145; 43; 176]. This underestimation can be partially solved by including the 2p–2h contribution, although it would introduce an overall increase across the entire T_μ range, leading to an overestimation where the calculations already match the data. In contrast with the analysis of the T2K experiment, the relative impact of the 2p–2h mechanism is expected to be more significant here, given the broader distribution of the MiniBooNE flux with a substantial contribution up to 3 GeV. In particular, within the SuSAv2 model [170], the 2p–2h contribution enhances the neutrino and antineutrino cross sections up to 25–35% compared to the pure quasielastic prediction.

On the other hand, the antineutrino data tend to be systematically larger than our predictions, except for the high T_μ tail at backward scattering angles, which is well reproduced in this case. Now, the agreement with data is not improved when two-body currents are included, having a significantly smaller effect compared to the neutrino case, in line with the trend observed in previous calculations. Meanwhile, it can be expected that this improvement would come from the contribution of 2p–2h mechanisms.

Overall, these results contrast with the generally good agreement obtained with T2K data. However, uncertainties in the MiniBooNE analysis limit the ability to extract firm conclusions from the comparison with theoretical predictions. The model dependent background subtraction

method adopted makes comparison with CCQE data difficult whereas, in the CCQE-like case, the comparison is hampered by the lack of 2p-2h and pion absorption contributions in our predictions. Additionally, it is worth noting that the estimated uncertainties in MiniBooNE data did not account for full correlation information, and unresolved tensions with other experiments still persist. Nevertheless, given the high quality of these data, a reanalysis of the events using more modern approaches would be highly valuable [175].

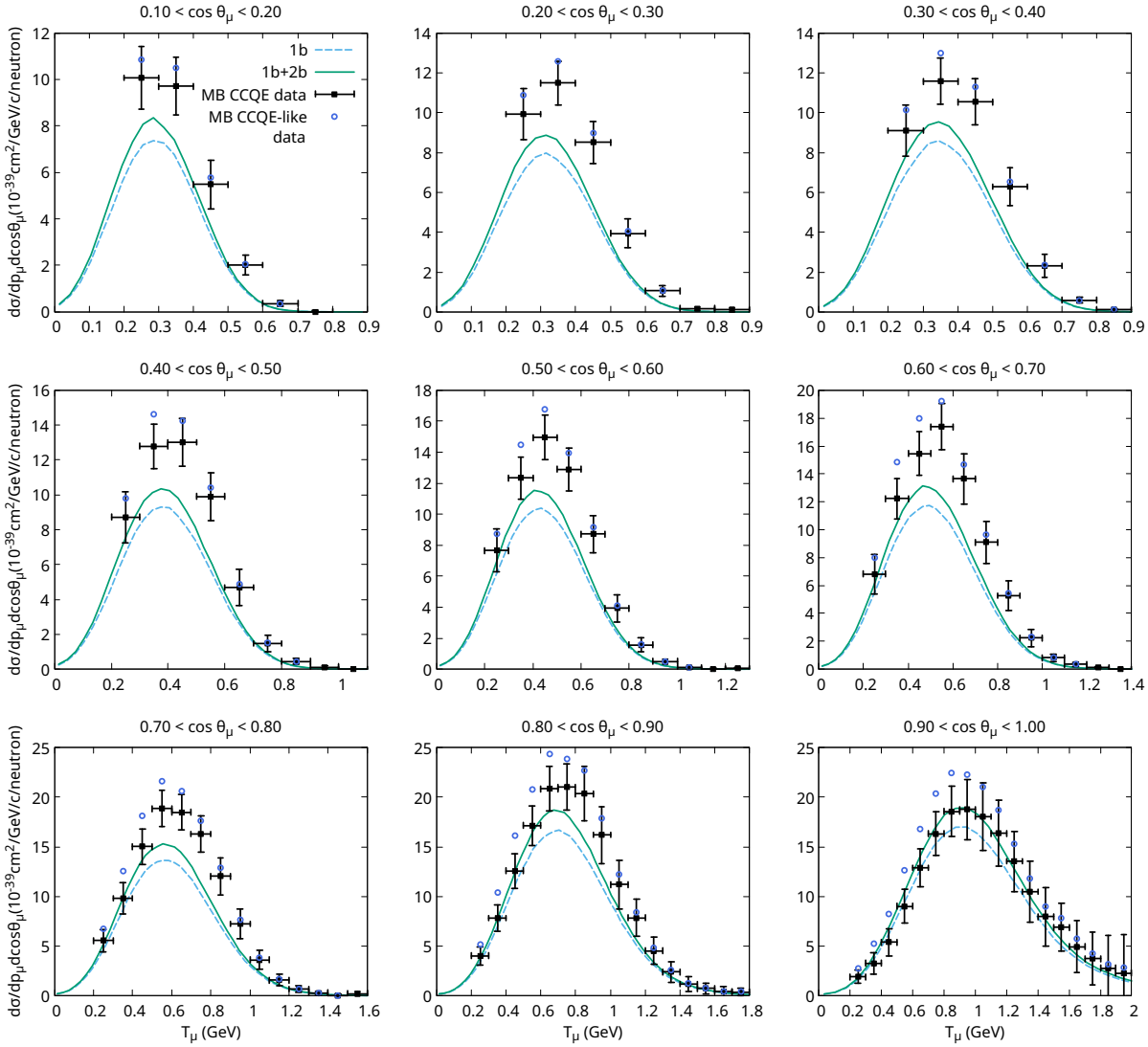

Figure 6.19: MiniBooNE flux-folded double-differential cross sections per neutron for ν_μ-CCQE inclusive scattering on hydrocarbon displayed as a function of the muon kinetic energy T_μ for different bins of $\cos\theta_\mu$. Theoretical predictions are compared with CCQE and CCQE-like experimental data from Ref. [168], where the latter have been obtained by adding the reported background.

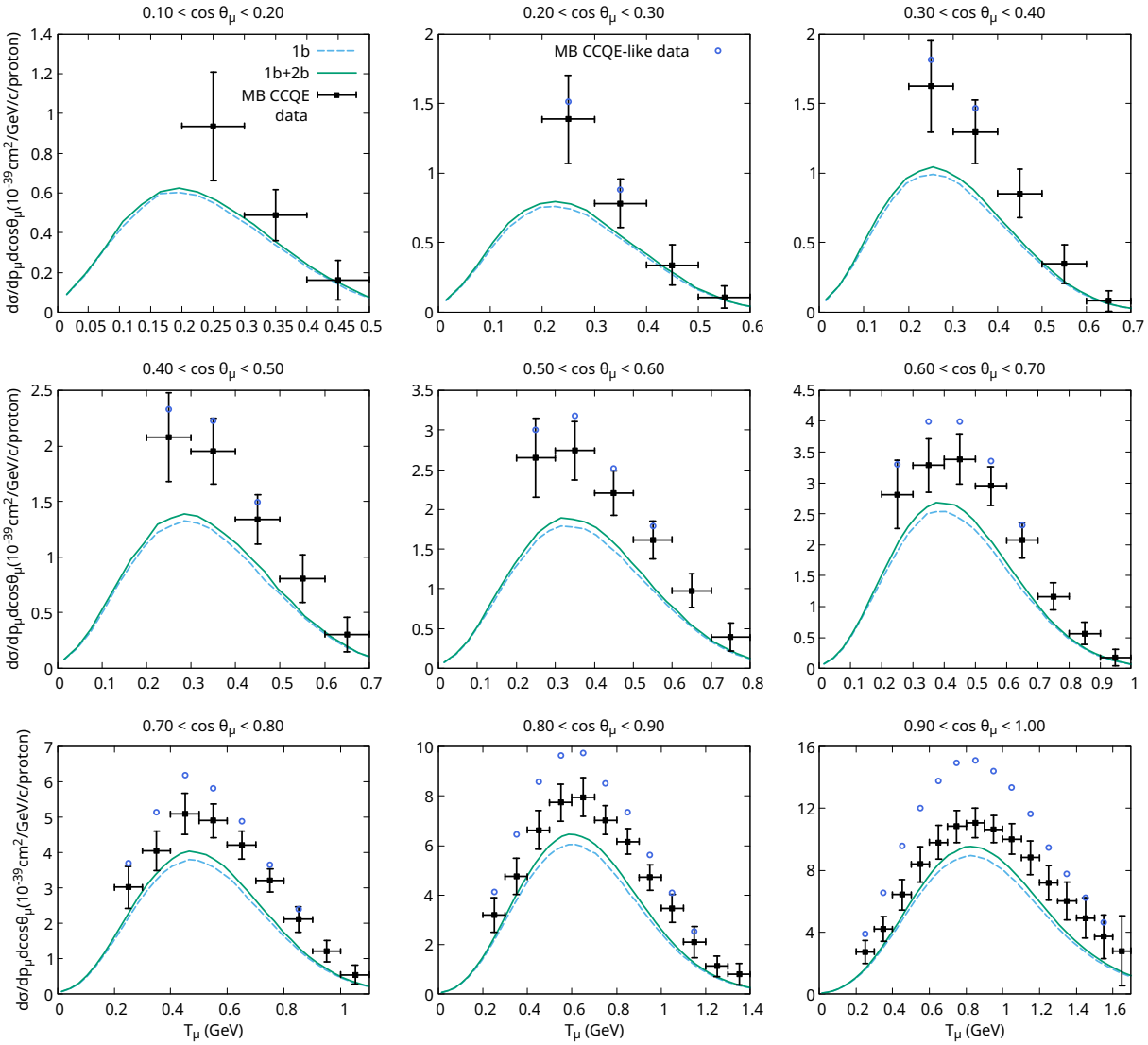

Figure 6.20: MiniBooNE flux-folded double-differential cross sections per proton for $\bar{\nu}_\mu$-CCQE inclusive scattering on hydrocarbon displayed as a function of the muon kinetic energy T_μ for different bins of $\cos\theta_\mu$. Theoretical predictions are compared with CCQE and CCQE-like experimental data from Ref. [169], where the latter have been obtained by adding the reported background.

Chapter 7

Conclusions

The precise measurement of neutrino properties is nowadays one of the highest priorities in fundamental particle physics. It has been firmly established that neutrinos oscillate and hence are massive particles. However, absolute neutrino masses, the neutrino mass hierarchy and the nature of the neutrino mass are still open questions in physics. Additionally, neutrinos open the door to investigate new physics, as the determination of charge-parity violation in the leptonic sector. Current experimental efforts focus on accelerator-based neutrino oscillation experiments, with large collaborations all over the globe. As neutrinos only interact weakly, the detection of these particles relies on their interaction with nuclear targets. Therefore, accurate oscillation analyses require a precise knowledge of the complexities of neutrino-nucleus interactions. Understanding the hadronic and nuclear physics of these interactions constitutes a challenging source of uncertainty, being one of the limiting systematic errors in neutrino oscillation physics. In the coming decades, next-generation experiments will accumulate an unprecedented number of neutrino events, shifting the main limitation from statistical to systematic uncertainties. Improving the theoretical description of neutrino–nucleus cross sections will therefore be essential for the success of neutrino oscillation experiments.

In the energy regime of accelerator-based experiments, the neutrino-nucleus interaction is driven by several reaction mechanisms. Our focus is placed on the quasielastic (QE) region, which represents a significant contribution in both current and future neutrino oscillation experiments. Several models have been proposed to study this process. In this thesis, we present a fully relativistic and quantum mechanical framework based on the relativistic mean-field (RMF) solutions. The ground state nucleus consists of single-particle orbitals with fixed energy and angular momentum, where the initial state is described by an unfactorized representation of the

spectral function based on single-particle solutions of the RMF. This approach allows to include effects beyond the mean-field approximation, like the depletion of the occupation of the shell model states and the appearance of nucleons at higher missing energies due to nucleon-nucleon correlations. Final-state interactions (FSI) between the outgoing nucleon and the residual nucleus are included within the relativistic distorted wave impulse approximation, with the final nucleon being described by a solution of the Dirac equation in the continuous with the energy-dependent relativistic mean-field (ED-RMF) potential [97; 98; 96]. This potential is constructed as the RMF potential used in the bound state but multiplied by a phenomenological function that weakens the scalar and vector potentials for increasing nucleon momenta. The main advantage of this choice is that it preserves orthogonality and consistency between the initial and final states at low energies of the final nucleon, while approaching the behavior of the phenomenological optical potentials at larger energies. The sensitivity of the calculations with the description of the knocked-out nucleon has been addressed by considering the relativistic plane wave impulse approximation (RPWIA), where FSI are neglected, and other choices for the potential, in particular, RMF and a relativistic optical potential. We observe that accurately accounting for nucleon distortion while maintaining orthogonality between initial and final states is essential to correctly reproduce the experimental data.

The key contribution of this work is the incorporation of two-body meson-exchange currents with a final particle-hole state. We extend the usual treatment of QE scattering within the impulse approximation, based on a one-body current operator, and include the interaction between nucleons through one pion exchange by incorporating a two-body current operator. It includes the contribution from the Δ-resonance mechanism (electroweak excitation of the $\Delta(1232)$ resonance and its subsequent decay into $N\pi$) and the background contributions deduced from the chiral perturbation theory (ChPT) Lagrangian of the pion-nucleon system [177]. Particle–hole excitations through two-body meson-exchange currents involve an intermediate bound-nucleon state, for which different modeling strategies have been explored. We begin by describing the intermediate nucleons as bound wave functions using the same RMF potential as that of the initial and final nucleons. The key point of this approach is that orthogonality is preserved between all particle states. However, computing the hadronic current involves the evaluation of a 9-dimensional integral with contributions from numerous diagrams, which demands extremely high computational time. To address this, we consider two possible approximations that reduce the complexity of the problem. First, the intermediate bound-nucleon state is approximated using free Dirac spinors in a Relativistic Fermi Gas. This simplification reduces the hadronic

current to a 6-dimensional integral with fewer contributing diagrams, thus significantly reducing the computational effort. However, this approach leads to the lost of consistency between the intermediate state and the initial and final ones, as well as the bound aspect of the nucleons. Then, to partially restore the bound character of the intermediate state, we have modified its energy and mass, accounting for the influence of the mean-field potential. When effective values for the intermediate nucleon energy and mass are introduced, the differences with respect to the full RMF treatment become significantly reduced. Therefore, this improved approximation has been employed in the calculations presented in this work.

Electron scattering provides a useful tool for validating nuclear models, with plenty of available experimental data with well-defined energies of the incident beam, unlike in the neutrino case where only flux distributions are known. For this reason, the comparison with electromagnetic data has been an essential step and the first one in our analysis. However, we stress that such a test is necessary but not sufficient to ensure the validity of a model, since only the vector part of the weak response can be tested through the electromagnetic response.

In this context, our relativistic mean-field based model, with one- and two-body current contributions, has been shown to be capable of simultaneously describing the inclusive longitudinal and transverse electromagnetic responses of ^{12}C in the quasielastic regime, and further the experimental cross sections. We find that the effect of two-body meson-exchange currents is only significant in the transverse channel, where the response is increased up to a 30%, while the longitudinal sector remains unaffected. The increase in the cross section depends on the relative contribution of the transverse response, which depends on the kinematics. The agreement with data is good in general and very good for R_L, for which isolation of the longitudinal contributions suppresses other processes not considered in the calculation, such as real pion production. Furthermore, the increase of the transverse component due to two-body meson-exchange currents is supported by carbon data on separated R_T response and cross sections.

The electromagnetic responses and cross sections have also been computed for ^{16}O, given the importance of this nucleus in current and future neutrino oscillation experiments. In this case, the available experimental data is significantly more limited, and to our knowledge, no Rosenbluth separation has been performed to extract longitudinal and transverse responses. Then, as a first step, our theoretical predictions for the nuclear responses have been compared with recent results from the Bayesian artificial neural network (BNN) [140] and coupled-cluster theory (LIT-CC) [141] approaches, showing good agreement despite the very different nature of these frameworks, which supports the consistency of our model. When comparing to cross section data, the scarcity

of measurements makes it difficult to draw clear conclusions. Our results show poor agreement with data for the very small energy kinematics, particularly in the position of the quasielastic peak, whereas at medium and higher energies the discrepancies vanish.

The computation of electromagnetic responses and cross sections concludes with the case of ^{40}Ca. For this nucleus, the results are presented as bands that account for the uncertainty associated with the modeling of the spectral function used to describe the initial state. In this case, the agreement of our model with the experimental R_L and R_T data is generally poor. Significant discrepancies exist between different experimental datasets. The interaction of the electron with the Coulomb field affects the Rosenbluth separation, causing a redistribution of the strength attributed to longitudinal and transverse responses and changing their shape [178; 179; 60]. This leads to considerable uncertainties in the extracted responses. Therefore, the study of the inclusive cross sections seemed to be more convenient in this case. For most of the kinematics studied, the data favor smaller shell occupations, with around $30 - 35\%$ of the nucleons contributing to the background. This makes clear the relevance of correlations that reduce the strength of the QE peak.

Motivated by the general good agreement with electron scattering experimental data, we extended our model to describe the analogous charged-current neutrino-induced scattering reaction. The complicating factor in neutrino experiments is the fact that the incoming neutrino energy is given by a broad distribution. Then, in order to compare theoretical predictions with experimental measurements, it is necessary to compute flux-folded cross sections.

We have started our study by computing inclusive cross sections for a fixed value of the initial (anti)neutrino energy and different scattering angles, allowing us to isolate and analyze the effect of two-body currents, without blurring the results due to the flux-folding in the neutrino energy. In all cases, the dominant contribution to the cross section comes from the T channel. Two-body meson-exchange currents lead to an increase in the magnitude of both T and T' responses, while the longitudinal contribution remains unchanged. The main difference between neutrino and antineutrino cross sections appears in the sign of the T' contribution, which adds up for neutrino scattering but reduces strength in the antineutrino case, almost canceling out the T component at high enough scattering angles. Therefore, the relative increase due to two-body currents is larger for neutrinos compared to antineutrinos as, for the latter, the enhancement of the T and T' responses has opposite signs, diminishing the overall effect. Additionally, the negative T' contribution for antineutrino reactions increases the relative importance of the longitudinal

channel, making it essential to correctly interpret antineutrino scattering at backward angles, even though its overall contribution is the smallest among the response functions.

Finally, our predictions for ^{12}C and ^{16}O flux-averaged inclusive cross sections are compared with T2K and MiniBooNE experimental datasets corresponding to charged-current interactions without pions in the final state. In general, T2K measurements for neutrino and antineutrino cross sections on hydrocarbon, as well as neutrino cross sections on water, are well reproduced by our theoretical predictions. Due to the large uncertainties shown by the data, both one-body results and those including two-body contributions are in accordance with the experiment in several kinematic regions. However, the data seem to prefer the incorporation of two-body meson-exchange currents, leading to an increase in strength that improves the agreement with the data when the one-body calculation underestimates it, while never causing an overestimation. Additionally, the sum, difference and asymmetry of neutrino and antineutrino cross sections on hydrocarbon have been also computed. Our results for the sum of cross sections show a good agreement with the experimental measurements when two-body contributions are included. Meanwhile, the results for the difference and asymmetry of cross sections are less conclusive, although our theoretical results seem to reproduce the experimental data, the latter are quite scattered and subject to large uncertainties, making it difficult to draw definite conclusions or determine whether the two-body contribution plays a significant role. Finally, we find discrepancies between our theoretical predictions and MiniBooNE experimental measurements for neutrino and antineutrino cross sections on hydrocarbon, which contrast with the generally good agreement obtained with T2K data. However, uncertainties in the MiniBooNE analysis limit the ability to extract firm conclusions.

Chapter 8

Outlook

We conclude this thesis by exploring potential applications of the results obtained and outlining directions for future research.

Beyond the inclusive processes studied in this work, where only the final-state lepton is detected, semi-inclusive experiments, in which an outgoing nucleon and lepton are detected in coincidence, are also of special interest for neutrino energy reconstruction [71]. An extension of the present model, describing the final nucleon using relativistic optical potentials that include both real and imaginary terms, has previously been applied to reproduce exclusive electron scattering $(e, e'p)$ data [60; 81; 180; 61; 181; 182]. The same approach can be employed in neutrino scattering processes corresponding to the experimental signature of having one proton detected and no other hadrons. Thus, the model provides a lower bound for semi-inclusive samples in which a lepton is detected in coincidence with (at least) one proton [183; 71; 72; 184].

An alternative strategy to address semi-inclusive predictions is the use of intranuclear cascade models, which are commonly employed in experimental analyses to simulate final-state interactions and predict the multiplicity and kinematics of outgoing hadrons. Neutrino event generators, such as NEUT [185], GENIE [186], ACHILLES [187] and NuWro [188], commonly treat the initial interaction at the vertex and the final-state propagation of the hadrons as discrete steps, assuming a temporal separation between them. In one-nucleon knock-out, for example, an outgoing nucleon with a given four-momentum is generated according to a model describing the primary interaction. In this context, RDWIA calculations with a real potential provide a realistic description by incorporating elastic FSI at the interaction vertex, and serve as the starting point for the cascade model. The outgoing nucleon is then introduced into the cascade, and propagated through the residual nucleus to model final-state interactions. The cascade redistributes

strength across various hadronic channels in the final state, such as multi-nucleon emission or pion production, by simulating further interactions within the nucleus. The result of this process is a complete prediction of the multiplicity of hadrons in the final state, including the kinematics of each particle. The cascade is implemented as a unitary process in the sense that it does not modify the inclusive cross section, i.e., after summation and integration over all final-state configurations resulting from the cascade, the inclusive cross section predicted by the primary interaction model is recovered. Therefore, it is important to start with a description of the primary vertex that already provides a good agreement with inclusive observables. To this end, the ED-RMF model employed in this work has already been implemented in the NEUT event generator [189]. Its predictions, based solely on one-body current interactions, yield a generally good agreement with T2K, MINERνA and MicroBooNE data. Work is currently ongoing to extend this approach by incorporating two-body meson-exchange current contributions. Importantly, events in which the nucleon exits the nucleus without interacting define an elastic channel whose cross section is expected to match that of RDWIA predictions employing a complex optical potential. This correspondence allows for benchmarking between the two frameworks [190; 191].

Lastly, extending this model to study isospin-asymmetric nuclei with partially filled shells would be particularly valuable, allowing its application to ^{40}Ar scattering, which is of great interest for the neutrino oscillation experiments MicroBooNE and DUNE.

Appendix A

Notation and conventions

This appendix summarizes the notation and conventions used through-out this work. We follow Bjorken and Drell convention (see Appendix A in [192]), which is the same as in Greiner and Reinhardt [46].

In this thesis, we use natural units, setting the reduced Planck constant and the speed of light equal to unity

$$\hbar = 1, \quad c = 1, \tag{A.1}$$

and, then, the transformation between energy and length is given by the factor $\hbar c = 197.33$ MeV fm. Under these conditions, the fine structure constant is expressed as

$$\alpha = \frac{e^2}{4\pi} = \frac{1}{137.04}, \tag{A.2}$$

where $e > 0$ denotes the electron charge.

Four-vectors and metric

Four-vectors are represented with capital letters, and sometimes, for clarity, with greek super- or sub-index, A^μ. Corresponding three-vectors are represented as $\mathbf{a}$, and their modules simply as a. Then,

$$A^\mu \equiv (a^0, a^1, a^2, a^3) \equiv (a^0, \mathbf{a}), \tag{A.3}$$

where a^0 is the time-like component and a^i, $i = 1, 2, 3$ are the spatial components, which form a vector in 3-dimensional space. In this way, the four-position in space-time of an event is denoted as

$$X^\mu = (t, \mathbf{x}), \tag{A.4}$$

and the four-momentum of a particle is

$$P^\mu = (E, \mathbf{p}), \tag{A.5}$$

which satisfies

$$P \cdot P = E^2 - \mathbf{p}^2 = M^2, \tag{A.6}$$

with M the invariant mass. As energy and momentum are separately conserved in interactions, the four-momentum is also a conserved quantity.

The metric tensor is given by

$$g_{\mu\nu} = \begin{pmatrix} 1 & 0 & 0 & 0 \\ 0 & -1 & 0 & 0 \\ 0 & 0 & -1 & 0 \\ 0 & 0 & 0 & -1 \end{pmatrix} = \begin{pmatrix} 1 & 0 \\ 0 & -\mathbb{1} \end{pmatrix}. \tag{A.7}$$

Four-vectors with an upper index are referred to as contravariant, while the corresponding four-vector with a lower index is referred to as covariant, and it is obtained as

$$A_\mu = g_{\mu\nu} A^\nu. \tag{A.8}$$

Thus, the scalar product of four-vectors is

$$A \cdot B = A_\mu B^\mu = g_{\mu\nu} A^\nu B^\mu = a^0 b^0 - a^1 b^1 - a^2 b^2 - a^3 b^3. \tag{A.9}$$

We define the Levi-Civita symbol $\epsilon^{\alpha\beta\gamma\delta}$, a totally antisymmetric tensor, with

$$\epsilon^{0123} = 1, \tag{A.10}$$

where if the indices $(\alpha\beta\gamma\delta)$ are an even permutation of (0,1,2,3) the sign is positive while for uneven permutations the sign is negative, the tensor is zero if any indices are repeated. Its covariant form is given by

$$\epsilon_{\alpha\beta\gamma\delta} = -\epsilon^{\alpha\beta\gamma\delta}. \tag{A.11}$$

Free Dirac equation

The Dirac equation for a free particle with rest mass M and spin 1/2 is

$$\left(i\gamma_\mu \frac{\partial}{\partial X^\mu} - M \right) \Psi(X) = 0, \tag{A.12}$$

where $\gamma^\mu = (\gamma^0, \gamma^1, \gamma^2, \gamma^3)$ are referred to as the Dirac matrices. These matrices satisfy the anticommutation relation

$$\{\gamma^\mu, \gamma^\nu\} = 2g^{\mu\nu} \tag{A.13}$$

and its conjugation is given by

$$(\gamma^0)^\dagger = \gamma^0\,, \tag{A.14}$$

$$(\gamma^k)^\dagger = -\gamma^k\,, \text{with } k = 1, 2, 3\,, \tag{A.15}$$

$$(\gamma^\mu)^\dagger = \gamma^0\gamma^\mu\gamma^0\,, \tag{A.16}$$

such that γ^0 is Hermitian while γ^i with $i \neq 0$ are anti-Hermitian.

As a standard representation of the Dirac matrices, we use the 4×4 matrices

$$\gamma^0 = \begin{pmatrix} \sigma_0 & 0 \\ 0 & -\sigma_0 \end{pmatrix}, \quad \gamma^i = \begin{pmatrix} 0 & \sigma_i \\ -\sigma_i & 0 \end{pmatrix} \quad (i \neq 0), \tag{A.17}$$

with σ the 2×2 Pauli matrices

$$\sigma^0 = \begin{pmatrix} 1 & 0 \\ 0 & 1 \end{pmatrix}, \quad \sigma^1 = \begin{pmatrix} 0 & 1 \\ 1 & 0 \end{pmatrix}, \quad \sigma^2 = \begin{pmatrix} 0 & -i \\ i & 0 \end{pmatrix}, \quad \sigma^3 = \begin{pmatrix} 1 & 0 \\ 0 & -1 \end{pmatrix}. \tag{A.18}$$

γ^μ matrices may be effectively treated as a four-vector, such as its scalar product with other four-vector is given by

$$\not{P} = P_\mu\gamma^\mu = p^0\gamma^0 - p^1\gamma^1 - p^2\gamma^2 - p^3\gamma^3, \tag{A.19}$$

where the Feynman slash notation has been introduced due to the common occurrence of such products.

In addition, the following combinations occur frequently,

$$\sigma^{\mu\nu} = \frac{i}{2}\left[\gamma^\mu, \gamma^\nu\right], \tag{A.20}$$

and

$$\gamma^5 = \gamma_5 = i\gamma^0\gamma^1\gamma^2\gamma^3 = \begin{pmatrix} 0 & \sigma_0 \\ \sigma_0 & 0 \end{pmatrix}, \tag{A.21}$$

which is Hermitian and anticommutes with the four gamma matrices,

$$\{\gamma^5, \gamma^\mu\} = 0\,. \tag{A.22}$$

Free solutions to the Dirac equation are given by plane waves for particles

$$\Psi^{(+)}(X) = \sqrt{\frac{M}{EV}} u(\mathbf{p}, s)\ e^{-iP\cdot X}, \tag{A.23}$$

and antiparticles

$$\Psi^{(-)}(X) = \sqrt{\frac{M}{EV}} v(\mathbf{p}, s)\ e^{iP\cdot X}, \tag{A.24}$$

where V is the volume containing the wave function, $\mathbf{p}$ is the 3-momentum and s the third component spin projection, which can assume the values $\pm 1/2$. $u(\mathbf{p}, s)$ and $v(\mathbf{p}, s)$ are referred to as free Dirac spinors and the Dirac equation yields

$$(\not{p} - M)u(\mathbf{p}, s) = 0, \tag{A.25}$$

$$(\not{p} + M)v(\mathbf{p}, s) = 0. \tag{A.26}$$

Explicitly, we have

$$u(\mathbf{p}, s) = \sqrt{\frac{E+M}{2M}} \begin{pmatrix} \chi_s \\ \dfrac{\boldsymbol{\sigma}\cdot\mathbf{p}}{E+M}\chi_s \end{pmatrix}, \tag{A.27}$$

$$v(\mathbf{p}, s) = \sqrt{\frac{E+M}{2M}} \begin{pmatrix} \dfrac{\boldsymbol{\sigma}\cdot\mathbf{p}}{E+M}\chi_{-s} \\ \chi_{-s} \end{pmatrix}, \tag{A.28}$$

with χ_s the bispinor defining the spin projection. The choice of χ_s is arbitrary, and allows for two independent solutions which correspond to the spin degrees of freedom of the Dirac spinor. One can choose two orthogonal two-component vectors, the two simplest options are

$$\chi_{+1/2} = \begin{pmatrix} 1 \\ 0 \end{pmatrix}, \quad \chi_{-1/2} = \begin{pmatrix} 0 \\ 1 \end{pmatrix}. \tag{A.29}$$

With this convention, the two spinors corresponding to $\chi_{+1/2}$ and $\chi_{-1/2}$ are spin-up and down solutions where the spin quantization axis is along the z-axis in the particle's rest frame.

The normalization of the spinors is such that

$$u^\dagger(\mathbf{p}, s)u(\mathbf{p}, s') = \frac{E}{M}\delta_{ss'}, \tag{A.30}$$

$$v^\dagger(\mathbf{p}, s)v(\mathbf{p}, s') = -\frac{E}{M}\delta_{ss'}, \tag{A.31}$$

and

$$\bar{u}(\mathbf{p},s)u(\mathbf{p},s') = \delta_{ss'}, \tag{A.32}$$

$$\bar{v}(\mathbf{p},s)v(\mathbf{p},s) = -\delta_{ss'}, \tag{A.33}$$

where $\bar{u}(\mathbf{p},s) = u^\dagger(\mathbf{p},s)\gamma^0$ and $\bar{v}(\mathbf{p},s) = v^\dagger(\mathbf{p},s)\gamma^0$ are referred to as adjoint spinors.

Other useful relations are

$$\sum_s u(\mathbf{p},s)\bar{u}(\mathbf{p},s) = \frac{\not{P} + M}{2M}, \tag{A.34}$$

$$\sum_s v(\mathbf{p},s)\bar{v}(\mathbf{p},s) = \frac{\not{P} - M}{2M}. \tag{A.35}$$

This leads to the completeness relation

$$\sum_s [u(\mathbf{p},s)\bar{u}(\mathbf{p},s) - v(\mathbf{p},s)\bar{v}(\mathbf{p},s)] = 1. \tag{A.36}$$

Fourier transform

The Fourier transform of a wave function $\Psi(\mathbf{x})$ is defined as

$$\Psi(\mathbf{p}) = \frac{1}{(2\pi)^{3/2}} \int d\mathbf{x}\ \Psi(\mathbf{x}) e^{-i\mathbf{x}\cdot\mathbf{p}}\,, \tag{A.37}$$

while the inverse transform is given by

$$\Psi(\mathbf{x}) = \frac{1}{(2\pi)^{3/2}} \int d\mathbf{p}\ \Psi(\mathbf{p}) e^{i\mathbf{x}\cdot\mathbf{p}}\,. \tag{A.38}$$

From these, one gets the following normalization,

$$\int d\mathbf{x}\ |\Psi(\mathbf{x})|^2 = \int d\mathbf{p}\ |\Psi(\mathbf{p})|^2 = 1. \tag{A.39}$$

Dirac delta

The Dirac delta function can be written in the form

$$\int d^4X\, e^{i(P'-P)\cdot X} = (2\pi)^4 \delta^4(P'-P). \tag{A.40}$$

Therefore, in the limit $P' = P$, $(2\pi)^4\delta^4(P'-P) \to V\cdot T$. The term $V\cdot T$ represents the total

volume of integration, with V the spatial volume and T the total time interval. Similarly, the squared Dirac delta satisfies

$$\left[(2\pi)^4\delta^4(P'-P)\right]^2 = TV\,(2\pi)^4\delta^4(P'-P). \tag{A.41}$$

More generally, the Dirac delta distribution may be composed with a smooth function $f(x)$. In this case, a useful property is

$$\delta(f(x)) = \sum_i \frac{\delta(x-x_i)}{|\partial f/\partial x|_{x_i}}, \tag{A.42}$$

where x_i is such that $f(x_i) = 0$.

Appendix B

Feynman rules in coordinate space

The amplitude of a Feynman diagram for a given scattering process is computed using the following Feynman rules in coordinate space.

1. Vertex: $i\int \mathrm{d}^4X\bar{\mathcal{L}}$, where $\bar{\mathcal{L}}$ is the Lagrangian without the fields.

2. Particle propagating from X to Y with 4-momentum P^μ:

   - W boson:
   $$D_W(X-Y) = \int \frac{\mathrm{d}^4P}{(2\pi)^4}\frac{-ig_{\mu\nu}}{P^2-M_W^2}e^{iP(X-Y)}\,.$$
   - Photon:
   $$D_\gamma(X-Y) = \int \frac{\mathrm{d}^4P}{(2\pi)^4}\frac{-ig_{\mu\nu}}{P^2}e^{iP(X-Y)}\,.$$
   - Pion:
   $$D_\pi(X-Y) = \int \frac{\mathrm{d}^4P}{(2\pi)^4}\frac{i}{P^2-m_\pi^2}e^{iP(X-Y)}\,.$$
   - Nucleon:
   $$D_N(X-Y) = \int \frac{\mathrm{d}^4P}{(2\pi)^4}\frac{i(\not{P}+M_N)}{P^2-M_N^2}e^{iP(X-Y)}\,.$$

3. External free particle with 4-momentum $P^\mu = (E,\mathbf{p})$:

   - Incoming fermion: $\Psi(X) = \sqrt{\frac{M}{VE}}u(\mathbf{p},s)e^{-iPX}$.
   - Outgoing fermion: $\overline{\Psi}(X) = \sqrt{\frac{M}{VE}}\overline{u}e^{iPX}$
   - Incoming pion: $\Phi(X) = \frac{1}{\sqrt{2EV}}e^{-iPX}$.
   - Outgoing pion: $\Phi^*(X) = \frac{1}{\sqrt{2EV}}e^{iPX}$.

Appendix C

Pion-nucleon system in ChPT: Non-resonant vertices

The ChPT Lagrangian for the pion-nucleon system provides all the necessary vertices for computing the ChPT background Feynman diagrams considered in this model. In this appendix, we present a detailed derivation of those vertices. We closely follow the procedure and convention of Ref. [177].

The effective Lagrangian of ChPT for the pion–nucleon system, including couplings to external fields and implementing the pattern of spontaneous chiral symmetry breaking in QCD, is given by

$$\mathcal{L}_{eff} = \overline{\Psi}\left(i\not{D} - M_N + ig_A\gamma^\mu\gamma^5\mathcal{A}_\mu\right)\Psi + \frac{f_\pi^2}{4}\mathrm{Tr}\left[D_\mu U(D^\mu U)^\dagger\right], \tag{C.1}$$

with $g_A = 1.26$, $f_\pi = 93$ MeV the pion weak decay constant and

$$\Psi = \begin{pmatrix}\psi_p\\ \\ \psi_n\end{pmatrix} \tag{C.2}$$

the nucleon field. The covariant derivative D_μ is defined as

$$D_\mu = \partial_\mu + \mathcal{V}_\mu - iv_\mu^{(s)}, \tag{C.3}$$

and

$$\mathcal{V}_\mu = \frac{1}{2}\Big[u^\dagger(\partial_\mu - ir_\mu)u + u(\partial_\mu - il_\mu)u^\dagger\Big], \tag{C.4}$$

$$\mathcal{A}_\mu = \frac{1}{2}\Big[u^\dagger(\partial_\mu - ir_\mu)u - u(\partial_\mu - il_\mu)u^\dagger\Big]. \tag{C.5}$$

C. PION-NUCLEON SYSTEM IN CHPT: NON-RESONANT VERTICES

The 2×2 matrix field u is the square root of the matrix field U containing the pion fields $\boldsymbol{\phi}$,

$$U = \exp\left(i\frac{\boldsymbol{\tau}\cdot\boldsymbol{\phi}}{f_\pi}\right), \quad u = \exp\left(i\frac{\boldsymbol{\tau}\cdot\boldsymbol{\phi}}{2f_\pi}\right). \tag{C.6}$$

The pions are the Goldstone bosons associated with the spontaneous breaking of the $\mathrm{SU}(2)_V \times \mathrm{SU}(2)_A$ chiral symmetry.

The fields r_μ, l_μ and $v_\mu^{(s)}$ provide the coupling to the external boson fields,

$$r_\mu = -e\frac{\tau_z}{2}A_\mu + \frac{g}{2\cos\theta_W}\sin^2\theta_W\tau_z Z_\mu, \tag{C.7}$$

$$l_\mu = -e\frac{\tau_z}{2}A_\mu + \frac{-g\,\cos\theta_c}{\sqrt{2}}\left(\tau_+ W_\mu^+ + \tau_- W_\mu^-\right) + \frac{-g}{2\cos\theta_W}(1-\sin^2\theta_W)\tau_z Z_\mu, \tag{C.8}$$

$$v_\mu^{(s)} = -\frac{e}{2}A_\mu + \frac{g}{2\cos\theta_W}\sin^2\theta_W Z_\mu, \tag{C.9}$$

where A_μ, $W_\mu^\pm$ and Z_μ are the fields of the photon, $\mathrm{W}^{+/-}$ boson and Z boson, respectively.

An expansion of the effective Lagrangian in Eq. C.1 in terms of the pion weak decay constant f_π results in

$$\mathcal{L}_{eff} = \overline{\Psi}[i\partial\!\!\!/ - M_N]\Psi + \frac{1}{2}\partial_\mu\boldsymbol{\phi}\partial^\mu\boldsymbol{\phi} - \frac{1}{2}m_\pi^2\boldsymbol{\phi}^2 + \mathcal{L}_{int}, \tag{C.10}$$

where only the interaction terms of the Lagrangian which contribute to the two-body meson-exchange currents at first order in f_π are kept,

$$\begin{aligned}\mathcal{L}_{int} = &\mathcal{L}_{\pi NN} + \mathcal{L}_{\pi\pi NN} \\ &+ \mathcal{L}_{\gamma NN} + \mathcal{L}_{\gamma\pi\pi} + \mathcal{L}_{\gamma\pi NN} \\ &+ \mathcal{L}_{WNN} + \mathcal{L}_{W\pi} + \mathcal{L}_{W\pi\pi} + \mathcal{L}_{W\pi NN} \\ &+ \mathcal{L}_{ZNN} + \mathcal{L}_{Z\pi} + \mathcal{L}_{Z\pi\pi} + \mathcal{L}_{Z\pi NN}.\end{aligned} \tag{C.11}$$

Each of these terms provides a different vertex function.

In what follows, we present the explicit expressions for each term of the Lagrangian in Eq. C.11. The physical fields of the pion are defined as $\phi^0 \equiv \phi_z$, $\phi^+ \equiv \frac{1}{\sqrt{2}}(\phi_x - i\phi_y)$ and $\phi^- \equiv \frac{1}{\sqrt{2}}(\phi_x + i\phi_y)$ [1]. The convention is such that ϕ^0 creates or annihilates a π^0, and $\phi^+(\phi^-)$ annihilates a $\pi^+(\pi^-)$ or creates a $\pi^-(\pi^+)$. The same convention is used for the boson fields. The

[1] The reciprocal relations are $\phi_x \equiv \frac{1}{\sqrt{2}}(\phi^+ + \phi^-)$ and $\phi_y \equiv \frac{i}{\sqrt{2}}(\phi^+ - \phi^-)$.

Pauli matrices correspond to τ_z, $\tau_+ \equiv \frac{1}{2}(\tau_x + i\tau_y)$ and $\tau_- \equiv \frac{1}{2}(\tau_x - i\tau_y)$ [1], with

$$\tau_z = \begin{pmatrix} 1 & 0 \\ 0 & -1 \end{pmatrix}, \quad \tau_+ = \begin{pmatrix} 0 & 1 \\ 0 & 0 \end{pmatrix}, \quad \tau_- = \begin{pmatrix} 0 & 0 \\ 1 & 0 \end{pmatrix}. \tag{C.12}$$

The scalar product of the cartesian pion fields with the Pauli isospin matrices leads to

$$\boldsymbol{\tau} \cdot \boldsymbol{\phi} = \phi^0 \tau_z + \sqrt{2}(\phi^+ \tau_+ + \phi^- \tau_-). \tag{C.13}$$

To conclude, we replace the derivatives of the pion fields in the Lagrangian with the corresponding particle four-momenta, as pions appear in the studied matrix elements through propagators. This replacement is performed considering that the four-momentum K_π^μ of the particle is incoming at the vertex, then, we use $\partial^\mu = -iK_\pi^\mu$. If the pion is outgoing, we must further apply the substitution $K_{\pi^{+(-)}} \to -K_{\pi^{-(+)}}$ and $K_{\pi^0} \to -K_{\pi^0}$.

Pion-nucleon Lagrangians

The πNN interaction is described by

$$\begin{aligned} \mathcal{L}_{\pi NN} &= -\frac{g_A}{2f_\pi} \overline{\Psi} \gamma^\mu \gamma^5 \partial_\mu \boldsymbol{\phi} \boldsymbol{\tau} \Psi \\ &= -\frac{g_A}{2f_\pi} \Big[\overline{\psi}_p (\gamma^\mu \gamma^5 \partial_\mu \phi^0) \psi_p - \overline{\psi}_n (\gamma^\mu \gamma^5 \partial_\mu \phi^0) \psi_n \\ &\quad + \sqrt{2}\, \overline{\psi}_p (\gamma^\mu \gamma^5 \partial_\mu \phi^+) \psi_n + \sqrt{2}\, \overline{\psi}_n (\gamma^\mu \gamma^5 \partial_\mu \phi^-) \psi_p \Big]. \end{aligned} \tag{C.14}$$

Replacing the derivative of the pion field by the momentum of the particle, we have

$$\begin{aligned} \mathcal{L}_{\pi NN} &= \frac{i g_A}{2f_\pi} \Big[\overline{\psi}_p (\not{K}_\pi \gamma^5 \phi^0) \psi_p - \overline{\psi}_n (\not{K}_\pi \gamma^5 \phi^0) \psi_n \\ &\quad + \sqrt{2}\, \overline{\psi}_p (\not{K}_\pi \gamma^5 \phi^+) \psi_n + \sqrt{2}\, \overline{\psi}_n (\not{K}_\pi \gamma^5 \phi^-) \psi_p \Big]. \end{aligned} \tag{C.15}$$

The $\pi\pi NN$ interaction is described by

$$\begin{aligned} \mathcal{L}_{\pi\pi NN} &= -\frac{1}{4f_\pi^2} \overline{\Psi} \gamma^\mu (\boldsymbol{\phi} \times \partial_\mu \boldsymbol{\phi}) \cdot \boldsymbol{\tau} \Psi \\ &= -\frac{i}{4f_\pi^2} \Big[\overline{\psi}_p \gamma^\mu (\phi^- \partial_\mu \phi^+ - \phi^+ \partial_\mu \phi^-) \psi_p - \overline{\psi}_n \gamma^\mu (\phi^- \partial_\mu \phi^+ - \phi^+ \partial_\mu \phi^-) \psi_n \\ &\quad + \sqrt{2}\, \overline{\psi}_p \gamma^\mu (\phi^+ \partial_\mu \phi^0 - \phi^0 \partial_\mu \phi^+) \psi_n + \sqrt{2}\, \overline{\psi}_n \gamma^\mu (\phi^0 \partial_\mu \phi^- - \phi^- \partial_\mu \phi^0) \psi_p \Big]. \end{aligned} \tag{C.16}$$

[1] The reciprocal relations are $\tau_x \equiv \tau_+ + \tau_-$ and $\tau_y = -i(\tau_+ - \tau_-)$.

Replacing the derivative of the pion fields by the momenta of the particles, we have

$$\mathcal{L}_{\pi\pi NN} = \frac{-1}{4f_\pi^2}\Big[\overline{\psi}_p(\not{K}_{\pi^+} - \not{K}_{\pi^-})\phi^-\phi^+\psi_p - \overline{\psi}_n(\not{K}_{\pi^+} - \not{K}_{\pi^-})\phi^-\phi^+\psi_n \\ + \sqrt{2}\,\overline{\psi}_p(\not{K}_{\pi^0} - \not{K}_{\pi^+})\phi^+\phi^0\psi_n + \sqrt{2}\,\overline{\psi}_n(\not{K}_{\pi^-} - \not{K}_{\pi^0})\phi^0\phi^-\psi_p\Big]. \tag{C.17}$$

Couplings to external fields: photon

The γee interaction is described by

$$\mathcal{L}_{\gamma ee} = e\overline{\Psi}_e\gamma^\mu\Psi_e A_\mu. \tag{C.18}$$

The γNN interaction is described by

$$\mathcal{L}_{\gamma NN} = -e\overline{\Psi}\gamma^\mu\frac{\mathbb{1}+\tau_z}{2}\Psi A_\mu = -e\overline{\psi}_p\gamma^\mu\psi_p A_\mu \to -e(\overline{\psi}_p\Gamma_p^\mu\psi_p + \overline{\psi}_n\Gamma_n^\mu\psi_n)A_\mu, \tag{C.19}$$

where the point-like coupling have been replaced by a vertex function, which takes into account the inner structure of the nucleon. The vertex, $\Gamma_{p,n}^\mu$, is described in Sec. 3.2.

The $\gamma\pi\pi$ interaction is described by

$$\mathcal{L}_{\gamma\pi\pi} = -e\epsilon_{zab}\phi_a\partial^\mu\phi_b A_\mu = -ie(\phi^-\partial^\mu\phi^+ - \phi^+\partial^\mu\phi^-)A_\mu. \tag{C.20}$$

with $\epsilon_{xyz} = 1$. Replacing the derivative of the pion fields by the momenta of the particles, we have

$$\mathcal{L}_{\gamma\pi\pi} = -e(K_{\pi^+} - K_{\pi^-})^\mu\phi^-\phi^+A_\mu. \tag{C.21}$$

The $\gamma\pi NN$ interaction is described by

$$\mathcal{L}_{\gamma\pi NN} = \frac{-eg_A}{2f_\pi}\epsilon_{zab}\overline{\Psi}\gamma^\mu\gamma^5\tau_a\phi_b\Psi A_\mu = \frac{-ieg_A}{\sqrt{2}f_\pi}(\overline{\psi}_p\gamma^\mu\gamma^5\phi^+\psi_n - \overline{\psi}_n\gamma^\mu\gamma^5\phi^-\psi_p)\;A_\mu. \tag{C.22}$$

Couplings to external fields: W boson

The $W\nu_\ell\ell$ interaction for particles is described by

$$\mathcal{L}_{W\nu_\ell\ell} = \frac{-g}{2\sqrt{2}}[\overline{\Psi}_\ell\gamma^\mu(1-\gamma^5)\Psi_{\nu_\ell}W_\mu^- + \overline{\Psi}_{\nu_\ell}\gamma^\mu(1-\gamma^5)\Psi_\ell W_\mu^+], \tag{C.23}$$

and, for antiparticles,

$$\mathcal{L}_{W\overline{\nu}_\ell\overline{\ell}} = \frac{-g}{2\sqrt{2}}[\overline{\Psi}_{\overline{\ell}}\gamma^\mu(1+\gamma^5)\Psi_{\overline{\nu}_\ell}W_\mu^+ + \overline{\Psi}_{\overline{\nu}_\ell}\gamma^\mu(1+\gamma^5)\Psi_{\overline{\ell}}W_\mu^-]. \tag{C.24}$$

The WNN interaction is described by

$$\begin{aligned}\mathcal{L}_{WNN} &= \frac{-g\cos\theta_c}{2\sqrt{2}}\Big[\overline{\psi}_p\gamma^\mu(1-g_A\gamma^5)\psi_n W_\mu^+ + \overline{\psi}_n\gamma^\mu(1-g_A\gamma^5)\psi_p W_\mu^-\Big] \\ &\to \frac{-g\cos\theta_c}{2\sqrt{2}}\Big[\overline{\psi}_p(\Gamma_V^\mu-\Gamma_A^\mu)\psi_n W_\mu^+ + \overline{\psi}_n(\Gamma_V^\mu-\Gamma_A^\mu)\psi_p W_\mu^-\Big],\end{aligned} \tag{C.25}$$

where, as in Eq. C.19, we have replaced the point-like coupling by vector (V) and axial (A) vertex functions, which takes into account the inner structure of the nucleon. The vertices, Γ_V^μ and Γ_A^μ, are described in Sec. 3.2.

The $W\pi$ interaction is described by

$$\mathcal{L}_{W\pi} = -\frac{g}{2}f_\pi\cos\theta_c(\partial^\mu\phi^- W_\mu^+ + \partial^\mu\phi^+ W_\mu^-). \tag{C.26}$$

Replacing the derivative of the pion field by the momentum of the particle, we have

$$\mathcal{L}_{W\pi} = \frac{ig}{2}f_\pi\cos\theta_c(K_{\pi^-}^\mu\phi^- W_\mu^+ + K_{\pi^+}^\mu\phi^+ W_\mu^-). \tag{C.27}$$

The $W\pi\pi$ interaction is described by

$$\mathcal{L}_{W\pi\pi} = i\frac{g}{2}\cos\theta_c\Big[(\phi^-\partial^\mu\phi^0 - \partial^\mu\phi^-\phi^0)W_\mu^+ - (\phi^+\partial^\mu\phi^0 - \partial^\mu\phi^+\phi^0)W_\mu^-\Big]. \tag{C.28}$$

Replacing the derivatives of the pion fields by the momenta of the particles, we have

$$\mathcal{L}_{W\pi\pi} = \frac{g}{2}\cos\theta_c\Big[(K_{\pi^0}-K_{\pi^-})^\mu\phi^-\phi^0 W_\mu^+ - (K_{\pi^0}-K_{\pi^+})^\mu\phi^+\phi^0 W_\mu^-\Big]. \tag{C.29}$$

The $W\pi NN$ interaction is described by vector and axial contributions,

$$\begin{aligned}\mathcal{L}_{W\pi NN}^V &= \frac{g\ g_A\cos\theta_c}{2\sqrt{2}}\frac{i}{\sqrt{2}f_\pi}\Big[\Big(\sqrt{2}\ \overline{\psi}_p\gamma^\mu\gamma^5\phi^0\psi_n - \overline{\psi}_p\gamma^\mu\gamma^5\phi^-\psi_p + \overline{\psi}_n\gamma^\mu\gamma^5\phi^-\psi_n\Big)W_\mu^+ \\ &\quad + \Big(\overline{\psi}_p\gamma^\mu\gamma^5\phi^+\psi_p - \overline{\psi}_n\gamma^\mu\gamma^5\phi^+\psi_n - \sqrt{2}\ \overline{\psi}_n\gamma^\mu\gamma^5\phi^0\psi_p\Big)W_\mu^-\Big],\end{aligned} \tag{C.30}$$

$$\begin{aligned}\mathcal{L}_{W\pi NN}^A &= \frac{g\cos\theta_c}{2\sqrt{2}}\frac{-i}{\sqrt{2}f_\pi}\Big[\Big(\sqrt{2}\ \overline{\psi}_p\gamma^\mu\phi^0\psi_n - \overline{\psi}_p\gamma^\mu\phi^-\psi_p + \overline{\psi}_n\gamma^\mu\phi^-\psi_n\Big)W_\mu^+ \\ &\quad + \Big(\overline{\psi}_p\gamma^\mu\phi^+\psi_p - \overline{\psi}_n\gamma^\mu\phi^+\psi_n - \sqrt{2}\ \overline{\psi}_n\gamma^\mu\phi^0\psi_p\Big)W_\mu^-\Big].\end{aligned} \tag{C.31}$$

Appendix D

Delta resonance

In this appendix, we provide explicit expressions for the Δ-resonance strong decay vertex, the electroweak excitation vertex, the form factors, the propagator and the decay width.

While all vertices that do not involve a resonance are derived from the ChPT Lagrangian [177] (Appendix C), this model does not provide the coupling with the Δ-resonance, which has to be introduced *ad hoc* from the formalism for the coupling to a spin-3/2 particle. Being separated pieces of the Lagrangian that are not derived from a common framework, the relative phase between the Δ-resonant and non-resonant terms is not unambiguously defined.

In the case of single pion production, hints on the relative phase can be inferred assuming Watson's theorem [193; 194], which follows from unitarity and time reversal invariance. Specifically, Watson's theorem states that the transition amplitude for a single pion production multipole with angular momentum ℓ, $\mathcal{A}_\ell^{\gamma\pi}$, is such that

$$(\mathcal{A}_\ell^{\gamma\pi})^* \mathcal{A}_\ell^{\pi\pi} \in \Re, \tag{D.1}$$

where $\mathcal{A}_\ell^{\pi\pi}$ is the corresponding pion-nucleon elastic scattering mutipole with the same quantum numbers. Hence, unitarity demands the following relation between the single pion production phase, $\phi_{\gamma\pi}$, and elastic pion-nucleon phase, $\phi_{\pi\pi}$,

$$\phi_{\gamma\pi} = \phi_{\pi\pi}\,, \quad \text{or} \quad \phi_{\gamma\pi} = \phi_{\pi\pi} + \pi\,. \tag{D.2}$$

The phases of the elastic $\pi - N$ elastic scattering amplitudes are experimentally determined and depend only on the total energy, W, thus allowing one to infer the phases of the single pion production amplitudes. Moreover, working in the center-of-mass frame, the direct Δ-resonance

contribution appears exclusively in the $J = 3/2$ and $\ell = 1$ multipoles. In this case, the Δ-resonance contribution dominates, while the ChPT background becomes negligible. As a result, Watson's theorem effectively constrains the phase of this amplitude, which is the relative phase between the Δ-resonant and non-resonant diagrams.

In principle, one could consider employing this phase obtained from single pion production in the calculations involving two-body meson-exchange currents with a 1p-1h final state. However, as mentioned above, the phase is a function of W, which for the processes we deal with in this work (virtual pions), this Δ-resonance energy is significantly different from the values of W relevant for real single pion production. Most important, Watson's theorem constrains the relative phase only up to an overall sign, see eq. D.2. This leads to the following implication. Suppose that a given model, using the choice $\phi(W)$, yields the best agreement with data. If an alternative approach includes the Δ-resonance contribution with an overall minus sign relative to the first, then the appropriate phase would be $\phi(W) + \pi$. Both models would produce identical predictions for the real single pion production case, and they both satisfy Watson's theorem.

Thus, there is no theoretical indication on which to lean to determine the choice of a positive or negative sign in the Δ-resonance amplitudes employed in this work for the two-body operators. The choice of this sign, however, has a direct impact on the interference with the one-body current contribution, thereby modifying the transverse response. The convention adopted in this work produces a constructive interference of the one-body and Δ-resonance contributions, resulting in an enhancement of the transverse channel, whereas the opposite-sign choice would produce a noticeable quenching of such response. Our choice of sign is supported and motivated by the agreement with experimental data, which clearly shows increased transverse strength with respect to the one-body-only results. This is further justified by previous studies on the effect of two-body currents on the transverse response in inclusive scattering. In particular, the enhancement of the transverse response has been observed within several frameworks, such as the relativistic Fermi gas model [124], a non-relativistic shell model that incorporates final state interactions [118], non-relativistic *ab initio* Green's Function Monte Carlo calculations [119; 120; 121; 43; 122], a variational Monte Carlo method with the short-time approximation [123], and the factorized spectral function formalism [94], among others. Notably, non-relativistic *ab initio* Green's Function Monte Carlo calculations, based on realistic two- and three-nucleon interactions and containing one- and two-body currents, have confirmed that the same choice of sign for the Δ-resonance contributions that leads to an increase in the transverse response also yields improved predictions of magnetic moments and M1 transitions in $A \leq 9$ nuclei [195]. In these cases, two-body

currents introduce significant corrections to the calculated observables, bringing them into excellent agreement with experimental data, further supporting our choice of sign. Additionally, the enhancement in the transverse response persists in GFMC calculations even when employing simplified ground-state wave functions that neglect strong tensor correlations [119], thus reinforcing the expected effect of this contribution in our approach, where correlations are not explicitly introduced via operators, but are effectively accounted for with the representation of the semi-phenomenological spectral function. This result contrasts, however, with earlier expectations based on Fermi-gas calculations of nuclear matter [196; 197; 127; 128; 198]. In these works, an opposite sign for the Δ-resonant contribution was adopted, resulting in a suppression of the transverse response. As a consequence, an alternative mechanism was required to account for the enhancement in the transverse channel necessary to reproduce the experimental data. In particular, in [197], it is attributed to the interplay between two-body currents and the presence of strong tensor correlations in the ground-state wave function.

Strong decay vertex

The $\pi N\Delta$ interaction is described by

$$\mathcal{L}_{\pi N\Delta} = \frac{f_{\pi N\Delta}}{m_\pi}\overline{\Psi}_\mu \mathbf{T}^\dagger(\partial^\mu \boldsymbol{\phi})\Psi + h.c. \tag{D.3}$$

where $f_{\pi N\Delta} = 2.18$, Ψ_μ is the Δ-resonance field, described as a Rarita-Schwinger $J^\pi = 3/2^+$ field, and $\mathbf{T}$ is the $\frac{1}{2} \to \frac{3}{2}$ isospin transition operator, defined in terms of Clebsch-Gordan coefficients as [106]

$$\langle \Delta | T^\dagger_\lambda | N\rangle = \left\langle \frac{3}{2}, \lambda_\Delta \middle| T^\dagger_\lambda \middle| \frac{1}{2}, \lambda_N \right\rangle = \left\langle \frac{3}{2}, \lambda_\Delta \middle| 1, \lambda; \frac{1}{2}, \lambda_N \right\rangle, \tag{D.4}$$

with $\lambda_\Delta = -3/2, -1/2, 1/2$ and $3/2$ for Δ^-, Δ^0, Δ^+ and Δ^{++}, $\lambda_N = -1/2$ and $1/2$ for neutron and proton, and $\lambda = -1, 0, 1$ with $T^\dagger_0 \equiv T^\dagger_z$, $T^\dagger_{+1} \equiv \frac{-1}{\sqrt{2}}(T^\dagger_x + iT^\dagger_y)$ and $T^\dagger_{-1} \equiv \frac{1}{\sqrt{2}}(T^\dagger_x - iT^\dagger_y)$ [1]. Explicitly, the isospin transition operators read

$$T^\dagger_z = \sqrt{\frac{2}{3}}\begin{pmatrix} -\sqrt{3} & 0 \\ 0 & -1 \\ 1 & 0 \\ 0 & \sqrt{3} \end{pmatrix}, \quad T^\dagger_+ = \frac{1}{\sqrt{3}}\begin{pmatrix} \sqrt{3} & 0 \\ 0 & 1 \\ 0 & 0 \\ 0 & 0 \end{pmatrix}, \quad T^\dagger_- = \frac{1}{\sqrt{3}}\begin{pmatrix} 0 & 0 \\ 0 & 0 \\ 1 & 0 \\ 0 & \sqrt{3} \end{pmatrix}. \tag{D.5}$$

Replacing the derivative of the pion field by the four-momentum of the particle, K^μ_π, considering

[1] The reciprocal relations are $T^\dagger_x \equiv \frac{-1}{\sqrt{2}}(T^\dagger_+ - T^\dagger_-)$ and $T^\dagger_y \equiv \frac{i}{\sqrt{2}}(T^\dagger_+ + T^\dagger_-)$.

that it is incoming at the vertex, we have

$$\mathcal{L}_{\pi N\Delta} = -i\frac{f_{\pi N\Delta}}{m_\pi} K_\pi^\mu \overline{\Psi}_\mu \mathbf{T}^\dagger \boldsymbol{\phi} \Psi + h.c. \tag{D.6}$$

We now study the isospin $\frac{1}{2} \to \frac{3}{2}$ transition term $\overline{\Psi}_\mu \mathbf{T}^\dagger \boldsymbol{\phi} \Psi$. The scalar product of the pion field and the $\frac{1}{2} \to \frac{3}{2}$ isospin transition operator leads to,

$$\boldsymbol{\phi} \cdot \mathbf{T}^\dagger = -\phi^+ T_+^\dagger + \phi^- T_-^\dagger + \phi_0 T_0^\dagger. \tag{D.7}$$

Then,

$$\overline{\Psi}_\mu \mathbf{T}^\dagger \boldsymbol{\phi} \Psi = \begin{pmatrix} \overline{\Psi}_\mu^{++} & \overline{\Psi}_\mu^{+} & \overline{\Psi}_\mu^{0} & \overline{\Psi}_\mu^{-} \end{pmatrix} \left(-\phi^+ T_+^\dagger + \phi^- T_-^\dagger + \phi_0 T_0^\dagger\right) \begin{pmatrix} \Psi^p \\ \Psi^n \end{pmatrix}, \tag{D.8}$$

and, using Eq. D.5, we get

$$\overline{\Psi}_\mu \mathbf{T}^\dagger \boldsymbol{\phi} \Psi = -\overline{\Psi}_\mu^{++} \phi^+ \Psi^p + \sqrt{\frac{2}{3}} \overline{\Psi}_\mu^{+} \phi^0 \Psi^p - \sqrt{\frac{1}{3}} \overline{\Psi}_\mu^{+} \phi^+ \Psi^n + \sqrt{\frac{1}{3}} \overline{\Psi}_\mu^{0} \phi^- \Psi^p + \sqrt{\frac{2}{3}} \overline{\Psi}_\mu^{0} \phi^0 \Psi^n + \overline{\Psi}_\mu^{-} \phi^- \Psi^n. \tag{D.9}$$

Finally, we define the $\Delta\pi N$ vertex function $\Gamma^\alpha_{\Delta\pi N}$ as

$$\Gamma^\alpha_{\Delta\pi N} = \frac{\sqrt{2} f_{\pi N\Delta}}{m_\pi} K_\pi^\alpha. \tag{D.10}$$

The isospin coefficients associated with this vertex, combined with those from the electroweak $Q\Delta N$ vertex, are given in Tables D.1 and D.2 for the possible $Q + N \to \pi + N'$ processes.

Electroweak excitation vertex

The electroweak $Q\Delta N$ vertex, where Q stands for the boson, is given by the parametrization

$$\Gamma^{\beta\nu}_{Q\Delta N} = \Gamma^{\beta\nu}_{Q\Delta N,V} + \Gamma^{\beta\nu}_{Q\Delta N,A}. \tag{D.11}$$

The vector part is given by

$$\Gamma^{\beta\nu}_{Q\Delta N,V} = \left[\frac{C_3^V}{M_N}(g^{\beta\nu} \not{Q} - Q^\beta \gamma^\nu) + \frac{C_4^V}{M_N^2}(g^{\beta\nu} Q \cdot P_\Delta - Q^\beta P_\Delta^\nu) + \frac{C_5^V}{M_N^2}(g^{\beta\nu} Q \cdot P - Q^\beta P^\nu) + C_6^V g^{\beta\nu} \right] \gamma^5, \tag{D.12}$$

and the axial part is

$$\Gamma^{\beta\nu}_{Q\Delta N,A} = \frac{C_3^A}{M_N}(g^{\beta\nu} \not{Q} - Q^\beta \gamma^\nu) + \frac{C_4^A}{M_N^2}(g^{\beta\nu} Q \cdot P_\Delta - Q^\beta P_\Delta^\nu) + C_5^A g^{\beta\nu} + \frac{C_6^A}{M_N^2} Q^\beta Q^\nu, \tag{D.13}$$

with P_Δ the four-momentum of the Δ-resonance.

The determination of the form factors of the resonance, $C_i^{V,A}(Q^2)$, follows from general principles and experimental results [130; 199]. The vector form factors are fitted to reproduce pion photo- and electro-production data given in terms of helicity amplitudes for the electromagnetic current. The information on the axial form factors is limited to restrictions provided by the PCAC hypothesis and BNL and ANL experimental data. Here, we use the parametrization proposed in [110]. The vector form factors are

$$\begin{aligned} C_3^V &= \frac{2.13\ G_D^V}{1-\frac{Q^2}{4M_V^2}}, \\ C_4^V &= \frac{-1.51}{2.13} C_3^V, \\ C_5^V &= \frac{0.48\ G_D^V}{1-\frac{Q^2}{0.776 M_V^2}}, \end{aligned} \tag{D.14}$$

with $G_D^V = (1 - Q^2/M_V^2)^{-2}$ and $M_V = 0.84$ GeV, and from the imposition of the conserved vector current hypothesis it follows that $C_6^V = 0$. The axial form factors are

$$\begin{aligned} C_5^A &= C_5^A(0) \frac{1}{\left(1-\frac{Q^2}{M_{A,\Delta}^2}\right)^2}, \\ C_4^A &= -\frac{C_5^A}{4}, \\ C_6^A &= C_5^A \frac{M_N^2}{m_\pi^2 - Q^2}, \end{aligned} \tag{D.15}$$

with $C_5^A(0) = 1.12$ and $M_{A,\Delta} = 953.7$ MeV, and C_3^A is set to zero.

Since the excitation of the Δ-resonance is a purely isovector transition, the electromagnetic form factors that parameterize the $N \to \Delta$ vertex are the same for neutrons and protons and, due to isospin symmetry, also for charged-current and electromagnetic interactions, i.e., $C_i^p = C_i^n = C_i^V$. Note that in the case of electromagnetic interactions, only vector form factors contribute. The difference between the possible Δ-resonance excitation channels is contained in the isospin Clebsch–Gordan coefficients associated with the $\frac{1}{2} \to \frac{3}{2}$ isospin transition operator. The electromagnetic Δ^+ and Δ^0 excitations share the same isospin coefficient, while the charged-current vertex differs from the electromagnetic one by a factor of $-\sqrt{3}$ for the Δ^{++} excitation, and by -1 for the Δ^+ excitation [199]. Finally, the isospin coefficients associated with this

vertex, combined with those from the $\pi N\Delta$ vertex, are listed in Tables D.1 and D.2 for the possible $Q + N \to \pi + N'$ processes.

Channel	ΔP	$C\Delta P$
$p \to \pi^0 + p$	$\sqrt{1/3}$	$\sqrt{1/3}$
$p \to \pi^+ + n$	$-\sqrt{1/6}$	$\sqrt{1/6}$
$n \to \pi^- + p$	$\sqrt{1/6}$	$-\sqrt{1/6}$
$n \to \pi^0 + n$	$\sqrt{1/3}$	$\sqrt{1/3}$

Table D.1: Isospin coefficients for the different channels of the EM process $\gamma + N \to \pi + N'$ occurring through Δ-resonance excitation.

Channel	ΔP	$C\Delta P$
$p \to \pi^+ + p$	$\sqrt{3/2}$	$\sqrt{1/6}$
$n \to \pi^0 + p$	$-\sqrt{1/3}$	$\sqrt{1/3}$
$n \to \pi^+ + n$	$\sqrt{1/6}$	$\sqrt{3/2}$
$n \to \pi^- + n$	$\sqrt{3/2}$	$\sqrt{1/6}$
$p \to \pi^0 + n$	$\sqrt{1/3}$	$-\sqrt{1/3}$
$p \to \pi^- + p$	$\sqrt{1/6}$	$\sqrt{3/2}$

Table D.2: Isospin coefficients for the different channels of the CC process $W+N \to \pi+N'$ occurring through Δ-resonance excitation. The first three rows correspond to neutrino-induced reactions. The second three rows correspond to their antineutrino counterparts.

Δ-propagator

A Δ-resonance propagating from X to Y is introduced in the matrix element as

$$D_\Delta(X - Y) = \int \frac{d^4P_\Delta}{(2\pi)^4} iS_{\Delta,\alpha\beta} e^{iP_\Delta(X-Y)}, \tag{D.16}$$

with P_Δ the four-momentum of the resonance, and the propagator is described by the Rarita-Schwinger spin-3/2 field propagator,

$$S_{\Delta,\alpha\beta} = \frac{-(\not{P}_\Delta + M_\Delta)}{P_\Delta^2 - M_\Delta^2 + iM_\Delta\Gamma^{\pi N}(W)} \Big(g_{\alpha\beta} - \frac{1}{3}\gamma_\alpha\gamma_\beta - \frac{2}{3M_\Delta^2} P_{\Delta,\alpha}P_{\Delta,\beta} - \frac{1}{3M_\Delta}(\gamma_\alpha P_{\Delta,\beta} - P_{\Delta,\alpha}\gamma_\beta) \Big). \tag{D.17}$$

$\Gamma^{\pi N}$ is the pion-nucleon resonance-decay width computed in the rest frame of the resonance [200],

$$\Gamma^{\pi N}(W) = \frac{1}{12\pi}\left(\frac{f_{\pi N R_3}}{m_\pi}\right)^2 \frac{(k_\pi^*)^3}{W}(E_N^* + M_N), \tag{D.18}$$

where W is the $\pi - N$ invariant mass, k_π^* is the pion center of mass momentum,

$$k_\pi^* = \sqrt{\frac{s + m_\pi^2 - M_N^2}{2W} - m_\pi^2}\,, \tag{D.19}$$

and $E_N^* = \sqrt{(k_\pi^*)^2 + M_N^2}$. The value of the strong coupling constant $f_{\pi N\Delta}$ is obtained from Eq. D.18 by imposing $\Gamma^{\pi N}(W = M_R) = \Gamma^{exp} = 120$ MeV, with Γ^{exp} the experimental value of the resonance-decay width. We use this value of $f_{\pi N\Delta}$ both in the decay width and in the decay vertex.

Appendix E

Relativistic mean-field model

The relativistic mean-field (RMF) model considered in this work is an extension of the linear $\sigma-\omega$ model originally introduced by Walecka [201], where the exchange of the scalar meson σ gives rise to the attractive part of the interaction, while the repulsive part is mediated by the exchange of the vector meson ω. The model is extended by including the ρ meson, the photon field A^μ and non-linear couplings of the σ meson [80]. The ρ meson accounts for the isospin dependence of the nuclear force through its isovector coupling to the nucleon field, while photon exchange describes the Coulomb interaction between protons. These contributions lead to the differences between proton and neutron wave functions. The non-linear couplings of the σ meson are introduced to improve the agreement with experimental data and represent the self-interaction of the scalar field. Finally, the ground state is assumed to have a well-defined parity, such that pion exchange is not considered. Then, the first step is the construction of a phenomenological Lorentz-covariant Lagrangian density that includes these fields and the nucleon-nucleon interaction through meson exchange,

$$\begin{aligned}\mathcal{L} &= \bar{\Psi}(i\gamma_\mu\partial^\mu - M_N)\Psi + \frac{1}{2}(\partial_\mu\sigma\partial^\mu - m_\sigma^2\sigma^2) - U(\sigma) - \frac{1}{4}\Omega_{\mu\nu}\Omega^{\mu\nu} + \frac{1}{2}m_\omega^2\omega_\mu\omega^\mu \\ &- \frac{1}{4}\mathbf{R}_{\mu\nu}\mathbf{R}^{\mu\nu} + \frac{1}{2}m_\rho^2\boldsymbol{\rho}_\mu\boldsymbol{\rho}^\mu - \frac{1}{4}F_{\mu\nu}F^{\mu\nu} \\ &- g_s\bar{\Psi}\sigma\Psi - g_\omega\bar{\Psi}\gamma_\mu\omega^\mu\Psi - g_\rho\bar{\Psi}\gamma_\mu\boldsymbol{\tau}\boldsymbol{\rho}^\mu\Psi - e\frac{1+\tau_3}{2}\bar{\Psi}\gamma_\mu A^\mu\Psi. \end{aligned} \tag{E.1}$$

M_N, m_σ, m_ω and m_ρ are the masses of the nucleon and the mesons. g_σ, g_ω and g_ρ are the coupling constants of the mesons and e of the photon field. $U(\sigma) = \frac{1}{3}g_2\sigma^3 + \frac{1}{4}g_3\sigma^4$ is the non-linear term

for the σ meson. The tensor fields are

$$\Omega^{\mu\nu} = \partial^\mu \omega^\nu - \partial^\nu \omega^\mu, \tag{E.2}$$

$$\mathbf{R}^{\mu\nu} = \partial^\mu \boldsymbol{\rho}^\nu - \partial^\nu \boldsymbol{\rho}^\mu, \tag{E.3}$$

$$F^{\mu\nu} = \partial^\mu A^\nu - \partial^\nu A^\mu. \tag{E.4}$$

Now, by applying the Euler–Lagrange equation,

$$\partial_\mu \left(\frac{\partial \mathcal{L}}{\partial(\partial_\mu q)} \right) - \frac{\partial \mathcal{L}}{\partial q} = 0, \tag{E.5}$$

one obtains the equations of motion for the meson and nucleon fields. However, the resulting set of coupled equations is difficult to handle. The coupling constants take relatively large values, making perturbative expansions unfeasible. Therefore, it becomes necessary to introduce certain approximations to simplify the Lagrangian. The mean-field approach is implemented by replacing the meson fields by classical fields, such that only the nucleon field have to be quantized. When this approach is applied to finite nuclear matter, the meson fields only have a time-like component and are constant, while for finite nuclei the spatial dependence is necessary. Considering spherical symmetry and static nuclear states, the vector fields only depend on r and their spatial components vanish. Thus, $\omega^\mu(r) = \delta^{\mu 0}\omega^0(r)$ and $\boldsymbol{\rho}^\mu(r) = \delta^{\mu 0}\boldsymbol{\rho}^0(r)$. Finally, we consider that isovector current is conserved, the nucleon states do not mix isospin, so only the third component of the isospin operator and the neutral meson ρ, referred to as ρ_3, contributes. Under these approximations, the equations of motion are significantly simplified, allowing their resolution within the Hartree approach.

The nucleon wave function corresponds to the solution of the Dirac equation in presence of scalar and vector potentials,

$$[-i\boldsymbol{\alpha} \cdot \boldsymbol{\nabla} + V(r) + \beta(M_N + S(r))]\Psi_i(\mathbf{r}) = E_i \Psi_i(\mathbf{r}), \tag{E.6}$$

where we have assumed $\Psi(X) = \Psi(\mathbf{r})e^{-iEt}$, and $\boldsymbol{\alpha}$ and β are the Dirac matrices. The subscript i indicates that Ψ_i is the single-particle wave function of a nucleon i, with well-defined isospin and charge (i.e. a proton or a neutron), and E_i is its energy. Each nucleon is also characterized by its own set of quantum numbers. The scalar and vector potentials that enter the Dirac equation

are given in terms of the fields as

$$S(r) = g_\sigma \sigma(r), \tag{E.7}$$

$$V(r) = g_\omega \omega^0(r) + g_\rho \tau_3 \rho_3^0(r) + e\frac{1+\tau_3}{2} A^0(r), \tag{E.8}$$

with $\tau_3 = +1(-1)$ for protons (neutrons). For the mesons and the photon, the equations of motion reduce to Klein-Gordon-like equations,

$$(\nabla^2 - m_\sigma^2)\sigma(r) = g_\sigma \rho_s(r) + g_2 \sigma^2(r) + g_3 \sigma^3(r), \tag{E.9}$$

$$(\nabla^2 - m_\omega^2)\omega^0(r) = g_\omega \rho_B(r), \tag{E.10}$$

$$(\nabla^2 - m_\rho^2)\rho_3^0(r) = g_\rho \rho_\rho(r), \tag{E.11}$$

$$\nabla^2 A^0 = -e\rho_e(r), \tag{E.12}$$

where the scalar, baryon, isovector and charge nuclear densities, namely ρ_s, ρ_B, ρ_ρ and ρ_e, have been introduced. They are defined as

$$\rho_s(r) = \sum_i^A \bar{\Psi}_i(\mathbf{r})\Psi_i(\mathbf{r}), \tag{E.13}$$

$$\rho_B(r) = \sum_i^A \Psi_i^\dagger(\mathbf{r})\Psi_i(\mathbf{r}), \tag{E.14}$$

$$\rho_\rho(r) = \sum_i^A \Psi_i^\dagger(\mathbf{r})\tau_3\Psi_i(\mathbf{r}) = \sum_i^Z \Psi_i^\dagger(\mathbf{r})\Psi_i(\mathbf{r}) - \sum_i^N \Psi_i^\dagger(\mathbf{r})\Psi_i(\mathbf{r}), \tag{E.15}$$

$$\rho_e(r) = \sum_i^A \Psi_i^\dagger(\mathbf{r}) \left(\frac{1+\tau_3}{2}\right) \Psi_i(\mathbf{r}) = \sum_i^Z \Psi_i^\dagger(\mathbf{r})\Psi_i(\mathbf{r}). \tag{E.16}$$

These equations, together with the nucleon Dirac equation, are then solved self-consistently until convergence is reached. First, given some initial values for the S and V potentials, the nucleon Dirac equations are solved. Then, the resulting nucleon wave functions, $\Psi_i(\mathbf{r})$, are used to compute the nuclear densities ρ_s, ρ_B, ρ_ρ and ρ_e, which are subsequently introduced into the meson and photon field equations. The solutions for these fields yield a new set of vector and scalar potentials, which are then used to start again the procedure. This process is iteratively repeated until convergence is achieved for both the fields and the nucleon wave functions.

The masses of the mesons m_ρ, m_ω and of the nucleon M_N, as well as the electromagnetic coupling constant $e/4\pi$, are fixed to their experimental values. The coupling constants g_ω, g_ρ,

g_σ, g_2 and g_3, together with the mass of the scalar meson m_σ, are chosen to reproduce properties of nuclear matter and finite nuclei. In this work, we use the NLSH model [80], which fits the parameters to reproduce the charge radius, the binding energy and the neutron radius of ^{16}O, ^{40}Ca, ^{90}Zr, ^{116}Sn, ^{124}Sn and ^{208}Pb. The complete set of parameters is shown in Table E.1. Finally, the values of the S and V potentials depend on the specific nucleus under study, as the nuclear densities are determined by the number of neutrons and protons.

M_N(MeV)	m_σ(MeV)	m_ω(MeV)	m_ρ(MeV)	g_σ	g_ω	g_ρ	g_2(fm^{-1})	g_3
939	526.059	783	763	10.444	12.945	4.383	-6.9099	-15.8337

Table E.1: RMF parameters from the NLSH model [80].

Publications and Conference Contributions

During the development of this PhD thesis, several results have been disseminated through publications in international journals and conferences related to the field. These are summarized below. Publications have been grouped into two categories: those directly related to the thesis, and other independent contributions.

Publications derived from this thesis

1. **T. Franco-Munoz**, R. González-Jiménez and J.M. Udías.
   Effects of two-body currents in the one-particle one-hole electromagnetic responses within a relativistic model.
   Journal of Physics G: Nuclear and Particle Physics, **52** 025103 (2025).
   DOI: 10.1088/1361-6471/ad9eca

2. **T. Franco-Munoz**, J. García-Marcos, R. González-Jiménez and J.M. Udías.
   Relativistic two-body currents for one-nucleon knockout in electron-nucleus scattering.
   Physical Review C, **108** 064608 (2023) [Editors' Suggestion].
   DOI: 10.1103/PhysRevC.108.064608

Other publications

1. J. García-Marcos, **T. Franco-Munoz**, R. González-Jiménez, A. Nikolakopoulos, N. Jachowicz and J.M. Udías.
   Towards a more complete description of nucleon distortion in lepton-induced single-pion production at low-Q^2.

Physical Review C, **109** 024608 (2024).
DOI: 10.1103/PhysRevC.109.024608

Conference contributions

1. Title: Two-body currents in one-particle one-hole lepton-nucleus interactions within a relativistic mean-field model
   Type: Oral
   Congress: NuFact 2024 - The 25th International Workshop on Neutrinos from Accelerators
   Date and place: 16-21 September 2024, Chicago
   Link: indico.fnal.gov/event/63406/

2. Title: Meson exchange currents in a relativistic mean-field model
   Type: Oral
   Congress: NuInt 2024 - 14th International Workshop on Neutrino-Nucleus Interactions
   Date and place: 11-20 April 2024, Sao Paulo
   Link: indico.fnal.gov/event/59963/

3. Title: Meson exchange currents within a relativistic mean-field model in the quasielastic regime
   Type: Oral
   Congress: Neutrino Scattering at Low and Intermediate Energies
   Date and place: 26-30 June 2023, Mainz
   Link: indico.mitp.uni-mainz.de/event/324/

4. Title: Realistic treatment of nuclear structure in the neutrino-nucleus interaction
   Type: Oral
   Congress: PhDay Físicas UCM 2022 (Award-winning contribution)
   Date and place: 10-14 October 2022, Madrid
   Link: fisicas.ucm.es/phday-fisicas-2022

5. Title: Contribution of meson exchange currents to the electromagnetic responses within a relativistic mean-field model
   Type: Oral
   Congress: European Nuclear Physics Conference 2022

Date and place: 24-28 October 2022, Santiago de Compostela
Link: indico.cern.ch/event/1104299/

6. Title: Realistic treatment of nuclear structure in the neutrino-nucleus interaction
   Type: Oral
   Congress: XXXVIII Reunión Bienal de la Real Sociedad Española de Física
   Date and place: 11-15 July 2022, Murcia
   Link: um.es/fisica/bienal-2022/

7. Title: Meson-exchange currents: simultaneous reproduction of the electromagnetic responses of carbon
   Type: Oral
   Congress: Neutrino Interactions in the Standard Model and Beyond
   Date and place: 17-21 January 2022, Online
   Link: indico.cern.ch/event/1047442/

List of Figures

List of Tables

References

[1] F. Reines and C. L. Cowan. Detection of the free neutrino. Phys. Rev., 92:830–831, Nov 1953. doi:10.1103/PhysRev.92.830.

[2] L. Alvarez-Ruso et al. Nustec white paper: Status and challenges of neutrino–nucleus scattering. Progress in Particle and Nuclear Physics, 100:1 – 68, 2018. doi:10.1016/j.ppnp.2018.01.006.

[3] A. D. Sakharov. Violation of CP Invariance, C asymmetry, and baryon asymmetry of the universe. Pisma Zh. Eksp. Teor. Fiz., 5:32–35, 1967. doi:10.1070/PU1991v034n05ABEH002497.

[4] K. Abe and others. Observation of large CP violation in the neutral B meson system. Phys. Rev. Lett., 87:091802, Aug 2001. doi:10.1103/PhysRevLett.87.091802.

[5] B. Pontecorvo. Neutrino Experiments and the Problem of Conservation of Leptonic Charge. Zh. Eksp. Teor. Fiz., 53:1717–1725, 1967.

[6] Z. Maki, M. Nakagawa, and S. Sakata. Remarks on the unified model of elementary particles. Prog. Theor. Phys., 28:870–880, 1962. doi:10.1143/PTP.28.870.

[7] R. Davis, D. S. Harmer, and K. C. Hoffman. Search for neutrinos from the sun. Phys. Rev. Lett., 20:1205–1209, May 1968. doi:10.1103/PhysRevLett.20.1205.

[8] Y. Fukuda et al. Evidence for oscillation of atmospheric neutrinos. Phys. Rev. Lett., 81:1562–1567, Aug 1998. doi:10.1103/PhysRevLett.81.1562.

[9] Q. R. Ahmad et al. Measurement of the rate of $\nu_e + d \rightarrow p + p + e^-$ interactions produced by ^8b solar neutrinos at the sudbury neutrino observatory. Phys. Rev. Lett., 87:071301, Jul 2001. doi:10.1103/PhysRevLett.87.071301.

[10] M. H. Ahn et al. Indications of neutrino oscillation in a 250 km long-baseline experiment. Phys. Rev. Lett., 90:041801, Jan 2003. doi:10.1103/PhysRevLett.90.041801.

[11] I. Esteban, M. C. Gonzalez-Garcia, M. Maltoni, I. Martinez-Soler, J. P. Pinheiro, and T. Schwetz. NuFit-6.0: updated global analysis of three-flavor neutrino oscillations. JHEP, 12:216, 2024. doi:10.1007/JHEP12(2024)216.

[12] NuFIT 6.0 (2024). URL: http://www.nu-fit.org/.

[13] M. Aker et al. Direct neutrino-mass measurement based on 259 days of katrin data. Science, 388(6743):180–185, 2025. doi:10.1126/science.adq9592.

[14] T. Wester et al. Atmospheric neutrino oscillation analysis with neutron tagging and an expanded fiducial volume in super-kamiokande i–v. Phys. Rev. D, 109:072014, Apr 2024. doi:10.1103/PhysRevD.109.072014.

[15] R. Abbasi et al. Measurement of Atmospheric Neutrino Oscillation Parameters Using Convolutional Neural Networks with 9.3 Years of Data in IceCube DeepCore. Phys. Rev. Lett., 134(9):091801, 2025. doi:10.1103/PhysRevLett.134.091801.

[16] F. T. Avignone, S. R. Elliott, and J. Engel. Double beta decay, majorana neutrinos, and neutrino mass. Rev. Mod. Phys., 80:481–516, Apr 2008. doi:10.1103/RevModPhys.80.481.

[17] K. Abe et al. First combined measurement of the muon neutrino and antineutrino charged-current cross section without pions in the final state at t2k. Phys. Rev. D, 101:112001, Jun 2020. doi:10.1103/PhysRevD.101.112001.

[18] T2K. URL: https://t2k-experiment.org/es/.

[19] K. Abe et al. Constraint on the matter-antimatter symmetry-violating phase in neutrino oscillations. Nature, 580:339–344, Apr 2020. doi:10.1038/s41586-020-2177-0.

[20] M. A. Acero et al. First measurement of neutrino oscillation parameters using neutrinos and antineutrinos by nova. Phys. Rev. Lett., 123:151803, Oct 2019. doi:10.1103/PhysRevLett.123.151803.

[21] T. Cai et al. Nucleon binding energy and transverse momentum imbalance in neutrino-nucleus reactions. Phys. Rev. D, 101:092001, May 2020. doi:10.1103/PhysRevD.101.092001.

[22] P. Abratenko et al. First measurement of differential charged current quasielasticlike ν_μ-argon scattering cross sections with the microboone detector. Phys. Rev. Lett., 125:201803, Nov 2020. doi:10.1103/PhysRevLett.125.201803.

[23] K. Abe et al. Physics potential of a long-baseline neutrino oscillation experiment using a j-parc neutrino beam and hyper-kamiokande. PTEP, 2015(5):053C02, 2015. doi:10.1093/ptep/ptv061.

[24] R. Acciarri et al. Long-Baseline Neutrino Facility (LBNF) and Deep Underground Neutrino Experiment (DUNE). 2016. arXiv:1601.05471.

[25] M. H. Ahn et al. Measurement of neutrino oscillation by the k2k experiment. Phys. Rev. D, 74:072003, Oct 2006. doi:10.1103/PhysRevD.74.072003.

[26] M. A. Acero et al. Improved measurement of neutrino oscillation parameters by the nova experiment. Phys. Rev. D, 106:032004, Aug 2022. doi:10.1103/PhysRevD.106.032004.

[27] L. Aliaga et al. Design, calibration, and performance of the minerva detector. Nuclear Instruments and Methods in Physics Research Section A: Accelerators, Spectrometers, Detectors and Associated Equipment, 743:130–159, 2014. doi:10.1016/j.nima.2013.12.053.

[28] A. A. Aguilar-Arevalo et al. Improved search for $\overline{\nu}_\mu \to \overline{\nu}_e$ oscillations in the miniboone experiment. Phys. Rev. Lett., 110:161801, Apr 2013. doi:10.1103/PhysRevLett.110.161801.

[29] A. A. Aguilar-Arevalo et al. Significant excess of electronlike events in the miniboone short-baseline neutrino experiment. Phys. Rev. Lett., 121:221801, Nov 2018. doi:10.1103/PhysRevLett.121.221801.

[30] R. Acciarri et al. A Proposal for a Three Detector Short-Baseline Neutrino Oscillation Program in the Fermilab Booster Neutrino Beam. 3 2015. arXiv:1503.01520.

[31] R. Acciarri et al. Design and construction of the microboone detector. Journal of Instrumentation, 12(02):P02017, feb 2017. doi:10.1088/1748-0221/12/02/P02017.

[32] S. Boyd, S. Dytman, E. Hernández, J. Sobczyk, and R. Tacik. Comparison of models of neutrino-nucleus interactions. AIP Conference Proceedings, 1189(1):60–73, 11 2009. doi:10.1063/1.3274191.

[33] T. Katori and M. Martini. Neutrino-nucleus cross sections for oscillation experiments. J. Phys. G: Nucl. Part. Phys., 45(1):013001, dec 2017. doi:10.1088/1361-6471/aa8bf7.

[34] A. A. Aguilar-Arevalo et al. Measurement of neutrino-induced charged-current charged pion production cross sections on mineral oil at $E_\nu \sim 1$ GeV. Phys. Rev. D, 83:052007, Mar 2011. doi:10.1103/PhysRevD.83.052007.

[35] C. L. McGivern et al. Cross sections for ν_μ and $\overline{\nu}_\mu$ induced pion production on hydrocarbon in the few-gev region using minerva. Phys. Rev. D, 94:052005, Sep 2016. doi:10.1103/PhysRevD.94.052005.

[36] K. Abe et al. First measurement of the muon neutrino charged current single pion production cross section on water with the t2k near detector. Phys. Rev. D, 95:012010, Jan 2017. doi:10.1103/PhysRevD.95.012010.

[37] J. W. Van Orden and T. W. Donnelly. Nuclear theory and event generators for charge-changing neutrino reactions. Phys. Rev. C, 100:044620, Oct 2019. doi:10.1103/PhysRevC.100.044620.

[38] M. Martini, M. Ericson, G. Chanfray, and J. Marteau. Unified approach for nucleon knock-out and coherent and incoherent pion production in neutrino interactions with nuclei. Phys. Rev. C, 80:065501, Dec 2009. doi:10.1103/PhysRevC.80.065501.

[39] J. Nieves and J. E. Sobczyk. In medium dispersion relation effects in nuclear inclusive reactions at intermediate and low energies. Annals of Physics, 383:455–496, 2017. doi:10.1016/j.aop.2017.06.002.

[40] S. Ahmad, M. S. Athar, and S. K. Singh. Neutrino induced charged current $1\pi^+$ production at intermediate energies. Phys. Rev. D, 74:073008, Oct 2006. doi:10.1103/PhysRevD.74.073008.

[41] O. Benhar, D. Day, and I. Sick. Inclusive quasielastic electron-nucleus scattering. Rev. Mod. Phys., 80:189–224, Jan 2008. doi:10.1103/RevModPhys.80.189.

[42] N. Rocco, C. Barbieri, O. Benhar, A. De Pace, and A. Lovato. Neutrino-nucleus cross section within the extended factorization scheme. Phys. Rev. C, 99:025502, Feb 2019. doi:10.1103/PhysRevC.99.025502.

[43] A. Lovato, J. Carlson, S. Gandolfi, N. Rocco, and R. Schiavilla. Ab initio study of (ν_ℓ, ℓ^-) and $(\overline{\nu}_\ell, \ell^+)$ inclusive scattering in ^{12}C: Confronting the miniboone and t2k ccqe data. Phys. Rev. X, 10:031068, Sep 2020. doi:10.1103/PhysRevX.10.031068.

[44] B. D. Serot and J. D. Walecka. The Relativistic Nuclear Many Body Problem. Adv. Nucl. Phys., 16:1–327, 1986.

[45] J. Carlson and R. Schiavilla. Structure and dynamics of few-nucleon systems. Rev. Mod. Phys., 70:743–841, Jul 1998. doi:10.1103/RevModPhys.70.743.

[46] W. Greiner and J. Reinhardt. Quantum Electrodynamics. Physics and Astronomy. Springer Berlin Heidelberg, 2008. doi:10.1007/978-3-540-87561-1.

[47] J. M. Udías. Análisis Relativista del proceso $(e, e'p)$ en Núcleos Complejos. PhD thesis, Instituto de Estructura de la Materia, C.S.I.C., Madrid, 1993.

[48] R. González-Jiménez. Parity violating elastic and quasielastic electron scattering from nucleons and nuclei. PhD thesis, Universidad de Sevilla, 2014.

[49] T. W. Donnelly. Electron scattering and neutrino reactions in nuclei. Prog. Part. Nucl. Phys., 13:183 – 236, 1985. doi:10.1016/0146-6410(85)90008-0.

[50] J. E. Amaro, M. B. Barbaro, J. A. Caballero, T. W. Donnelly, A. Molinari, and I. Sick. Using electron scattering superscaling to predict charge-changing neutrino cross sections in nuclei. Phys. Rev. C, 71:015501, Jan 2005. doi:10.1103/PhysRevC.71.015501.

[51] V. Lyubushkin et al. A Study of quasi-elastic muon neutrino and antineutrino scattering in the NOMAD experiment. Eur. Phys. J. C, 63:355–381, 2009. doi:10.1140/epjc/s10052-009-1113-0.

[52] C. Rubbia et al. Underground operation of the icarus t600 lar-tpc: first results. Journal of Instrumentation, 6(07):P07011, jul 2011. doi:10.1088/1748-0221/6/07/P07011.

[53] A.M. Szelc. Developing lar scintillation light collection ideas in the short baseline neutrino detector. Journal of Instrumentation, 11(02):C02018, feb 2016. doi:10.1088/1748-0221/11/02/C02018.

[54] D. Dutta, , et al. Quasielastic $(e, e^{'}p)$ reaction on ^{12}C,^{56} Fe, and ^{197}Au. Phys. Rev. C, 68:064603, Dec 2003. doi:10.1103/PhysRevC.68.064603.

[55] K. G. Fissum, , et al. Dynamics of the quasielastic ^{16}O$(e, e^{'}p)$ reaction at $Q^2 \approx 0.8$ (GeV/c)^2. Phys. Rev. C, 70:034606, Sep 2004. doi:10.1103/PhysRevC.70.034606.

[56] G.J. Kramer, H.P. Blok, J.F.J. Van Den Brand, H.J. Bulten, R. Ent, E. Jans, J.B.J.M. Lanen, L. Lapikás, H. Nann, E.N.M. Quint, G. Van Der Steenhoven, P.K.A. De Witt Huberts, and G.J. Wagner. Proton ground-state correlations in ^{40}Ca studied with the reaction ^{40}Ca(e,e'p)^{49}K. Physics Letters B, 227(2):199–203, 1989. doi:10.1016/S0370-2693(89)80022-X.

[57] Y. Yasuda et al. Spectroscopic factors and strength distributions for the deeply bound orbitals in ^{40}Ca obtained from the $(\vec{p}, 2p)$ reaction at 392MeV. Phys. Rev. C, 81:044315, Apr 2010. doi:10.1103/PhysRevC.81.044315.

[58] S. S. Volkov et al. (p,2p) and (p,pn) quasielastic scattering reactions at 1-GeV and deformation properties of the d shell nuclei. (In Russian). Sov. J. Nucl. Phys., 52:848–857, 1990.

[59] L. Jiang et al. Determination of the argon spectral function from $(e, e^{'}p)$ data. Phys. Rev. D, 105:112002, Jun 2022. doi:10.1103/PhysRevD.105.112002.

[60] J. M. Udías, P. Sarriguren, E. Moya de Guerra, E. Garrido, and J. A. Caballero. Spectroscopic factors in ^{40}Ca and ^{208}Pb from (e,e'p): Fully relativistic analysis. Phys. Rev. C, 48:2731–2739, Dec 1993. doi:10.1103/PhysRevC.48.2731.

[61] C. Giusti, A. Meucci, F. D. Pacati, G. Co', and V. De Donno. Quasifree $(e, e^{'}p)$ reactions on nuclei with neutron excess. Phys. Rev. C, 84:024615, Aug 2011. doi:10.1103/PhysRevC.84.024615.

[62] M. C. Atkinson, H. P. Blok, L. Lapikás, R. J. Charity, and W. H. Dickhoff. Validity of the distorted-wave impulse-approximation description of ^{40}Ca$(e, e^{'}p)^{39}$K data using only ingredients from a nonlocal dispersive optical model. Phys. Rev. C, 98:044627, Oct 2018. doi:10.1103/PhysRevC.98.044627.

[63] K. S. Egiyan et al. Measurement of two- and three-nucleon short-range correlation probabilities in nuclei. Phys. Rev. Lett., 96:082501, Mar 2006. doi:10.1103/PhysRevLett.96.082501.

[64] M. Duer et al. Probing high-momentum protons and neutrons in neutron-rich nuclei. Nature, 560:617–621, Aug 2018. doi:10.1038/s41586-018-0400-z.

[65] C. Mahaux and R. Sartor. Extrapolation from positive to negative energy of the woods-saxon parametrization of the n-^{208}Pb mean field. Nuclear Physics A, 468(2):193–236, 1987. doi:10.1016/0375-9474(87)90515-X.

[66] Z.Y. Ma and J. Wambach. Quasiparticle properties of protons in ^{208}Pb. Physics Letters B, 256(1):1–5, 1991. doi:10.1016/0370-2693(91)90207-7.

[67] C. Ciofi degli Atti. In-medium short-range dynamics of nucleons: Recent theoretical and experimental advances. Physics Reports, 590:1–85, 2015. doi:10.1016/j.physrep.2015.06.002.

[68] C. Colle, W. Cosyn, and J. Ryckebusch. Final-state interactions in two-nucleon knockout reactions. Phys. Rev. C, 93:034608, Mar 2016. doi:10.1103/PhysRevC.93.034608.

[69] O. Benhar, A. Fabrocini, S. Fantoni, and I. Sick. Spectral function of finite nuclei and scattering of GeV electrons. Nuclear Physics A, 579(3):493 – 517, 1994. doi:10.1016/0375-9474(94)90920-2.

[70] A. M. Ankowski, O. Benhar, and M. Sakuda. Determination of the proton spectral function of C12 from (e,e'p) data. Phys. Rev. C, 110(5):054612, 2024. doi:10.1103/PhysRevC.110.054612.

[71] R. González-Jiménez, M. B. Barbaro, J. A. Caballero, T. W. Donnelly, N. Jachowicz, G. D. Megias, K. Niewczas, A. Nikolakopoulos, J. W. Van Orden, and J. M. Udías. Neutrino energy reconstruction from semi-inclusive samples. Phys. Rev. C, 105:025502, Feb 2022. doi:10.1103/PhysRevC.105.025502.

[72] J. M. Franco-Patino, R. González-Jiménez, S. Dolan, M. B. Barbaro, J. A. Caballero, G. D. Megias, and J. M. Udias. Final state interactions in semi-inclusive neutrino-nucleus scattering: Applications to the t2k and MINERνA experiments. Phys. Rev. D, 106:113005, Dec 2022. doi:10.1103/PhysRevD.106.113005.

[73] O. Benhar, N. Farina, H. Nakamura, M. Sakuda, and R. Seki. Electron- and neutrino-nucleus scattering in the impulse approximation regime. Phys. Rev. D, 72:053005, Sep 2005. doi:10.1103/PhysRevD.72.053005.

[74] International Atomic Energy Agency Nuclear Data Section. URL: https://www-nds.iaea.org/.

[75] K. Niewczas. Multinucleon knock-out in neutrino-nucleus scattering. PhD thesis, Ghent University, 2023.

[76] H. Kurasawa and T. Suzuki. Quasielastic electron scattering in the relativistic $\sigma\omega$ model. Nuclear Physics A, 445(4):685–705, 1985. doi:10.1016/0375-9474(85)90566-4.

[77] K. Wehrberger and F. Beck. Relativistic random-phase-approximation response function for quasielastic electron scattering in local density approximation. Phys. Rev. C, 35:298–304, Jan 1987. doi:10.1103/PhysRevC.35.298.

[78] K. Wehrberger and F. Beck. Erratum: Relativistic random-phase-approximation response function for quasielastic electron scattering in local density approximation. Phys. Rev. C, 35:2337–2337, Jun 1987. doi:10.1103/PhysRevC.35.2337.

[79] V. Pandey, N. Jachowicz, M. Martini, R. González-Jiménez, J. Ryckebusch, T. Van Cuyck, and N. Van Dessel. Impact of low-energy nuclear excitations on neutrino-nucleus scattering at miniboone and t2k kinematics. Phys. Rev. C, 94:054609, Nov 2016. doi:10.1103/PhysRevC.94.054609.

[80] M.M. Sharma, M.A. Nagarajan, and P. Ring. Rho meson coupling in the relativistic mean field theory and description of exotic nuclei. Physics Letters B, 312(4):377 – 381, 1993. doi:10.1016/0370-2693(93)90970-S.

[81] J. M. Udías, P. Sarriguren, E. Moya de Guerra, E. Garrido, and J. A. Caballero. Relativistic versus nonrelativistic optical potentials in a(e,e'p)b reactions. Phys. Rev. C, 51:3246–3255, Jun 1995. doi:10.1103/PhysRevC.51.3246.

[82] M. C. Martínez, P. Lava, N. Jachowicz, J. Ryckebusch, K. Vantournhout, and J. M. Udías. Relativistic models for quasielastic neutrino scattering. Phys. Rev. C, 73:024607, Feb 2006. doi:10.1103/PhysRevC.73.024607.

[83] J. J. Kelly. Simple parametrization of nucleon form factors. Phys. Rev. C, 70:068202, Dec 2004. doi:10.1103/PhysRevC.70.068202.

[84] N. J. Baker et al. Quasielastic neutrino scattering: A measurement of the weak nucleon axial-vector form factor. Phys. Rev. D, 23:2499–2505, Jun 1981. doi:10.1103/PhysRevD.23.2499.

[85] K. L. Miller et al. Study of the reaction $\nu_\mu d \to \mu^- pp_s$. Phys. Rev. D, 26:537–542, Aug 1982. doi:10.1103/PhysRevD.26.537.

[86] T. Kitagaki et al. High-energy quasielastic $\nu_\mu n \to \mu^- p$ scattering in deuterium. Phys. Rev. D, 28:436–442, Aug 1983. doi:10.1103/PhysRevD.28.436.

[87] L. A. Ahrens et al. Measurement of neutrino-proton and antineutrino-proton elastic scattering. Phys. Rev. D, 35:785–809, Feb 1987. doi:10.1103/PhysRevD.35.785.

[88] V. Bernard, L. Elouadrhiri, and U. Meissner. Axial structure of the nucleon. Journal of Physics G: Nuclear and Particle Physics, 28(1):R1, nov 2001. doi:10.1088/0954-3899/28/1/201.

[89] G. S. Bali, Lorenzo Barca, Sara Collins, Michael Gruber, Marius Löffler, Andreas Schäfer, Wolfgang Söldner, Philipp Wein, Simon Weishäupl, and Thomas Wurm. Nucleon axial structure from lattice QCD. JHEP, 05:126, 2020. doi:10.1007/JHEP05(2020)126.

[90] Y.-C. Jang, R. Gupta, B. Yoon, and T. Bhattacharya. Axial vector form factors from lattice qcd that satisfy the pcac relation. Phys. Rev. Lett., 124:072002, Feb 2020. doi:10.1103/PhysRevLett.124.072002.

[91] S. Park, R. Gupta, B. Yoon, S. Mondal, T. Bhattacharya, Y.-C. Jang, B. Joó, and F. Winter. Precision nucleon charges and form factors using (2+1)-flavor lattice qcd. Phys. Rev. D, 105:054505, Mar 2022. doi:10.1103/PhysRevD.105.054505.

[92] A. S. Meyer, A. Walker-Loud, and C. Wilkinson. Status of Lattice QCD Determination of Nucleon Form Factors and their Relevance for the Few-GeV Neutrino Program. Ann. Rev. Nucl. Part. Sci., 72:205–232, 2022. doi:10.1146/annurev-nucl-010622-120608.

[93] T. Cai et al. Measurement of the axial vector form factor from antineutrino–proton scattering. Nature, 614(7946):48–53, 2023. doi:10.1038/s41586-022-05478-3.

[94] A. Lovato, N. Rocco, and N. Steinberg. One and Two-Body Current Contributions to Lepton-Nucleus Scattering. 12 2023. arXiv:2312.12545.

[95] A. Nikolakopoulos. Towards a more complete description of final-state interactions in electroweak single-pion production off atomic nuclei. PhD thesis, Ghent University, 2021.

[96] R. González-Jiménez, M. B. Barbaro, J. A. Caballero, T. W. Donnelly, N. Jachowicz, G. D. Megias, K. Niewczas, A. Nikolakopoulos, and J. M. Udías. Constraints in modeling the quasielastic response in inclusive lepton-nucleus scattering. Phys. Rev. C, 101:015503, Jan 2020. doi:10.1103/PhysRevC.101.015503.

[97] R. González-Jiménez, A. Nikolakopoulos, N. Jachowicz, and J. M. Udías. Nuclear effects in electron-nucleus and neutrino-nucleus scattering within a relativistic quantum mechanical framework. Phys. Rev. C, 100:045501, Oct 2019. doi:10.1103/PhysRevC.100.045501.

[98] A. Nikolakopoulos, N. Jachowicz, N. Van Dessel, K. Niewczas, R. González-Jiménez, J. M. Udías, and V. Pandey. Electron versus muon neutrino induced cross sections in charged current quasielastic processes. Phys. Rev. Lett., 123:052501, Jul 2019. doi:10.1103/PhysRevLett.123.052501.

[99] R. González-Jiménez, G. D. Megias, M. B. Barbaro, J. A. Caballero, and T. W. Donnelly. Extensions of superscaling from relativistic mean field theory: The susav2 model. Phys. Rev. C, 90:035501, Sep 2014. doi:10.1103/PhysRevC.90.035501.

[100] M. B. Barbaro, J. A. Caballero, A. De Pace, T. W. Donnelly, R. González-Jiménez, and G. D. Megias. Mean-field and two-body nuclear effects in inclusive electron scattering on argon, carbon, and titanium: The superscaling approach. Phys. Rev. C, 99:042501, Apr 2019. doi:10.1103/PhysRevC.99.042501.

[101] G. D. Megias, M. V. Ivanov, R. González-Jiménez, M. B. Barbaro, J. A. Caballero, T. W. Donnelly, and J. M. Udías. Nuclear effects in neutrino and antineutrino charged-current quasielastic scattering at MINERνA kinematics. Phys. Rev. D, 89:093002, May 2014. doi:10.1103/PhysRevD.89.093002.

[102] J. Jourdan. Quasi-elastic response functions. the coulomb sum revisited. Nuclear Physics A, 603(2):117–160, 1996. doi:10.1016/0375-9474(96)00143-1.

[103] P. Barreau, M. Bernheim, J. Duclos, J.M. Finn, Z. Meziani, J. Morgenstern, J. Mougey, D. Royer, B. Saghai, D. Tarnowski, S. Turck-Chieze, M. Brussel, G.P. Capitani, E. De Sanctis, S. Frullani, F. Garibaldi, D.B. Isabelle, E. Jans, I. Sick, and P.D. Zimmerman. Deep-inelastic electron scattering from carbon. Nuclear Physics A, 402(3):515–540, 1983. doi:10.1016/0375-9474(83)90217-8.

[104] E. D. Cooper, S. Hama, B. C. Clark, and R. L. Mercer. Global dirac phenomenology for proton-nucleus elastic scattering. Phys. Rev. C, 47:297–311, Jan 1993. doi:10.1103/PhysRevC.47.297.

[105] J.D. Walecka. Theoretical Nuclear and Subnuclear Physics. World Scientfic, Imperial College Press, 2004. doi:10.1142/5500.

[106] T. E. O. Ericson and W. Weise. Pions and Nuclei. Clarendon Press, Oxford, UK, 1988.

[107] M. E. Peskin and D. V. Schroeder. An Introduction to quantum field theory. Addison-Wesley, Reading, USA, 1995. doi:10.1201/9780429503559.

[108] R. González-Jiménez, N. Jachowicz, K. Niewczas, J. Nys, V. Pandey, T. Van Cuyck, and N. Van Dessel. Electroweak single-pion production off the nucleon: From threshold to high invariant masses. Phys. Rev. D, 95:113007, Jun 2017. doi:10.1103/PhysRevD.95.113007.

[109] J. Nieves, I. Ruiz Simo, and M. J. Vicente Vacas. Inclusive charged-current neutrino-nucleus reactions. Phys. Rev. C, 83:045501, Apr 2011. doi:10.1103/PhysRevC.83.045501.

[110] O. Lalakulich, E. A. Paschos, and G. Piranishvili. Resonance production by neutrinos: The second resonance region. Phys. Rev. D, 74:014009, Jul 2006. doi:10.1103/PhysRevD.74.014009.

[111] J. Ryckebusch, V. Van der Sluys, M. Waroquier, L.J.H.M. Kester, W.H.A. Hesselink, E. Jans, and A. Zondervan. Two-nucleon knockout contributions to the ^{12}C$(e, e'p)$ reaction in the dip and $\Delta(1232)$ regions. Physics Letters B, 333(3):310–315, 1994. doi:10.1016/0370-2693(94)90147-3.

[112] J. W. Van Orden and T. W. Donnelly. Mesonic processes in deep-inelastic electron scattering from nuclei. Annals of Physics, 131(2):451–493, 1981. doi:10.1016/0003-4916(81)90038-5.

[113] A. De Pace, M. Nardi, W.M. Alberico, T.W. Donnelly, and A. Molinari. The 2p-2h electromagnetic response in the quasielastic peak and beyond. Nuclear Physics A, 726(3):303 – 326, 2003. doi:10.1016/S0375-9474(03)01625-7.

[114] J. E. Amaro, M. B. Barbaro, J. A. Caballero, R. González-Jiménez, G. D. Megias, and I. Ruiz Simo. Electron- versus neutrino-nucleus scattering. J. Phys. G: Nucl. Part. Phys., 47(12):124001, nov 2020. doi:10.1088/1361-6471/abb128.

[115] N. Rocco, A. Lovato, and O. Benhar. Unified description of electron-nucleus scattering within the spectral function formalism. Phys. Rev. Lett., 116:192501, May 2016. doi:10.1103/PhysRevLett.116.192501.

[116] J.E. Amaro, G. Có, and A.M. Lallena. Meson-exchange currents in quasi-elastic electron scattering from ^{12}C and ^{40}Ca nuclei. Nuclear Physics A, 578(3):365–396, 1994. doi:10.1016/0375-9474(94)90752-8.

[117] S. Boffi and M. Radici. Quasielastic electron scattering at high momenta beyond the impulse approximation. Phys. Lett. B, 242:151–157, 1990. doi:10.1016/0370-2693(90)91452-H.

[118] V. Van der Sluys, J. Ryckebusch, and M. Waroquier. Two-body currents in inclusive electron scattering. Phys. Rev. C, 51:2664–2670, May 1995. doi:10.1103/PhysRevC.51.2664.

[119] J. Carlson, J. Jourdan, R. Schiavilla, and I. Sick. Longitudinal and transverse quasielastic response functions of light nuclei. Phys. Rev. C, 65:024002, Jan 2002. doi:10.1103/PhysRevC.65.024002.

[120] A. Lovato, S. Gandolfi, J. Carlson, S. C. Pieper, and R. Schiavilla. Electromagnetic and neutral-weak response functions of ^{4}He and ^{12}C. Phys. Rev. C, 91:062501, Jun 2015. doi:10.1103/PhysRevC.91.062501.

[121] A. Lovato, S. Gandolfi, J. Carlson, S. C. Pieper, and R. Schiavilla. Electromagnetic response of ^{12}C: A first-principles calculation. Phys. Rev. Lett., 117:082501, Aug 2016. doi:10.1103/PhysRevLett.117.082501.

[122] L. Andreoli, J. Carlson, A. Lovato, S. Pastore, N. Rocco, and R. B. Wiringa. Electron scattering on $a = 3$ nuclei from quantum monte carlo based approaches. Phys. Rev. C, 105:014002, Jan 2022. doi:10.1103/PhysRevC.105.014002.

[123] L. Andreoli, G. B. King, S. Pastore, M. Piarulli, J. Carlson, S. Gandolfi, and R. B. Wiringa. Quantum monte carlo calculations of electron scattering from ^{12}C in the short-time approximation. Phys. Rev. C, 110:064004, Dec 2024. doi:10.1103/PhysRevC.110.064004.

[124] M. J. Dekker, P. J. Brussaard, and J. A. Tjon. Relativistic meson exchange and isobar currents in electron scattering: Noninteracting fermi gas analysis. Phys. Rev. C, 49:2650–2670, May 1994. doi:10.1103/PhysRevC.49.2650.

[125] Y. Umino, J. M. Udias, and P. J. Mulders. Exchange current corrections to neutrino-nucleus scattering. Phys. Rev. Lett., 74:4993–4996, Jun 1995. doi:10.1103/PhysRevLett.74.4993.

[126] Y. Umino and J. M. Udias. Exchange current corrections to neutrino-nucleus scattering. i. nuclear matter. Phys. Rev. C, 52:3399–3415, Dec 1995. doi:10.1103/PhysRevC.52.3399.

[127] J.E. Amaro, M.B. Barbaro, J.A. Caballero, T.W. Donnelly, and A. Molinari. Gauge and lorentz invariant one-pion exchange currents in electron scattering from a relativistic fermi gas. Physics Reports, 368(4):317–407, 2002. doi:10.1016/S0370-1573(02)00195-3.

[128] J. E. Amaro, M. B. Barbaro, J. A. Caballero, and F. Kazemi Tabatabaei. Semirelativistic meson-exchange currents in (e, e') and $(e, e'p)$ reactions. Phys. Rev. C, 68:014604, Jul 2003. doi:10.1103/PhysRevC.68.014604.

[129] J.A. Caballero, T.W. Donnelly, E. Moya de Guerra, and J.M. Udías. Analysis of factorization in (e,e'p) reactions: A survey of the relativistic plane wave impulse approximation. Nuclear Physics A, 632(3):323 – 362, 1998. doi:10.1016/S0375-9474(97)00817-8.

[130] E. Hernández, J. Nieves, and M. Valverde. Weak pion production off the nucleon. Phys. Rev. D, 76:033005, Aug 2007. doi:10.1103/PhysRevD.76.033005.

[131] I.S. Towner. Enhancement in axial-charge matrix elements from meson-exchange currents. Nuclear Physics A, 542(4):631–658, 1992. doi:10.1016/0375-9474(92)90261-H.

[132] V. L. Martinez-Consentino, I. Ruiz Simo, and J. E. Amaro. Meson-exchange currents and superscaling analysis with relativistic effective mass of quasielastic electron scattering from ^{12}C. Phys. Rev. C, 104:025501, Aug 2021. doi:10.1103/PhysRevC.104.025501.

[133] J. E. Amaro, V. L. Martinez-Consentino, E. Ruiz Arriola, and I. Ruiz Simo. Global superscaling analysis of quasielastic electron scattering with relativistic effective mass. Phys. Rev. C, 98:024627, Aug 2018. doi:10.1103/PhysRevC.98.024627.

[134] V. L. Martinez-Consentino, I. Ruiz Simo, and J. E. Amaro. Meson-exchange currents and superscaling analysis with relativistic effective mass of quasielastic electron scattering from ^{12}C. Phys. Rev. C, 104:025501, Aug 2021. doi:10.1103/PhysRevC.104.025501.

[135] M. V. Ivanov and A. N. Antonov. Superscaling analysis of inclusive electron and (anti)neutrino scattering within the coherent density fluctuation model. Phys. Rev. C, 109:064621, Jun 2024. doi:10.1103/PhysRevC.109.064621.

[136] I. Ruiz Simo, J. E. Amaro, M. B. Barbaro, A. De Pace, J. A. Caballero, and T. W. Donnelly. Relativistic model of 2p-2h meson exchange currents in (anti)neutrino scattering. Journal of Physics G: Nuclear and Particle Physics, 44(6):065105, apr 2017. doi:10.1088/1361-6471/aa6a06.

[137] L. Gu et al. Measurement of the Ar$(e, e^{'}p)$ and Ti$(e, e^{'}p)$ cross sections in jefferson lab hall a. Phys. Rev. C, 103:034604, Mar 2021. doi:10.1103/PhysRevC.103.034604.

[138] M. Khachatryan et al. Electron-beam energy reconstruction for neutrino oscillation measurements. Nature, 599(7886):565–570, 2021. doi:10.1038/s41586-021-04046-5.

[139] A. Bodek, M. E. Christy, Z. Lin, G. M. Bulugean, A. M. Delgado, A. M. Ankowski, G. D. Megias, and J. Tena Vidal. Global Extraction of the ^{12}C Nuclear Electromagnetic Response Functions ($\mathcal{R}_L$ and $\mathcal{R}_T$) and Comparisons to Nuclear Theory and Neutrino/Electron Monte Carlo Generators. 2024. arXiv:2409.10637.

[140] J.E Sobczyk, N. Rocco, and A. Lovato. Modeling inclusive electron-nucleus scattering with bayesian artificial neural networks. Physics Letters B, 859:139142, 2024. doi:10.1016/j.physletb.2024.139142.

[141] B. Acharya, J. E. Sobczyk, S. Bacca, G. Hagen, and W. Jiang. ^{16}O electroweak response functions from first principles. Phys. Rev. Lett., 134:202501, May 2025. doi:10.1103/PhysRevLett.134.202501.

[142] Z. E. Meziani, P. Barreau, M. Bernheim, J. Morgenstern, S. Turck-Chieze, R. Altemus, J. McCarthy, L. J. Orphanos, R. R. Whitney, G. P. Capitani, E. De Sanctis, S. Frullani, and F. Garibaldi. Coulomb sum rule for ^{40}Ca, ^{48}Ca, and ^{56}Fe for $|\vec{q}| <\sim 550$MeV/c. Phys. Rev. Lett., 52:2130–2133, Jun 1984. doi:10.1103/PhysRevLett.52.2130.

[143] Z. E. Meziani, P. Barreau, M. Bernheim, J. Morgenstern, S. Turck-Chieze, R. Altemus, J. McCarthy, L. J. Orphanos, R. R. Whitney, G. P. Capitani, E. De Sanctis, S. Frullani, and F. Garibaldi. Transverse response functions in deep-inelastic electron scattering for ^{40}Ca, ^{48}Ca, and ^{56}Fe. Phys. Rev. Lett., 54:1233–1236, Mar 1985. doi:10.1103/PhysRevLett.54.1233.

[144] C. F. Williamson, T. C. Yates, W. M. Schmitt, M. Osborn, M. Deady, Peter D. Zimmerman, C. C. Blatchley, Kamal K. Seth, M. Sarmiento, B. Parker, Yanhe Jin, L. E. Wright, and D. S. Onley. Quasielastic electron scattering from ^{40}Ca. Phys. Rev. C, 56:3152–3172, Dec 1997. doi:10.1103/PhysRevC.56.3152.

[145] N. Jachowicz and A. Nikolakopoulos. Nuclear medium effects in neutrino- and antineutrino-nucleus scattering. Eur. Phys. J. Spec. Top., 230(24):4339–4356, 2021. doi:10.1140/epjs/s11734-021-00286-8.

[146] J. E. Sobczyk, B. Acharya, S. Bacca, and G. Hagen. Ab initio computation of the longitudinal response function in ^{40}Ca. Phys. Rev. Lett., 127:072501, Aug 2021. doi:10.1103/PhysRevLett.127.072501.

[147] J. E. Sobczyk, B. Acharya, S. Bacca, and G. Hagen. ^{40}Ca transverse response function from coupled-cluster theory. Phys. Rev. C, 109:025502, Feb 2024. doi:10.1103/PhysRevC.109.025502.

[148] T. Franco-Munoz, J. García-Marcos, R. González-Jiménez, and J. M. Udías. Relativistic two-body currents for one-nucleon knockout in electron-nucleus scattering. Phys. Rev. C, 108(6):064608, 2023. doi:10.1103/PhysRevC.108.064608.

[149] R. R. Whitney, I. Sick, J. R. Ficenec, R. D. Kephart, and W. P. Trower. Quasielastic electron scattering. Phys. Rev. C, 9:2230–2235, Jun 1974. doi:10.1103/PhysRevC.9.2230.

[150] J. S. O'Connell et al. Electromagnetic excitation of the delta resonance in nuclei. Phys. Rev. C, 35:1063–1071, Mar 1987. doi:10.1103/PhysRevC.35.1063.

[151] R. M. Sealock et al. Electroexcitation of the $\Delta(1232)$ in nuclei. Phys. Rev. Lett., 62:1350–1353, Mar 1989. doi:10.1103/PhysRevLett.62.1350.

[152] D. T. Baran, B. F. Filippone, D. Geesaman, M. Green, R. J. Holt, H. E. Jackson, J. Jourdan, R. D. McKeown, R. G. Milner, J. Morgenstern, D. H. Potterveld, R. E. Segel, P. Seidl, R. C. Walker, and B. Zeidman. Δ electroproduction and inelastic charge scattering from carbon and iron. Phys. Rev. Lett., 61:400–403, Jul 1988. doi:10.1103/PhysRevLett.61.400.

[153] D. S. Bagdasaryan et al. Measurement of the spectra of (e,e') scattering ^{9}Be and ^{12}C nuclei in the inelastic region at q^2 approximately 0.4 (gev/c)^2. 1988. YERPHI-1077-40-88.

[154] M. Mihovilovič et al. Measurement of the $^{12}\mathrm{C}(e,e')$ Cross Sections at $Q^2 = 0.8\,\mathrm{GeV}^2/c^2$. Few Body Syst., 65(3):78, 2024. doi:10.1007/s00601-024-01944-y.

[155] M. Anghinolfi et al. Quasielastic and inelastic inclusive electron scattering from an oxygen jet target. Nucl. Phys. A, 602:405–422, 1996. doi:10.1016/0375-9474(96)00093-0.

[156] G. D. Megias, T. W. Donnelly, O. Moreno, C. F. Williamson, J. A. Caballero, R. González-Jiménez, A. De Pace, M. B. Barbaro, W. M. Alberico, M. Nardi, and J. E. Amaro. Meson-exchange currents and quasielastic predictions for charged-current neutrino-^{12}C scattering in the superscaling approach. Phys. Rev. D, 91:073004, Apr 2015. doi:10.1103/PhysRevD.91.073004.

[157] T. Van Cuyck, N. Jachowicz, R. González-Jiménez, J. Ryckebusch, and N. Van Dessel. Seagull and pion-in-flight currents in neutrino-induced $1n$ and $2n$ knockout. Phys. Rev. C, 95:054611, May 2017. doi:10.1103/PhysRevC.95.054611.

[158] V. L. Martinez-Consentino, J. E. Amaro, and I. Ruiz Simo. Semiempirical formula for electroweak response functions in the two-nucleon emission channel in neutrino-nucleus scattering. Phys. Rev. D, 104:113006, Dec 2021. doi:10.1103/PhysRevD.104.113006.

[159] A. Nikolakopoulos, V. Pandey, J. Spitz, and N. Jachowicz. Modeling quasielastic interactions of monoenergetic kaon decay-at-rest neutrinos. Phys. Rev. C, 103:064603, Jun 2021. doi:10.1103/PhysRevC.103.064603.

[160] K. Abe et al. First t2k measurement of transverse kinematic imbalance in the muon-neutrino charged-current single-π^+ production channel containing at least one proton. Phys. Rev. D, 103:112009, Jun 2021. doi:10.1103/PhysRevD.103.112009.

[161] P. Abratenko et al. First double-differential measurement of kinematic imbalance in neutrino interactions with the microboone detector. Phys. Rev. Lett., 131:101802, Sep 2023. doi:10.1103/PhysRevLett.131.101802.

[162] J. Kleykamp et al. Simultaneous measurement of ν_μ quasielasticlike cross sections on ch, c, h_2O, fe, and pb as a function of muon kinematics at minerva. Phys. Rev. Lett., 130:161801, Apr 2023. doi:10.1103/PhysRevLett.130.161801.

[163] T. Leitner and U. Mosel. Neutrino-nucleus scattering reexamined: Quasielastic scattering and pion production entanglement and implications for neutrino energy reconstruction. Phys. Rev. C, 81:064614, Jun 2010. doi:10.1103/PhysRevC.81.064614.

[164] K. Abe et al. Measurement of double-differential muon neutrino charged-current interactions on c_8h_8 without pions in the final state using the t2k off-axis beam. Phys. Rev. D, 93:112012, Jun 2016. doi:10.1103/PhysRevD.93.112012.

[165] K. Abe et al. Measurement of inclusive double-differential ν_μ charged-current cross section with improved acceptance in the t2k off-axis near detector. Phys. Rev. D, 98:012004, Jul 2018. doi:10.1103/PhysRevD.98.012004.

[166] K. Abe et al. First measurement of the ν_μ charged-current cross section on a water target without pions in the final state. Phys. Rev. D, 97:012001, Jan 2018. doi:10.1103/PhysRevD.97.012001.

[167] K. Abe et al. Simultaneous measurement of the muon neutrino charged-current cross section on oxygen and carbon without pions in the final state at t2k. Phys. Rev. D, 101:112004, Jun 2020. doi:10.1103/PhysRevD.101.112004.

[168] A. A. Aguilar-Arevalo et al. First measurement of the muon neutrino charged current quasielastic double differential cross section. Phys. Rev. D, 81:092005, May 2010. doi:10.1103/PhysRevD.81.092005.

[169] A. A. Aguilar-Arevalo et al. First measurement of the muon antineutrino double-differential charged-current quasielastic cross section. Phys. Rev. D, 88:032001, Aug 2013. doi:10.1103/PhysRevD.88.032001.

[170] G. D. Megias, J. E. Amaro, M. B. Barbaro, J. A. Caballero, T. W. Donnelly, and I. Ruiz Simo. Charged-current neutrino-nucleus reactions within the superscaling meson-exchange current approach. Phys. Rev. D, 94:093004, Nov 2016. doi:10.1103/PhysRevD.94.093004.

[171] G. D. Megias, M. B. Barbaro, J. A. Caballero, J. E. Amaro, T. W. Donnelly, I. Ruiz Simo, and J. W. Van Orden. Neutrino-oxygen CC0π scattering in the SuSAv2-MEC model. J. Phys. G: Nucl. Part. Phys., 46(1):015104, dec 2018. doi:10.1088/1361-6471/aaf3ae.

[172] M. Martini and M. Ericson. Inclusive and pion production neutrino-nucleus cross sections. Phys. Rev. C, 90:025501, Aug 2014. doi:10.1103/PhysRevC.90.025501.

[173] A. Nikolakopoulos, R. González-Jiménez, K. Niewczas, J. Sobczyk, and N. Jachowicz. Modeling neutrino-induced charged pion production on water at t2k kinematics. Phys. Rev. D, 97:093008, May 2018. doi:10.1103/PhysRevD.97.093008.

[174] B. Eberly et al. Charged pion production in ν_μ interactions on hydrocarbon at $<E_\nu> = 4.0$ GeV. Phys. Rev. D, 92:092008, Nov 2015. doi:10.1103/PhysRevD.92.092008.

[175] M. Buizza Avanzini et al. Comparisons and challenges of modern neutrino-scattering experiments. Phys. Rev. D, 105:092004, May 2022. doi:10.1103/PhysRevD.105.092004.

[176] A. Nikolakopoulos, A. Lovato, and N. Rocco. Relativistic effects in green's function monte carlo calculations of neutrino-nucleus scattering. Phys. Rev. C, 109:014623, Jan 2024. doi:10.1103/PhysRevC.109.014623.

[177] S. Scherer and M. R. Schindler. Quantum Chromodynamics and Chiral Symmetry, pages 1–48. Springer Berlin Heidelberg, Berlin, Heidelberg, 2012. doi:10.1007/978-3-642-19254-8_1.

[178] C. Giusti and F.D. Pacati. Electron distortion in quasifree (e,e'p) reactions. Nuclear Physics A, 473(4):717 – 735, 1987. doi:10.1016/0375-9474(87)90276-4.

[179] Y. Jin, D. S. Onley, and L. E. Wright. Single particle analysis of (e,e') and the value of separated structure functions. Phys. Rev. C, 45:1333–1338, Mar 1992. doi:10.1103/PhysRevC.45.1333.

[180] J. M. Udías, J. A. Caballero, E. Moya de Guerra, Javier R. Vignote, and A. Escuderos. Relativistic mean field approximation to the analysis of $^{16}\mathrm{O}(e,e'p)^{15}\mathrm{N}$ data at $|Q^2| <\sim 0.4(\mathrm{GeV}/c)^2$. Phys. Rev. C, 64:024614, Jul 2001. doi:10.1103/PhysRevC.64.024614.

[181] A. V. Butkevich. Quasi-elastic neutrino charged-current scattering off medium-heavy nuclei: ^{40}ca and ^{40}ar. Phys. Rev. C, 85:065501, Jun 2012. doi:10.1103/PhysRevC.85.065501.

[182] H. Gil, C. H. Hyun, and K. Kim. Quasielastic electron scattering with the kids nuclear energy density functional. Phys. Rev. C, 104:044613, Oct 2021. doi:10.1103/PhysRevC.104.044613.

[183] A. V. Butkevich. Analysis of flux-integrated semiexclusive cross sections for charged-current quasielastic neutrino scattering off ^{40}Ar at energies available at the microboone experiment. Phys. Rev. C, 105:025501, Feb 2022. doi:10.1103/PhysRevC.105.025501.

[184] J. M. Franco-Patino, S. Dolan, R. González-Jiménez, M. B. Barbaro, J. A. Caballero, and G. D. Megias. New model comparison for semi-inclusive charged-current electron and muon neutrino scattering by ^{40}Ar in the energy range of the microboone experiment. Phys. Rev. D, 109:013004, Jan 2024. doi:10.1103/PhysRevD.109.013004.

[185] Y. Hayato and L. Pickering. The NEUT neutrino interaction simulation program library. Eur. Phys. J. ST, 230(24):4469–4481, 2021. doi:10.1140/epjs/s11734-021-00287-7.

[186] C. Andreopoulos, C. Barry, S. Dytman, H. Gallagher, T. Golan, R. Hatcher, G. Perdue, and J. Yarba. The GENIE Neutrino Monte Carlo Generator: Physics and User Manual. 10 2015. arXiv:1510.05494.

[187] J. Isaacson, W. I. Jay, A. Lovato, P. A. N. Machado, and N. Rocco. Introducing a novel event generator for electron-nucleus and neutrino-nucleus scattering. Phys. Rev. D, 107(3):033007, 2023. doi:10.1103/PhysRevD.107.033007.

[188] T. Golan, J. T. Sobczyk, and J. Zmuda. NuWro: the Wroclaw Monte Carlo Generator of Neutrino Interactions. Nucl. Phys. B Proc. Suppl., 229-232:499–499, 2012. doi:10.1016/j.nuclphysbps.2012.09.136.

[189] J. McKean, R. González-Jiménez, M. Kabirnezhad, J. M. Udías, and Y. Uchida. Implementation of a relativistic distorted wave impulse approximation model into the NEUT event generator. 2 2025. arXiv:2502.10629.

[190] A. Nikolakopoulos, R. González-Jiménez, N. Jachowicz, K. Niewczas, F. Sánchez, and J. M. Udías. Benchmarking intranuclear cascade models for neutrino scattering with relativistic optical potentials. Phys. Rev. C, 105:054603, May 2022. doi:10.1103/PhysRevC.105.054603.

[191] A. Nikolakopoulos, A. Ershova, R. González-Jiménez, J. Isaacson, A. M. Kelly, K. Niewczas, N. Rocco, and F. Sánchez. Final-state interactions in neutrino-induced proton knockout from argon in MicroBooNE. Phys. Rev. C, 110(5):054611, 2024. doi:10.1103/PhysRevC.110.054611.

[192] J. D. Bjorken and S. D. Drell. Relativistic Quantum Mechanics. McGraw-Hill, New York, 1964.

[193] K. M. Watson. The effect of final state interactions on reaction cross sections. Phys. Rev., 88:1163–1171, Dec 1952. doi:10.1103/PhysRev.88.1163.

[194] L. Alvarez-Ruso, E. Hernández, J. Nieves, and M. J. Vicente Vacas. Watson's theorem and the $n\Delta(1232)$ axial transition. Phys. Rev. D, 93:014016, Jan 2016. doi:10.1103/PhysRevD.93.014016.

[195] S. Pastore, S. C. Pieper, R. Schiavilla, and R. B. Wiringa. Quantum monte carlo calculations of electromagnetic moments and transitions in $a \leq 9$ nuclei with meson-exchange currents derived from chiral effective field theory. Phys. Rev. C, 87:035503, Mar 2013. doi:10.1103/PhysRevC.87.035503.

[196] J. Carlson and R. Schiavilla. Inclusive electron scattering and pion degrees of freedom in light nuclei. Phys. Rev. C, 49:R2880–R2884, Jun 1994. doi:10.1103/PhysRevC.49.R2880.

[197] A. Fabrocini. Inclusive transverse response of nuclear matter. Phys. Rev. C, 55:338–348, Jan 1997. doi:10.1103/PhysRevC.55.338.

[198] P. R. Casale, J. E. Amaro, V. Belocchi, M. B. Barbaro, A. De Pace, and M. Martini. On the Interference between Meson Exchange and One-Body Currents in Quasielastic Electron Scattering. 3 2025. arXiv:2503.08391.

[199] J. Żmuda. Consistent Many-Body Models of Lepton-Nucleus Scattering in the Energy Range Between 500 and 1200 MeV. PhD thesis, University of Wroclaw, 2014.

[200] T. J. Leitner. Neutrino-Nucleus Interactions In A Coupled-Channel Hadronic Transport Model. PhD thesis, Justus-Liebig-Universität Giessen, 2009.

[201] J.D Walecka. A theory of highly condensed matter. Annals of Physics, 83(2):491–529, 1974. doi:10.1016/0003-4916(74)90208-5.